Second and Outer Coordination Sphere Effects in Nitrogenase, Hydrogenase, Formate Dehydrogenase, and CO Dehydrogenase

Sven T Stripp, Benjamin R Duffus, Vincent Fourmond, Christophe Léger, Silke Leimkühler, Shun Hirota, Yilin Hu, Andrew Jasniewski, Hideaki Ogata, Markus W Ribbe

Second and Outer Coordination Sphere Effects in Nitrogenase, Hydrogenase, Formate Dehydrogenase, and CO Dehydrogenase

Sven T. Stripp[1]*, Benjamin R. Duffus[2], Vincent Fourmond[3], Christophe Léger[3], Silke Leimkühler[2], Shun Hirota[4], Yilin Hu[5], Andrew Jasniewski[5], Hideaki Ogata[4,6], Markus W. Ribbe[5,7]

[1] Freie Universität Berlin, Experimental Molecular Biophysics, Berlin 14195, Germany

[2] University of Potsdam, Molecular Enzymology, Potsdam 14476, Germany

[3] Laboratoire de Bioénergétique et Ingénierie des Protéines, CNRS, Aix-Marseille Université, Institut de Microbiologie de la Méditerranée, Institut Microbiologie, Bioénergies et Biotechnologie, Marseille 13402, France

[4] Nara Institute of Science and Technology, Division of Materials Science, Graduate School of Science and Technology, Nara 630-0192, Japan

[5] University of California, Department of Molecular Biology & Biochemistry, Irvine 92697-3900, USA

[6] Hokkaido University, Institute of Low Temperature Science, Sapporo 060-0819, Japan

[7] University of California, Department of Chemistry, Irvine, CA 92697-2025, USA

*To whom correspondence should be addressed: sven.stripp@gmail.com

Abstract

Gases like H_2, N_2, CO_2, and CO are increasingly recognized as critical feedstock in ‘green’ energy conversion and as sources of nitrogen and carbon for the agricultural and chemical sectors. However, the industrial transformation of N_2, CO_2, and CO, and the production of H_2 requires significant energy input, rendering routines like steam reformation or the Haber process economic and environmental dead ends. Nature, on the other hand, performs similar tasks efficiently at ambient temperature and ambient pressure, exploiting gas-processing metalloenzymes (GPMs) that bind low-valent metal cofactors based on iron, nickel, molybdenum, tungsten, and sulfur. Such systems are studied to understand the biocatalytic principles of gas conversion, including N_2 fixation by nitrogenase, H_2 production by hydrogenase, as well as CO_2 and CO conversion by formate dehydrogenase, carbon monoxide dehydrogenase, and nitrogenase.

In this review, we emphasize the importance of the cofactor/protein interface, discussing how second and outer coordination sphere effects determine, modulate, and optimize the catalytic activity of GPMs. This may comprise ionic interactions in the second coordination sphere that shape the electron density distribution across the cofactor, hydrogen bonding changes, and allosteric effects. In the outer coordination sphere, proton transfer and electron transfer are discussed, alongside the role of hydrophobic substrate channels and protein structural changes. Combining the information gained from structural biology, enzyme kinetics, and various spectroscopic techniques, we aim towards a comprehensive understanding of catalysis beyond the first coordination sphere.

Contents

1 Introduction

Enzymes enhance the probability of a chemical reaction to proceed on biologically relevant time scales. Kinetic rates may differ by a factor of up to10^6, from the exclusively diffusion-limited enzymes carbonic anhydrase, catalase, or superoxide dismutase to average performers like RuBisCO that produces only three equivalents of product per second. To catalyze a given reaction, the enzyme must provide a specific binding pocket for reactants, *e.g.*, offering electrostatic interactions with polar and charged amino acid sidechains, the protein backbone, and water molecules. Additionally, hydrophobic interactions play an important role (*e.g.*, in the binding pockets of ATP synthase the separation of reactants and water drives ATP formation). Many enzymes rely on essential cofactors that are not formed by the protein fold. These may be organic 'coenzymes' (covalently bound prosthetic groups and loosely bound 'cosubstrates') or inorganic clusters of metal ions. The later defines the class of metalloenzymes.[1–3]

Metalloenzymes are ubiquitous throughout all kingdoms of life and catalyze important energy conversion reactions, often involving redox chemistry. The fast-performing enzymes mentioned above (carbonic anhydrase, catalase, and superoxide dismutase) are metalloenzymes as well. Introducing two prominent examples, photosystem II (PSII, oxygenic photosynthesis) and cytochrome *c* oxidase (C*c*O, aerobic respiration) are high-valent, gas-processing metalloenzymes (GPMs). At the 'oxygen evolving complex' of PSII, a high-potential heterometallic manganese cluster (Mn^{III}–Mn^{V}, E° ≈ 1.0 V vs. SHE) catalyzes water splitting[4–6] whereas C*c*O catalyzes the reverse reaction at a binuclear heme-copper center (E° ≈ 0.8 V vs. SHE, Fe^{II}–Fe^{IV}).[7–9]

In contrast, low-valent GPMs operate under more reducing conditions, exploiting soft, electron-rich metal ions in the catalytic activation of N_2, H_2, CO_2, and CO (E° ≈ –0.4 V vs. SHE).[10] Such systems carry cofactors reminiscent of abiotic metal clusters like pyrite, mackinawite, and pentlandite. These minerals show residual activity catalyzing CO_2-, N_2-, and proton reduction[11–13], but only as "molecularly tuned derivates"[14] within the active sites of GPMs like nitrogenase, hydrogenase, or CO dehydrogenase, can efficient turnover be achieved. From an evolutionary perspective, it is debatted whether mineral cofactors were a prerequisite for catalysis or optimized the activity of protoenzymes. Russell and co-workers argue that metalloenzymes seem to be older than all-organic enzymes[15], suggesting atmospheric CO_2 and hydrothermal H_2 and CH_4 as earliest sources of electrons and carbon.[16]

Similarily, Martin and co-workers argue that life could have evolved from gases that reacted with the help of transition metals.[17] Embedding metal ions or mineral cofactors, simple peptide "nests" may represent the onset of metalloenzyme evolution[18–20] that produced the GPMs discussed in this review, including nitrogenase (**Section 2**), hydrogenase (**Section 3**), as well as formate dehydrogenase and carbon monoxide dehydrogenase (FDH and CODH, **Section 4** and **Section 5**). All of these enzymes rely on iron, either as part of the active site cofactor (hydrogenase and nitrogenase) or in iron-sulfur clusters that primarily serve in long range electron transfer.[21] Further metal ions include nickel (CODH and [NiFe]-hydrogenase) and molybdenum (FDH and nitrogenase). In certain isoenzymes, molybdenum is replaced with tungsten (FDH), vanadium, or iron (nitrogenase). Such systems are studied to understand the biocatalytic principles of gas conversion that may inspire the design of biomimetic catalysts for the activation of N_2, CO_2, and CO as well as the production of H_2 as a climate-neutral fuel.

Second and outer coordination sphere effects critically impact the catalytic performance of GPMs. Although the influences are manifold and difficult to predict *a priori*, comparing the reaction stoichiometries (**Eq. 1–4**) certain similarities become evident:

Eq. 1 $N_2 + 8\,H^+ + 8\,e^- \rightarrow 2\,NH_3 + H_2$ (nitrogenase)

Eq. 2 $H_2 \rightleftharpoons 2\,H^+ + 2\,e^-$ (hydrogenase)

Eq. 3 $CO_2 + H^+ + e^- \rightleftharpoons HCOO^-$ (FDH)

Eq. 4 $CO + H_2O \rightleftharpoons CO_2 + 2\,H^+ + 2\,e^-$ (CODH)

Each enzyme catalyzes a redox reaction that involves one proton per electron, which hints at proton-coupled electron transfer (PCET)[22–24] as a common principle in GPMs. This demands (*i*) electron transfer to or from a redox site or redox partner in the outer coordination sphere of the metal ion coupled to (*ii*) proton transfer *via* polar amino acid residues or functional water molecules in the second coordination sphere (**Figure 1**). Proton transfer pathways and (*iii*) hydrophobic gas channels further modulate the exchange of reactants between active site and bulk solution, sometimes across several nanometers.[25] [FeFe]-hydrogenase, shown in **Figure 1**, illustrates how individual second coordination sphere effects may comprise (*iv*) hydrophobic interactions and (*v*) hydrogen-bonding contacts.[26] Moreover, the protonation state and polarity of the active site niche influences the (*vi*) charge distribution across the cofactor and redox centers in channeling distance.[27]

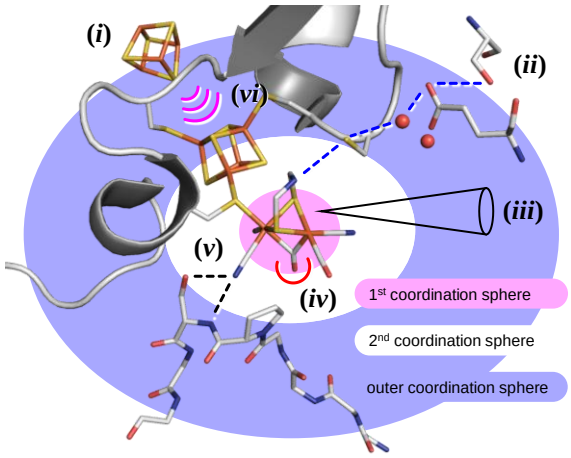

Figure 1 | Definitions. The figure shows the active site of [FeFe]-hydrogenase (PDB ID 4XDC). For this enzyme, the first coordination sphere (light magenta) is defined by the two iron ions of the catalytic cofactor and its ligands. The second coordination sphere (white) comprises a [4Fe-4S] cluster as well as (*iv*) hydrophobic interactions and (*v*) hydrogen-bonding contacts with the protein fold. 'Outer' coordination sphere effects include (*i*) electron transfer, (*ii*) proton transfer, (*iii*) hydrophobic gas channels, and (*vi*) electric field effects.

Long-distance effects play a crucial role in enzyme catalysis. Within each enzyme family, defined by a common active site structure, homologous enzymes may have very different catalytic properties in terms of turnover rates, catalytic bias (defined here as the ratio of the maximal rates in the two directions of the reactions[28]), reversibility (the requirement for a thermodynamic driving force to trigger catalysis[29]), and resistance to 'stress' (*e.g.*, sensitivity to O_2 or visible light). The immediate environment of the active sites in each family is very much conserved, but these enzymes differ by their protein sequences, cofactor composition, and quaternary structures. Nature therefore provides a quasi-infinite playground for examining outer coordination sphere effects in catalysis. For example, certain microorganisms produce many homologous enzymes to catalyze the same reaction (isoenzymes), which suggests that distinct catalytic properties are needed for different physiological functions.

In this article, we highlight and compare the role of second and outer coordination sphere effects on the activation of gaseous substrates such N_2, H_2, CO_2, or CO by various low-valent GPMs. We provide a comprehensive overview on protein variants that were found to affect the catalytic properties of nitrogenase, hydrogenase, FDH, and CODH. To understand or mimic GPMs, we emphasize that second and outer coordination sphere effects must not be neglected.

2 Nitrogenase

Nitrogen is an essential element for life necessary for the synthesis of biomolecules such as deoxyribonucleic acid (DNA), ribonucleic acid (RNA) and amino acids. While nitrogen can be found in many different chemical forms throughout atmospheric and geological sources, the largest reservoir of nitrogen on the surface of the Earth is found in the form of dinitrogen (N_2); a small, gaseous, nonpolar, diatomic molecule with a strong triple bond.[30] The strength of this bond is on the order of ~940 kJ/mol, which makes its scission into bioavailable forms, also called 'N_2 fixation', one of the most challenging transformations in Nature.

Two main processes are recognized as natural engines for N_2 fixation within the global nitrogen cycle): lighting strikes and biological N_2 fixation (BNF).[31–33] The high temperature environment in the air surrounding lightning causes N_2 to react with other components in the atmosphere, such as dioxygen (O_2), ozone (O_3), or oxygen-based radical species, forming various nitrogen oxides (NO_x).[31,34,35] The NO_x species are then converted to nitric acid (HNO_3) in the atmosphere, and brought down to the ground through rainfall or surface deposition, where the fixed nitrogen species can be utilized.[30,36] This lightning-based process requires extreme conditions such as high temperature, and is completely unregulated which causes many chemical pathways to converge and ultimately produce the highly oxidized HNO_3. In contrast, biological N_2 fixation occurs in diazotrophic microorganisms that span across multiple phyla between Bacteria and Archaea.[37–39] These organisms are found in many environments, such as surface soils, sediments, marine and fresh waters, and geothermal sources, in both the presence or absence of oxygen.[40–43] Some organisms can live freely within microbial communities, such as the obligate aerobe *Azotobacter vinelandii*[44], or the thermophilic methanogen *Methanococcus thermolithotrophicus*[45,46], while others, such as *Rhizobium leguminosarum*, form symbiotic relationships with specific plant species.[47,48] In all cases, N_2 is converted into the highly reduced nitrogen species ammonia (NH_3), although more often ammonium (NH_4^+) is the observed product.[30] Despite the wide variation in living conditions, each of the diazotrophs have genes that encode for the common enzyme nitrogenase.

Nitrogenase is a gas-processing metalloenzyme composed of two proteins, the reductase component NifH (also called the 'Fe protein'), as well as the catalytic component NifDK (also called the 'MoFe protein') that contains a unique molybdenum-containing iron sulfur cluster

called the M-cluster (or 'FeMoco').[49,50] There are also so-called 'alternative' nitrogenases that replace the Mo ion in FeMoco for either vanadium ('FeVco' in the VFe protein) or iron ('FeFeco' in the FeFe protein).[51] All nitrogenases are capable of reducing small molecule substrates, such as acetylene (C_2H_2) and cyanide (CN^-), under ambient temperature and pressure, but the native reaction catalyzed by the enzyme is the reduction of N_2 to NH_3.[51–53] In comparison, humans have developed the Haber-Bosch process that takes N_2 and dihydrogen (H_2) under high temperature and intense pressure conditions to yield NH_3.[54] Nitrogenase also catalyses the reduction of protons (H^+) to H_2, and in all reactions with other substrates (including N_2), some portion of the electron equivalents (or electron flux) is diverted to produce H_2.[50,55] During the native nitrogenase reaction H_2 is generated as an additional product (**Eq. 1**), but the mechanism of its synthesis is distinct from simple proton reduction.[52,56–60]

Eq. 1 $$N_2 + 8\,H^+ + 8\,e^- \rightarrow 2\,NH_3 + H_2$$

The complexity of nitrogenase has captivated researchers for decades as they seek out answers to the question, how does nitrogenase carry out these difficult chemical transformations? Many scientific approaches have been utilized in its study, each providing complimentary information that can add to the larger picture. Since nitrogenase has been extensively reviewed[50–52,61–63], this section shall primarily focus on secondary and outer sphere effects that modulate the function of the Mo-dependent enzyme.

2.1 Structural Features of Nitrogenase

The Mo-nitrogenase from *A. vinelandii* is the most extensively studied nitrogenase protein, and under N_2 fixing conditions up to 10% of all cell proteins are nitrogenase related.[44,64] The MoFe protein is an $\alpha_2\beta_2$ heterotetramer of the *nifD* and *nifK* gene products that form NifDK (~220 kDa), where two αβ-dimer units pair together.[61] Each αβ-dimer houses two different metalloclusters that are critical for enzyme function, the P- and M-clusters, such that each copy of NifDK binds a total of four cofactors (**Figure 2**).[61,65,66] The *nifH* gene product, NifH, serves as the reductase partner of NifDK, and is composed of a homodimeric protein (γ_2) with a molecular weight of ~60 kDa that binds an [4Fe-4S] cluster at the subunit interface.[67] Additionally, each subunit can bind one molecule of MgATP.[63,67,68] One NifH protein can bind to each αβ-dimer of NifDK, forming an Fe:MoFe protein stoichiometry of 2:1.[69,70]

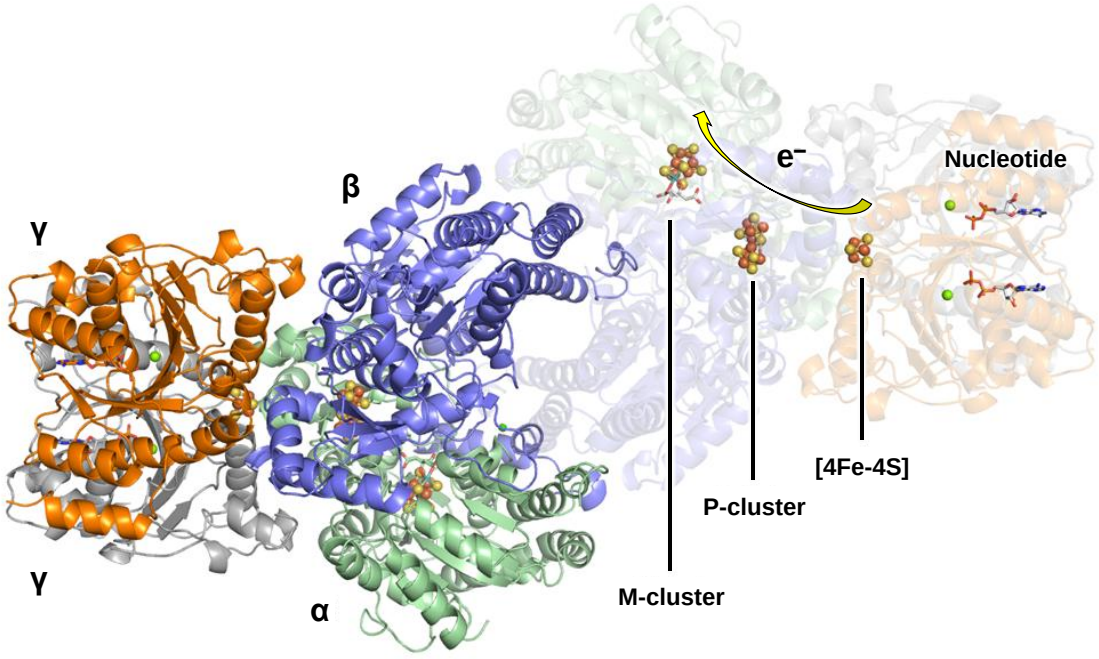

Figure 2 | Crystal structure of the NifH:NifDK complex (PDB ID 1N2C). The relevant cofactors are highlighted and the proposed direction of electron flow through the enzyme is depicted as a yellow arrow. The coloring scheme is as follows: NifD (green cartoon), NifK (blue cartoon), NifH (orange and gray cartoon), Fe, orange; S, yellow; C, gray. Reprinted (Adapted or Reprinted in part) with permission from ref. [50]. Copyright 2020 American Chemical Society.

The P-cluster mediates electron transfer between the reductase component, NifH, and the M-cluster during catalysis.[71] The cofactor is composed of a [8Fe-7S] cluster positioned at the α/β interface of NifDK ~10 Å below the surface of the protein.[65,72] It appears as the fusion of two [4Fe-4S] clusters that share a μ_6-sulfide vertex, with ligation from six cysteine residues, α-C62, α-C88, α-C154, β-C70, β-C95, β-C153, three of which come from each subunit (**Figure 3**). Interestingly, the cysteine residues bind terminally to some of the Fe centers, as is typically found with canonical [4Fe-4S] clusters, but two of them bind in bridging modes between the two cubane halves of the P-cluster. Structurally, this fused cubane geometry of the P-cluster is unique and has not been identified elsewhere in biology. The P-cluster has three interconvertible oxidation states that have been identified as relevant for catalysis: the as-isolated P^N state, the one-electron-oxidized P^{1+} state and the two-electron oxidized P^{OX} (or P^{2+}) state.[62,73] The P^N-cluster has been characterized as an all ferrous (Fe^{2+}) cluster,[74–77] and subsequent oxidations result in reversible structural changes that physically open the cofactor.[78–80] This structural fluctuation of the P-cluster during redox changes has been proposed as a means of regulating or 'gating' electron transfer within NifDK.[62,81–83]

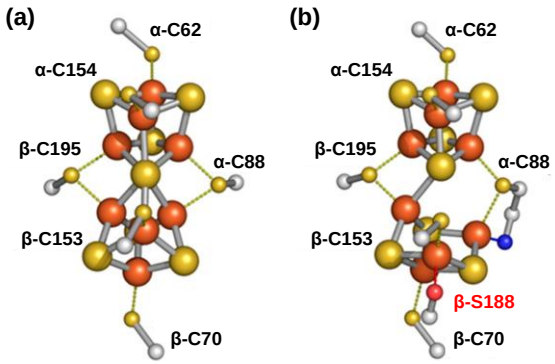

Figure 3 | Structure of the P-cluster. (a) the dithionite-reduced state (P^N, PDB ID 3U7Q) and **(b)** the indigo disulfonate-oxidized state (P^{OX}, PDB ID 3MIN). Atomic coloring: Fe, orange; S, yellow; C, gray; N, blue. Reprinted (Adapted or Reprinted in part) with permission from ref [84]. Copyright 2014 American Chemical Society.

The M-cluster is an asymmetric [Mo-7Fe-9S-C-*R*-homocitrate] species, with the Mo-capped end ligated by the organic acid *R*-homocitrate through the 2-hydroxy and carboxyl groups, as well as by the α-442His residue, and the opposite, Fe-capped end ligated by α-C275 residue (**Figure 4A**).[65,66,85] The cluster is buried within the α subunit of NifDK and is positioned ~19 Å from the P-cluster and over 60 Å from the clusters of the partner αβ-dimer. The structure of the M-cluster is similar to the P-cluster, as both are a fusion of two different cubane species with a common vertex, but the two partial cubane units of the M-cluster, [Mo-3F2-3S] and [4Fe-3S], are not identical, and the common vertex is an interstitial μ_6-carbide as opposed to a sulfide.[66,86–88] Additionally, there are three 'belt' μ_2-sulfido ligands that bridge between the Mo- and Fe-capped ends of the cofactor. These belt sulfide ligands have been shown to exhibit lability in both Mo- and V-nitrogenases, and this apparent flexibility has been implicated to be important during catalysis.[89–95] In V-nitrogenase (or VnfDGK), the V-cluster is a structural analog of the M-cluster (**Figure 4B**), but with a V ion in place of the Mo ion, and one of the μ_2-sulfide ligands replaced with a carbonate (CO_3^{2-}) ligand.[92–95] There are physical metrics that vary between the M- and V-clusters, but they are still remarkably similar.[51]

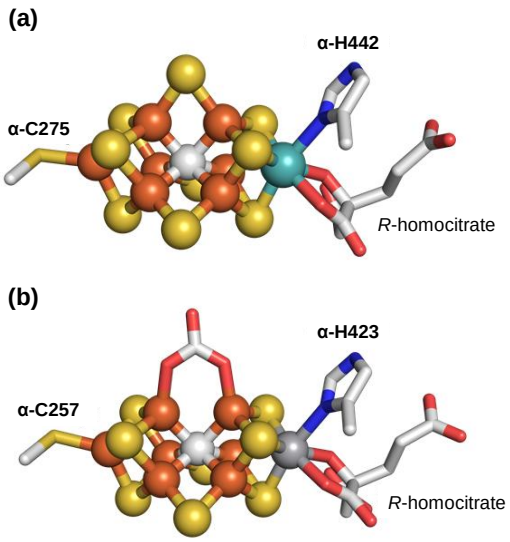

Figure 4 | Catalytic cofactors from crystal structures of NifDK (a) and VnfDGK (b). The atoms of the clusters are shown as ball-and-stick models with the amino acid residues, *R*-homocitrate and carbonate represented as sticks. Atomic coloring: Fe, orange; S, yellow; Mo, teal; V, dark gray; C, light gray; N, blue; O, red (PDB ID 3U7Q, NifDK; 5N6Y, VnfDGK).

The electronic description of the M-cluster has been of interest for decades, as the M-cluster is capable of supporting many redox states,[56] and so the cluster has been experimentally studied using combinations of Mössbauer, X-ray absorption (XAS), magnetic circular dichroism (MCD), and electron paramagnetic resonance (EPR) spectroscopic techniques.[62,75,96–98] Many of these techniques probe the sample in an ill-defined state, and as such, there can be great difficulty in deconvoluting the specific contributions of individual clusters. The most commonly observed state of the M-cluster is the resting, dithionite ($S_2O_4^{2-}$) reduced M^N state that is associated with the diagnostic S = 3/2 rhombic signal from EPR spectroscopy (g = 4.3, 3.7 and 2.0).[73,96,99,100] Computations and high-energy resolution fluorescence detected (HERFD) Mo K-edge XAS experiments identified that the Mo center of the M^N-cluster is best described as an S = 1/2 Mo^{3+} center, as opposed to the classical assignment of Mo^{4+}.[98] This indicates that the Mo exists in an atypical 'non-Hund' configuration, and additional spectroscopy and density functional theory (DFT) calculations support a $[3Fe^{2+}:4Fe^{3+}:Mo^{3+}]^{1-}$ assignment.[97,98,101,102] Further, a crystallographic spatially resolved anomalous dispersion (SpReAD) analysis compared electron densities to Fe K-edge XAS experiments to determine the oxidation states of specific Fe atoms of the M-cluster, and this study agreed with the previously described oxidation assignment.[103] The M^N-cluster can also be oxidized by one electron to the M^{OX} form, which coincides with a loss of the S = 3/2 EPR signal, and is generally not believed to be relevant for catalysis.[73,104,105]

While NifH binds a smaller, more prevalent type of biological [4Fe-4S] cluster, the Fe protein is far from simple. NifH has three recognized physiological functions: (1) Mo and homocitrate insertase in the biosynthesis of the M-cluster, (2) reductase involved in P-cluster biosynthesis on NifDK, (3) obligate reductase for nitrogenase catalysis that couples electron transfer to MgATP hydrolysis.[68] The [4Fe-4S] cluster binds between the two subunits of NifH and is positioned on a C_2 rotation axis with cysteine coordination by two residues (γ-C97 and γ-C132) from each subunit.[67] This cluster is located in a solvent-exposed position, which differs from [4Fe-4S] ferredoxins that have clusters buried within the protein.[63] Further, MgATP molecules that bind to the Walker's motif A protein fold have been shown to affect the position of the [4Fe-4S] cluster despite being bound ~20 Å away from the cluster (**Figure 2**).[68,106,107] This apparent cluster movement has been studied by various structural and spectroscopic methods and is associated with modulation of the reduction potential of NifH.[63,108–112] The protein can support $[4Fe\text{-}4S]^{2+}$, $[4Fe\text{-}4S]^{1+}$, and $[4Fe\text{-}4S]^{0}$ oxidation states, which is abnormal compared to other iron-sulfur cluster containing proteins that only support two redox states.[113] In NifH, the $[4Fe\text{-}4S]^{1+}$ state is favored in the presence of dithionite,[51,100] and interestingly exists as a mixture of two different spin states, $S = 1/2$ and $S = 3/2$; the composition of which changes with additives such as glycerol or urea.[96,114] During catalysis, the $[4Fe\text{-}4S]^{2+/1+}$ couple is proposed to be operative, transferring one electron to NifDK for every two molecules of MgATP cleaved by NifH, and NifH becomes reduced *in vivo* through physiological reductants such as ferredoxins or flavodoxins.[63,83,115–118] The $[4Fe\text{-}4S]^{0}$ 'all ferrous' or 'super-reduced' state has been implicated in adventitious reactivity by NifH, yet has also been proposed to play a role in nitrogenase catalysis, but the characterization of this species is fraught with complications that make understanding a physiological role difficult.[51]

2.2 Assembly of Nitrogenase Cofactors

Nitrogenase is a complicated system, not only because of the multimeric metalloprotein composition and unique cofactors, but there are many genes that regulate nitrogenase and cofactor biosynthesis.[50,51,119] For the NifDK protein from the model organism *A. vinelandii*, a minimum set of nitrogenase proteins that includes NifU, NifS, NifB, NifEN, NifH, NifV, and NifZ are required for *in vitro* activation of N_2 fixation.[49,120] These proteins are encoded by *nif* or 'nitrogen fixation' genes, and the *nif* operon is specific to the Mo-nitrogenase system. Organisms that encode for V- or Fe-only nitrogenase (*vnf* and *anf* genes, respectively) still require some of the *nif* operon for proper function.[51] For Mo-nitrogenase, the biochemistry

and assembly of the MoFe protein and the cofactors bound therein have been extensively studied over the past two decades, yielding crucial insights into the process.

The biosynthesis of NifDK involves the assembly of both the P- and M-clusters in addition to the polypeptide, but cofactor generation occurs through different routes (**Figure 5**). While the P-cluster is assembled *in situ* on the NifDK polypeptide scaffold the M-cluster is assembled *ex situ* on a series of different proteins before terminally reaching NifDK.[49,50,120] The P-cluster originates from a pair of [4Fe-4S] clusters, called the P*-cluster, that are synthesized at the α/β subunit boundary of apo NifDK.[84,121–124] The iron-sulfur fragments are assembled and delivered to apo-NifDK through the action of NifU, a scaffold protein that binds iron-sulfur clusters, and NifS, a cysteine desulfurase that provides sulfide from cysteine.[125,126] The P*-cluster is then fused together with concomitant loss of sulfur by the stepwise action of NifH and NifZ in a MgATP- and electron-dependent process. The result is an apo-NifDK protein with two equivalents of P-cluster bound and a lack of M-cluster.

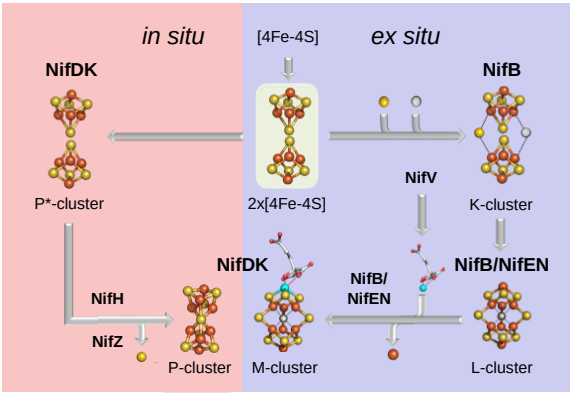

Figure 5 | Biosynthetic diagram for the assembly of nitrogenase cofactors. The red portion represents the *in situ* pathway for the synthesis of the P-cluster on NifDK. The blue portion reflects the *ex situ* synthesis of the M-cluster. Proteins are labeled in black; cluster species are labeled in white. Atoms are represented as ball-and-stick models and have atomic coloring of: Fe, orange; S, yellow; C, gray; O, red; Mo, teal. Reprinted (Adapted or Reprinted in part) with permission from ref [51]. Copyright 2020 American Chemical Society.

In contrast, the assembly of the M-cluster starts with the construction of [4Fe-4S] clusters by NifU and NifS that are subsequently delivered to NifB, a radical *S*-adenosyl-L-methionine (SAM) dependent enzyme.[127,128] NifB binds three [4Fe-4S] clusters; one is specifically for catalyzing SAM reactivity while the other two are the substrate clusters (K1 and K2) known collectively as the K-cluster.[129–131] Under reducing conditions, two equivalents of SAM are cleaved to first transfer a methyl group to the K2 cluster on NifB, and the second equivalent

of SAM initiates a hydrogen atom abstraction of the transferred methyl group.[87,88,131] In a series of uncharacterized subsequent steps, carbide (C^{4-}) replaces the remaining hydrogen atoms. The two K-cluster cubane units are fused yielding a [8Fe-8S-C] cluster, called the L*-cluster, that contains an interstitial carbide bound to the six central Fe atoms of the cluster.[132,133] A final '9th sulfur' is then incorporated into the L*-cluster through the reduction of a sulfite (SO_3^{2-}) ion to produce the [8Fe-9S-C] L-cluster. The L-cluster on NifB is transferred to another scaffold protein, NifEN, that facilitates the conversion of the L-cluster into the M-cluster through the loss of an Fe atom and the incorporation of Mo and *R*-homocitrate.[134–137] *In vitro* experiments demonstrate that M-cluster-loaded NifEN can then interact directly with apo NifDK (containing only P-clusters) to transfer the M-cluster and produce active NifDK, although additional chaperone proteins have been suggested to assist with this process *in vivo*.[49,50]

2.3 Nitrogen Reduction Mechanism

N_2 reduction requires a high degree of regulation to successfully carry out the reaction, and one of the key factors to this process is the shuttling of electrons. Electrons are transferred from NifH to NifDK through direct complexation of both proteins and the hydrolysis of two MgATP molecules for each electron delivered.[63] This creates a complex system that has been the subject of study for decades. Extensive investigation of the mechanism of N_2 reduction in the 1970s and 1980s led to a kinetic framework known as the Lowe-Thorneley model or cycle.[51,52,63] This model can be viewed from two different perspectives; one is an Fe protein-centric view known as the 'Fe protein cycle' and the other, more common view is that of the MoFe protein, or the 'MoFe protein cycle'.

The Fe protein cycle begins with the NifH protein being in the reduced $[4Fe\text{-}4S]^{1+}$ state ($NifH^R$), binding two equivalents of MgATP.[63,83] The reduction to $NifH^R$ has been facilitated *in vitro* by dithionite but other reducing agents such as Eu(II) chelates have been used as well. The nucleotide-bound Fe protein then interacts with NifDK, forming a 2:1 complex that has been crystallographically characterized.[69,70,138] Subsequently, there are a series of steps that involve conformational changes, electron transfer, ATP hydrolysis, and phosphate release, resulting in oxidized NifH ($NifH^{OX}$, $[4Fe\text{-}4S]^{2+}$) with two equivalents of MgADP bound in complex with NifDK.[63,83] $NifH^{OX}$ and NifDK undergo dissociation, releasing the reductase before $NifH^{OX}$ is reduced back to the $NifH^R$ state, which becomes capable of exchanging MgADP for MgATP, restarting the cycle. This cycle is presumably active during the

reduction of most substrates by NifDK, though in the absence of NifDK, NifH has also been shown to carry out adventitious activity through alternative mechanisms.[51,68]

The Lowe-Thorneley model for N_2 reduction by NifDK, or the MoFe protein cycle, describes the catalytic intermediates in the reaction, each designated by an E_n notation where *n* is the number of proton and electron equivalents that have accumulated on one αβ-dimer of NifDK (**Figure 6**).[56] However, the value of *n* does not indicate where proton and electron equivalents are located, only that they have been delivered to the system, which has sparked considerable research efforts in the field.[52] The first state, E_0, reflects the resting, as-isolated state of NifDK associated with the well-characterized $S = 3/2$ EPR signal of the M-cluster.[62] As each proton and electron pair is accumulated through the early ($n = 2–4$) steps of the cycle, it is possible for a 'relaxation' to occur, releasing H_2 with concomitant transition to an $n - 2$ state.[52,60] N_2 has been proposed to bind to the M-cluster in the E_3 and E_4 states, but reduction of N_2 only occurs in the E_4 (or E_4(4H)) state.[52,56,139] This makes the E_4 state one of the most studied of the cycle, because either E_4 can relax backwards to lower E_n with release of H_2, or the cycle can proceed forward with the cleavage of the N_2 bond. Intriguingly, when N_2 binds to E_4(4H), one equivalent of H_2 is produced with concomitant formation of the E_4(2N2H) state through a proposed mechanism of reversible reductive elimination or oxidative addition.[52,60,140] The E_4(4H) to E_4(2N2H) reaction represents the first lowering of the N_2 bond order, though several possibilities have been put forward as to the identity of the resultant E_4(2N2H) species.[51,52]

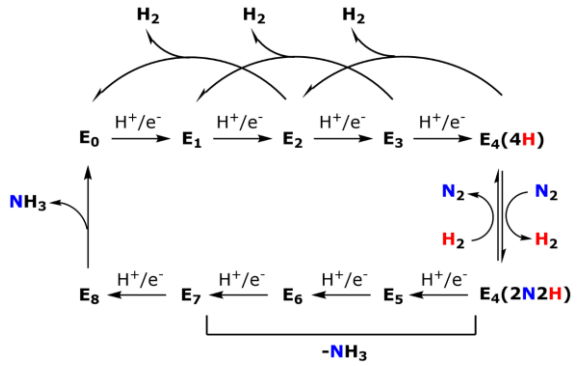

Figure 6 | Modified Lowe-Thorneley model for N_2 reduction by Mo-dependent nitrogenase. The E_n labeling indicates *n* number of proton and electron pairs that have been loaded on one of the αβ-dimers of NifDK. Reprinted (Adapted or Reprinted in part) with permission from ref. [51]. Copyright 2020 American Chemical Society.

The subsequent steps of the MoFe protein cycle E_5–E_8 promote the further reduction of the N_2 bond. Initially, there were two competing proposals for this latter half of the cycle that differed in the location where proton and electron equivalents are delivered to the reduced nitrogen species: a 'distal' and an 'alternating' pathway. The distal pathway posits that protons are delivered to the unbound N atom of N_2 first, forming an M=N–NH_2 hydrazido species that undergoes further proton/electron addition to yield one equivalent of NH_3 and a terminal M≡N metal nitrido species by the E_5 state.[141–146] The E_5 species is then sequentially protonated to release the second equivalent of NH_3 after the E_8 state. The alternating pathway, based on synthetic Fe-catalyzed versus Mo-catalyzed N_2 reduction,[147,148] proposes that protons are distributed between both N atoms of N_2, starting with diazene (HN=NH), proceeding through hydrazine (H_2N–NH_2) and releasing NH_3 after E_6 and E_8. While there is still uncertainty in distinguishing between these two mechanistic possibilities, mounting evidence supports the alternating pathway for biological N_2 reduction,[51,52] including crystallographic evidence of a putative N_2-bound species.[91] However, evidence from the V-dependent nitrogenase potentially suggests a distal pathway may be operative in that system, but kinetic analysis and calculations propose that the Mo-, V-, and Fe-only nitrogenases all share a common mechanism.[51,93,149,150] Clearly, further investigation will be necessary.

2.4 Nitrogenase Active Site Pocket

To understand the outer sphere environment surrounding the M-cluster, it is necessary to take a critical look at the residues that make up the active site pocket. However, there is no 'best' way to discuss the location of amino acid residues with relation to the catalytic cofactor of nitrogenase. High resolution crystallography has provided three-dimensional representations of nitrogenase and the cofactors with precision, but it can be difficult to gain a sense of which direction is 'up.' The three-fold rotation axis that runs from the Mo-capped end to the Fe-capped end of the cluster does not inherently provide a landmark around the M-cluster by which relative position can be compared other than the Mo and Fe subcubanes. The crystallographic labeling of the cofactor atoms provides some basis of orientation, but the labeling convention is also not intuitive; for instance, the three belt sulfur positions are given labels of S2B, S3A, and S5A, whereas other SXA and SXB labeled sulfur atoms are bound to the Fe-capped (or Fe1) and Mo-capped subcubane structures, respectively (**Figure 7**). In this discussion, a helpful means to navigate the M-cluster site is to establish an origin at the central carbide atom, followed by an '*x*-axis' that incorporates the C_3 symmetry axis running between Fe1 and Mo. The Fe1 end of the M-cluster is pointed towards the surface of the α-

subunit adjacent to the bulk solvent (designated as the 'negative' *x* direction), whereas the Mo end of the cluster is directed towards the αβ-subunit interface (designated as the 'positive' *x* direction). The S2B sulfur site has been established as a labile position on the catalytic cofactor[89,90], and is adjacent to several residues critical for reactivity, so a '*z*-axis' would bisect S2B as well as the central carbide atom of the cluster, with the direction of the S2B atom being positive. There is no convenient atom to position a '*y*-axis' relative to the carbide, but the S3A side of the *xz* plane can be the positive direction of *y* and the S5A side can be negative. Within this framework of (*x*, *y*, *z*) coordinates, α-H442 would be in the (+, +, -) direction relative to carbide, α-C275 would have a (-, 0, 0) position, and the nearest P-cluster would have a bearing of (+, -, +). While also an imperfect system due to constraints, such as α-R359 (**Figure 8**) and the *R*-homocitrate ligand running through positive and negative values of *y*, the coordinates should generally provide a spatial navigation within the active site.

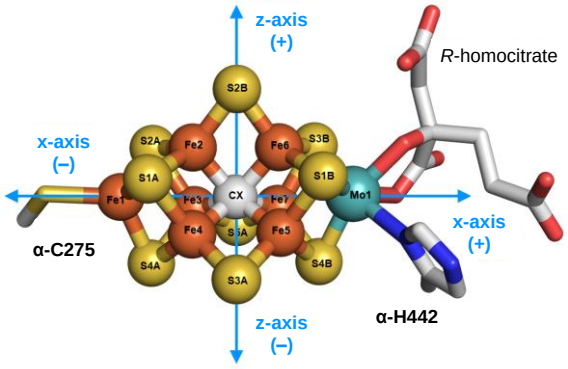

Figure 7 | Labeling of the M-cluster based on crystallography. A relative coordinate system is overlaid (blue arrows). The coordinate system assumes CX as the origin (0, 0, 0), the *x*-axis passes through Fe1, CX and Mo1 with positive values towards Mo1, the *y*-axis passes through CX into the page with positive values pointing out of the page, and the *z*-axis passes through S2B and CX with positive values towards S2B. The cluster is represented as a ball-and-stick model with atomic coloring as Fe, orange; S, yellow; C, gray; O, red; N, blue.

The catalytic M-cluster of nitrogenase is one of the largest, most complicated biological cofactors known so far but it is only bound to the protein scaffold through two amino acid residues, α-C275 and α-H442.[61,65,66,85,151] While *R*-homocitrate does bind to the Mo-end of the cluster, the lack of additional ligation to the M-cluster indicates that second coordination sphere effects play a crucial role in catalysis. Many amino acids have side chains with nitrogen-containing functional groups such as histidine, arginine and glutamine that are capable of hydrogen-bonding interactions. Non-polar or otherwise bulky residues such as valine, phenylalanine and tryptophan have been found to play roles in the steric environment

for substrate access and binding, as well as appropriate positioning of the M-cluster within the active site. All of these residues are connected to each other in a tightly regulated way, and disruptions in this network tend to be detrimental to the function of the enzyme. **Figure 8** shows the relative position of some of the important residues discussed within this review compared to the M-cluster.

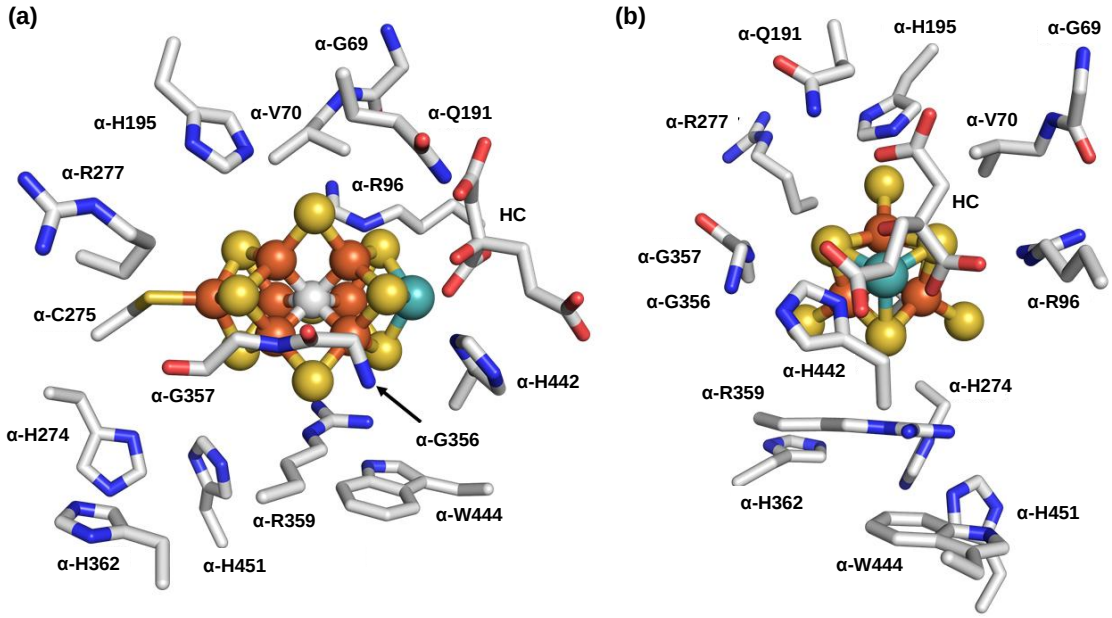

Figure 8 | Display of amino acid residues targeted for mutagenesis within the M-cluster active site of NifDK from *A. vinelandii*. A side view **(a)** and 90° clockwise rotation **(b)** of the M-cluster site are shown (PDB ID 3U7Q). The cluster is represented as a ball-and-stick model while the homocitrate ligand (HC) and amino acid side chains are shown as sticks. Atomic coloring: Fe, orange; S, yellow; C, gray; O, red; N, blue.

In 1991, before crystals of NifDK were solved, a series of point mutations of conserved histidine residues were reported, hoping to identify those interacting with the M-cluster. Making use of electron spin echo envelop modulation (ESEEM) spectroscopy,[152] microwave pulses are used in a specific sequence within an EPR experiment to probe nuclei (such as ^{14}N or ^{1}H) that are coupled to a paramagnetic species.[62] Specifically, the intense $S = 3/2$ EPR signal (**Figure 9**) associated with the M-cluster was probed to search for ^{14}N atoms from histidine residues that may be hyperfine-coupled with or covalently bound to the cofactor.[152]

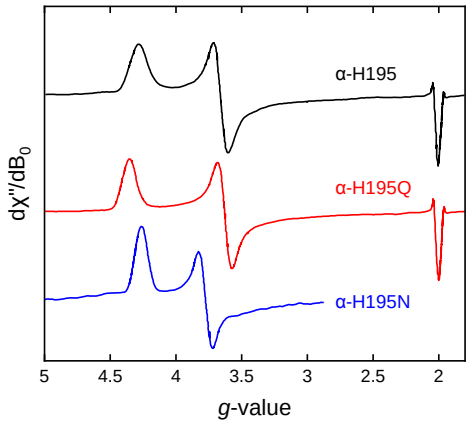

Figure 9 | EPR characterization of the M-cluster. The figure depicts wild-type (black), α-H195Q (red), and α-H195N (blue) NifDK proteins from *A. vinelandii*. The $g \sim 2$ region is not shown for α-H195N due to contamination. Adapted with permission from ref. [153]. Copyright 1995 American Chemical Society. Data digitalized *via* WebPlotDigitizer v4.5.

Residues α-H83 (+, -, +), α-H195 (-, 0, +), α-H196 (-, 0, +), α-H274 (-, -, -), and β-H90 (+, +, +) were targeted for single point mutations. ESEEM studies on whole cells were carried out and signals assigned to N atoms from histidines were observed in all variants, only the variant α-H195 NifDK proteins showed no ESEEM signal, and it was concluded that α-H195 must bind to the M-cluster. However, once the crystal structure of NifDK became available in 1992, it was clear that α-H195 was too far from the M-cluster to bind directly, but instead was likely involved with a hydrogen-bonding interaction to the S2B sulfur of the cofactor. In 1995, Dean, Hoffman, and co-workers studied the EPR and ESEEM signature of partially purified NifDK variants, namely α-H195N and α-H195Q.[153] Consistent with the previous observations, it was found that the ESEEM signal was dramatically attenuated in the α-H195N NifDK variant but α-H195Q NifDK showed nearly identical signals in both EPR and ESEEM experiments to the wild-type enzyme. If the hydrogen bond of α-H195 was responsible for the ESEEM signals, then both variants should express similar spectra, but they did not. This suggested that a nitrogen-containing residue that is sensitive to the position of the α-H195 residue was responsible for the signal. Subsequently, ESEEM studies were expanded to include purified variant proteins targeting residues α-R96 (+, -, 0), α-H195 (-, 0, +), α-R359 (0, +, -), α-F381 (0, +, +), and α-H442 (+, +, -).[154] The spectra of α-H195N NifDK showed that the ESEEM signal (labeled as 'N1') was indeed eliminated as previously reported,[152,153] but a weaker signal 'N2' that was buried underneath was also observed.[154] Mutation at α-R96 only showed the N1 signal, eliminating this residue as the source of N1,

and substitution of α-H442 resulted in a lack of observable EPR signal, consistent with loss of the M-cluster entirely. However, mutation of α-R359 or α-F381 resulted in a loss of the N1 signal while the N2 signal remained intact. Together, these experiments were used to assign the N1 signal to α-R359 and the N2 signal to the peptide NH groups of one or both of the residues α-G356 (+, +, 0) and α-G357 (-, +, 0).[154] However, the catalytic activity of the variant NifDK proteins could not be correlated to the ESEEM signals. Despite this, the study demonstrates that changes in the second coordination sphere on one side of the M-cluster can perturb the interactions occurring on the other side of the cluster, as seen by the loss of the N1 signal at α-G357 (-, +, 0) when α-H195 (-, 0, +) is modified. In fact, changing the steric environment as seen with α-F381L NifDK variants (0, +, +) was enough to disrupt hydrogen-bonding interactions around the cluster even though α-F381 is not directly involved in such an interaction, reinforcing that the active site residues are highly interconnected.

Another salient observation about the active site of nitrogenase comes from the crystal structure of an M-cluster depleted NifDK, called Δ*nifB* NifDK.[155] In 2002, Burgess, Rees, and co-workers managed to crystallize the NifDK protein without the catalytic cofactor, which resulted in changes to the tertiary structure as compared to wild-type enzyme. Rearrangements of the amino acids left a 'funnel' on the surface of the protein that was positively charged, with a loop of residues from α-353 to α-364 positioned at the entrance to the funnel. This loop also contained residues that had positively charged, nitrogen-containing side chains, and the authors proposed that the electrostatic charge of the funnel would help direct the negatively charged M-cluster into the appropriate position so it could be locked into the active site through movement of the funnel loop. Interestingly, a similar concept was discussed for the insertion of the active site cofactor of [FeFe]-hydrogenase (**Section 3.2.2**). Subsequent point-mutation studies further explored this proposal by targeting specific residues that may assist in guiding the M-cluster into NifDK.[156–158] Thus, the side chain selection within the nitrogenase active site has the demonstrated capability to support a robust network of hydrogen bonds, while at the same time functioning in a biosynthetic capacity to orient the M-cluster optimally within the protein for catalysis.

2.5 Assessing the Nitrogenase Second Coordination Sphere

Before the publication of the crystal structures in the 1990s,[65,67,69,80,85,159] the study of nitrogenase was based on genetic, spectroscopic, and reactivity experiments that were used to gain insight into the structure of the protein as well as the bound metallocofactors. At that time, there was little in the way of direct information regarding the properties of the

individual P- and M-clusters, and their three-dimensional relationship. Even after the appearance of high-quality crystallographic data, the study of structure-function relationships in nitrogenase was difficult due in no small part to the multiple, unique iron-sulfur clusters that are bound to the enzyme. Some of the early efforts to characterize and understand the nitrogenase cofactors involved chemical extraction into organic solvents.[160,161] The P-cluster is integral to the nitrogenase structure, so the acid quenching required for extraction destroys the P-cluster and disrupts the protein fold such that the M-cluster can be removed. This allowed for new avenues of study and analysis, but to date, there have been no successful reports of recrystallized M-cluster outside of the nitrogenase protein.[162]

In order to better assess the nitrogenase protein structure, amino acid sequencing, both through genetic analysis and protein digestion, was carried out in the 1970s and 1980s to compare nitrogenases from different species.[163–168] Conserved residues were identified and targeted for single-point mutations as a way to connect information about the cofactors to the protein structure and function. Initially, conserved cysteine residues were investigated for their widespread use in biology as ligands for iron-sulfur clusters, as it was understood that nitrogenase likely contained multiple [4Fe-4S] clusters. These cysteine residues were changed into serine or alanine, and the resulting bacterial strains (of *A. vinelandii* or *Klebsiella pneumoniae*) were studied.[169–172] Growth rates in the absence of a fixed nitrogen source were used to establish the N_2 fixation phenotype, and whole cell and/or crude extract activity assays were carried out in an acetylene atmopshere to compare diazotrophic growth rates with nitrogenase activity.[169,172] In addition, EPR spectra of whole cell variants or crude extracts of these cells would be collected to search for the intense $S = 3/2$ signal associated with the M-cluster as a means to cross reference the observed reactivity.[172] Generally, when the cysteine residues (that would later be found to bind to the P- and M-clusters) were mutated to alanine, diazotrophic growth and acetylene-based nitrogenase activity would be eliminated. Serine subsitutions of cysteine residues bound to cofactors would also eliminate activity, but in one case, Newton and co-workers found that substitution of C183 (+, -, +) on the NifD subunit (or α-C183) from *A. vinelandii* to serine did not arrest activity but resulted in diminished diazotrophic growth rates.[169] Conserved residues such as α-Q191 (+, +, +) were mutated to change the polarity or charge; for instance, changing the polar, amide-bearing amino acid side chain of glutamine to the carboxyl group of glutamate (α-Q191E).[169] In this case, the activity was eliminated, despite the fact that glutamine residues are not typically found as ligands to iron-sulfur clusters in biology.[113,173] These findings were unanticipated, but provided indications of the active site of nitrogenase in the absence of structural data, and marked the

beginning of targeted efforts to understand the secondary sphere effects within nitrogenase. In the years that followed, many mutagenic studies were reported with a focus on determining effects to nitrogenase activity as well as the number and location of substrate binding sites on the M-cluster. The residues that have been targeted for mutagenic studies related to the M-cluster site in NifDK from *A. vinelandii* have been summarized in **Table 1** and **Table 2**.

Table 1 | List of single point mutations reported for *Azotobacter vinelandii* NifDK with proximity to M-cluster site.[a,b]

NifDK residue	Arg (R)	His (H)	Lys (K)	Asp (D)	Glu (E)	Ser (S)	Thr (T)	Asn (N)	Gln (Q)	Cys (C)	Gly (G)	Pro (P)	Ala (A)	Ile (I)	Leu (L)	Phe (F)	Tyr (Y)	Trp (W)	Ref.
α-G69						x													174,175
α-V70											x		x	x					176–179
α-H83				x				x		x						x	x		152
α-R96		x	x						x				x		x				154,179–181
α-Q151					x														169
α-C154						x													169
α-D161					x														169
α-C183						x													169
α-S190											x								174
α-Q191			x		x							x	x						139,169,174,178,181–185
α-S192	x			x	x		x	x	x						x			x	174,186
α-H195							x	x	x		x				x		x		139,152,154,179,182–184,187–189
α-H196	x			x	x									x	x				152
α-H274									x				x						152,156,158
α-C275						x													169
α-R277		x	x				x			x	x	x			x	x			181,186,190
α-G356	[c]																		186
α-R359			x						x										154,174,181
α-H362				x									x						157
α-F381														x	x				154,174
α-H442								x		x									154
α-W444											x		x			x	x		158
α-H451													x						156,158

[a] NifD = α, NifK = β.

[b] NifDK residues listed have been mutated to the marked amino acids.

[c] No specific mutations are listed.

Table 2 | List of *A. vinelandii* NifDK residues near the M-cluster that have been investigated through mutagenesis.

NifDK residue	Location near M-cluster[a]	Coordinate[b]	Proposed Role(s)
α-G69	outer sphere near S2B	(+, -, +)	Hydrophobic interactions with substrate
α-V70	2nd sphere near S2B	(0, -, +)	Hydrophobic interactions with substrate
α-R96	2nd sphere near S5A	(+, -, 0)	Steric / Hydrogen-bonding interactions with M-cluster, substrates
α-S190	outer sphere near S2B	(0, +, +)	Steric or hydrogen-bonding interactions
α-Q191	2nd sphere near S2B, HC	(+, +, +)	Hydrogen-bonding interactions with *R*-homocitrate ligand of M-cluster
α-S192	outer sphere near S2B	(-, +, +)	Hydrogen-bonding interactions with conserved H_2O molecules
α-H195	2nd sphere near S2B	(-, 0, +)	Hydrogen-bonding and steric interactions with M-cluster, substrates
α-H196	outer sphere near S2B, Fe1	(-, 0, +)	Unknown
α-H274	outer sphere near Fe1, S4A	(-, -, -)	Assists with M-cluster incorporation, adjacent to α-C275
α-C275	cofactor bound	(-, 0, 0)	Ligates Fe-capped end of M-cluster
α-R277	2nd sphere near S1A	(-, +, +)	Hydrogen-bonding interactions with conserved H_2O molecules
α-G356	2nd sphere near S3A	(+, +, 0)	Hydrogen-bonding interaction with M-cluster
α-R359	2nd sphere near S5A	(0, +, -)	Hydrogen-bonding interaction with M-cluster
α-H362	outer sphere near Fe1	(-, +, -)	Assists with M-cluster incorporation
α-F381	2nd sphere between S2B, S3A	(0, +, +)	Hydrophobic interactions with M-cluster
α-H442	cofactor bound	(+, +, -)	Ligates Mo-capped end of M-cluster
α-W444	outer sphere near S4B	(+, -, -)	Hydrophobic interactions with M-cluster
α-H451	outer sphere near S4A	(-, -, -)	Assists with M-cluster incorporation

[a] Locations are based on proximity to the M-cluster atoms from the resting state crystal structure PDB ID 3U7Q.[38]

[b] The general location of the amino acid side chain in the coordinate system defined in **Figure 7**.

One complicating factor when discussing the results of site-directed mutagenic studies is that often the modification substantially reduces or eliminates nitrogenase activity, but it is not always clear why this occurs. In studies of the MoFe protein from *K. pneumoniae*, Buck and co-workers tested the activity of cell extracts from several cysteine to alanine variants and found almost no acetylene reduction, implying their mutations have made nitrogenase non-functional.[172] They employed a parallel experiment to assess the stability of the variant proteins where wild-type apo NifDK (Δ*nifB* NifDK) was added to their cell extracts and would show activity only if free M-cluster were found in solution. Low acetylene reduction activity was observed for many variants, but the α-C275A NifDK protein that targeted the residue that binds M-cluster showed an increased activity by an order of magnitude.[172] This indicated that some variant proteins are unable to retain the M-cluster, a conclusion that was validated by adding additional M-cluster to cell extracts of the NifDK variants alone with no observed increase in activity. Indeed, extracts were commonly used because of the difficulty associated with purification, and this problem becomes exacerbated when the stability of the protein is affected. Several reports from Newton and Dean acknowledge that certain proteins could only be partially purified because they would not survive heat treatment steps.[139,153,183,185,191] In some instances where purification was successful, the Mo content of the NifDK variant would be lower than in the wild-type enzyme (< 50%), implying that cofactor loading was impaired resulting in variable mixtures of apo and holo NifDK proteins.[139,183,191] These studies still provide valuable insight, but it is important to recognize that it can be difficult to make definitive assessment of outer sphere effects when activities can be attenuated from simple loss of the M-cluster or degradation of the protein.

However, there are investigations targeting the assembly of NifDK that use the retention or loss of the M-cluster as means to probe the function of certain amino acids.[156–158] Ribbe and co-workers have carried out site-directed mutagenesis on several outer coordination sphere residues ≥6 Å from the M-cluster (**Figure 10**): α-W444 (+, -, -), α-H274 (-, -, -), α-H362 (-, +, -), and α-H451 (-, -, -). A crystal structure of apo NifDK from a Δ*nifB* background revealed that α-H442 in the absence of the M-cluster shifts ~5 Å within the active site.[155,158] The α-H442 residue is rearranged and placed nearby two other histidine residues, α-H274 and α-H451, forming a 'triad' while another residue, α-W444, is found to take up the same space as α-H442 does in the holo enzyme (**Figure 10**). The apparent position swapping of α-H442 and α-W444 was intriguing, so mutagenesis was carried out to replace α-W444. In the α-W444Y and α-W444F NifDK variants, the M-cluster loading was ~90% of the wild-type enzyme, whereas α-W444A and α-W444G contained only 14% and 3% of wild-type M-cluster,

respectively.[158] As the side chain of the α-444 residue was changed to smaller, less sterically bulky groups, the Mo concentration decreased. The reactivity assays of the variant proteins with N_2, C_2H_2, and protons, as well as the intensity of the EPR signals all roughly decreased by the same magnitude as the Mo concentration. Paired with heat treatment studies, it was suggested that the variant proteins themselves were stable, leading to the conclusion that α-W444 must be involved in a steric interaction that keeps the M-cluster secure within the active site pocket.[158] It was also observed that in the α-W444A and α-W444G variants, the EPR signal of the P-cluster appeared to distort relative to the larger substituent-containing variants, implying that α-W444 may also have longer range effects in NifDK than immediately around the M-cluster site.

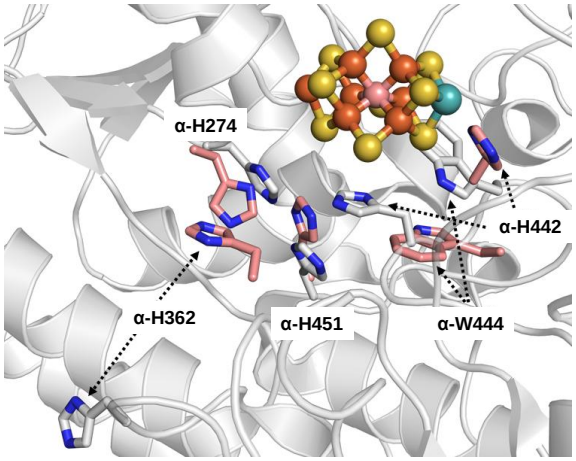

Figure 10 | Crystal structure of Δ*nifB* NifDK (PDB ID 1L5H). The M-cluster and selected residues included from wild-type *Av*NifDK are overlaid (in pink; PDB ID 3U7Q). The two structures were aligned, and the M-cluster and specific residues from the wild-type protein were superimposed on top of the Δ*nifB* NifDK structure. The residues α-H274, α-H442, and α-H451 represent the identified 'histidine triad'. The cluster atoms are shown as ball-and-stick models, and the amino acid residues are represented as sticks. Atomic coloring: Fe, orange; S, yellow; C, gray; O, red; N, blue.

The other two residues of the histidine triad, α-H274 and α-H451 (**Figure 10**), were also targets for point mutations.[156] *A. vinelandii* cells separately expressing NifDK variants α-H274A, α-H451A and a double mutant α-H274A/α-H451A grew more slowly under N_2-fixing conditions, indicating issues with nitrogenase activity; the double mutant being the most deleterious. Assessment of the standard substrate reduction assays showed decreased activity of 67%, 56%, and 43% for the α-H274A, α-H451A, and α-H274A/α-H451A NifDK variants, respectively. The decreased activity also correlated well to the Mo concentration, and intensity of EPR signals for each of the variants. The α-H451A NifDK protein in the

dithionite-reduced state had a very similar EPR spectrum for the S = 3/2 M-cluster as wild-type NifDK (**Figure 9**), but the introduction of α-H274A as either the single or double mutant yielded a spectrum with large distortions in g-values as well as line shapes. The rationalization for this observation was that α-H274 is adjacent to α-C275, which binds the M-cluster and may have more of a direct impact on the M-cluster environment than the more distant α-H451.[156] Additionally, none of the studied mutations affected the EPR signals of the P-cluster, indicating that these residues have less of a long-range steric effect than α-W444. Introduction of isolated M-cluster into solutions of M-cluster depleted α-H274A, α-H451A, and α-H274A/α-H451A Δ*nifB* NifDK variants did not allow for full activation of the protein to wild-type levels of reactivity. Thus, it was concluded that both α-H274A and α-H451A are required during the biosynthesis of NifDK through sequential binding events that draw the M-cluster into the protein.[156] These residues may also play roles in the proton shuttling within the active site, as seen from shifts from N_2 reduction towards proton reduction in the variants, but one factor that was not explored is what steric effect the size of the side chain played in going from histidine to alanine. Alanine substitutions were certainly deleterious, but it would be interesting to see how the protein would retain the M-cluster if uncharged residues larger in size than alanine were studied.

Along similar lines, a final outer coordination sphere residue, α-H362 (-, +, -), had been studied with respect to M-cluster insertion into the NifDK protein (**Figure 10**).[157] In the crystal structure of the apo NifDK protein, α-H362 is surface exposed and is at the entrance to the insertion funnel of positively charged residues that have been proposed to guide a negatively charged M-cluster into the protein.[155,157] After M-cluster incorporation, the residue moves with the protein secondary structure to pin the cofactor in place. Single point mutants were generated and two variant NifDK proteins were studied, α-H362D and α-H362A.[157] Much like the previous mutations described, the α-362 variants grew more slowly under N_2-fixing conditions, expressed a decreased reactivity profile that correlated with Mo content, and had perturbations to the line shape and intensity of EPR signals, relative to wild-type enzyme. The decreased activities of the α-H362D and α-H362A NifDK variants are ~80% and ~40%, respectively. While modification of this residue did not cause a cessation of activity like that observed for α-W444,[158] substitution of α-H362 for aspartate induces a ~20% reduction in activity while alanine substitution results in a more drastic reduction of ~60%. This suggests that either α-H362 is involved in directing the M-cluster into the NifDK active site (supported by the decreased Mo concentration), or the residue is structurally important for adequately positioning the M-cluster within the active site (supported by the observed

perturbations of the M- and P-cluster signals). The best answer is likely a combination of both, but further structural characterization of these NifDK variants may shed light on the M-cluster insertion process.

2.5.1 Reduction of Nitrogen, Acetylene, and Protons

As mentioned earlier (**Eq. 1**), the reduction of N_2 by nitrogenase is a challenging transformation that requires the delivery of 8 electrons, 8 protons, as well as 16 equivalents of MgATP to produce NH_3, H_2, and MgADP.[51,52,100] Not only is NH_3 produced, but H_2 is generated as an integral part of the N_2 reduction mechanism.[57,58,192] As discussed in **Section 2.2**, electron and proton equivalents are sequentially delivered to the catalytic cofactor by way of NifH and the P-cluster, leading to distinct E_n steps along the Lowe-Thorneley model reaction pathway.[56,60] At the E_4(4H) level, N_2 has been shown to bind through a reductive elimination/oxidative addition mechanism, forming a reduced nitrogen species E_4(2N2H) and liberating one equivalent of H_2 (**Figure 6**). It is important to emphasize that while the bond order of N_2 is lowered when binding to E_4, the conversion between E_4(4H) and E_4(2N2H) technically requires no additional energy input, and the process is reversible in the presence of H_2. In fact, this reversibility is what allows H_2 to act as an inhibitor of N_2 reduction. This phenomenon has also been exploited to investigate N_2 binding. If isotopically labeled D_2 ($^2H_2$) is mixed with N_2, the wild-type NifDK can produce HD gas, and, if separately, T_2 ($^3H_2$) is mixed with N_2, NifDK does not significantly accumulate mixed label TOH.[56–60] This means that the reversible H_2 production through N_2 binding is not a simple proton exchange process with solvent, which supports the notion that hydrides (H^-) are generated in the Lowe-Thorneley model.[52,60] Moreover, the relative rates between the forward and reverse reactions have been proposed to favor N_2 reduction over N_2 release,[52,149,150] but these rates change when moving to the alternative nitrogenases.

Protons are also reduced by nitrogenase in a hydrogenase-like process (hydrogenases are discussed in **Section 3**) that competes with other substrate reduction reactions, but also occurs in the absence of substrates such as N_2, C_2H_2, or CO.[55] Additionally, there is no known additive that can increase the proton reduction of the wild-type enzyme, and it is unclear what the site(s) of proton reduction is. This can complicate analysis of nitrogenase catalysis, as often enough N_2 or acetylene reduction is reported without proton reduction under the same conditions. Consequently, it becomes difficult to rigorously compare systems, particularly from single-point mutagenic studies. For instance, if N_2 reduction decreases between two NifDK variants, the proton reduction under those same conditions could either increase or

decrease, and each scenario would lead to a different conclusion. There also is difficulty in the accurate measurement of NH_3/NH_4^+ produced from catalysis compared to gaseous H_2, particularly a low concentration. For this reason, acetylene is often used as an N_2 surrogate due to the analogous triple bond and gaseous nature of both the substrate and product states. Acetylene was first discovered as a competent substrate for nitrogenase in 1966 by Michael J. Dilworth,[193] and since then it has become crucial to the study of the nitrogenase mechanism despite the non-physiological role the substrate plays.[51,52,100,194] Wild-type Mo-nitrogenase reacts with C_2H_2 such that >90% of electron equivalents are funneled to produce exclusively ethylene (C_2H_4), substantially attenuating the H^+ reduction pathway.[100,195] The alternative substrate is thought to bind to nitrogenase while in the E_1 or E_2 states, although, C_2H_4 is not released from the protein until three proton/electron equivalents are delivered to the M-cluster so that the E_1 state can be reformed.[195] This is in contrast to the proposed N_2 binding states of E_3 or E_4, the latter of which is the only productive binding state that results in N_2 reduction (**Figure 6**). Further, the analysis of acetylene reduction in the presence of the nitrogenase inhibitor carbon monoxide (CO) has led to the proposal that there are multiple substrate binding sites on the M-cluster, and that N_2, C_2H_2 and CO occupy different positions.[195] Finding where the substrate binding sites are located as well as the properties of each has been a driving force behind the analysis of single-point mutations of NifDK. There have been many amino acid residues that have been targeted for single-point mutagenesis, so only examples pertinent to the outer sphere effects on catalysis will be discussed. **Table 3** summarizes some of the available assay data for NifDK variant proteins.

Table 3 | Reactivity of Select Purified NifDK Variants[a]

NifDK Protein Type	NH_3[b] (N_2)	H_2[b] (N_2)	C_2H_4[c] (C_2H_2)	C_2H_6[c] (C_2H_2)	H_2[c] (C_2H_2)	H_2[d] (Ar)	NH_3[e] (N_2/CO)	H_2[e] (N_2/CO)	C_2H_4[f] (C_2H_2/CO)	C_2H_6[f] (C_2H_2/CO)	H_2[f] (C_2H_2/CO)	H_2[g] (Ar/CO)	Ref.
Av Wild-type	860	615	1706	0	276	2494	0	2727	1134	0	959	2841	185
α-V70A	800					1800							176
α-V70I	170	1940	130	0	2000	2340							177
α-R96K	373		804			972							154
α-Q191K	0	514	40	7.2	528	540	0	182	14	2.3	340	254	185
α-H195Q	-	-	1350	0	1115	2860							183
α-H195N	-	-	535	135	355	1470							183
α-R277C						1400						2400[h]	186
α-R359K	709		1523			1587							154
α-F381L	816		1656			1844							154
Av Wild-type	989	555	2096			2211							158
α-W444Y	1036	507	2066			2069							158
α-W444F	906	505	1906			1795							158
α-W444A	212	101	364			410							158
α-W444G	0	6	8			11							158
Av Δ*nifV*						840							181
Kp Wild-type	725	471	1127	-	-	1527							196
Kp Δ*nifV*	318	842	1044	-	-	1242							196
Kp Δ*nifV*	-	812	-		202	1369	-	574	-	-	585	718	197

[a] Specific activity is reported with units of nmol product × min^{-1} × $(mg\ protein)^{-1}$. Gas in parenthesis reflects the substrate conditions used for the assay. [b] Assays are reported in an atmosphere of 100% N_2. [c] Assays reported in an atmosphere of 10% C_2H_2, 90% Ar. [d] Assays reported in an atmosphere of 100% Ar. [e] Assays are reported in an atmosphere of 3% CO, 97% N_2. [f] Assays are reported in an atmosphere of 3% CO, 10% C_2H_2, 87% Ar. [g] Assays are reported in an atmosphere of 3% CO, 97% Ar. [h] Assays are reported in an atmosphere of 10% CO, 90% Ar.

In the 1990s, NifDK variants at the α-Q191 (+, +, +) and α-H195 (-, 0, +) residues were reported based on sequence conservation between NifDK analogs, as well as to the biosynthetic precursor protein NifEN.[182,185,187,188] The cells of variant α-Q191K and α-H195N NifDK expressing strains had a Nif^- phenotype where the cells did not appear to grow without the addition of a nitrogen source (such as ammonium chloride or urea).[182] This indicated that these NifDK variants were unable to reduce N_2 under standard conditions. Crude extracts of cells expressing α-Q191K and α-H195N NifDK variants were found to yield no N_2 fixation products, however, reaction with C_2H_2 produced C_2H_4 with < 10% of the activity of the wild-type enzyme. Furthermore, ethane (C_2H_6) was found as a product from the variant protein strains, with 12.5% and 35% of the electron equivalents diverting towards ethane production for the α-Q191K and α-H195N NifDK proteins, respectively.[182] This was an interesting result at the time because it demonstrated that the M-cluster site was likely nearby the targeted residues prior to the publication of crystallographic data.

The α-Q191K NifDK protein was purified in 1992 and the reactivity of the enzyme was found to be ~30% of the activity of the wild-type NifDK. It produced no N_2 reduction products, and diverted 90% of electron equivalents to the production of H_2 in the presence of C_2H_2, compared to wild-type enzyme that uses 90% of electron flux to generate C_2H_4.[185] Subsequent characterization showed that the Michaelis constant (K_m) for C_2H_2 to produce C_2H_4 is 35 kPa, which is two orders of magnitude higher than in wild-type enzyme (K_m = 0.5 kPa), indicating that acetylene is not a great substrate for α-Q191K NifDK.[183] It was further shown that α-Q191K NifDK does not react with C_2H_4 to produce C_2H_6, in contrast to wild-type NifDK that will produce only a small amount (< 1% of electron flux) of C_2H_6 from C_2H_4 when C_2H_2 is absent. This and isotope labeling experiments led to the assertion that there must be a longer-lived, common ethylenic intermediate that can be differentiated to release ethylene, or ethane.[183] The lack of N_2 reduction was also explored through the introduction of N_2 gas into C_2H_2 and proton reduction assays.[139] Under standard conditions, wild-type NifDK will divert electron flux from proton reduction to N_2 reduction if N_2 is introduced into the reaction vessel, indicating that N_2 binds to or otherwise interacts with the M-cluster. HD will also be observed as a product in the presence of both N_2 and D_2. On the other hand, α-Q191K NifDK does not appear to even bind N_2 because the catalytic performance is unaffected when N_2 is added into the typical acetylene or proton reduction assays.[139] When mixtures of N_2 and D_2 are added to reactions of α-Q191K NifDK, the product HD is absent, consistent with a lack of N_2 binding as well as inability to access the E_4 state. A rationalization provided for these observations is that the α-Q191K variant is unable to even reach the E_3 level of the Lowe-

Thorneley cycle (**Figure 6**).[139] From crystallography, it is known that α-Q191 is in proximity to the *R*-homocitrate ligand, and both the protein residue and the ligand are involved in hydrogen-bonding interactions[65,85,151], potentially causing deleterious modulation of the redox properties of the M-cluster. Interestingly, when *R*-homocitrate is exchanged for citrate in a Δ*nifV* variant of NifDK from *K. pneumoniae* (see below), N_2 reduction decreases to 40% of the wild-type activity, diverting more electron flux towards the production of H_2, exceeding that for wild-type but still is capable of binding N_2.[196] Clearly, α-Q191 plays a key role in regulating the energetics in the active site, but the mechanism by which this is accomplished remains elusive.

In parallel, α-H195 (-, 0, +) variants have also been purified and studied.[139,183,187,188] The initial report of α-H195N showed that the enzyme was relatively unstable, did not have a high reactivity towards C_2H_2 and proton compared to wild-type, and was unable to form N_2 reduction products.[182,185] EPR spectra of whole cells indicated that while α-H195N NifDK showed a low intensity $S = 3/2$ M-cluster signal, the α-H195Q variant had an EPR signal of comparable intensity to wild-type enzyme with some perturbations of the *g*-values, suggesting that the electronic properties of the cluster had not substantially changed.[187] The α-H195Q variant showed a modest decrease in activity towards C_2H_2 compared to wild-type enzyme, but there was no observable products of N_2 reduction, even under acid-quenched conditions that would yield N_2H_4 in wild-type NifDK.[198,199] However, in the presence of N_2, the α-H195Q protein proton reduction is reversibly inhibited by slowing the reaction rate, but does not divert electron flux towards other observable products.[187] This indicated that N_2 would bind to the M-cluster of the variant, but would not become reduced. To further explore this notion, Fisher and co-workers increased the pressure of N_2 used in reduction assays of α-H195Q NifDK and saw that under hyperbaric conditions NH_3/NH_4^+ was observed at a rate < 2% of the wild-type enzyme.[188] Additionally, in the presence of a mixture of N_2 and D_2, α-H195E NifDK produced measurable HD gas, indicating that the protein variant could access the same E_4 state as the wild-type enzyme, but could just not reduce N_2 well. A crystal structure of the α-H195E NifDK protein was later published, showing that in agreement with EPR spectra, the N–H---S2B hydrogen bond stayed intact between the wild-type and α-H195Q proteins.[184] Thus, the hydrogen bond does not sufficiently control N_2 reduction capabilities, and additional factors, such as proton donors and redox potentials should be considered. The α-H195N variant was also tested for the ability to bind N_2, finding that N_2 would inhibit proton reduction much like in the α-H195Q variant, but no HD evolution was measured. This suggests that the α-H195N variant could bind N_2 (that is, achieving the E_3

state) but was unable to reduce N_2 (inaccessible E_4 state).[139] In this case, it is unlikely that any hydrogen-bonding interaction between α-N195 and the M-cluster exists, but the protein is still able to bind, but not reduce, N_2. In comparison, α-Q191K NifDK likely maintains the hydrogen bond between α-H195 and S2B of the cofactor, but the protein variant is unable to bind N_2 at all.

Acetylene reduction was also investigated with the variant α-H195 proteins, finding that N_2 would inhibit the production of both C_2H_4 and C_2H_6, but this inhibition could be reversed with H_2.[139,183,188] In the presence of 10% acetylene, the α-H195N and α-H195Q proteins used 69% and 55% of electron equivalents to generate reduced products, but the former protein yields both C_2H_4 and C_2H_6 while the latter yields C_2H_4 exclusively.[183] The α-H195Q protein behaves similarly to wild-type enzyme, with a K_m for C_2H_2 of 0.5 kPa for both enzymes, and neither producing C_2H_6 from C_2H_2, but is less efficient than wild-type enzyme diverting more electron flux towards proton reduction. In comparison, the α-H195N variant has a similar affinity for C_2H_2 (K_m = 1.0 kPa) but produces ethane which accounts for 23% of the total electron flux. Ethylene was also tested as a substrate for the variant proteins, with K_m values of 120 kPa for both wild-type and α-H195Q proteins, using less than 1% of total electron flux towards ethane production, and K_m = 48 kPa for the α-H195N variant with a ten-fold increase in activity. These experiments reveal that the high affinity for acetylene in the wild-type enzyme and α-H195Q variants likely prevents ethane production, because once ethylene is produced, it is rapidly replaced by a new molecule of acetylene.[183] The slightly lower affinity for the substrate in α-H195N NifDK may explain why ethane can be observed as a product, but it is also possible that the steric environment also contributes, as asparagine has a shorter side chain than glutamine. These acetylene reduction experiments, in comparison to N_2 reduction, show how more rigorous conditions are required for the cleavage of the triple bond of N_2 compared to alkyne or alkane substrates.

To better identify and understand substrate binding sites on the M-cluster, additional mutations to nitrogenase were studied.[174–178,180] In wild-type NifDK, several observations have been made with respect to the competition between N_2 and acetylene binding to the catalytic cofactor; namely, that two binding sites with different affinities for acetylene exist, and that acetylene is a non-competitive inhibitor of N_2 reduction while N_2 is a competitive inhibitor of acetylene reduction.[193,200–203] Additionally, C_2H_2 has also been found to be a more potent inhibitor of N_2 reduction under low electron flux conditions, where the rate of electron delivery is decreased, compared to those under high flux conditions.[204] In 2000, a study was

reported that used a NifDK strain with a β-Y98H (+, -, +) mutation, known for having lower electron flux as a progenitor for a genetic study.[174] The β-Y98H variant would not grow well under diazotrophic conditions in the presence of 2.5% C_2H_2, because N_2 reduction by the low flux NifDK protein would be strongly inhibited by C_2H_2. The goal was to screen for a mutation that would remove the acetylene sensitivity while maintaining similar levels of N_2 reduction activity. After analysis, it was found that in addition to the β-Y98H mutation, an α-G69S (+, -, +) mutation would allow for cells to grow under N_2 fixing condition in the presence of C_2H_2. A separate protein was then generated that only possessed the α-G69S mutation. The Michaelis-Menten parameters of the α-G69S NifDK protein for C_2H_2, N_2, and proton reduction were similar to those of the wild-type enzyme, indicating that this mutation did not affect nitrogenase activity. In contrast, the affinity for C_2H_2 decreased for α-G69S NifDK (K_m = 14.2 kPa) compared to wild-type enzyme (K_m = ~0.71 kPa), and the variant protein now showed a competitive inhibition of N_2 reduction in the presence of C_2H_2, instead of noncompetitive inhibition.[174] The rationale for these observations was that the mutation of α-G69 removed the high-affinity C_2H_2 binding site through steric changes nearby the M-cluster. However, the authors proposed that α-V70 was the actual residue that blocked the substrate binding site, due to the closer proximity to the cofactor. They also identified that α-R96 is positioned nearby α-V70 and is likely to be involved in determining access to the binding site. A separate study concluded that using the α-G69S NifDK protein, two substrate binding sites could be better distinguished on the α-V70 (0, -, +) face of the cluster.[175] One site is denoted as a 'high-affinity site' for acetylene binding that may also accommodate CO, while N_2, N_2O, and N_3^- do not bind. Site two is designated the 'low-affinity' acetylene-binding site that also binds CO, N_2, N_2O, and N_3^-.

Substitutions of the α-R96 (+, -, 0) and α-V70 (0, -, +) positions in NifDK were then explored for their effects on the access and binding of substrates and inhibitors.[176,180] In 2001, multiple mutations of α-R96 were reported, finding that the EPR spectra of all of the NifDK variants were essentially the same as the spectrum of the wild-type enzyme.[180] This result was used to conclude that the substitution had little to no effect on the electron properties of the M-cluster, and as such, the authors selected the α-R96L NifDK variant as a representative example to further study. When high concentrations of C_2H_2 were added to the protein, a new EPR signal appeared in a 70% acetylene atmosphere with *g*-values of 4.5, 3.5, and < 2.0, constituting 40% of the total spin (**Figure 11**). The addition of N_2 or CO did not affect the appearance of this signal, which is totally absent in the wild-type enzyme. It was found that addition of CN^-

to α-R96L NifDK would yield a new paramagnetic species with a *g*-value at 4.5, that also was absent from the wild-type system. Pulsed electron nuclear double resonance (ENDOR) experiments with ^{13}C-enriched acetylene and cyanide showed that CN^- definitively binds to the M-cluster, while it was inconclusive if C_2H_2 did as well, but in both cases the new EPR signals were derived from the M- as opposed to the P-cluster.[180] These results led to the conclusion that α-R96 must play a steric 'gatekeeping' role during catalysis. The change in size of the α-R96 residue presumably opened the active site allowing the small molecules to bind on or near the M-cluster. However, this finding should be taken with some scrutiny: the concentrations required to affect a change in the EPR spectrum are far beyond what is required under usual catalytic conditions, and other molecules, such as N_2, CO, and N_3^- do not cause perturbations in the EPR spectrum of α-R96L NifDK. Interestingly, the α-R96 variants do not product ethane, in contrast to α-Q191 and α-H195 variants.[205] The α-R96 variants do all have different affinities and rates for the reduction of C_2H_2, some similar to wild-type enzyme while α-R96L NifDK has a three-fold higher affinity, so it is unclear to what extent physiologically relevant conclusions can be made.

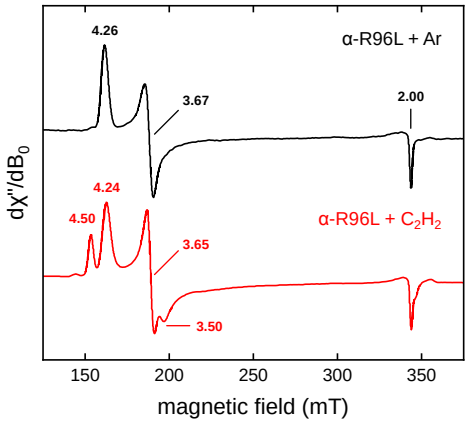

Figure 11 | EPR spectra of α-R96L NifDK under nonturnover conditions with acetylene. The α-R96L NifDK protein was prepared under 1 atm of Ar (top spectrum, black) or under 1 atm of acetylene (bottom spectrum, red). Reprinted (Adapted or Reprinted in part) with permission from ref. [180]. Copyright 2001 American Chemical Society. Data digitalized *via* WebPlotDigitizer v4.5.

In 2002, a follow up to the mutagenesis study of α-G69 NifDK was reported with the substitution of α-V70 (0, -, +) for alanine.[176] The α-V70A NifDK protein was able to grow under diazotrophic conditions, indicating that N_2 reduction was unaffected by the substitution. The active site access of the variant compared to wild-type enzyme was assessed through the

introduction of the water-soluble acetylene derivate propargyl alcohol ($HC{\equiv}C–CH_2–OH$). When added to the growth media, the wild-type enzyme was unaffected while the α-V70A protein was unable to grow, presumably due to a larger substrate pocket that allows the larger alcohol in. Propargyl alcohol was a potent inhibitor of α-V70A NifDK with respect to proton and N_2 reduction, but direct reduction of propargyl alcohol resulted in propene ($H_2C{=}CH–CH_3$; 4-electron product) as a minor product, as well as allyl alcohol ($HC{=}C–CH_2–OH$; 2-electron product) as the major product. Propyne ($HC{\equiv}C–CH_3$) was also found to serve as a substrate for α-V70A NifDK, producing the 2-electron product propene, in contrast to the wild-type enzyme where propyne is a poor substrate.[55,59] Additionally, α-V70A NifDK was unable to product ethane from the reduction of acetylene.[176] Dean, Seefeldt, and co-workers then published a study of the NifDK protein, using the smaller (α-V70A) and larger (α-V70I) side chain variants to study the effect the substitutions at α-V70 had on N_2 reduction.[177] The ability of the α-V70I variant to reduce N_2 was decreased by ~70% compared to wild-type enzyme while electron flux was diverted towards proton reduction, with a concomitant increase in the K_m values for N_2 reduction from K_m = 0.1 atm to >1.5 atm. Acetylene reduction was analogously affected with a substantial decrease to C_2H_4 production, and an increase to both proton reduction and the K_m value compared to wild-type NifDK. These results were rationalized by stating that the longer side chain of isoleucine must impinge on the 'catalytic face' of the M-cluster where N_2 and C_2H_2 bind, including Fe2, Fe3, Fe6, and Fe7 from the crystallographic labeling scheme (**Figure 7**). Substitution of glycine at position α-70 resulted in a nitrogenase protein that is unable to react with N_2 at all, but maintains activity with acetylene and larger carbon-based substrates.[178] The lack of N_2 reduction with the smallest side chain variant was attributed to the inability to access higher redox states of the M-cluster, but this hypothesis was not further tested. A double mutation consisting of α-V70A and α-Q191A was also generated, and the increased substrate pocket allowed for longer chain alkynes, such as 2-butyne ($H_3C–C{\equiv}C–CH_3$), to be reduced near the proposed reactive site at Fe6 on the M-cluster.[178] Undoubtedly, the second coordination sphere environment is important for determining substrate access through steric effects, but with the drastic changes that sometimes occur in variant proteins, it is logical to be cautious in extending insights gained to the native system. The α-V70I and α-V70A NifDK proteins have been used to trap and study a variety of intermediate states with a battery of spectroscopic and computational techniques, the like of which have been described at length elsewhere[52,60,206] and will not be further discussed in this review.

Recently, a crystal structure was published by Ribbe, Hu, and co-workers that provides some structural insight into substrate binding on wild-type NifDK.[91] Previous attempts at trapping intermediates of nitrogenase have employed single-point mutations in combination with rapid freeze-quench techniques that can capture transient species.[52,60,206] The strategy used in the recent crystallographic study involved isolation of NifDK in an anaerobic environment that did not contain the exogenous reductant dithionite ($S_2O_4^{2-}$).[91] Previous work showed that when dithionite and other sulfur sources are stringently excluded from *in vitro* maturation assays, an M-cluster precursor called the L*-cluster ([8Fe-8S-C]) can be isolated on NifB that lacks a μ_2-sulfide ligand that it otherwise binds in the presence of dithionite.[133] This sulfur-deficient cluster cannot be matured into the active M-cluster unless a source of SO_3^{2-} is added, which is usually provided by the decomposition of dithionite. Drawing from this inspiration, it was reported that when NifDK was anaerobically purified under a N_2 atmosphere in the absence of dithionite (denoted NifDK*), the resultant protein was initially unreactive towards substrate reduction.[91] However, reactivity could be restored upon the addition of dithionite. When cells expressing NifDK* were grown in the presence of $^{15}N_2$, the subsequent protein was reported to have $^{15}N_2$ bound, as acid quenching samples of NifDK* yielded labeled N_2 by gas chromatography mass spectrometry (GC-MS) analysis. The labeled N_2 ligand was not observed when dithionite was included as part of the purification protocol.

Isolated NifDK* was then crystallized, and a structure was solved that contained M-clusters with additional electron density between central Fe ions of the cluster (**Figure 12**).[91] Not only that, the two M-cluster sites within the heterotetrametric NifDK each had different sets of electron density; at 'Site 1', this density appeared in the usual place of S2B (0, 0, +), and at 'Site 2', density was observed in the location of S3A (0, +, -) and S5A (0, -, -). On the basis of anomalous sulfur density, it was concluded that Site 1 lacked a sulfur atom at the S2B position, and Site 2 lacked sulfur atoms at both S3A and S5A. During refinement, best fits of the data resulted in N_2 molecules displacing the respective sulfur atoms at the two different M-cluster sites. At Site 1 (**Figure 12A**), the N_2 unit appears in a pseudo $\mu_{1,2}$-bridging mode with N6A sitting 1.8 Å from Fe2 and N6B being 2.3 Å from Fe6. N6A is also within 2.9 Å of α-H195 (-, 0, +), indicative of a potential hydrogen-bonding interaction. A stabilizing interaction between the putative N_2 unit and α-H195 would be consistent with observations from the mutagenesis studies described in this review.[139,182–185,187] At Site 2 (**Figure 12B**), the N_2 units are bound in asymmetric $\mu_{1,1}$-bridging modes where the proximal N atom is within 1.8 Å of one Fe ion, and 2.1 Å from the other (Fe4/Fe5 for the 'S3A position' and Fe7/Fe3 for the 'S5A position', respectively).[91] The distal N atom at the S3A position is 2.9–3.4 Å from

the backbone amide groups of α-G356 (+, +, 0) and α-G357, and at the S5A position the distal N is within 3.2 Å of the side chain of α-R96 (+, -, 0) and a water molecule, also suggesting potential hydrogen-bonding interactions. These positions have not been previously proposed as substrate binding sites, which is an interesting finding, although in crystal structures of V-nitrogenase, an unusual carbonate (CO_3^{2-}) ligand is found to displace the equivalent S3A atom.[92–95] Additionally, in both Site 1 and 2 of sulfur-deficient NifDK*, the *R*-homocitrate ligand appears to be bound to the Mo center through one O atom exclusively; at Site 1 the O atom from the –OH group is 2.7 Å from Mo and the $-COO^-$ group is closer, while at Site 2 the opposite is observed.[91] This could potentially indicate protonation, which may elongate the refined Mo–O distances, consistent with the proposed role *R*-homocitrate may play in proton transfer, but additional evidence is required to validate the protonation states. Moreover, when NifDK* is put under turnover conditions in the presence of dithionite and then recrystallized (PDB ID 6VXT), the cofactor returns to the normal resting state of NifDK, indicating that the displacement of sulfur is not deleterious.[91] The resolution of the crystallographic data for NifDK* does not allow for the absolute determination of the N_2 unit as a reduced species or otherwise;[207–209] however, the assignment of the N_2 unit is supported by available structural data, and it would further validate the importance of residues such as α-H195 and α-R96, as well as the 'catalytic face' of the M-cluster, while putting forward sulfur displacement as a critical mechanistic necessity for substrate reduction by Mo-nitrogenase. Further crystallographic, biochemical, spectroscopic, and computational work will be required to explore and validate these unique findings.

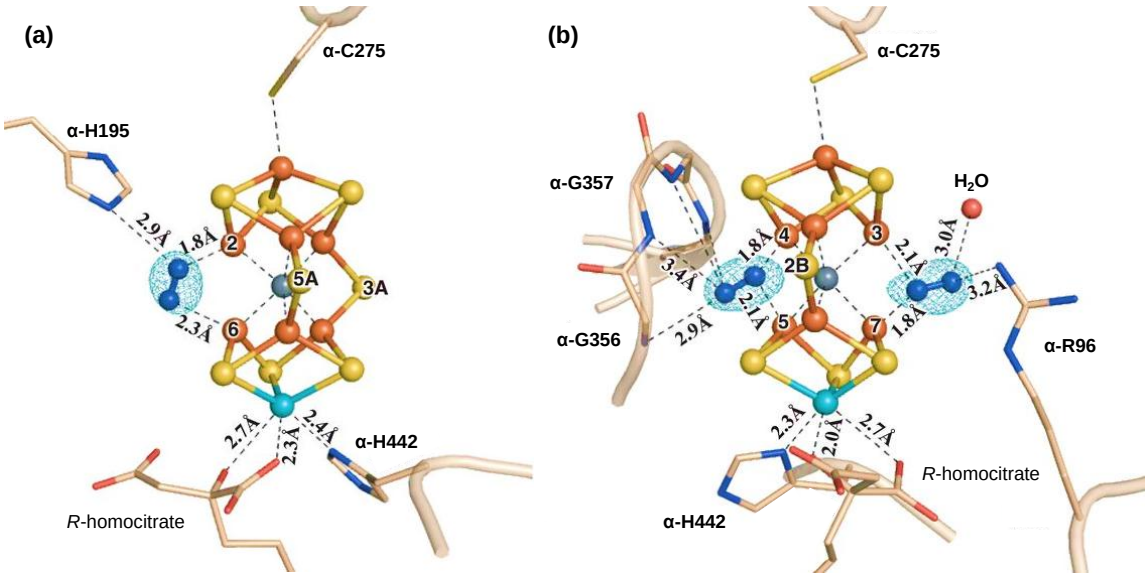

Figure 12 | Crystal structure of NifDK*. The M-cluster and key interacting residues at Site 1 **(a)** and Site 2 **(b)** are depicted (PDB ID 6UGO). The cluster and N molecules are presented

as ball-and-stick models while the residues are shown as sticks. The M-clusters are superimposed with the $F_o - F_c$ omit map of the N_2 ligands contoured at 10σ (mesh). Atomic coloring: Fe, orange; S, yellow; C, gray; O, red; N, blue. Reprinted (Adapted or Reprinted in part) with permission from ref. [91]. Copyright 2020 American Association for the Advancement of Science.

2.5.2 Inhibition by and Reduction of Carbon Monoxide

Carbon monoxide has long been characterized as an inhibitor of nitrogenase reactivity in the Mo-dependent systems that affects the reduction of all substrates apart from protons.[52,100,200,210] Mo-nitrogenase has multiple CO-related states that have been spectroscopically characterized under different conditions and concentrations of CO.[52,62] Under low electron flux conditions (1:5 Fe:MoFe protein) and in the presence of low concentration of CO (< 1% in argon), the typical $S = 3/2$ EPR signal associated with the M-cluster converts to an $S = 1/2$ signal with g values of 2.09, 1.97, and 1.93 of the 'lo-CO state', whereas under high concentrations of CO (> 50% in argon) a new $S = 1/2$ signal arises called the 'hi-CO state' with $g = 2.17$ and 2.06 (**Figure 13**).[184,202,203,211–213] Under higher electron flux conditions (1:1 Fe:MoFe protein) and high concentrations of CO, a third state known as 'hi(5)-CO' with g values at 5.78, 5.15, and 2.7 was observed in wild-type NifDK (**Figure 13**).[181,184,211] A low intensity EPR signal was observed for VnfDGK in the presence of 1 atm of CO with g values at 2.09, 1.99, and 1.91, and the intensity of this signal could be increased with more potent reducing agents.[214,215] By comparison to NifDK, the EPR signal in VnfDGK was assigned to the lo-CO form of the enzyme. In the presence of strong Europium-based reducing agents and 2.6 atm of CO, a new set of EPR signals were observed that could be described as the superposition of the lo-CO state, and a newly identified species with g-values at 2.13, 2.01, and 1.97.[215,216] Although not identical, this new signal was assumed to be analogous to the hi-CO state of NifDK. No equivalent of the hi(5)-CO state has been reported for the VFe protein.

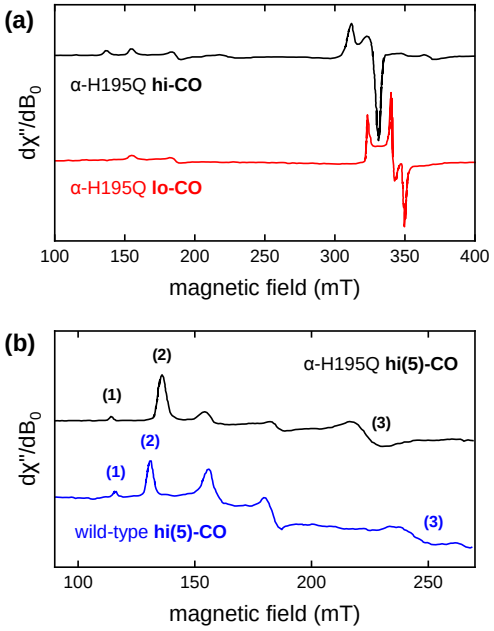

Figure 13 | EPR characterization of *A. vinelandii* NifDK during enzymatic turnover in the presence of CO. (a) α-H195Q NifDK in the presence of 1.0 atm CO (top, black) and 0.001 atm CO (bottom, red) showing the hi-CO and lo-CO signals, respectively. The small inflections are associated with the $S = 3/2$ signal of the resting state of the M-cluster. **(b)** EPR spectra of α-H195Q NifDK (top, black) and wild-type NifDK (bottom, blue) during turnover with 1 atm of CO, with the three lowest inflections (1)–(3) of the hi(5)-CO signal. The CO-related spectra of α-H195Q and wild-type NifDK are nearly identical. Reprinted (Adapted or Reprinted in part) with permission from ref. [184]. Copyright 2001 American Chemical Society. Data digitalized *via* WebPlotDigitizer v4.5.

As the crystallographic characterization of CO-bound states was not reported until 2014,[89] many of the earlier studies employed competitive substrate reduction experiments where separate N_2, C_2H_2, and proton reduction assays were compared in the presence and absence of CO.[51,52] The behavior of nitrogenase in the presence of multiple substrates could then be analyzed and extrapolated to provide insight into CO-bound states of the M-cluster. Additionally, a series of spectroscopic and computational studies revealed EPR signals that were associated with CO binding to Mo-nitrogenase. As described above, an $S = 1/2$ spin species trapped under low concentrations of CO was designated 'lo-CO' and at higher CO concentrations, another $S = 1/2$ signal would appear that was assigned 'hi-CO'.[202,211,217–221] When the initial characterization of V-dependent nitrogenase was undertaken, it was found that CO inhibited reactivity in a similar manner to Mo-nitrogenase, so it was reasonable to anticipate analogous EPR signals in V-nitrogenase. Hales and co-workers constructed a hybrid nitrogenase that used the polypeptide for V-nitrogenase from *A. vinelandii* and the M-

cluster from the *A. vindelandii* Mo-nitrogenase, hereafter labeled M-VFe protein.[222] It was found that the hybrid M-VFe protein had an activity profile more like the native V-nitrogenase. However, in the presence of CO, no EPR signals analogous to the lo-CO or hi-CO signals of Mo-nitrogenase could be observed, despite the M-VFe protein carrying the same cofactor as native M-nitrogenase. This result was puzzling, but was a strong indication that second and outer coordination sphere effects play a pivotal role in determining the properties of nitrogenase.[51,222] Later, it would be found by Ribbe and co-workers that *Av* V-nitrogenase (and to a lesser degree, wild-type *Av* Mo-nitrogenase) could catalyze the coupling of gaseous CO into longer chain hydrocarbon products following Fischer-Tropsch-like chemistry, but with an observed decrease of ~75% in the specific activity for proton reduction by the V-nitrogenase.[223–225] This finding further expanded the known capabilities of the Mo- and V-nitrogenases, but still lacked a comprehensive structural understanding of CO activity.

With the advent of crystallographically characterized, CO-bound intermediates, insight into structural features of CO binding to nitrogenase could be obtained.[89,94,95,226] In 2014, Spatzal, Rees, and co-workers published the first structure of CO binding to the M-cluster of NifDK (NifDK-CO) which corresponded to an inhibited state of the enzyme (**Figure 14A**).[89] The CO molecule was ligated between Fe2 and Fe6 of the M-cluster in a μ_2-binding mode, apparently displacing the μ_2-S2B sulfur atom that is usually found in resting state structures of NifDK.[61,66,151] The CO ligand was bound symmetrically between the two Fe ions, with Fe–CO distances of 1.86 Å to both metal centers, and the oxygen atom of the CO moiety within close proximity to the side chains of residues α-H195 (2.8 Å) and α-V70 (3.4 Å). The interaction between α-195His and CO is within range of a hydrogen bond, which would affect the stability of the CO moiety, while non-bonding interactions from α-V70 may provide stability. When crystals of NifDK-CO were dissolved into buffer in the absence of exogenous CO, the S2B atom and acetylene reduction activity were quantitatively recovered.[89] EPR spectra of NifDK-CO in the solution state, obtained under analogous conditions to crystallography, demonstrated the appearance of an $S = 1/2$ signal previously assigned to the lo-CO species, connecting spectroscopy and structural biology.[214]

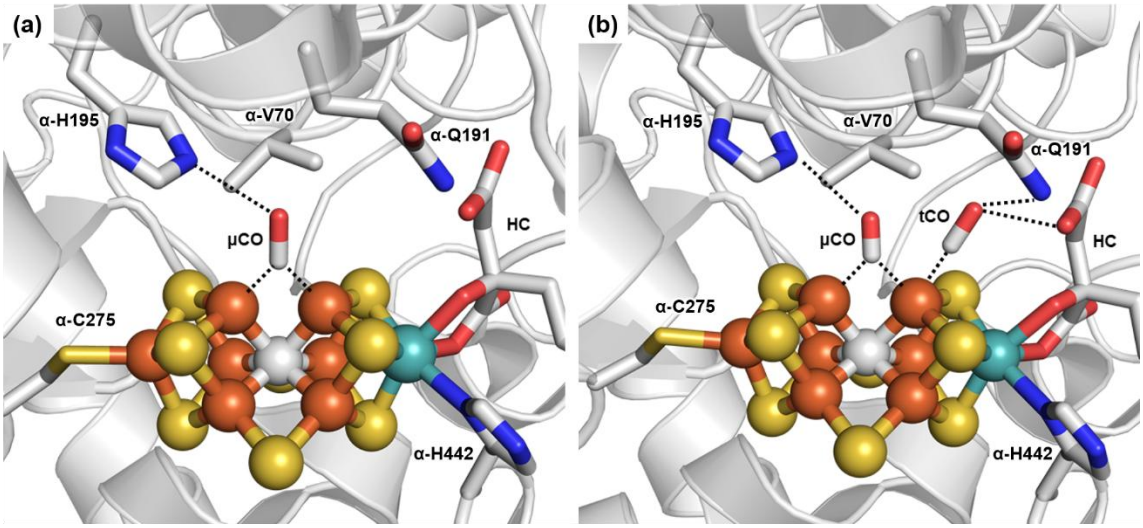

Figure 14 | Crystal structure of NifDK-CO (a) and NifDK-(2CO) (b) from *A. vinelandii*. The cluster atoms are shown as ball-and-stick models, the CO, *R*-homoctirate (HC), and amino acid residues are represented as sticks. Black dotted lines represent a bonding interaction, blue dotted lines represent potential hydrogen bonding interactions. Atomic coloring: Fe, orange; S, yellow; C, gray; O, red; N, blue. PDB ID 4TKV for NifDK-CO and PDB ID 7JRF for NifDH-(2CO).

Recently, Spatzal, Rees, and co-workers reported another CO-bound crystal structure of NifDK (**Figure 14B**), but with two CO ligands as opposed to one (NifDK-(2CO).[226] This species was isolated when crystals of NifDK-CO were pressurized with CO at 5.4 atm. The first CO ligand ('μCO') is found in a bridging position between Fe2 and Fe6 of the M-cluster in a μ_2-binding mode analogous to that in NifDK-CO, with Fe–CO distances of 1.93 and 1.92 Å, respectively. The second CO ligand ('tCO') is bound in a terminal mode to Fe6, with an Fe–CO distance of 2.03 Å. This causes the Fe6–C distance to slightly elongate from 2.01 Å in NifDK-CO to 2.06 Å in NifDK-(2CO).[89,226] The oxygen atom of tCO may interact with the amide N of the α-Q191 residue (~3.3 Å) and an carboxylic acid group of *R*-homocitrate (~2.7 Å), while μCO maintains analogous interactions with the side chains of α-V70 and α-H195, in a similar manner as in NifDK-CO. Although tCO is modeled with only 50% occupancy, likely because the binding of this ligand is relatively weak (compared to μCO with 100% occupancy), parallel EPR spectra of solution state and crystal slurry NifDK-(2CO) were used to assign μCO and tCO to the lo- and hi-CO states, respectively.[226]

Analogous crystal structures were solved by Einsle and co-workers of the V-dependent nitrogenase with one (VnfDGK-CO) and two (VnfDGK-(2CO) CO molecules bound (**Figure 15**).[94,95] For the 1.0-Å resolution structure of VnfDGK-CO, the CO molecule is bound in a μ_2-

bridging mode between Fe2 and Fe6, much like that found in the lo-CO state of NifDK-CO, but with a slight asymmetry (Fe2–CO = 2.03 Å, Fe6–CO = 1.94 Å).[94] The μCO ligand has similar interactions with local amino acid side chains, being within 2.9 Å of α-H180 and 3.6 Å of α-V57 (analogous to α-H195 and α-V70 in NifDK, respectively). Unlike NifDK-CO, when VnfDGK-CO crystals are used for activity assays in the absence of exogenous CO, the typical S2B ligand is not found between Fe2 and Fe6. Instead, a monoatomic ligand that interacts with the nearby α-176Gln residue is observed and was assigned as a putative μ_2-OH species. The authors propose that this oxygen-based ligand may reflect a reduction product of a previously bound CO ligand.[94] When crystals of VnfDGK-CO were pressurized with 1.5 atm of CO for 1 minute, a 1.05-Å crystal structure of the VnfDGK-(2CO) was obtained (**Figure 15B**).[95] The μCO ligand in VnfDGK-(2CO) is positioned in the same manner as in VnfDGK-CO, and the terminal CO ligand is bound to Fe6 with an occupancy of 50%, analogous to the structure of NifDK-(2CO); however, the tCO in VnfDGK-(2CO) has an Fe6–tCO distance of 1.89 Å, compared to 2.03 Å in NifDK.[95,226] The oxygen atom of tCO in VnfDGK-(2CO) is also in close proximity to the *R*-homocitrate ligand (~2.9 Å) and the α-176Gln residue (~3.1 Å). Despite the high degree of similarity in active site for the two structures, the tCO ligand appears to be more strongly bound in VnfDGK-(2CO) versus NifDK-(2CO), which may align with the difference in reactivity observed for both systems.[51] However, there are strong indications that the lo-CO and not the hi-CO state of V-nitrogenase is catalytically competent for CO reduction.[215,216] A parallel set of EPR measurements using solution and crystal slurry samples of VnfDGK-(2CO) was not reported by Einsle and co-workers,[95] so the crystallography could not be directly connected to the available spectroscopic characterization of the lo- and hi-CO states. Instead, *in situ* Fourier-transform infrared (FTIR) difference spectroscopy was conducted using a film of VnfDGK in the presence of N_2 and CO isotopes.[95] Supporting the crystallographic assignment, isotopically sensitive features at 1931 and 1888 cm^{-1} were assigned to $t^{12}CO$ and $t^{13}CO$, respectively. Due to strong background signals at lower frequencies, a vibration for the $\mu^{12}CO$ could not unambiguously be assigned, but a putative signal was identified at 1720 cm^{-1}. More work in the future will be needed to fully understand the structure-function relationships gleaned from these structural studies.

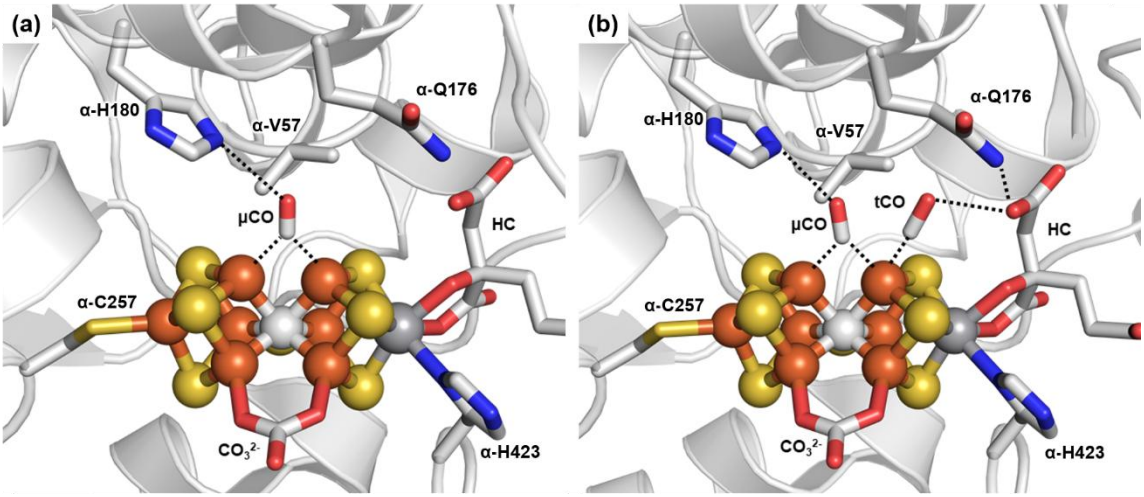

Figure 15 | Crystal structure of VnfDGK-CO (a) and VnfDGK-(2CO) (b) from *A. vinelandii*. The cluster atoms are shown as ball-and-stick models, the CO, *R*-homoctirate (HC), carbonate, and amino acid residues are represented as sticks. Black dotted lines represent a bonding interaction, blue dotted lines represent potential hydrogen bonding interactions. Atomic coloring: Fe, orange; S, yellow; C, gray; O, red; N, blue. PDB ID 7ADR for VnfDGK-CO and PDB ID 7AIZ for VnfGDH-(2CO).

Based on the crystallographic information, what can be said is that α-Q191, α-H195, and α-V70 in NifDK (and equivalent analogs in VnfDGK) are residues that can interact with the catalytic cofactor when CO molecules are bound. The α-H195 residue is in hydrogen-bonding distance to the μCO ligand and has been proposed to generally be involved in proton delivery during substrate turnover.[227–229] The α-Q191 residue is within an appropriate distance from the tCO ligand to potentially interact, but additionally does help stabilize the *R*-homocitrate ligand that binds to the Mo or V ion of the catalytic cofactor.[95,226] As stated previously, the hi-CO state does not appear to be competent for CO catalysis,[215,216] thus binding to tCO may not be relevant, but the equivalent residue in VnfDGK, α-Q176, has been shown to stabilize a putative N_2 reduction intermediate through a hydrogen-bonding interaction, which further reinforces the importance of this residue.[93] These details regarding CO-bound species provide a measure of perspective previously inaccessible and allows for a retrospective look on experiments conducted to assess the structural basis of CO inhibition within nitrogenase.

The Influence of Point Mutations on the Reaction with CO. The research groups of Dean and Newton have generated a multitude of single-point mutants of NifDK that have been used to study substrate interactions with the enzyme, including CO. Many of these studies yield overlapping information regarding the properties of NifDK variants, including insights gleaned from experiments with crude extracts of *A. vinelandii* cells and purified variant

proteins, so it can be difficult to comprehensively describe the results. Instead of addressing every possible variant reported, the effects of mutations to the α-H195 and α-Q191 residues on CO reactivity will be the primary focus, as well as relevant comparisons to other variants, as necessary.

As described earlier, the site-directed mutagenesis in NifDK of α-H195 (-, 0, +) and α-Q191 (+, +, +) to α-H195N and α-Q191K were reported for *A. vinelandii*.[182] The crude extracts of variant cells were individually assayed in an atmosphere of 10% acetylene (C_2H_2), demonstrating that the variant NifDK proteins were much less active than wild-type enzyme for the generation of C_2H_4, but they also produced some amount of ethane (C_2H_6), whereas wild-type NifDK does not. This raised interest in these variants, as crystallographic evidence would not be available for several years, and the pattern of reactivity was similar to that found for V-nitrogenases.[51] When C_2H_2 reduction assays were carried out, the α-H195N variant was less sensitive to inhibition by CO, showing 50% activity in the presence of 0.5% CO, compared to wild-type NifDK that showed the same reduction already at 0.02% CO. It is important to note that these effects were observed with only the crude extracts, as the protein could not be purified at that time. EPR spectra of whole cells indicated that the S = 3/2 M-cluster signal was still present in the variant, albeit with axial perturbations, and low intensity (~6% compared to wild-type enzyme).[182,185] Several years later, five additional variants of α-H195 were reported.[187] Similar to the previous reports of α-H195N,[182,185] the crude extracts of the tyrosine, threonine, and glycine variants were not particularly active, but the glutamine and leucine variants expressed slightly higher activity, with α-H195Q NifDK maintaining ~70% the activity of crude extracts of wild-type enzyme.[187] Whole cell EPR of all variants had similar line shapes to wild-type enzyme, but the glycine and leucine variants had much lower intensities of the S = 3/2 signal ($\leq$ 10%), whereas α-H195Q NifDK had comparable intensity to native enzyme, with slight perturbations of the *g*-values. The proton reduction activities in the presence and absence of CO were assayed, finding that the asparagine, glutamine, and leucine variants are relatively insensitive to CO, but α-H195T NifDK was sensitive to the presence of CO, with ~50% reduction of activity. The α-H195Q NifDK protein was further purified for more accurate comparisons to wild-type enzyme. It was found that CO is a noncompetitive inhibitor of C_2H_2 and N_2 reduction for both proteins, but CO had a more potent inhibition of α-H195Q NifDK compared to wild-type enzyme. The authors suggested that α-H195 could be involved in steric interactions, as the much smaller glutamine residue would be unable to fill the same space as a histidine side chain, leaving room within the active site. Additionally, it was noted that the glutamine residue could still provide a

hydrogen-bonding interaction to the S2B sulfur, although the electronic effect of the histidine-derived versus the glutamine-derived interaction could modulate the redox potential of the M-cluster, but not sufficiently to completely change the activity profile. We now know that the S2B site is the location of the μCO ligand in the lo-CO state,[89] and a subsequent 2.5 Å crystal structure of α-H195Q NifDK showed the glutamine and histidine residues at position 195 have a similar distance to the S2B sulfur (**Figure 16**).[184] This could rationalize why some of the other α-H195 variants do not generally exhibit any sensitivity to CO – the responsible residues are simply too far from the μCO site to strongly interact. The crystal structure also shows that the substitution of histidine for glutamine greatly destabilizes the local hydrogen-bonding network surrounding the M-cluster, complicating the interpretation. Moreover, different substitutions at α-H195 resulted in protein variants with CO-insensitive proton reduction and CO-inhibited acetylene reduction,[187] which led to the proposal of multiple CO binding site at the M-cluster. In pursuit of this idea, Newton, Fisher, and co-workers used the α-H195Q and α-H195N NifDK proteins in reactivity experiments with HCN, CN^-, and N_3^- in combination with CO.[183,188,191] For the variants, CO was found to remove the inhibitory effects of CN^- and N_3^-, implying that these classic nitrogenase inhibitors all bind to the same sites, albeit with different affinities. In other GPMs like formate dehydrogenase (**Section 4**) and CO dehydrogenase (**Section 5**), CN^- and N_3^- inhibit activity, which highlights a functional connection between the low-valent metalloenzymes discussed herein. Recent structural evidence now shows a second CO binds terminally to Fe6 of the M-cluster, but α-H195 is located near Fe2 and is generally unperturbed going from the NifDK-CO to the NifDK-(2CO) structures.[89,226] Moreover, it may be possible for CO molecules (or other inhibitors) to bind to the Fe2 site on the M-cluster in α-H195 variants due to the change in the relative steric protection provided by the imidazole ring, underlining the importance of second coordination sphere effects. Additional structural information with other inhibitory molecules would be important for better understanding these complex effects.

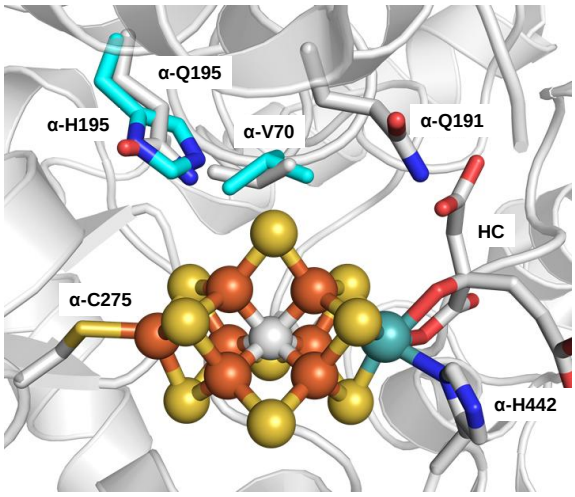

Figure 16 | Crystal structure of α-H195Q NifDK from *A. vinelandii*. The grey color protein represents α-H195Q NifDK (PDB ID 1FP4) and the light blue color protein represents residues from wild-type NifDK (PDB ID 3U7Q). The cluster atoms are shown as ball-and-stick models, the *R*-homocitrate (HC), and amino acid residues are represented as sticks. Atomic coloring: Fe, orange; S, yellow; C, gray; O, red; N, blue.

The α-Q191 (+, +, +) residue of NifDK has been a target of mutagenic studies for as long as α-H195.[182,185] Crude extracts of α-Q191E and α-Q191K NifDK were assayed with C_2H_2 and in the presence of 0.02% CO, activity was inhibited by 50% and 75%, respectively.[185] The α-Q191K NifDK was then further purified because the α-Q191E variant was less stable. The purified α-Q191K NifDK protein exhibited an EPR spectrum that had similar line shape to that of the wild-type NifDK, but with perturbations to the *g*-values, suggesting that the M-cluster was bound to the protein similarly in both proteins. The introduction of 3% CO into substrate reduction assays showed that electron flux for reactions with α-Q191K NifDK decreased by about 70%, 40%, and 50% for N_2, C_2H_2, and proton reduction, respectively, compared to in the absence of CO.[185] This is an unusual finding considering that wild-type NifDK generally redistributes electron equivalents from the reduction of N_2 and C_2H_2 towards proton reduction in the presence of CO.[51,185] Much like for the α-H195His variants, the purified α-Q191K NifDK was also assayed for proton reduction in the presence of both CN^- and CO.[191] The α-Q191K variant showed a mild inhibition of proton reduction in the presence of CN^-, and subsequent introduction of a 10% CO atmosphere further decreased the H_2-specific activity. In contrast, the wild-type and α-H195 variant proteins show inhibition of total electron flux by CN^- but this activity is restored in the presence of CO. The result agrees with the previous observation of CO-derived inhibition of the electron flux for α-Q191K NifDK,[185] but supports that α-Q191 likely can interact with both substrates and inhibitors.

It is now possible to glean additional insight from the crystal structures of NifDK-CO and NifDK-(2CO). **Figure 14** shows how the α-Q191 residue of NifDK in both structures is bent away from the M-cluster, but the residue is in proximity to several molecules, 3.6 Å from an H_2O molecule, 3.3 Å from the tCO ligand and 2.9 Å from a terminal carboxylate of the *R*-homocitrate ligand.[89,226] Similar distances are also found to the analogous α-Q176 residue in the CO-bound structures of the V-nitrogenase (**Figure 15**).[94,95] In addition, it has been noted that the α-Q176 residue can swing in to interact with the V-cluster at the S2B position, so the residue is less static.[93] The closest and likely strongest interaction is between α-Q191 and *R*-homocitrate, so when glutamine is mutated to lysine, the sidechain is extended by an additional carbon atom, which may introduce steric misalignment of the Lys residue in the active site. Lysine may clash with the tCO binding site, preventing substrate molecules from properly accessing the M-cluster. This would be consistent with an observation made by Hales, Newton, and co-workers that α-Q191K NifDK does not generate a hi-CO EPR signal (thus, does not bind tCO), only showing the lo-CO signal, even under 100% CO atmosphere.[181]

The Role of the Homocitrate Ligand. While a physical blockage by lysine may be the source of the aberrant properties of α-Q191K NifDK, another important factor is that disrupting the α-Q191–homocitrate interaction may destabilize the hydrogen-bonding network within the M-cluster active site thought to be critical for proton delivery during catalysis.[102,181,229–232] When the *nifV* gene is knocked out of a nitrogenase-expressing organism, the resulting Δ*nifV* NifDK protein has an M-cluster with citrate in place of *R*-homocitrate.[196,197] In the presence of 3% CO, crude extracts of Δ*nifV* NifDK from *Klebsiella pneumoniae* (*Kp*) demonstrate a ~50% decrease of proton reduction, similar to what was observed for α-Q191K NifDK.[185,196,233] Further investigation showed that CO would decrease the electron flow through *Kp* Δ*nifV* NifDK, and uncouple MgATP hydrolysis from electron transfer with a corresponding decrease to the observed proton reduction.[233] This analysis by Dixon and co-workers also indicated that CO is unlikely to be reduced by the variant Mo-nitrogenase from *K. pneumoniae*. Analogous Δ*nifV* NifDK variants were also generated in *A. vinelandii*, showing a range of activities in the presence of CO.[181,234,235] Newton, Hales, and co-workers showed that proton reduction by *Av* Δ*nifV* NifDK was inhibited by ~40% in the presence of CO, a similar magnitude to the protein from *K. pneumoniae*, and that *Av* Δ*nifV* NifDK was capable of supporting lo-CO, hi-CO, and hi(5)-CO states.[181,234] However, CO reduction by a Δ*nifV* NifDK protein was not reported until 2021.[235] This protein, compared to

wild-type NifDK, expressed lower activities for all substrates, including CO. It was reported that the Mo content of the *in vivo* isolated *Av* Δ*nifV* NifDK was only ~30% of that in the wild-type protein, which may in part explain the low observed reactivity of the protein. To improve incorporation, an *in vitro* reconstitution of Δ*nifV* NifDK was carried out, which increased the M-cluster present, while showing similar reactivity patterns as the *in vivo* isolated variant with higher activity. In the presence of CO, Δ*nifV* NifDK diverts more electron flux from proton reduction towards hydrocarbon formation while still maintaining lower specific activity than wild-type enzyme. These observations were not made previously for the *A. vinelandii* variant because it was not reported that *Av* NifDK could reduce CO to hydrocarbons until 2011 when scaled up reaction conditions were used to detect low-yielding products for V-nitrogenase.[223] An analogous Δ*nifV* variant was also generated for V-nitrogenase, showing that citrate also binds to the V-cluster.[236] However, unlike in the Mo-dependent system, the Δ*nifV* VnfDGK protein produces a decreased amount of longer chain hydrocarbon products compared to wild-type VnfDGK, favoring a slight increase in proton reduction.

Initially, it was unclear what role the *nifV* gene played in nitrogenase biosynthesis, but in 1990, Burris and co-workers reported that the organic ligand bound to the M-cluster was identified as citrate, which was subsequently confirmed in 2002 by Lawson and co-workers who reported a 1.9 Å resolution crystal structure of the *Kp* Δ*nifV* NifDK.[197,237] The structure of the Δ*nifV* protein is highly similar to wild-type NifDK, but while *R*-homocitrate can form hydrogen-bonding interactions with the backbone amide of α-I423 (~2.8 Å), the citrate ligand in Δ*nifV* NifDK is further away from α-I423 (~3.7 Å) and requires H_2O molecules to facilitate an interaction.[237] This would potentially serve to leave the citrate ligand loosely bound to the protein scaffold, disrupting the hydrogen-bonding network necessary for proton delivery to the M-cluster. An additional ramification would be that the loss of second coordination sphere interactions may also modulate the redox properties of the catalytic cofactor, similar to what was proposed for certain α-H195 NifDK variants (*vide infra*). This also means that it might be rather difficult to deconvolute the effects of α-191Gln substitutions from those of Δ*nifV* knockout proteins, because the Gln residue is involved in stabilizing interactions with the citrate ligand. However, there are distinct differences. The α-Q191K NifDK protein only supports the lo-CO EPR signal, while *Av* Δ*nifV* NifDK supports all three CO-based EPR signals. In fact, Newton and co-workers expanded investigations of CO on the reactivity of NifDK by introducing mutations to residues α-R96 (+, -, 0), α-R277 (-, +, +), and α-R359 (0, +, -).[181,186] In this study, CO-bound states were generated for a series of NifDK variants and

the EPR spectra were collected along with proton reduction assays in order to correlate the spectroscopic signals to catalytic activity. Wild-type NifDK, as well as α-R96Q NifDK, and *Av* Δ*nifV* NifDK all showed the lo-CO, hi-CO, and hi(5)-CO states. However, the variants α-R96K, α-R277C, and α-R359K supported only lo-CO and hi(5)-CO, but not the hi-CO state. Interestingly, α-R277H only showed the hi(5)-CO signal. Inhibition of proton reduction by CO was also equally dynamic, with instances of no inhibition in α-R96Q but ~50% inhibition with the α-R96K substitution, among others.[181] With this, the authors concluded that the CO-related EPR signals and proton reduction activity could not be correlated, noting that the single-point mutations did not introduce additional CO-binding sites.[181] The α-R277C NifDK variant was slightly different, in that it demonstrated a 70% increase in proton reduction in the presence of 10% CO compared to the wild-type enzyme.[186] With higher electron flux conditions, the proton reduction activity was enhanced, but dropping the flux resulted in a lack of H_2 inhibition albeit with slower rates, similar to wild-type NifDK. It was proposed that CO binding to α-R277C NifDK affected catalytic proton transfer and additionally prevented the M-cluster from accessing more reduced states (*i.e.*, E_3 and E_4 from the Lowe-Thorneley cycle). Instead, the variant may divert all the electron equivalents into the E_2 state which subsequently generates H_2.[186] It is unclear why CO binding would have such a different effect on the reactivity in the α-R277C variant compared to the others, and more work is needed to gain further understanding of CO reactivity.

Reduction of Carbon Monoxide. Attempts to stimulate CO reduction in Mo-nitrogenase have been carried out using combinations of point mutations to α-V70 (0, -, +), α-R96 (+, -, 0), α-H195 (-, 0, +), and α-Q191 (+, +, +).[179] Modifications of α-V70 in *Av* NifDK have been shown to increase the substrate scope of the enzyme by changing the steric environment around the M-cluster.[52,194] The α-V70G and α-V70A NifDK variants, were reported to react with CO, producing hydrocarbons ethylene (C_2H_4), propene (C_3H_6), ethane (C_2H_6), and propane (C_3H_8) in a ratio of 7:4:2:1.[179] The reported rates are much lower than those reported for V-nitrogenase, but greater than those reported for wild-type Mo-nitrogenase.[223] Double mutations were then incorporated to assess the effect of α-R96, α-H195, and α-Q191 on the α-V70-mediated CO reactivity.[179] The α-V70A/α-R96H and α-V70A/α-Q191A NifDK variants show a different product pattern than the single substitutions, with similar values for all C_2 and C_3 products, as well as the inclusion of trace amounts of methane (CH_4). The α-V70A/α-Q191A NifDK, though, produces twice as much C_3H_6 than the α-V70A/α-R96H variant. Additionally, α-V70A/α-H195Q was shown to drastically decrease product formation compared to the single α-V70A NifDK variant. It is difficult to make definitive statements

about the exact effect of point mutations in this case because of the interconnected nature of the second coordination sphere effects. What can be said is that the α-V70 residue seems important for regulating the size of substrates and products, consistent with previous observations.[52] The size reduction of the α-70 residue side chain allowed for the coupling of multiple CO molecules, and by extension, additional modification of α-R96 and α-Q191 further expanded the active site to favor the generation of longer chain hydrocarbons. However, the loss of activity in the α-V70A/α-H195Q NifDK protein shows that the size of the cavity is not the only factor governing reactivity toward CO. The α-Q191 and α-H195 residues are known to be involved in proton transfer[102,181,229–232], but the present data may reflect a more direct role of α-H195 in protonation of reduced, CO-coupled species whereas α-Q191 may play more of a structural role. It may also be possible that substitution of α-Q191 could affect the rate of protonation and allow for intermediate species to accumulate, increasing the hydrocarbon length. Rigorous studies involving additional mutations that vary the size and proton donor ability of the side chains may be necessary to shed further light on the 'steric vs. protonation' arguments for the reaction of CO with nitrogenase. It is also possible that yet unidentified factors such as electron transfer rate or allosteric changes may play a role.

2.5.3 Reduction of Carbon Dioxide

The triatomic carbon dioxide (CO_2) is a highly oxidized small molecule that was found to react with Mo-nitrogenase in 1995.[238] CO was initially found as the product of the reaction, as the concentration of CO would increase only in the presence of NifH and MgATP, indicating it was a nitrogenase-dependent phenomenon. However, the exact substrate form, CO_2, CO_3^{2-}, or HCO_3^-, was unclear because of the equilibrium between CO_2 and bicarbonate (HCO_3^-) in solution. It was later found that NifDK was capable of generating CH_4 and C_2H_4 from from CO_2, although the rate of hydrocarbon formation was an order of magnitude slower than CO formation.[239] Interestingly, V-nitrogenase was found to reduce CO_2 to CO in H_2O buffers, but in deuterated buffers, deuterated hydrocarbons (CD_4, C_2D_4, C_2D_6) were observed while NifDK was unable to generate deuterated products under these same conditions. For both Mo- and V-nitrogenase, the specific activity of CO evolution from CO_2 increased in the deuterated buffer system resulting in an *inverse* kinetic isotope effect (KIE).[239] This could indicate that the formation of CO is carried out through similar mechanisms in both nitrogenases, but the change in hydrocarbon product profile between the two nitrogenases is reflective of something more complex, requiring further investigation.

Subsequently, Mo-nitrogenase variants α-V70A and α-H195Q were shown to convert CO_2 into methane (CH_4), confirmed by use of ^{13}C-labeled bicarbonate.[240] Under the reported conditions, C_2 and C_3 hydrocarbon products were not observed. As the NifH:NifDK ratio in the reaction was increased, the rate of the competing proton reduction reaction decreased, diverting electron flux to the formation of CH_4. Even with a high electron flux (50:1), the primary product was H_2, which makes sense considering that proton reduction is a two-electron process while the conversion of CO_2 to CH_4 requires eight electrons. To separate the reaction of the α-V70A and α-H195Q NifDK variants between CO and CO_2, deoxyhemoglobin was added to the activity assays so that any released CO molecule would be rapidly removed from the analysis.[240] The resultant reactions demonstrated a ~25% decrease in the production of CH_4, indicating that two different processes were being observed: one where CO_2 remains bound to nitrogenase throughout the reduction reaction and another where CO dissociates and presumably rebinds to the M-cluster before reduction to CH_4. CO_2 reduction was further explored when the NifDK variant was incubated in an atmosphere of 45% CO and Ar, including 1–3% acetylene (C_2H_4). Propylene (C_3H_6) was observed as the major product with propane (C_3H_8) as a minor component, and isotopically labeled ^{13}C atom from bicarbonate was found to incorporate into propylene. This indicates that one molecule each of CO_2 and acetylene can couple to form the product. Adjustments of the electron flux would favor CH_4 formation at a higher nitrogenase ratio and C_3H_6 formation at lower ratios. Additionally, introduction of ethylene to the CO_2 reaction did not yield propylene, suggesting that the mechanism requires that both molecules must bind and be activated by the cluster before they can be coupled.

It is interesting that in the double mutant α-V70A/α-H195Q NifDK, the reactivity with CO is inhibited compared to α-V70A NifDK, but the same α-H195Q mutation enhances the reactivity of the variant NifDK with CO_2. Electron transfer rates seem to be important factors for determining the result of CO_2 reduction. A slower rate would favor reduced intermediate species that are long-lived, encouraging C–C bond formation, whereas faster electron delivery appears to more quickly generate CH_4, discouraging carbon coupling.[240] However, electron transfer in nitrogenase must also be understood in the context of proton transfer, because the two are closely linked.[63] In the α-V70A NifDK variant, CO molecules are readily coupled to form longer chain hydrocarbons, but this activity becomes disrupted when the α-H195 residue is exchanged for one less capable of proton transfer. The timing of proton-coupled electron transfer to the substrate is affected for CO reduction but happens to function well for the eight-electron reduction of CO_2. What should be emphasized is that a new activity was

generated by controlling the second coordination sphere *via* the steric environment to house larger substrates in the active site nice and the tuning of protonation to one of the oxygen atoms of CO_2 to generate CO and H_2O. Recently, CO_2 has also been converted to CH_4 by the wild-type Fe-only nitrogenase from *Rhodopseudomonas palustris*,[241] but without additional mutational or structural information about the Fe-only nitrogenase it is difficult to gain further insight into the factors that control CO_2 reduction. The structure and catalytic mechanism of other low-valent GPMs active in CO_2 reduction like formate dehydrogenase and CO dehydrogenase are discussed in **Section 4** and **Section 5**, respectively.

3 Hydrogenase

Hydrogen turnover (**Eq. 2**) is a very important reaction in many microorganisms that thrive under reducing, anoxic conditions, and also plays a role in certain aerobes.[242–244] Trace amounts of H_2 provide electrons to power the anabolism of numerous archaea and bacteria in the soil, aqueous environments, or host tissue (H_2 oxidation or 'H_2 uptake').[245–247] although H_2 gas barely accumulates in the atmosphere, the high affinity of the enzymes responsible for H_2 oxidation easily compensates for low substrate levels. Under fermentative or 'microaerobic' conditions, proton reduction and H_2 release has been shown to be a key in the redox regulation of autotrophs like photosynthetic bacteria and algae.[248–250] Additionally, H_2 contributes to the cellular redox equilibrium as a side product of N_2 fixation by nitrogenase, as discussed in **Section 2**. Besides nitrogenases, the GPMs responsible for proton reduction and H_2 oxidation are referred to as hydrogenases.[251]

Eq. 2 $$H_2 \rightleftharpoons 2\,H^+ + 2\,e^-$$

Three classes of phylogenetically unrelated hydrogenases have been defined.[252] In archaea, Hmd [Fe]-hydrogenase is involved in the conversion of CO_2 to CH_4 (methanogenesis), catalyzing H_2 splitting and hydride transfer at a cofactor with a monometallic iron center, *i.e.*, only the forward direction of **Eq. 2**.[253–255] Not much is known about the influence of second or outer coordination sphere effects, thus we will focus on the remaining two classes in this article. Unlike Hmd [Fe]-hydrogenase, [NiFe]- and [FeFe]-hydrogenase are iron-sulfur enzymes and carry a bimetallic active site cofactor (**Figure 17**).

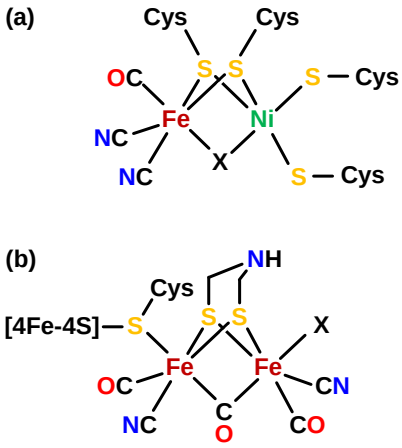

Figure 17 | Schematic representation of hydrogenase cofactors. (a) [NiFe]-hydrogenase active site cofactor and **(b)** [FeFe]-hydrogenase active site cofactor. The [4Fe-4S] cluster is coordinated by three further cysteines (not shown). Note the presence of an azadithiolate ligand (ADT, $S_2(CH_2)_2NH$) at the diiron site. 'X' marks the catalytic binding site in both cofactors.

[NiFe]-hydrogenases have been found in archaea and bacteria, and are typically involved in heterotrophic H_2 uptake and the 'recycling' of H_2 during methanogenesis or N_2 fixation (**Section 2**).[255–257] A classification into groups 1–4 has been proposed[246], in which the soluble 'standard' [NiFe]-hydrogenases are distinguished from membrane-bound, multimeric, as well as O_2-tolerant and bidirectional [NiFe]-hydrogenases.[257–259] Although highly diverse, all [NiFe]-hydrogenases share the same active site cofactor. It is comprised of a nickel and an iron ion, covalently attached to the enzyme by either four cysteine residues, or three cysteine and one selenocysteine (**Figure 17A**). The iron ion is coordinated by two CN^- and one CO ligand, the latter being a common feature of hydrogenases.[260]

[FeFe]-hydrogenases have been found in bacteria, lower eukaryotes, and green algae, representing the phylogenetically most recent class.[261–263] The physiological diversity among [NiFe]-hydrogenases is less pronounced than in [FeFe]-hydrogenases[246]: often, [FeFe]-hydrogenases are involved in redox regulation (H_2 release upon proton reduction) but in complex with other metalloproteins, additional roles in CO_2 reduction (**Section 4**) or bifurcation have been suggested.[264–266] 'Standard' [FeFe]-hydrogenases belong to group A and have been investigated intensively whereas knowledge about group B–C [FeFe]-hydrogenase is only beginning to emerge.[267,268] **Figure 17B** shows the active site cofactor including the covalently attached [4Fe-4S] cluster. The metal ions of the diiron site are modified with a bridging carbonyl ligand (μCO) and two terminal CN^- and a CO ligands. Going on, we will elaborate on the active site architecture, catalytic mechanism, and

second/outer coordination sphere effects in [NiFe]-hydrogenase (**Section 3.1**) and [FeFe]-hydrogenase (**Section 3.2**).

3.1 [NiFe]-hydrogenase

3.1.1 Structural Features of [NiFe]-hydrogenase

[NiFe]-hydrogenases are divided into Group 1–4, according to the classification by Morales, Greening, and co-workers.[246] In these groups, [NiFe]-hydrogenases are initially divided into 'H_2 uptake' (Groups 1 and 2), 'bidirectional' (Group 3), and 'H_2 evolving' (Group 4) clades. Each group is divided into subgroups, *e.g.*, the O_2-sensitive prototypical or standard-type hydrogenases in Group 1b and the O_2-tolerant membrane-bound hydrogenases in Group 1d. The complete list is available in the 'hydrogenase database', HydDB.[269] [NiFe]-hydrogenases are multi-subunit proteins, which contain at least the catalytic subunit and an iron-sulfur cluster subunit. For example, standard [NiFe]-hydrogenases (Group 1b) are comprised of two subunits, large and small, with molecular weights of approximately 60 kDa and 30 kDa, respectively (**Figure 18A**).[270] The large subunit binds the catalytic cofactor and the small subunit embeds the accessory iron-sulfur cluster. The first crystal structure of a standard [NiFe]-hydrogenase was determined for the enzyme from *Desulfovibrio gigas* (*Dg*) in 1995 at 2.85 Å resolution[271], followed by the structures of [NiFe]-hydrogenases from *Desulfovibrio vulgaris* Miyazaki F (*Dv*MF)[272–276] and other species.[277–290] The Ni–Fe active site cofactor is located inside the large subunit, where the Ni and Fe ions are bridged with two cysteine thiolates, and another two cysteine residues are bound to the Ni ion in a terminal fashion.[273,291,292] In addition to two CN^- and one CO ligand coordinated to the Fe ion, a bridging hydride ligand (μH^-) may exist between the metal ions (**Figure 18B**).[273] The Ni site changes its oxidation state (*i.e.*, Ni^{3+}, Ni^{2+}, and Ni^+) among various intermediate states, some of which (Ni^{3+} and Ni^+) are characterized by electron paramagnetic resonance (EPR) spectroscopy. On the other hand, the Fe site maintains the low oxidation, low spin state (Fe^{2+}, $S = 0$).[293–299] In the O_2-tolerant NAD^+-reducing [NiFe]-hydrogenase (Group 3d) from *Hydrogenophilus thermoluteolus* TH-1, three cysteine thiolates bridge the Ni and Fe ions while one cysteine residue terminally ligates to the Ni ion in the oxidized state.[284] In the case of [NiFeSe]-hydrogenase, a terminal cysteine is replaced by a selenocysteine.[300–304] In standard [NiFe]-hydrogenases, three iron-sulfur clusters are located in the small subunit and mediate the electron transfer between the Ni–Fe active site and physiological redox partners.[305–308] In the crystal structure of the O_2-tolerant membrane-bound [NiFe]-

hydrogenases (Group 1d, see **Figure 18C**), a proximal [3Fe-4S] cluster harbored by six cysteine residues has been identified.[286,288,289]

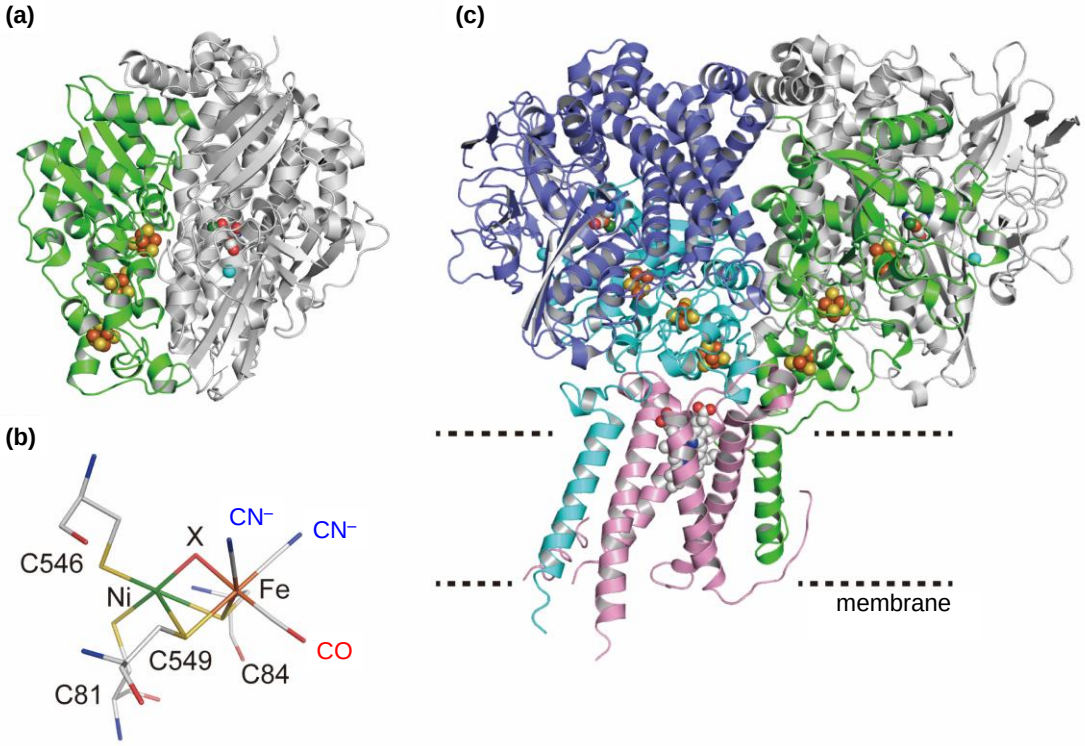

Figure 18 | Crystal structures of [NiFe]-hydrogenase. (a) Crystal structure of the standard [NiFe]-hydrogenase from *D. vulgaris* Miyazaki F (PDB ID 1WUJ). **(b)** Stick representation of the Ni−Fe active site with two CN^-, one CO, and a bridging ligand X that may be μOH^-, μOOH^-, or μH^- (PDB ID 1WUJ shows the Ni-B state). The Ni–Fe active site cofactor is located inside the large subunit, whereas three iron-sulfur clusters are located almost linearly (each ~12 Å apart) in the small subunit. **(c)** Crystal structure of O_2-tolerant membrane-bound [NiFe]-hydrogenase from *E. coli* (PDB ID 4GD3). Atomic coloring**:** Ni, green; Fe, orange; S, yellow; C, gray; O, red; N, blue.

The substrate (H_2) or inhibitors (O_2 and CO) are transferred *via* hydrophobic channels from the molecular surface to the Ni−Fe active site.[309–312] After splitting H_2 into electrons and protons (**Eq. 2**), proton transfer pathways provide an exit route to the molecular surface where protobs are release into the solvent. The crystal structures of [NiFe]-hydrogenases revealed that highly conserved amino acid residues like arginine, serine, glutamate, and histidine are located in the second coordination sphere of the Ni−Fe active site (**Figure 19**). The CO ligand on the Fe ion interacts with the hydrophobic side chains of valine and leucine (V500 and L482 in *Dv*MF). On the other hand, the two CN^- ligands accept hydrogen bonds from arginine R479 and serine S502, respectively, in *Dv*MF.[273] One of the bridging cysteine thiolates is hydrogen-bonded to histidine H88.[313] These interactions have been confirmed in the electron

density map of the hydrogen atoms in the subatomic resolution structure of *Dv*MF [NiFe]-hydrogenase.[273]

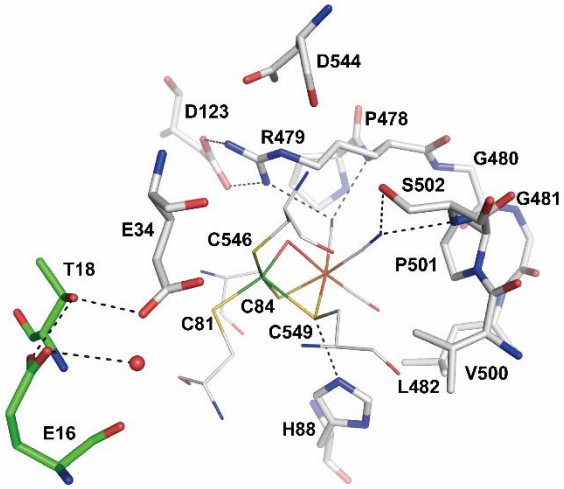

Figure 19 | Second and outer coordination spheres of the Ni−Fe active site. Crystal structure of the standard [NiFe]-hydrogenase from *D. vulgaris* Miyazaki F in the Ni-B state (PDB ID 1WUJ). Glutamate E34, histidine H88, arginine R479, and serine S502 are important residues located in the second coordination sphere of the Ni−Fe active site. The dotted lines indicate the hydrogen bond network. Atomic coloring**:** Ni, green; Fe, orange; S, yellow; C, gray; O, red; N, blue.

3.1.2 Ni-Fe cofactor and Catalytic Cycle

Standard [NiFe]-hydrogenases form two inactive oxidized states, Ni-A and Ni-B (Ni^{3+}, S = 1/2).[259,314,315] The Ni-A state requires a long activation time (up to hours) in the presence of H_2 or other reductants, whereas the Ni-B state is readily activated.[293,297] A hydroxide ligates at the bridging position in the Ni-B state (μOH^-, **Figure 20C**)[275]; however, the identification of the bridging ligand in the Ni-A state remains controversial.[313,316,317] The crystal structures of the Ni-A state in *Dv*MF was interpreted to represent a peroxide ligand (μOOH^-, **Figure 20A**), while a μOH^- ligand was found in *Allochromatium vinosum* (*Av*, **Figure 20B**).[275,277,278] The later is in agreement with density functional theory (DFT) calculations and single-crystal electron nuclear double resonance (ENDOR) spectroscopy that indicated a μOH^- ligand in both Ni-A and Ni-B.[316] It was proposed that the differences in the EPR spectra of the two states are caused by a ligand rotation of 7–10° involving C546 and C549 in *Dv*MF. Accordingly, the bridging μOH^- ligand of the active site could be same in Ni-A and Ni-B, and the differences of the activation rates between these states may result from the slight distortion in the coordination of the cysteine residues. Further investigation is needed to clarify the difference of these states.

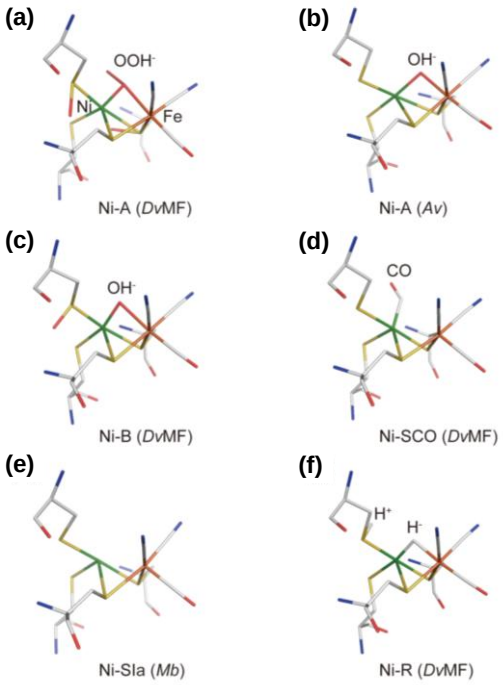

Figure 20 | Crystal structures of the Ni−Fe active site in various oxidation states. (a) The Ni-A state of *Dv*MF hydrogenase (PDB ID 1WUI) and **(b)** of *Av* hydrogenase (PDB ID 3MYR). **(c)** The Ni-B state (PDB ID 1WUJ). **(d)** The CO-inhibited Ni-SCO state (PDB ID 1UBH). **(e)** The Ni-SI_a state (PDB ID 6QGR). **(f)** The Ni-R state (PDB ID 4U9H). A bridging ligand exists in the Ni-A (μOH^- and μOOH^-), Ni-B (μOH^-), and Ni-R states (μH^-), while the bridging position is vacant in the Ni-SI_a state. Atomic coloring**:** Ni, green; Fe, orange; S, yellow; C, gray; O, red; N, blue.

One-electron reduction of the Ni-A and Ni-B states leads to the EPR-silent inactive states, Ni-SU and Ni-SI_r (Ni^{2+}), respectively.[318] The midpoint redox potential for the interconversion between the Ni-A and Ni-SU states was shown to decrease by ~60 mV per pH unit in various [NiFe]-hydrogenases, indicating that the one-electron reduction of Ni-A is coupled to the uptake of one proton.[297,319–322] While the crystal structure of the Ni-SU state is not yet available, DFT calculations proposed coordination of a water molecule to the Fe ion and modification of the Ni coordination structure.[323]

A glutamate residue in the second coordination sphere of the Ni−Fe cofactor plays an important role for the inactivation process. This highly conserved glutamate residue (E34 in *Dv*MF) is located next to the Cys residue which is terminally bound to the Ni ion (C546 in *Dv*MF, see **Figure 19**). When the catalytically active [NiFe]-hydrogenase is oxidized under anaerobic conditions, the enzyme converts from the Ni-SI_a state to the Ni-B state *via* the Ni-SI_r state (**Figure 21**). The first order rate constants of the anaerobic inactivation process in the E25Q (equivalent E34 in *Dv*MF) variant of [NiFe]-hydrogenase from *Desulfovibrio*

fructosovorans (*Df*) was 5.6 times smaller than that of the wild-type enzyme, although the activation rate constants were little affected by the replacement.[324,325] Thus, the glutamate residue is important for the incorporation of the bridging OH^- ligand to the Ni−Fe cofactor. Under anaerobic conditions, formation of the Ni-B state with a bridging OH^- ligand from the Ni-SI_a state requires not only the transfer of a water molecule into the active site but also the extraction of a proton from a water molecule and oxidation of the Ni ion (Ni^{2+} to Ni^{3+}). The carboxylic group of the glutamate residue may deprotonate the bound water molecule at the active site, producing the bridging OH^- ligand of the Ni−Fe cofactor.[324] Interestingly, the Ni-B state was not produced when the E28Q variant (E34 in *Dv*MF and E25 in *Df*) of the [NiFe]-hydrogenase 1 from *Escherichia coli* (*Ec* Hyd-1) was oxidized on an electrode in the presence of H_2, indicating that the interaction of H_2 with the Ni−Fe cofactor is maintained in the E28Q variant and that the early stages of H_2 activation outpace electrochemical oxidation.[326] It may become much easier to start another cycle by activating H_2 and generating the Ni-R state in the E28Q variant, since protons may not easily leave from the Ni−Fe cofactor in the variant and thus it becomes difficult to produce OH^- from water.

During the catalytic cycle, the Ni–Fe cofactor changes the oxidation states in the following order: from Ni-SI_a (Ni^{2+}), Ni-R (Ni^{2+}), and Ni-C (Ni^{3+}) to the Ni-L (Ni^+) state (**Figure 21**).[293–298,309] These states convert among each other by addition or release of H_2, protons, and/or electrons. In the first step of the cycle, the Ni-SI_a state (with the bridging ligand position vacant) reacts with H_2 (**Figure 20E**). H_2 is cleaved heterolytically to a proton (H^+) and a hydride (H^-), which initiates the transition of the Ni-SI_a state to the fully reduced Ni-R state. The high-resolution crystal structure of *Dv*MF revealed that the Ni-R state possesses a μH^- ligand and a protonated cysteine (C546-SH) at the Ni–Fe cofactor (**Figure 20F**).[273] The μH^- ligand and the protonated cysteine residue in the Ni-R state was also elucidated by nuclear resonance vibrational spectroscopy (NRVS), which is particularly suited to monitor ^{57}Fe ligand vibrations, in combination with DFT calculations.[327–329] The hydride ligand was located closer to the Ni ion in the Ni-R state of the enzyme, whereas a short Fe−H^- bond and a long Ni−H^- bond were found in nearly all synthetic Ni−Fe models.[330–333] The protonated cysteine residue is considered as a part of the proton transfer pathways (see below).

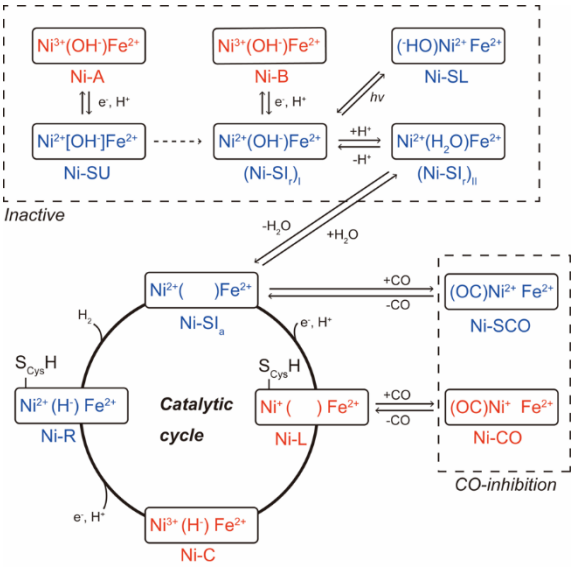

Figure 21 | Proposed catalytic cycle of [NiFe]-hydrogenase. The catalytic cycle comprises four states (Ni-SI_a, Ni-R, Ni-C, and Ni-L) that interconvert in direction of H_2 oxidation or proton reduction. The EPR-active states are shown in red, diamagnetic states are shown in blue. Among the inactive states, a μOH^- ligand is tentatively assigned in the Ni-SU state.

The H_2 binding site at the first step of the cycle is still unclear, and either of the two metal ions may be involved in the formation of a (side-on) H_2 σ-bond complex. Although experimental data on H_2 binding to the Ni−Fe cofactor are not yet available due to the transient nature of intermediate, theoretical studies suggest the Ni ion as the initial site of H_2 binding.[334–338] In addition, complementary studies showed that the competitive inhibitor CO binds to the Ni ion at the Ni−Fe active site (**Figure 20D**).[274,339] The coordination geometry of the Ni ion is key to the thermodynamically favorable interaction of H_2 with the Ni−Fe cofactor. Theoretical calculations predicted that a peculiar seesaw-shaped geometry in the Ni-SI_a state with *trans* S–Ni–S angles near 120° and 180° is necessary for favorable binding of H_2 to the Ni site.[336] In line with this proposal, the crystal structure of the Ni−Fe cofactor of F_{420}-reducing [NiFe]-hydrogenase from *Methanosarcina barkeri* (*Mb*) exhibited no ligand at the bridging position with an unusual *trans* S–Ni–S angles of 107° and 171° in the Ni-SI_a state (**Figure 20E**).[340] Similar angles have also been suggested by resonance Raman studies of the O_2-tolerant, membrane-bound [NiFe]-hydrogenase from *Ralstonia europha* (*Re* MBH).[341]

One-electron oxidation of the Ni-R state leads to the paramagnetic Ni-C state (Ni^{3+}, S = 1/2) with a μH^- ligand and deprotonated C546-S^- at the Ni−Fe active site.[342,343] The Ni-C state is then converted to the paramagnetic Ni-L state (Ni^+), with a vacant bridging position and a (re-) protonated cysteine C546-SH (see below).[297,298,343–346] In the last step of the catalytic cycle,

one-electron oxidation coupled with removal of the proton from C546-SH results in conversion of the Ni-L state to the Ni-SI_a state.[296,347–352]

3.1.3 Proton Transfer and Proton-Coupled Electron Transfer

The proton acceptor during the catalytic H_2 oxidation cycle has been proposed by theoretical[353] and Raman spectroscopic studies.[341,354] Apparently, the proton is transferred from the Ni–Fe cofactor to the Ni-coordinating terminal cysteine thiolate (C546 in *Dv*MF), which is the first step in the proton transfer pathway from the Ni–Fe cofactor to the outer coordination sphere (**Figure 19**).[273,298,347,355–357] The H_2 oxidation activity of the E25Q variant (E34 in *Dv*MF) in *Df* [NiFe]-hydrogenase decreased to less than 0.1% compared to the wild-type enzyme.[358] These results indicated that the glutamate residue located close to the C546 ligand plays an important role for the proton transfer during the catalytic reaction, which was supported by theoretical studies.[359,360] Time-resolved infrared spectroscopy addressing the E17Q variant of O_2-tolerant *Pyrococcus furiosus* [NiFe]-hydrogenase (*Pf* SH-1) showed that glutamic acid E17 (E34 in *Dv*MF) is a proton relay for the interconversion between the Ni-C and Ni-SI_a states.[352] The replacement E17Q did not interfere with the μH^- photolysis of the Ni-C state but it disrupted PCET from the Ni-L states to the Ni-SI_a state, preventing formation of the Ni-SI_a state.

Alternatively, the highly conserved arginine (R479 in *Dv*MF and R509 in *Ec* Hyd-1) has been proposed as a proton acceptor, forming a frustrated Lewis pair for the oxidation of H_2 in *Ec* Hyd-1 from studies using variants R509K, D574N, D118A, P508A, and D118N/D574N (R479, D544, D123, P478 and D123/D544 in *Dv*MF, see **Figure 19**).[361,362] The turnover rate of the R509K variant decreased by a factor of 100 compared to that of the wild-type enzyme. The H_2 oxidation efficiency of the D118A variant, in which aspartate D118 forms a salt bridge to arginine R509, also decreased compared to native *Ec* Hyd-1. In the case of the soluble [NiFe]-hydrogenase 1 from *Pf* SH-1, the R355K (R479 in *Dv*MF) variant altered the ligand binding environment at the Ni−Fe cofactor and destabilized the Ni-C state, resulting in a Ni-C/Ni-L tautomeric equilibrium.[363]

The SH stretching frequency at 2505 cm^{-1} has been detected by highly sensitive Fourier-transform infrared (FTIR) difference spectra utilizing the photoconversion of the Ni-C state to the Ni-L and Ni-SI_a states in *Dv*MF [NiFe]-hydrogenase. The data showed that C546 is protonated in the Ni-L state (Cys-SH) and deprotonated in the Ni-C and Ni-SI_a states (Cys-S^-).[298,347] Glutamic acid E34-COOH was found to be double hydrogen-bonded in the Ni-L state and single hydrogen-bonded in the Ni-C and Ni-SI_a states (**Figure 22**) according to the

COOH stretching frequency between 1700–1730 cm^{-1}. Additionally, a stretching mode of a 'dangling' water molecule was observed in the Ni-L and Ni-C states. These results suggest that the Ni–Fe cofactor and its surrounding amino acids function as an optimized proton transfer system in standard [NiFe]-hydrogenases, and the direction of the proton transfer is regulated by the rearrangement of the hydrogen bond network around C546, E34, and a dangling water molecule (**Figure 22**).

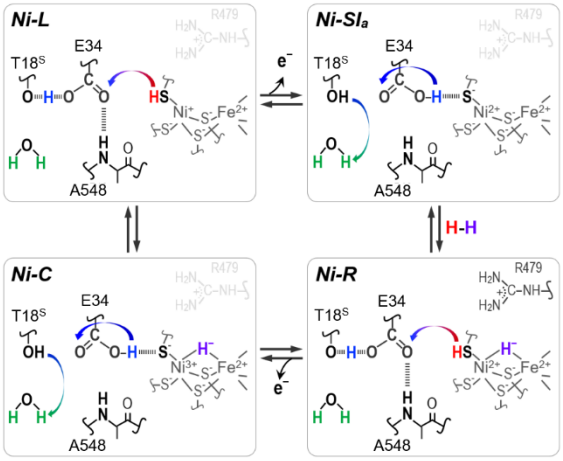

Figure 22 | Proposed proton transfer mechanism for [NiFe]-hydrogenase. The hydrogen bond network between C546 (*Dv*MF nomenclature, the respective sulfur atom is bold), E34, T18, A548, and a dangling water molecule is rearranged during the catalytic reaction. An involvement of R479 (grey) is possible. Reprinted (Adapted or Reprinted in part) with permission from ref. [347]. Copyright 2019 Wiley.

The Ni-L and Ni-R states of *Dv*MF [NiFe]-hydrogenase are likely to construct a similar hydrogen bond network between C546-SH, E34, T18, a backbone contact including A548-NH, and a dangling water molecule (**Figure 22**).[347] Several Ni-L states have been identified by light irradiation of the Ni-C state under anaerobic conditions at T < 100 K.[343,364–367] From temperature-dependent FTIR studies of *Dv*MF, the ΔH and ΔS values for the equilibrium between the protonated/deprotonated forms (*i.e.*, Cys-SH and Cys-S^-) of two Ni-L states were obtained as 6.4 ± 0.8 kJ mol^{-1} and 25.5 ± 10.3 J mol^{-1} K^{-1}, respectively.[349] The small ΔH and ΔS values indicate efficient proton transfer at the cysteine residue C546 of the Ni–Fe cofactor between the two Ni-L states.

The Ni-SI_a and Ni-C states may form a similar hydrogen bond network between C546-S^-, E34, A548-NH, and a dangling water molecule (**Figure 22**). Theoretical studies have indicated involvement of a threonine residue in the proton transfer of the transmembrane proton pump bacteriorhodopsin[368]; however, T18 seems to be non-essential for proton transfer

in *Df* [NiFe]-hydrogenase and rather stabilizes the local protein structure. The alter was suggested by structural and spectroscopic studies of variants in which threonine was replaced with serine, valine, glutamine, glycine, and asparagine.[369]

3.1.4 Accessory Iron-Sulfur Clusters

In standard [NiFe]-hydrogenases, three accessory iron-sulfur clusters (denoted proximal [4Fe-4S]$^{2+/+}$, medial [3Fe-4S]$^{+/0}$, and distal [4Fe-4S]$^{2+/+}$) are located almost linearly (each ~12 Å apart) in the small subunit (**Figure 23**)[273]**,** and mediate the electron transfer between the Ni–Fe active site and physiological redox partner, such as cytochrome c_3.[305–308] The proximal [4Fe-4S]$^{2+/+}$, medial [3Fe-4S]$^{+/0}$, and distal [4Fe-4S]$^{2+/+}$ clusters of *Dg* [NiFe]-hydrogenase exhibit redox potentials of -315, -80, and -445 mV vs SHE, respectively.[370]

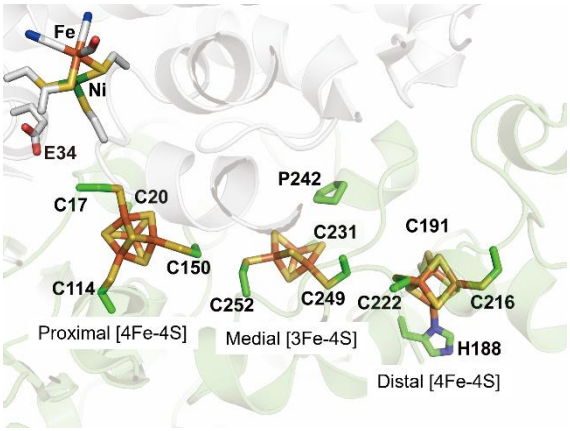

Figure 23 | Location of the accessory iron-sulfur clusters. The large subunit with the Ni–Fe cofactor is shown in white cartoon, the small subunit with the proximal [4Fe-4S], the medial [3Fe-4S], and the distal [4Fe-4S] cluster is shown in green (*Dv*MF [NiFe]-hydrogenase, PDB ID 1H2R). The three accessory iron-sulfur clusters are located almost linearly. Atomic coloring: Ni, green; Fe, orange; S, yellow; C, gray; O, red; N, blue.

The accessory iron-sulfur clusters are not only important for electron transfer but may also play a role with respect to hydrogen turnover in the presence of O_2: some [NiFe]-hydrogenases are 'O_2-sensitive' (*i.e.*, inhibited by O_2) while the 'O_2-tolerant' [NiFe]-hydrogenases maintain activity under aerobic conditions. The latter have been shown to quickly reactivate from the Ni-B state in a process that appears to be very dependent on the nature of the proximal cluster.[371–373] The reactivity toward O_2 clearly distinguishes the bimetallic hydrogenases; as discussed in **Section 3.2.2**, [FeFe]-hydrogenases are irreversibly destroyed by O_2.

The Proximal Cluster. When the proximal [4Fe-4S]$^{2+/+}$ cluster is reduced in standard [NiFe]-

hydrogenases, the $[4Fe\text{-}4S]^{+}$ cluster interacts magnetically with the $Ni^{3+/+}$ center, which causes splitting of the Ni-C/Ni-L EPR signals below 10 K.[374] Spectroscopic studies revealed that the conversion of Ni-C to Ni-SI_a *via* the Ni-L state is controlled by the redox state of the proximal $[4Fe\text{-}4S]^{2+/+}$ cluster in *Dv*MF [NiFe]-hydrogenase.[348] The transition of the Ni-L state to the Ni-SI_a state may occur when the proximal $[4Fe\text{-}4S]^{2+/+}$ cluster is oxidized but not when it is reduced. These results suggest that the catalytic cycle is controlled by the redox state of the proximal $[4Fe\text{-}4S]^{2+/+}$ cluster, which may act as a gate for the catalytic electron transfer.

Most of the standard [NiFe]-hydrogenases possess a glutamate near the proximal [4Fe-4S] cluster (**Figure 24A**), while some [NiFe]-hydrogenases possess an aspartate instead. The crystal structure of membrane-bound *Av* [NiFe]-hydrogenase in the Ni-A state showed that there are two different forms for the proximal [4Fe-4S] cluster; one is a standard cubane, while in the other form the proximal [4Fe-4S] cluster is distorted with one of the Fe ions bound to aspartate D75, which is located nearby the cluster (**Figure 24B**).[278] It was proposed that the negatively charged side chain of aspartate stabilizes the distorted form of the [4Fe-4S] cluster. A similar coordination was found in the O_2-tolerant [NiFe]-hydrogenase from *Citrobactor* sp. S-77.[285] Additionally, the water molecules near the proximal cluster relocated upon reduction, emphasizing the importance of the water network in this hydrogenase.[285]

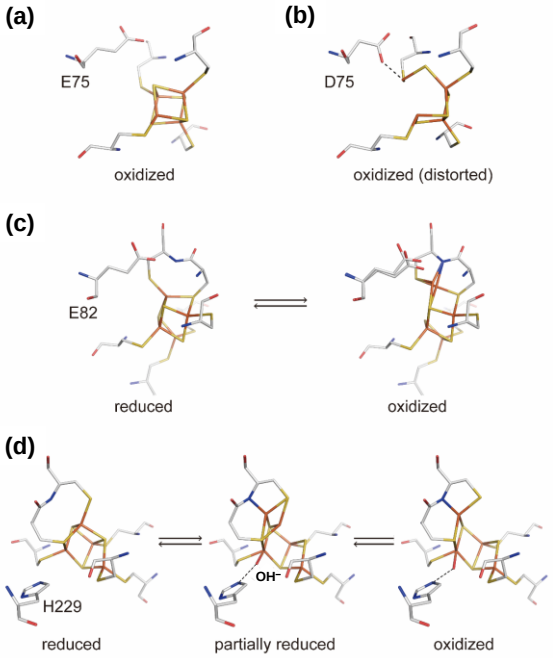

Figure 24 | Structural changes of the proximal iron-sulfur cluster in various [NiFe]-hydrogenases. (a) The oxidized form (PDB ID 1UBH). **(b)** The oxidized distorted form (PDB ID 3MYR). **(c)** The reduced and oxidized forms of the [4Fe-3S] cluster in *Hm* MBH (PDB ID 3AYX and 5Y34). **(d)** The reduced, partially reduced, and oxidized forms of the [4Fe-3S] cluster in *Re* MBH (PDB ID 3RGW, 4IUD, and 4IUB). The proximal [4Fe-4S]

cluster is distorted with one of the Fe ions bound to D75 in one of the oxidized forms (b). Atomic coloring: Ni, green; Fe, orange; S, yellow; C, gray; O, red; N, blue.

Contrary to the standard [NiFe]-hydrogenases, some of the O_2-tolerant, membrane-bound [NiFe]-hydrogenases, such as *Ec* Hyd-1, *Re* MBH, *Hydrogenovibrio marinus* (*Hm* MBH), and *Aquifex aeolicus* (*Ae* MBH), possess a unique proximal [4Fe-3S]$^{5+/4+/3+}$ cluster ligated by six cysteine residues (**Figure 24CD**).[286,288–290] This cluster can be oxidized twice within a very small potential range.[375] Its electronic structure has been characterized and debated.[376–379] The importance of the coordination by six cysteines to the proximal iron-sulfur cluster has been shown by site-directed mutagenesis studies in *Re* MBH and *Ec* Hyd-1.[380–383] Replacement of the two supernumerary cysteine residues C19 and C120 in *Re* MBH with glycine residues altered the electronic structure of the proximal cluster, and the double variant was unable to sustain activity under prolonged O_2 exposure.[380] Similar mutagenesis studies in *Ec* Hyd-1 showed that O_2 tolerance depends on C19 and not on the two-electron oxidation at the proximal cluster, which is detected with the O_2-sensitive C19G variant but not with the O_2-tolerant C120G variant.[381] For another example, the O_2-tolerant NAD^+-reducing soluble [NiFe]-hydrogenase from *R. eutropha* (*Re* SH) can produce trace amounts of superoxide in H_2-driven NAD^+ reduction with O_2.[382] The C41S variant of *Re* SH displayed up to 10% of wild-type activity, suggesting that the coordinating role of C41 at the proximal [4Fe-4S] cluster might be partly substituted by the nearby C39 residue, whereas the C39G, C39A, and C39S variants increased the O_2 sensitivity compared to wild-type *Re* SH.[383]

EPR and ^{57}Fe Mössbauer spectroscopic studies have shown that the proximal [4Fe-3S]$^{3+}$ cluster donates two electrons to the Ni–Fe active site, resulting in the 'super-oxidized' state [4Fe-3S]$^{5+}$.[375] A charged glutamate near the cluster (COO^-, *e.g.* in *Hm* MBH and *Ec* Hyd-1) or a deprotonated water molecule (OH^-, *e.g.* in *Re* MBH) stabilizes the [4Fe-3S]$^{5+}$ cluster.[286,288,289,308,384] The deprotonated amide nitrogen of the backbone formed by cysteine C26 (in *Hm* MBH) may bind to one of the Fe ions of the cluster, also stabilizing the highly oxidized state. In *Ae* MBH, the proximal [4Fe-3S]$^{5+/4+/3+}$ and medial [3Fe-4S]$^{+/0}$ clusters show mid-point potentials that are higher than the E_m value for the conversion of the Ni-SI_a to Ni-L/Ni-C states in standard [NiFe]-hydrogenase.[346,375,385] Additionally, a kinetic argument favoring the appearance of the Ni-L state in *Ec* Hyd-1 is that the proximal [4Fe-3S]$^{3+}$ cluster is fully reduced at the potentials that are required for both the Ni-C and Ni-L states, impeding the elementary electron transfer step that converts the Ni-L to Ni-SI_a state.

The conserved glutamic acid residue (E34 in *Dv*MF) plays an important role for the mechanism of O_2 protection in the O_2-tolerant NAD^+-reducing [NiFe]-hydrogenase from *H. thermoluteolus* TH-1, which is revealed by the crystal structures (**Figure 25**).[284] The Ni−Fe cofactor of *Ht* TH-1 in the H_2-reduced state exhibits a similar coordination structure as those of standard [NiFe]-hydrogenases, whereas in the air-oxidized state, an octahedral Ni geometry was found; three bridging thiol ligands between the Ni and Fe ions, one terminally bound cysteine thiolate, and an unprecedented bidentate ligation of the glutamate side chain (E32 in *Ht* and E34 in *Dv*MF) (**Figure 25**). The fully occupied octahedral Ni geometry protects the Ni−Fe cofactor from direct attack by O_2. Higuchi, Shomura, and co-workers suggested that the conformational change of the Ni−Fe active site was triggered by the reduction of the proximal [4Fe-4S] cluster (Y1 in **Figure 25**). The coordination structure of the amino acid residues located in between the Ni−Fe cofactor and the proximal [4Fe-4S] cluster also changed upon reduction. In the reduced state, E32 does not bind to the Ni ion and forms a hydrogen bond network including E32, S464, and E56, notably unrelated to the catalytic proton transfer pathway as discussed above. The side chain of arginine R58 flips between E56 and the proximal [4Fe-4S] cluster (**Figure 25**), which may affect the efficiency of catalytic electron transfer.

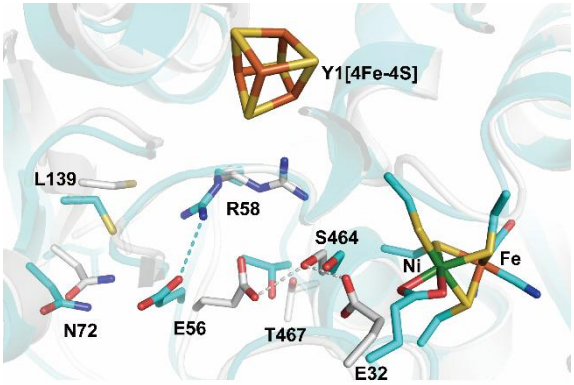

Figure 25 | Proposed proton transfer in the O_2-tolerant [NiFe]-hydrogenase *Ht* TH-1. The oxidized state is shown in cyan (PDB ID 5XF9) and the H_2-reduced state is shown in white (PDB ID 5XFA). Y1 refers to the proximal iron-sulfur cluster. The side chain of E32 binds to the Ni ion in the oxidized state, while it does not bind to the Ni ion and forms a hydrogen bond network including E32, S464, and E56 in the reduced state. The metal centers in the reduced state are omitted for clarity. Atomic coloring: Ni, green; Fe, orange; S, yellow; C, gray; O, red; N, blue.

The Medial and Distal Clusters. In standard [NiFe]-hydrogenases, the medial $[3Fe\text{-}4S]^{+/0}$ cluster possesses a rather high midpoint potential, which may play a role in effectively

'trapping' electrons from the Ni–Fe cofactor, facilitating the reaction of the Ni-SI_r state with H_2 *via* the acid-base equilibrium between the Ni-SI_r and Ni-SI_a states.[374,386,387] Substitution of proline to cysteine (P238C in *Df* [NiFe]-hydrogenase, equivalent P242 in *Dv*MF) triggered the conversion of the medial [3Fe-4S] cluster to a [4Fe-4S] cluster decreasing the midpoint potential from +65 mV to -250 mV vs SHE. This potential decrease caused a 30% reduction in H_2 oxidation activity and a two-fold increase in H_2 evolution activity without significantly altering the spectroscopic properties of the Ni−Fe active site and the proximal and distal [4Fe-4S] clusters.[388] The distal [4Fe-4S] cluster is located very close to the solvent and interacts with electron acceptors.[293] Three cysteines and one histidine coordinate this cluster (**Figure 23**). The H184C and H184G variants of *Df* [NiFe]-hydrogenase (H188 in *Dv*MF) showed only 1.5% and 3% oxidative activity compare to the wild-type enzyme, respectively.[389] The activity of the H184G variants decreases or increases upon addition of mercaptoethanol or imidazole to the assay, respectively: these ligands modulate electron transfer rates upon binding to a free coordination site on the distal cluster.[389,390] The affinity of the variants H184G, P238C/H184G, and P238C/H184C for the electron acceptors methyl viologen or cytochrome c_3 was similar or greater than that of the wild-type enzyme, suggesting that H184 is not an enzyme-acceptor recognition site.[390] DFT calculations demonstrated that substitution of the histidine ligand to a cysteine in *Df* [NiFe]-hydrogenase does not change the reorganization energy of the distal [4Fe-4S] cluster.[391] The calculated rate of electron transfer was, however, reduced by three order of magnitude, resulting from a change in electronic donor-acceptor coupling including histidine H184 and phenylalanine F193 (F197 in *Dv*MF). These results indicated that the protein environment is tuned for efficient electron transfer. A systematic survey of the substitution of amino acid residues related to the medial and distal iron-sulfur clusters has been reported for the [NiFe]-hydrogenase from *Alteromonas macleodii* (which belongs to Group 1e but shows modest O_2 tolerance).[392–394] For example, the double substitution of P285C at the medial [3Fe-4S] cluster (P242 in *Dv*MF)and H230C at the distal [4Fe-4S] cluster (H188 in *Dv*MF) increased the H_2 evolution activity three- to four-fold compared to the wild-type enzyme.[394] Electrochemistry measurements showed that in the R193L variant of O_2-tolerant *Ec* Hyd-1, in which R193 is located near the histidine ligand (**Figure 26**, L194 in *Dv*MF), the E_m values of the medial $[3Fe\text{-}4S]^{1+/0}$ and distal $[4Fe\text{-}4S]^{2+/+}$ clusters are more negative than those of the wild-type enzyme.[395] The R193L variant also enhanced bias toward H_2 evolution and slightly diminished the O_2 tolerance, whereas the catalytic activity of the K189N and Y191E variants (equivalent Q190 and P192 in *Dv*MF) did not change compared to that of wild-type *Ec* Hyd-1.[395]

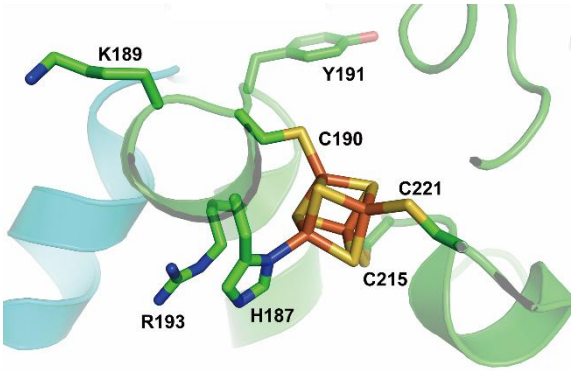

Figure 26 | Amino acids surrounding the distal [4Fe-4S] cluster. The [NiFe]-hydrogenase *Ec* Hyd-1 is shown (PDB ID 3UQY). Arginine R193 in the second sphere affects the electron transfer rate. Atomic coloring: Fe, orange; S, yellow; C, gray; O, red; N, blue.

The electron transfer route between the Ni–Fe cofactor and the protein surface is complicated, and theoretical calculations proposed that multiple routes co-exist between the metal centers during catalysis.[396] Thus, enzymatic activity is tuned by not only in the second coordination sphere of the Ni−Fe cofactor but also *via* the electron transfer trajectory in the outer coordination sphere. Furthermore, in the case of O_2-tolerant [NiFe]-hydrogenases, most variants at the proximal iron-sulfur cluster became O_2 sensitive.[380] Controlling electron transfer the accessory iron-sulfur clusters also play an important role in the O_2 tolerance.

3.1.5 Gas channels in [NiFe]-hydrogenase

The Ni–Fe cofactor is deeply buried in the center of the large subunit (**Figure 27**).[293] Both substrate and inhibitory gas molecules, such as H_2, O_2, and CO, can access the Ni−Fe active site from the solvent region through hydrophobic gas channels predicted from the crystal structure of the protein.[310,355,397–399] Cavity calculations of these cavities using a 1 Å radius probe showed that there are four gas access points at the protein surface, combining into one channel that leads to the Ni−Fe active site.[397,398] In vicinity of the Ni−Fe cofactor, the end of the channel becomes narrower due to a ‘bottleneck’ comprised of two hydrophobic amino acid residues, typically valine and leucine (**Figure 27**).[398,399] Noble gases like Xe and Kr bind to the hydrophobic area of the protein and are well visible in electron density maps; thus, protein crystal structures pressurized with Xe or Kr provide useful information for hydrophobic gas channels.[355,397,400,401] The crystal structures of the Xe-bound standard [NiFe]-hydrogenases from *Df* and *Dv*MF have been determined at 6.0 and 1.8 Å resolution, respectively, where the Xe atoms were observed in the hydrophobic cavities of these

enzymes.[355,397] Controversially, molecular dynamics (MD) simulations suggested that gas molecules like H_2 and O_2 could reach the Ni−Fe active site *via* several pathways.[399,402]

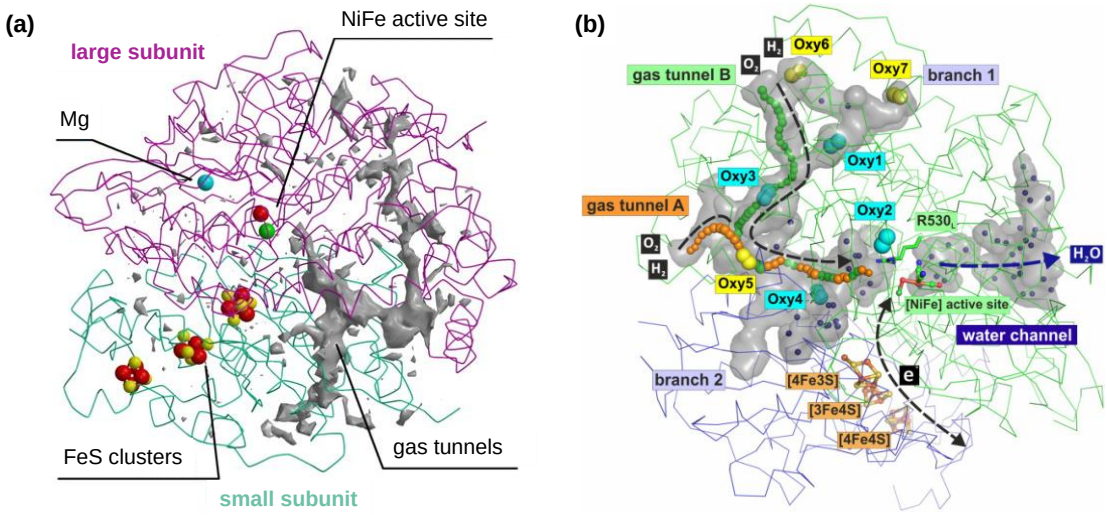

Figure 27 | Gas transfer channels. (a) Standard *Df* [NiFe]-hydrogenase. Reprinted (Adapted or Reprinted in part) with permission from ref. [310]. Copyright 2008 National Academy of Sciences. **(b)** O_2 pathway in O_2-tolerant Re MBH. Two entrances for gas transfer channels have been revealed, which are combined and extend to the Ni−Fe active site. Reprinted (Adapted or Reprinted in part) with permission from ref. [401]. Copyright 2018 National Academy of Sciences.

The O_2 transfer pathways of O_2-tolerant *Re* MBH has also been investigated by X-ray crystallography together with computational studies and compared with those of O_2-sensitive [NiFe]-hydrogenases.[400,401] The channels of [NiFe]-hydrogenases span distances of 28–76 Å between the protein surface and the Ni−Fe active site, wherein O_2-sensitive [NiFe]-hydrogenases have a wider bottleneck and a more complex channel network than those of their O_2-tolerant counterparts. Several O_2 binding sites have been revealed within the hydrophobic channels that have two entrances and extend to the Ni−Fe active site (**Figure 27**).

Various site-directed mutagenesis studies have tested the suggestion that the presence of bulky residues at the end of the gas channel in the so-called O_2-tolerant, regulatory hydrogenases (RH) may prevent O_2 access to the active site (*e.g.*, isoleucine and phenylalanine instead of valine and leucine).[398] The H_2 oxidation activity of the I62V and F110L variants of the regulatory [NiFe]-hydrogenase from *R. eutropha* (*Re* RH) decreased under aerobic conditions 25-fold and 5.5-fold, respectively, compared to the O_2-tolerant wild-type enzyme.[403] These results indicate that *Re* RH exhibits O_2 and CO tolerance owing to

interruption of the gas channel at the bottleneck to the Ni−Fe active site with the bulky amino acid residues isoleucine I62 and phenylalanine F110. Furthermore, the double variant I62V/F110L was completely inactive, indicating that the shape of the gas channels may play a key role in O_2 tolerance.[403] The I65V/F113L double variant of the RH from *Rhodobacter capsulatus* is also more active and more O_2-sensitive than the native enzyme.[404] The hypothesis is that narrower gas channels and fewer gas entrances limit the mass transport to the catalytic active site, presumably contributing to the net O_2 tolerance of these enzymes. However, site-directed mutagenesis studied aimed at narrowing the end of the gas channel of the O_2-sensitive *Df* [NiFe]-hydrogenase showed that steric hindrance slows down intramolecular diffusion and O_2 inhibition, but without making the variant O_2-tolerant. These gas diffusion processes have been studied intensively using many residue replacements at the bottleneck position, namely V74 and L122 in *Df* [NiFe]-hydrogenase.[310,311,405–407] The rates of intramolecular gas diffusion were measured by using the bimolecular rate constant of inhibition by CO as a proxy of the rate of ligand access to the active site, by analyzing the results of isotope exchange assays, and by measuring the Michaelis constant for H_2.[310–312] The results show that the variations have the same relative effects on the transport of all ligands, CO, O_2, and H_2, and that not only the size but also the charge of the residues in the bottleneck have a very strong effect (up to nearly four orders of magnitude) on the kinetics of ligand access. Slowing down H_2 egress has the direct consequence of selectively slowing H_2 production and increasing the catalytic bias of the enzyme in the direction of H_2 oxidation.[312] Some of the observed effects of the variations on the rates of diffusion could be explained by the results of MD simulations, according to which two distinct gates determine the kinetics, namely V74/R476 and V74/L122.[402,408] Although site-directed mutagenesis slows down the intramolecular diffusion rates, the resulting effect on the kinetics of inhibition by O_2 is ten-fold or less, because the transport towards the active site limits the reaction with O_2 only when it is very slow (*e.g.*, in the V74M and V74Q variants).[407,409] However, some V74 substitutions (in particular V74C and V74H) have a very beneficial effect on O_2 inhibition that is not related to the kinetics of diffusion: for reasons that have not been clarified, these variations strongly increase the rate of *reactivation* after O_2 inhibition. The rate of reactivation of *Df* [NiFe]-hydrogenase V74H is close to that observed with the O_2-tolerant enzyme from *A. aeolicus*[405,410], and mutation to cysteine further increases the O_2 tolerance of *Ec* Hyd-1.[411]

According to the type of [NiFe]-hydrogenase, the gas channels differ in size, shape, and branching, with respect to the physiological requirement of each [NiFe]-hydrogenase. The crystal structure of the *Mb* F_{420}-reducing [NiFe]-hydrogenase in the Xe-bound form revealed

an additional gas channel (**Figure 28**).[340] Interestingly, the [NiFeSe]-hydrogenase from *Desulfovibrio vulgaris* Hildenborough (*Dv*H) has a similar hydrophobic channel[340,412], although this channel is not observable in the crystal structures of standard [NiFe]-hydrogenases.[355,397,400,401] In the case of *Dv*H [NiFeSe]-hydrogenase site-directed mutagenesis experiments suggest that O_2 reaches the active site through a hydrophilic water channel.[413]

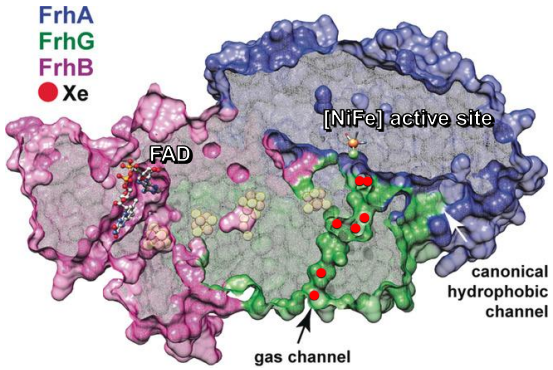

Figure 28 | Gas tunnels of *Mb* F_{420}-reducing [NiFe]-hydrogenase. Seven Xe atoms (red spheres) were detected within an additional gas tunnel from the surface to the Ni–Fe cofactor (PDB ID 6QII). Reprinted (Adapted or Reprinted in part) with permission from ref. [340]. Copyright 2019 Wiley.

3.2 [FeFe]-hydrogenase

3.2.1 Structural Features of [FeFe]-hydrogenase

Standard [FeFe]-hydrogenases are in most cases monomeric enzymes with a molecular weight ranging between 50–80 kDa. The [FeFe]-hydrogenase from *Clostridium pasteurianum*, *Cp*I, whose X-ray crystal structure has been published in 1998, shows a mushroom-like shape with four iron-sulfur clusters binding to the 'stipe' (**Figure 29A**).[414–416] Due to the sequence similarity with ferredoxin, this fold is referred to as 'F-domain'. The [FeFe]-hydrogenase from *C. acetobutylicum*, *Ca*I, albeit not crystalized, is likely of similar architecture.[417] In both enzymes, the iron-sulfur clusters form a conductive chain that serves in electron exchange between soluble redox partners and the catalytic active site. This chain consists of two [4Fe-4S] clusters and surface-exposed [2Fe-2S] and [4Fe-4S] clusters, the later which is bound by a three cysteine and one histidine ligand. From a comparison of *Ca*I variants, it was concluded that the [2Fe-2S] cluster is the main electron transfer conduit, at least when the enzyme is wired to an electrode.[418] On the other hand, docking simulations with *Cp*I suggest that the physiological electron donor, ferredoxin, interacts predominantly with the surface-exposed [4Fe-4S] cluster. According to EPR titrations this cluster has the lowest potential.[419] The

authors investigated a catalytically inactive cofactor variant to facilitate steady-state conditions, notably below the H^+/H_2 Nernstian potential, where *Cp*I spontaneously re-oxidizes as a result of proton reduction, which prevents equilibrium conditions during the redox titration at low potential.[419,420]

The [FeFe]-hydrogenase from *Desulfovibrio desulfuricans*, *Dd*H, whose X-ray crystal structure was published in 1999, features a smaller F-domain with only two [4Fe-4S] clusters and is surround by a peptide 'belt' (**Figure 29B**).[421,422] The [FeFe]-hydrogenase from *Megasphaera elsdenii*, *Me*HydA, lacks this subunit but displays an equally small F-domain.[423] Voltammetry experiments suggested that intramolecular electron transfer in *Me*HydA is rate limiting in H_2 oxidation primarily thus determining the catalytic bias of this enzyme.[424] The electron transfer chain of the recently crystallized hydrogenase from *Clostridium beijeirincki*, *Cb*A5H, consists of only two [4Fe-4S] clusters and an additional *N*-terminal cluster located more than 20 Å away from any other cluster.[425] Due to significant disorder, these clusters are not visible in PDB entry 6TTL. A crystal structure of the functional [FeFe]-hydrogenase from the green alga *Chlamydomonas reinhardtii*, *Cr*HydA1, has yet to be published; however, based on several lines of evidence[426–431], it can be concluded that *Cr*HydA1 completely lacks the F-domain and any additional metal centers. The homology model shown in **Figure 29C** highlights an insertion or 'loop' that is typical for [FeFe]-hydrogenases of the *Chlorophyta*-type.[26]

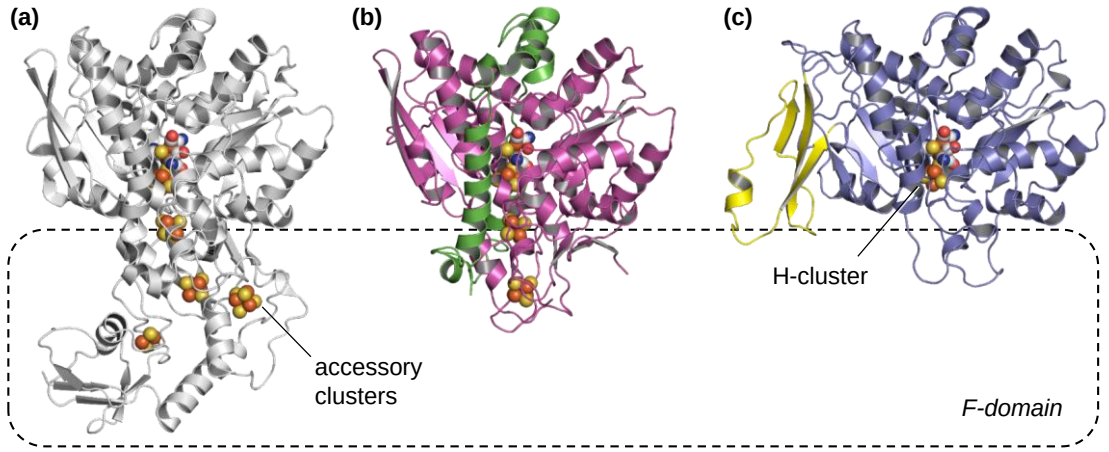

Figure 29 | Crystal structures of various [FeFe]-hydrogenases. (a) *C. pasteurianum Cp*I (PDB ID 4XDC) and **(b)** *D. desulfuricans Dd*H (PDB ID 1HFE). The characteristic peptide belt of *Dd*H is shown in green. Panel **(c)** depicts a homology model of the [FeFe]-hydrogenase from *C. reinhardtii Cr*HydA1. Here, the characteristic 'loop' that is specific for this enzyme is shown in yellow. Accessory iron-sulfur clusters and the catalytic H-cluster are highlighted as spheres. Note the successive miniaturization of the F-domain from (a) to (c). Atomic coloring: Fe, orange; S, yellow; C, gray; O, red; N, blue.

The above-mentioned hydrogenases have been crystallized and thoroughly studied using biophysical methods; however, they are not representative of the diversity of the [FeFe]-hydrogenases, some of which are much larger and associated in multienzyme complexes.[266] As an example, the hydrogen-dependent carbon dioxide reductase from *Acetobacterium woodii* has four subunits and eleven predicted iron-sulfur clusters, with an apparent mass around 169 kDa[432,433] while the respiratory formate hydrogen lyase complex (FHL) of *Thermococcus onnurineus* consists of 18 subunits, with a molecular weight of approximately 600 kDa.[434] The coupling of CO_2 and H_2 turnover is discussed in **Section 4**. The small number of [FeFe]-hydrogenases that have been crystalized so far is certainly an obstacle to learning about how diverse structures and outer sphere effects modulate activity; this is actually true for all GPMs discussed in this review.

Unlike the F-domain, the catalytic 'H-domain' shows a high degree of similarity in all [FeFe]-hydrogenases.[246] Four cysteine residues bind a [4Fe-4S] cluster that is part of the active site cofactor and facilitates electron exchange with the accessory iron-sulfur clusters (or soluble redox partners, in case of *Cr*HydA1). These residues are part of at least three protein loops 1–3 (**Figure 30**).[26] A strictly conserved cysteine residue in loop 3 additionally coordinates the diiron site, which is equipped with CO and CN^- ligands and an azadithiolate group (ADT, compare **Figure 17B**).[435–437] Together, the [4Fe-4S] cluster and the diiron site form the active site 'H-cluster'. **Figure 30** depicts the H-cluster, including a number of functionally relevant amino acid residues and water molecules in the second and outer coordination sphere.

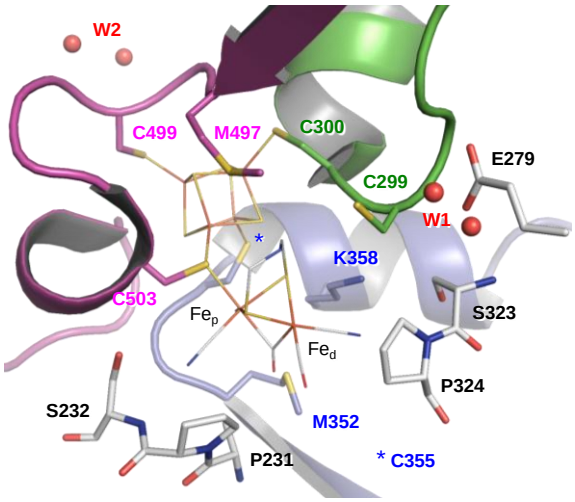

Figure 30 | Active site cavity and catalytic cofactor of [FeFe]-hydrogenase *Cp*I. The H-cluster is comprised of an [4Fe-4S] cluster and the diiron site (**PDB ID 4XDC**). Loop 1–3 provide four cysteine residues to bind the [4Fe-4S] cluster and the diiron site. In loop 1

(green), C299 is part of the PT pathway (further including water cluster W1, E279, and other groups). In loop 2 (blue), M352 may interact with the μCO ligand while K358 was suggested to form a hydrogen bond with the CN^- ligand at the distal iron ion, Fe_d. In loop 3 (magenta), M497 may form a hydrogen bond with the ADT group. Cysteine C499 was proposed to be the 1st proton acceptor of the PT pathway. Serine S232 provides a hydrogen bond to the CN^- ligand of the proximal iron ion, Fe_p, presumably involving a backbone contact with P231. Atomic coloring: Fe, orange; S, yellow; C, gray; O, red; N, blue.

The standard or group A [FeFe]-hydrogenases *Cp*I, *Ca*I, *Dd*H, and *Cr*HydA1 have been studied intensively and most of what is known about the influence of second and outer coordination sphere is based on the biochemical and biophysical analysis of these enzymes. The diversity of [FeFe]-hydrogenases has been emphasized[438–440]; however, on the molecular level no [FeFe]-hydrogenase of group B has been investigated yet, and a molecular detailed analysis of group C and D hydrogenases was achieved only recently. This includes the sensory or bifurcating [FeFe]-hydrogenases from *Thermotoga maritima* (*Tm*HydS, *Tm*HydABC) and *Thermoanaerobacter mathranii* (*Tam*HydS).[441–444] A cryo-EM structure of *Tm*HydABC has recently been published as a preprint.[445] **Table 4** shows a comparison of important amino acid residues in the H-domain, highlighting the level of similarity among group A [FeFe]-hydrogenases and the differences to group C and D [FeFe]-hydrogenases. In addition to the above-mentioned enzymes, the table also includes *Cp*II and *Cp*III, *Me*HydA1, and *Cr*HydA2.[425] This comparison is not comprehensive and restricted to experimentally characterized [FeFe]-hydrogenases. As such, **Table 4** allows correlating amino acid composition and catalytic function and will serve as a guideline for the analysis of second and outer coordination sphere effects. Additionally, **Table 5** provides a compilation of all amino acid and H-cluster variants that have been published in the last 20 years. We will discuss the influence of natural and artificial variations of the H-domain in **Section 3.2.2**. Next to the biochemical and electrochemical analysis of turnover activity, the spectroscopic signatures of the active site cofactor have been a major source of information. We define the various H-cluster states hereafter.

Table 4 | Conservation of amino acid residues in the H-domain of experimentally characterized [FeFe]-hydrogenases. Representative PDB accession codes for *Cp*I, *Dd*H, *Cb*A5H, and the apoprotein of *Cr*HydA1 are given in the last row. Legend: HB, hydrogen bonding; HP, hydrophobic; PT, proton transfer; CC, cluster coordination.

	***Cp*I**	***Cp*II**	***Cp*III**	**CaI**	***Dd*H**	***Me*HydA**	***Cb*A5H**	***Cr*HydA1**	***Cr*HydA2**	***Tm*HydA**	***Tm*HydS**	***Tam*HydS**
HB	S232	S101	A162	S231	A109	A113	A294	A94	A97	A227	S79	S81
PT	E279	E148	E202	E278	E156	E151	E341	E141	E144	E274	E118	F119
PT	E282	E151	E205	E281	E159	E154	E344	E144	E147	E277	E121	E122
PT	R286	R155	R209	R285	R163	R158	R348	R148	R151	R281	G125	K126
PT	C299	C169	C222	C298	C178	C171	C367	C169	C172	C294	A131	A137
CC	C300	C170	C223	C299	C179	C172	C368	C179	C173	C295	C132	C138
PT	S319	S189	S242	S318	S189	S192	S387	S189	S192	S314	A151	L157
HP/HB	M353	T223	G268	M352	M232	T227	M421	M223	M226	M348	G177	S191
CC	C355	C225	C270	C354	C234	C229	C423	C225	C228	C350	C179	C193
HB	S357	A227	A272	D356	A236	A231	A425	R227	R230	A352	A181	A195
HB	K358	K228	K273	K357	K237	K232	K426	K228	K231	K353	K182	K196
HB	M497	M367	M381	M497	M376	M381	M565	M415	M426	M480	S267	L291
CC	C499	C369	C383	C498	C378	C391	C567	C417	C428	C482	C269	C293
CC	C503	C382	C387	C502	C382	C395	C571	C421	C432	C486	C273	C297
PDB IDs	6N59	-	-	-	1FEH	-	6TTL	3LX4	-	-	-	-

Table 5 | List of [FeFe]-hydrognase variants and H-cluster variants. The majority of amino acid variants was produced for *Cp*I and *Cr*HydA1, with most H-cluster variants being produced for *Cr*HydA1. Other enzymes include *Ca*I, *Cb*A5H, and *Cr*HydA2.

	Variant	PDB ID	Target	Ref.
***Cp*I**	G412H, G414A/H, G418A/H, G421H, G422H, K358N, R449A/H	*N/A*	Maturation	446
	E279A	5LA3	Proton transfer, formation of H_{hyd}	447
	C299A	6GLY	Proton transfer	448–450
	C299D	6GLZ		
	C299S	*N/A*		
	E279A	*N/A*		
	E279D	6YF4		
	E279Q	6GM0		
	E282A	6GM1		
	E282D	6GM2		
	E282Q	6GM8		
	R286A/L	6GM3		
	S319A	6GM4		
	C299S, M353L, K358N, M497L	*N/A*	Hydrogen bonding	451
	S31P, E47G, R86H, C153Y, N160D, D186G, T188A, I197V, K208E, K252R, I253V, A280V, N289D	*N/A*	Hydrogen turnover, O_2 sensitivity	452
	L192G, G194C, N189C, T356C/T/V, S357C/G/P/T, M397C, A498C	*N/A*	Hydrogen turnover, O_2 sensitivity	453
	M70L, M211L, M243L, M277L, M387L, M481L, M485L, M551L	*N/A*	O_2 sensitivity	454
	C48A, C100A, C298D	*N/A*	Proton transfer, electron transfer	418,455,456
***Cr*HydA1**	C169A/S	*N/A*	Proton transfer, formation of H_{hyd}	457–460
	C169A/D/S	*N/A*	Proton transfer	449
	E141A	6GM5		
	E141D	*N/A*		

	E141Q	6GM6		
	E144A	6GM7		
	E144D/Q	*N/A*		
	R148A	*N/A*		
	S189A	*N/A*		
	C417H*	6GL6	[4Fe-4S]	461
	C170A/D/S, C225A/D/S, C417A/D/S, C421A/D/S*	*N/A*	[4Fe-4S]	462
	T226K/V	*N/A*	[4Fe-4S]	463
	R171D/W**	*N/A*	Electron transfer	464
	A92S, A94S, S193C, E231D	*N/A*	Hydrogen bonding to CN–	465
	C169S, M223L, K228N, M415L	*N/A*	Hydrogen bonding	451
	C169D, F290Y, V296F	*N/A*	O_2 diffusion	466
	R96Q, K179Q, K262Q, R349Q, R353Q, R379Q, K396Q, K397E, K433Q	*N/A*	Interaction with ferredoxin	467
Other	L364F, C367D/A, P386L, A561F (in *Cb*A5H)	*N/A*	O_2 inhibition, formation of H_{inact}	425
	C48A, C100A, C298D (in *Ca*I)	*N/A*	Proton transfer and electron transfer	418,455,456
	V229T (in *Cr*HydA2)	*N/A*	[4Fe]H	468c
Cofactor Variants	PDT, ODT, SDT, and other headgroups	*N/A*	Maturation, hydrogen turnover	419,469–475
	Other modifications	*N/A*	Hydrogen turnover	476–480
	ODT	5BYQ	Hydrogen turnover, hydrogen bonding	480,481
	PDT	5BYR		
	SDT	5BYS		
	EDT	6H63		

* In reference [461] and [462], the numbering is different due to the deletion of 55 *C*-terminal amino acids.
** In reference [464], arginine R171 resembles R227 following the nomenclature used for *Cr*HydA1 in this work.

3.2.2 H-cluster, Catalytic Cycle, and Artificial Maturation

The oxidized states. In the absence of H_2 or other reductants, the H-cluster in standard [FeFe]-hydrogenases adopts the 'active-ready', oxidized state, H_{ox}. Moderate spin exchange coupling between [4Fe-4S] cluster and diiron site gives rise to the characteristic, rhombic EPR signal (g = 2.105, 2.044, 2.001, see **Figure 31**), indicating that the [4Fe-4S] cluster is oxidized (+2 state, a pair of Fe(II)-Fe(III)) while the diiron site adopts a mixed-valence +3 state (Fe(II)-Fe(I)).[482–484] The distribution of charges among Fe_p and Fe_d is debated.[267] [FeFe]-hydrogenase in the H_{ox}-state was analyzed by EPR spectroscopy within cells, isolated in solution, and in crystallized form.[485] X-ray diffraction structures of such crystals indicated a Fe-Fe bridging CO ligand[414,421], which reflects in a low-frequency IR absorbance band at 1802 cm^{-1}, accompanied by two terminal CO and CN^- bands at higher frequencies (**Table 6**).[486–488] A small upshift in frequency relative to H_{ox} has been explained by a protonation of a cysteine residue that coordinates the [4Fe-4S] cluster (see below)[489]; the EPR signal shifts accordingly (g = 2.106, 2.048, 2.001, see **Figure 31**).[267] This state is referred to as $H_{ox}H$. In the presence of CO, no H_2 oxidation and proton reduction activity is observed[490] as the oxidized H-cluster reacts with exogenous CO to form the CO-inhibited state, H_{ox}-CO.[415,416] The rhombic EPR signal of H_{ox} converts into an axial signature (g = 2.05, 2.01, see **Figure 31**), indicative of pronounced spin exchange coupling.[491–493] While the crystal structure of H_{ox} shows an open, apical binding site at Fe_d, the crystal structure of H_{ox}-CO hints at a labile, inhibiting ligand in apical position. Spin polarization favors an apical CO ligand[493], which is opposed to IR spectroscopy that suggested ligand rotation and the stabilization of an apical CN^- ligand.[480,494,495] The IR spectrum shows four CO ligands instead of three (**Table 6**), but due to significant vibrational energy transfer[496–498] the assignment of normal modes is less intuitive than in H_{ox}.[494] Under acidic conditions, $H_{ox}H$-CO is formed.[489] The EPR spectrum of this state has not yet been reported.

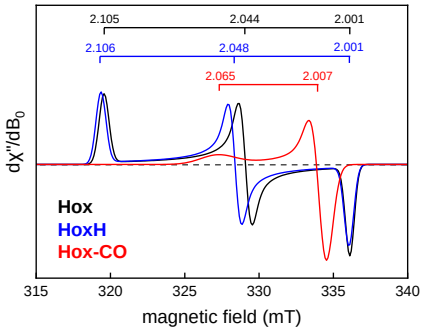

Figure 31 | EPR spectra of the oxidized H-cluster. Simulations of EPR spectra for the oxidized states Hox, HoxH, and Hox-CO as observed in *Cr*HydA1. The g-values are indicated. Reprinted (Adapted or Reprinted in part) with permission from ref. [267]. Copyright 2020 American Chemical Society.

The one-electron reduced states. The H-cluster may adopt two one-electron reduced states, both of which are largely diamagnetic. Reduction of the [4Fe-4S] cluster from +2 to +1 gives rise to the characteristic IR signature of $H_{red'}$ (sometimes referred to as just 'H_{red}'), which looks similar to H_{ox} but shifted to smaller frequencies (**Figure 32A**).[471,499,500] In H_{ox} and $H_{red'}$ the H-cluster binds a μCO ligand and maintains the 'rotated' structure' with an open, apical biding site at Fe_d (**Figure 33A**).[501] As such, the H-cluster readily interacts with exogenous CO, forming the reduced, CO-inhibited state $H_{red'}$-CO.[495] As in $H_{ox}H$, protonation of a cysteine has been proposed, stabilizing the excess electron of the [4Fe-4S] cluster in $H_{red'}$.[489,502] This may also explain the small upshift of frequencies under acidic conditions that has been assigned to the $H_{red'}H$ state (**Figure 32A**).

Reduction of the diiron site from +3 to +2 ((Fe(I)-Fe(I)) gives rise to the characteristic IR signature of H_{red}. Reduction and protonation of the diiron site under ambient conditions triggers the release of the μCO ligand into a terminal position[422] and the formation of a Fe-Fe bridging hydride ligand, μH.[503] Accordingly, H_{red} shows three terminal CO ligands and the apical position is occupied by a CO ligand, most likely (**Figure 32A**).[480] In variance to H_{ox} and $H_{red'}$, the square-pyramidal geometry of the diiron site is symmetrical (**Figure 33B**). Under cryogenic conditions, such changes in geometry are precluded and result in an IR signature that clearly shows a μCO ligand.[504–506] The latter is likely to be protonated at the ADT ligand and should be referred to as '$H_{red}H^+$'. Whether H_{red} or $H_{red}H^+$ are catalytically relevant cofactor intermediates or representative of an H_2-inhbited H-cluster geometry has been debated.[507–510]

The two-electron reduced states. Reduction of the [4Fe-4S] cluster starting from H_{red} results in the formation of H_{sred}.[511] This redox state was first described for *Cr*HydA1, where it accumulates under H_2, presumably due to the lack of accessory iron-sulfur clusters that distribute reducing equivalents between H-domain and F-domain.[512] The H-cluster is diamagnetic in this 'super-reduced' state; however, the assignment of the rhombic EPR spectrum with g = 2.08, 1.94, 1.87 has recently been questioned by Zebger, Horch, and co-workers who assigned an axial signal to H_{sred} (g = 2.15, 1.86).[505] The IR difference between H_{red} and H_{sred} is similar to H_{ox} and $H_{red'}$, *i.e.*, a small shift to lower energies (**Figure 32B**).[513] Just like H_{red}, the rotation of the μCO ligand into terminal position is precluded under cryogenic conditions ('$H_{sred}H^+$').[504–506]

A catalytic intermediate with a terminal hydride ligand was first suggested by Krasna and Rittenberg in 1954, based on H_2 and D_2 exchange experiments with the [FeFe]-hydrogenase from *Proteus vulgaris*.[514] 60 years later, the FTIR, Mössbauer, and EPR signatures (g = 2.07, 1.93, 1.88) of the so-called hydride state, H_{hyd}, were identified investigating protein and cofactor variants (**Table 5**).[457–459] In wild-type enzyme, accumulation of H_{hyd} was achieved upon H_2 oxidation starting from $H_{ox}H$, which confirmed the hydride state as a 'natural', catalytically relevant H-cluster intermediate (**Table 6**).[447] Subsequent NRVS and NMR studies further established our knowledge about H_{hyd}.[460,475,515] The diiron site resides in a formally 'super-oxidized' state (Fe(II)-Fe(II)), binding the terminal hydride in apical position at the distal iron ion. This position *trans* to μCO has been exploited to demonstrate the hydride character of the ligand in FTIR H/D exchange experiments.[447,458] Similar to $H_{red'}$, the [4Fe-4S] cluster is reduced (+1) and likely protonated.[507] The geometry of H_{hyd} resembles H_{ox} and $H_{red'}$ (**Figure 33A**).

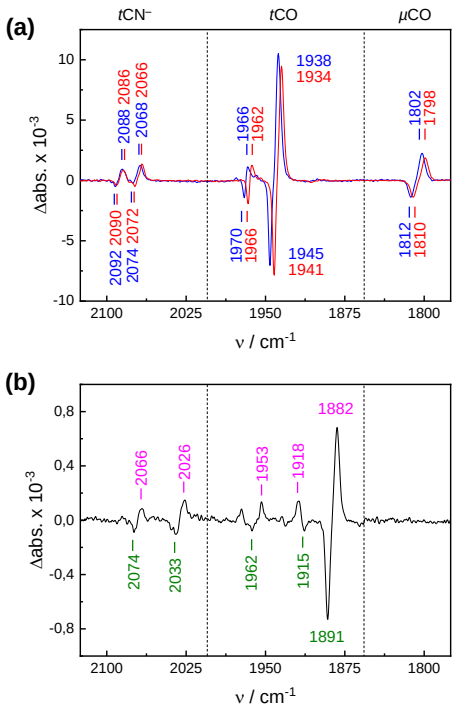

Figure 32 | Influence of the [4Fe-4S] cluster on the IR signature of the H-cluster. (a) 'H_2 – N_2' difference spectra of *Cr*HydA1 cofactor variant pdt at pH 5 ('H_{red}H – H_{ox}H', blue trace) and pH 8 ('$H_{red'}$ – H_{ox}', red trace). Negative and positive bands are assigned to H-cluster states with an oxidized and reduced [4Fe-4S] cluster, respectively. The small frequency shifts between the oxidized and reduced states are assigned to a protonation at or near the [4Fe-4S] cluster. Data taken from ref. [489]. **(b)** Spectro-electrochemical difference spectrum of *Cr*HydA1 that shows the accumulation of H_{sred} (magenta labels, -650 mV vs. SHE) over H_{red} (green labels, -450 mV vs. SHE) at pH 9. Negative and positive bands are assigned to H-cluster states with an oxidized and reduced [4Fe-4S] cluster, respectively. At ambient temperature, the bridging carbonyl ligand (μCO) converts into a terminal ligand, which results in three *t*CO bands.

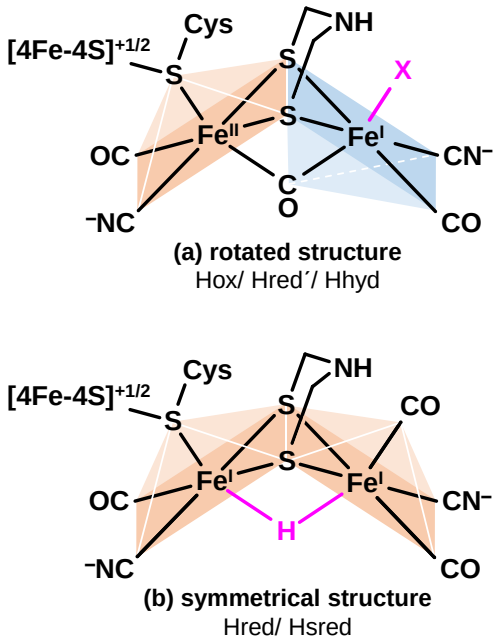

Figure 33 | Changes in geometry upon reduction. (a) In the paramagnetic II/I state of the diiron site (H_{ox} and $H_{red´}$), the μCO ligand stabilized the 'rotated structure' that is characterized by a square-pyramidal/ inverted square-pyramidal arragenment and an open coordination site at Fe_d (X). In H_{hyd}, the diiron site is 'super-oxidized' (II/II) and X is a terminal hydride. **(b)** Upon reduction (I/I), the diiron site adopts the symmetrical square-pyramidal/ square-pyramidal arrangement. No μCO ligand is observed in the respective redox states H_{red} and H_{sred}.

Table 6 | Vibrational and electronic properties of the main H-cluster states. All data stem from *Dd*H (H_{inact} and H_{trans}) or *Cr*HydA1 (other H-cluster states).

	νCN^- / cm^{-1}		νCO / cm^{-1}			[4Fe-4S]	[FeFe]	μ / t
H_{ox}	*2088*	*2070*	1964	1940	1802	+2	II / I	CO/–
$H_{ox}H$	*2092*	*2074*	1970	1946	1812	+2	II / I	CO/–
H_{ox}-CO	*2091*	*2081*	1968	1962[b]	1808	+2	II / I	CO/CN^-
$H_{ox}H$-CO	*2094*	*2086*	1972	1966[b]	1816	+2	II / I	CO/CN^-
$H_{red´}$	*2084*	*2066*	1962	1933	1792	+1	II / I	CO/–
$H_{red´}H$	*2086*	*2068*	1966	1938	1800	+1	II / I	CO/–
$H_{red´}$-CO	*2086*	*2076*	1967	1951[b]	1793	+1	II / I	CO/CN^-
H_{red}	*2070*	*2033*	1961	1915	1891	+2	I / I	H/CO[a]
H_{hyd}	*2088*	*2076*	1980	1960	1860	+1	II / II	CO/H^-
H_{sred}	*2068*	*2026*	1953	1918	1882	+1	I / I	H/CO[a]
H_{inact}	*2106*	*2087*	2007	1983	1848	+2	II / II	CO/?
H_{trans}	*2100*	*2075*	1983	1977	1836	+1	II / II	CO/?

[a] Under cryogenic conditions, $H_{red}H^+$ and $H_{sred}H^+$ are formed that bind a bridging carbonyl ligand and are likely to feature an open coordination site (μ/t = CO/–)

[b] In the CO-inhibited states, the coupled *p*CO/*d*CO stretching vibration gives rise to an additional band at 2012 cm^{-1} (H_{ox}-CO), 2006 cm^{-1} (H_{ox}H-CO), or 2002 cm^{-1} ($H_{red'}$-CO).

Catalytic mechanism of hydrogen turnover. The ongoing debate about the catalytic mechanism of [FeFe]-hydrogenase[507,510] is inseparable from questions regarding the influence of second and outer coordination sphere effects that are discussed in **Section 3.2.3** and **Section 3.2.4**. In the following, the two main models will be introduced. The key difference between the models is the assumption of a protonated and reduced diiron site in the '5-step model' or a protonation event at the [4Fe-4S] cluster in the '3-step model'.

In the absence of H_2 or other reducing components, all standard [FeFe]-hydrogenases adopt the H_{ox} state[482–484], which is widely accepted as the start- and endpoint of a catalytic cycle that accounts for hydrogen turnover (**Eq. 2**). **Figure 34** shows a simplified proposal for the succession of redox intermediates in the direction of H_2 evolution. Under the assumption that the H-cluster maintains the μCO geometry upon reduction of the diiron site[504–506], $H_{red}H^+$ and $H_{sred}H^+$ may be catalytic intermediates. The 5-step model starts with reduction of the [4Fe-4S] cluster and the formation of $H_{red'}$ over H_{ox} (transition A in **Figure 34**). It is conceivable that the ADT ligand of the diiron site is protonated *via* the catalytic proton transfer pathway (**Section 3.2.5**), which may induce intramolecular electron transfer from the [4Fe-4S] cluster to the diiron site, resulting in the formation of $H_{red}H^+$ over $H_{red'}$ (transition B). From here, $H_{sred}H^+$ is formed upon reduction of the [4Fe-4S] cluster (transition C).[511] Although there is no experimental evidence for a protonation of the ADT ligand in any H-cluster state[507], the formation of a terminal hydride at Fe_d upon intramolecular proton transfer and oxidation of the diiron site seems a reasonable assumption (H_{hyd} over $H_{sred}H^+$, transition D).[499] In the final step of the 5-step model (transition E), protonation of the terminal hydride would lead to H_2 evolution and the recovery of the oxidized resting state, H_{ox}.[515]

Based on the observation that the H-cluster undergoes geometry changes upon reduction of the diiron site at ambient temperatures (**Figure 32**), H_{red} and H_{sred} have been excluded as catalytic intermediates.[506–509] In the alternative '3-step model', $H_{red'}$ is formed over H_{ox} upon proton-coupled electron transfer to the [4Fe-4S] cluster (transition A*).[502] Here, the protons may reach the H-cluster via the regulatory proton transfer pathway (**Section 3.2.4**) while in the 5-step model, transition A is a simple reduction process. $H_{red'}$ may convert directly into H_{hyd} in a second step of proton-coupled electron transfer (transition B* in **Figure 34**) before protonation of the terminal hydride ligand leads to H_2 evolution, analogous to the 5-step model (transition E). It is debated whether H_{ox} or the protonated resting state $H_{ox}H$ is recovered upon H_2 evolution.[489]

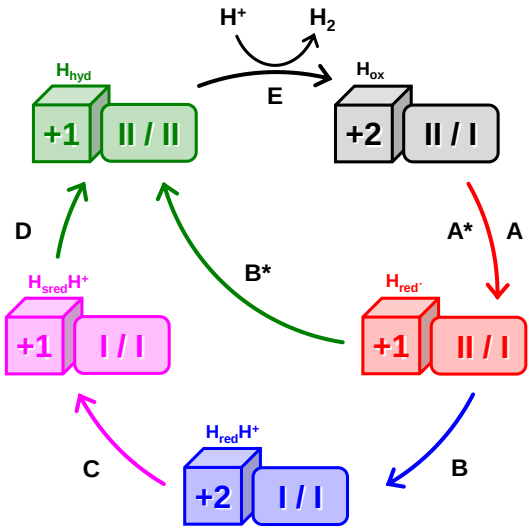

Figure 34 | Proposed catalytic cycle. The 5-step model (A–E) includes $H_{red}H^+$ and $H_{sred}H^+$, presuming the H-cluster retains the μCO ligand upon reduction of the diiron site. The 3-step model (A–B*–E) suggests a 'short-cut' from $H_{red'}$ to H_{hyd} as both species share the same geometry. The geometry of the reduced diiron site (I/I) under ambient conditions is debated. Reprinted (Adapted or Reprinted in part) with permission from ref. [267]. Copyright 2020 Amerian Chemical Society.

Other H-cluster species are also described in the literature. Electrochemistry experiments have shown that various inactive states are formed under *reducing* conditions; whether these forms correspond to any spectroscopically identified species is unclear, although it can be said that not all species that have been isolated and characterized are necessarily catalytic intermediates.[516] Inactive states also accumulate under certain *oxidizing* conditions. H_{inact} (or 'H_{ox}^{air}') and H_{trans} represent unready, 'super-oxidized' H-cluster states that have been observed in some [FeFe]-hydrogenases.[420,517,518] The states differ in the redox state of the [4Fe-4S] cluster, and the IR difference between H_{inact} and H_{trans} is similar to H_{ox} and $H_{red'}$ (**Table 6**). H_{trans} is paramagnetic and gives a sub-stoichiometric rhombic EPR spectrum with g = 2.06, 1.96, 1.89.[517] Remarkably, [FeFe]-hydrogenases in the H_{inact} state do not react with CO or O_2.[519]

The reductive activation of unready *Dd*H was long believed to be irreversible but it has recently been demonstrated that H_{ox} can be converted into H_{trans} and H_{inact} in the presence of exogenous sulfide, which binds to Fe_d.[520–522] The formation of H_{inact} in the absence of sulfide was considered to cause the reversible high potential inactivation of the enzyme as detected in electrochemistry experiments.[523] Later, it became clear that sulfide-independent oxidative inactivation results from the inhibition of the enzyme by traces of halide ions like chloride or

bromide.[524] Recently, the formation of H_{inact} was observed in a the [FeFe]-hydrogenase *Cb*A5H, notably in the absence of either sulfide or halides.[525] The structure of the air-oxidized H-cluster suggests that Fe_d is coordinated by the sulfur atom of the conserved cysteine residue C367 (**Figure 35**). The formation of H_{inact} in *Cb*A5H and the resulting resistance to O_2 are lost when this cysteine is replaced by site-directed mutagenesis (**Table 5**).[425] This mechanism explains why the same H_{inact} IR signature is observed in air-oxidized *Cb*A5H[525], in *Dd*H natively produced in the sulfate-reducing bacterium *Desulfovibrio desulfuricans*[488], and in certain standard [FeFe]-hydrogenases exposed to sulfide.[521] However, it is unclear why *Cp*I is reported insensitive towards exogenous sulfide, unlike other standard [FeFe]-hydrogenases like *Cr*HydA1 and *Dd*H. Moreover, direct coordination of Fe_d by the cysteine sidechain was observed exclusively in *Cb*A5H and not in standard [FeFe]-hydrogenases. It has been shown that C367 in *Cb*A5H is located on a loop whose unique flexibility depends on residues up to 13 Å away from the H-cluster (**Figure 35**).[425] The investigation of how the conversion between active and inactive states depends on the nature of these residues provided a clear demonstration of long-range outer coordination sphere effects on active site reactivity.

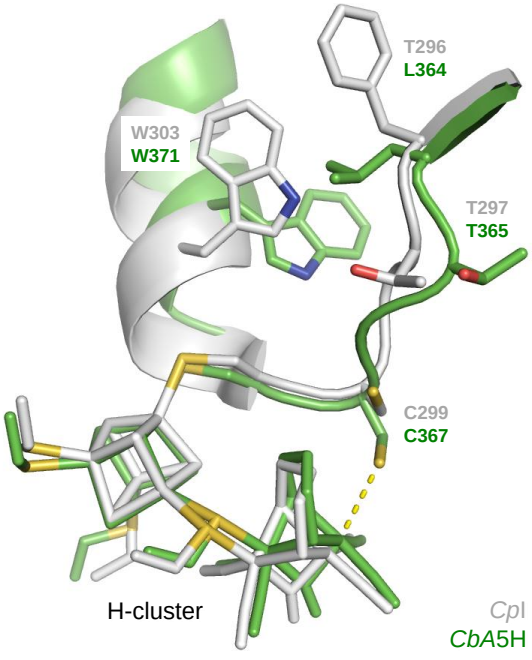

Figure 35 | Comparison of *Cp*I (white) and *Cb*A5H (green) in the H_{ox} and H_{inact} state. The distance of the sulfur atom of C299/C367 shrinks from ~6 Å to ~3 Å, making a direct coordination of the distal iron ion (Fe_d) in the H_{inact} state of *Cb*A5H likely (dashed line). The annotated amino acid residues have been identified to cause the flexibility of the unique loop in *Cb*A5H. Drawn after PDB IDs 4XDC and 6TTL.

Overall, the mechanism of aerobic inactivation is not well understood. While O_2 inhibition of *Dd*H and *Cb*A5H is reminiscent of the reaction of [NiFe]-hydrogenase with O_2 (**Section 3.1.4**), most [FeFe]-hydrogenases are irreversibly destroyed under aerobic conditions. It is believed that O_2 binds to the H-cluster like a ligand[526–529] and becomes reduced to superoxide, H_2O_2, or other ROS that subsequently damage the H-cluster.[530–534] Outer coordination sphere effects are likely to play a role, *e.g.*, considering O_2 diffusion through the enzyme[466] and the influence of electron transfer[424] or proton transfer[533] on ROS formation. The comparatively sluggish reaction of sensory [FeFe]-hydrogenases with O_2 had been explained with inefficient proton transfer.[444] Additionally, second coordination sphere effects may influence the formation of the H_{ox}-O_2 state where the superoxide ligand is stabilized by hydrogen-bonding interactions with the ADT headgroup, not unlike H_{ox}-CO and H_{hyd}.[480] As the hydride state is a key intermediate in the catalytic cycle (**Figure 34**) O_2-tolerant [FeFe]-hydrogenases may not be feasible.

Artificial Maturation of the H-cluster. *In vivo*, the iron-sulfur clusters of [FeFe]-hydrogenase are inserted by the regular iron-sulfur machinery, namely the *isc* system.[535] This includes the [4Fe-4S] cluster of the H-domain that serves are 'nucleation core' for the synthesis of the H-cluster.[536] This task is performed by three auxiliary enzymes, HypEFG.[537] A precursor of the diiron site is assembled on HypF[538–540] by the help of radical *S*-adenosylmethionine (rSAM) enzyme HypG.[541–545] Then, HypF delivers the active site precursor to the hydrogenase apo-protein where it fuses with the bridging cysteine upon CO release to form the H-cluster. A mechanism has been proposed that includes guidance by charged amino acids[446], not unlike the channel proposal for the maturation of nitrogenase (**Section 2.2**). It has been suggested that the role of the rSAM enzyme HypE is the synthesis of the ADT ligand.[546–548]

In vitro, the rather intricate maturation process can be hijacked by loading HypF with diiron compounds and mixing HypF with apo-hydrogenase.[469] This allowed for inserting different diiron site mimics into otherwise unaltered enzyme, creating 'cofactor variants' or semisynthetic enzymes that do not exist in nature.[481,549,550] Further, it has been shown that even HypF can be avoided in the maturation process: incubation of apo-hydrogenase with diiron compounds lead to functional enzyme.[470] The protocol established by Happe and co-workers led to a great variety of cofactor variants, including different dithiolate and diatomic ligands[419,469–475], chalcogenides[476,477], and metal ions (**Table 5**).[479] For example, replacing the

central atom X of the dithiolate ligand from nitrogen (ADT) with carbon (PDT), suppresses any redox change at the diiron site.[471] This allowed for studying the protonation and redox chemistry of the [4Fe-4S] cluster in detail (**Figure 32**).[489]

3.2.3 Direct Interactions between H-cluster and Protein

The presence of CO and CN^- ligand at the active site cofactor of [FeFe]-hydrogenase was proven by FTIR spectroscopy in 1996.[518] When the H-cluster was modelled into the first electron density of [FeFe]-hydrogenases *Cp*I and *Dd*H, the position of the diatomic ligands was assigned according to second coordination sphere interactions.[414,421] The chemical identity of the CO and CN^- ligands cannot be deduced from the electron densities alone. In *Cp*I, the proximal CN^- ligand may accept a hydrogen bond from the sidechain of serine S232 and the secondary amine of the backbone formed by S232 and P231 (**Figure 36**).[26] The latter is strictly conserved in [FeFe]-hydrogenase and most likely is responsible for the correct orientation of the backbone amine towards Fe_p-CN^-; in *Cp*I and *Dd*H; the angle between ligand and backbone is ~170°, indicative of a strong hydrogen bond. Serine S232 of *Cp*I is replaced with an alanine in *Dd*H (A109), which cannot form a bond with the H-cluster. Phylogenetically, the low level of conservation (**Table 4**) suggests a minor role in the second coordination sphere; however, the effect can be demonstrated. Winkler, Happe, Rüdiger, and co-workers identified site-selective shifts of the Fe_p-CN^- IR band analyzing *Cp*I-S232A and the corresponding variant of *Cr*HydA1, A92S.[465] The authors even introduced an additional hydrogen bond by changing alanine A94 to serine, which doubled the IR shift observed for A92S (**Figure 36**). Affecting the electron density at Fe_p and the coupling with the [4Fe-4S] cluster, these variants had a clear influence on the directionality of hydrogen turnover[465], which may explain the difference in catalytic performance between wild-type *Cp*I and *Cr*HydA1.

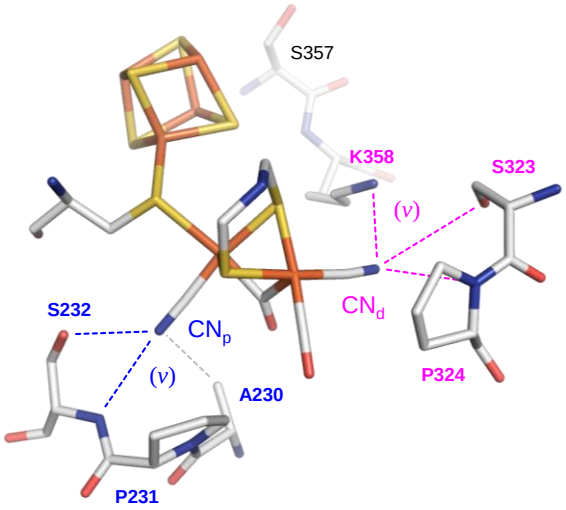

Figure 36 | Hydrogen-bonding environment of the CN^- ligands. In proximal (p) position, polar interactions (*v*) with a backbone amine, S232, and variant A230S have been experimentally verified in *Cp*I and *Cr*HydA1. The hydrophilic pocket including K358, S323, and a P324 backbone contact inspired the assignment of the CN^- ligand in distal (d) position in *Cp*I and *Dd*H. The putative hydrogen-bonding environment (*v*) is shown. Drawn after PDB ID 6NAC. Atomic coloring: Fe, orange; S, yellow; C, gray; O, red; N, blue.

The hydrogen-bonding environment of the distal CN^- ligand is difficult to characterize experimentally. Early on, the strictly conserved lysine K358 (*Cp*I) and K237 (*Dd*H) was suggested as hydrogen-bonding donor to Fe_d-CN^- (**Figure 36**).[551] As the chemical nature of the ADT ligand was still unknown in 1999, Fontecilla-Camps and co-workers even proposed a catalytic proton transfer pathway based on K237 in *Dd*H.[421] Site-directed mutagenesis of this lysine, *e.g.*, towards alanine[451] or asparagine[446], precluded any cofactor insertion and hinted at a key role in the activation of apo-hydrogenase.[431] This renders functional studies of hydrogen bonding difficult. Investigating ^{14}N-labelled *Dd*H by hyperfine sublevel correlation spectroscopy (HYSCORE)[484], Lubitz, Silakov, and co-workers assigned the large quadrupole couplings to a hydrogen bond between Fe_d-CN^- and K237.[437] On the contrary, similar experiments on the *Cr*HydA1 cofactor variant PDT by the same group resulted in substantially simplified ^{14}N HYSCORE spectra that showed no coupling with K228 (equiv. K358 or K237).[552] While the role of K358 in hydrogen-bonding remains ambiguous, the sum of weak interactions around Fe_d-CN^- certainly results in a certain level of structural rigidity in the oxidized state[553]; however, this might not preclude ligand rotation upon H-cluster state transitions. For example, DFT calculations based on 16 different ^{13}CO isotopomers of the H-cluster suggested an apical CN^- ligand in the H_{ox}-CO state[494], stabilized by an 'internal' hydrogen bond with the ADT ligand. While this interpretation is not without controversy[493],

the stability of H_{ox}-CO was found to be largely reduced upon modification of the dithiolate ligand, following a trend, which cannot be explained with an apical CO ligand.[480] In contrast to CN^-, carbonyl ligands are poor hydrogen bond acceptors.[554] A similar concept of internal hydrogen bonding may play a role in the formation and stabilization of H_{hyd}.[459] Moreover, CO/CN^- ligand rotation was discussed in the context of the temperature-dependent interconversion of H_{ox} and H_{red}/H_{sred}.[506,507] While the role of K357 in hydrogen-bonding remains ambiguous, other conserved residues in the vicinity of Fe_d have been proposed to interact with the CN^- ligand, including S323 as well as a backbone contact involving P234 (**Figure 36**).[26]

Steric or hydrophobic interactions of the protein fold with the terminal CO ligand have not yet been explored experimentally, but the influence of methionine M353 on the bridging carbonyl was subject to dedicated analysis. Triggering the formation of H_{ox} from H_{ox}-CO by visible light irradiation, Lemon & Peters observed an elongation of the distance between μCO and the sulfur atom of the M353 sidechain in *Cp*I.[416] Although both H_{ox}-CO and H_{ox} carry a μCO ligand[486–488], the increased intensity of the μCO band in the CO-inhibited state may be related to the lack of steric pressure and a greater change in dipole moment. 20 years later, Peters, King, and co-workers revisited *Cp*I by cryogenic XFEL crystallography, assigning similar differences to an oxidized 'conformation A' and a reduced 'conformation B' (**Figure 37**).[555] This includes reorientation of both M353 and sereine S357, the latter which is located close to the [4Fe-4S] cluster in *Cp*I (potential effect are discussed in **Section 3.2.4**). The presence of a μCO ligand has been recognized as a key requirement for hydrogen turnover by various authors.[504,507,556] Precluding the formation of bridging hydride intermediates[503], the orientation of M353 may play a key role in maintaining the CO-bridged, rotated H-cluster geometry. Note that M353 and K358 are part of Loop 2 (**Figure 30**), which may indicate coupling between Fe_d-CN^- and μCO. On the contrary, **Table 4** indicates that M353 is moderately conserved at best. [FeFe]-hydrogenases with a glycine or sereine residues instead of methionine feature altered catalytic properties (*Cp*III or *Tam*HydS) or pronounced downshifts of the μCO frequency (*Cp*II and *Tm*HydS).[441,444,555] No such shift was observed in *Me*HydA, despite the unique variation from methionine to threonine.[423] In the case of the sensory hydrogenases *Tm*HydS and *Tam*HydS, multiple variations seem to contribute to the catalytic phenotype, which makes it difficult to pinpoint individual effects. Replacement of methionine with leucine in the standard hydrogenases *Cp*I and *Cr*HydA1 greatly diminished catalytic activity.[451]

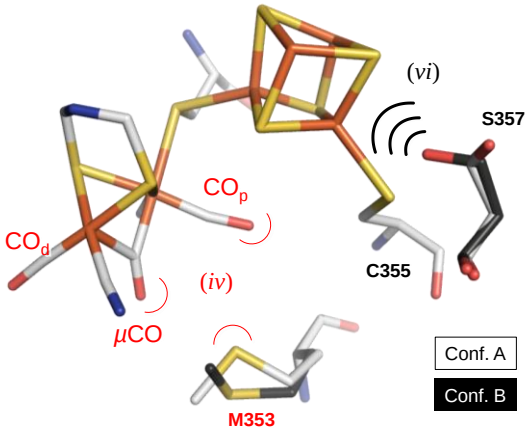

Figure 37 | Structural differences between 'conformation A' and 'conformation B'. The M353 side chain shifts by ~0.4 Å away from μCO and Fe$_p$-CO in the 'reduced' state (equivalent conformation B), which lowers the steric constraints (*iv*). Concomitantly, the side chain of S357 switches to an orientation towards the [4Fe-4S] cluster and the cysteine ligand C355. This may influence the electron density distribution across the cluster (*vi*). Drawn after PDB ID 6NAC. Atomic coloring: Fe, orange; S, yellow; C, gray; O, red; N, blue.

Methionine M353 may interact with the μCO ligand while M497 and cysteine C299 are hydrogen-bonded to the ADT ligand (**Figure 37**). These residues are strictly conserved in Group A [FeFe]-hydrogenases but replaced with glycine, leucine, or sereine in *Tm*HydS and *Tam*HydS (**Table 4**). The cysteine plays a key role in proton transfer and will be discussed in the next paragraph. Methionine M497 is part of Loop 3, which also bears C499 and C503 (**Figure 30**). Its function is unclear; it has been discussed as an alternative proton transfer relay or hydrogen-bonding partner that keeps the ADT ligand in position.[267] Site-directed mutagenesis of *Cp*I (M497L) and *Cr*HydA1 (M415L) demonstrated the importance of this residue.[451]

3.2.4 Proton Transfer and Proton-coupled Electron Transfer

In all hydrogenases, proton transfer is a key determinant of catalytic efficiency.[298] Protons enter the enzyme to be consumed in the evolution of H_2 or leave the enzyme upon H_2 oxidation, following a Grotthuß-type mechanism. This demands a network of hydrogen-bonded amino acid residues, water molecules, or hydrophilic cofactors. Proton transfer across the second and outer coordination sphere has been recognized as one of the major differences between biomimetic catalysts and enzymes.[557–559]

Based on the crystal structure of [FeFe]-hydrogenases *Cp*I and *Dd*H various proton transfer pathways have been proposed.[560–563] As an experimental marker for an involvement of individual amino acids, the analysis was initially restricted to catalytic activity.[455,564]

However, when it was discovered that the H-cluster accumulates the H_{hyd} in variants specifically impaired in proton transfer (**Table 5**)[457–459], spectroscopic methods could be used to investigate the minutiae of proton uptake and release. X-ray crystallography[449] and FTIR difference spectra[565] uncovered a tight hydrogen-bonding network in *Cr*HydA1 and *Cp*I, stretching across > 20 Å including a small water cluster W1, and C299, the cysteine residue close to the distal iron ion (**Figure 38**). Based on the first crystal structure of *Cp*I, this pathway was proposed early on.[414] The reduction and protonation of the H-cluster upon formation of H_{red} over H_{ox} has been exploited to trigger proton transfer. The changes in protonation and hydrogen bonding gave rise to distinct FTIR difference spectra, suggesting only subtle changes, *e.g.*, the formation of a hydrogen bond between E279 and S319 as well as changes with respect to W1. The lack of difference signals in the SH regime hints at a largely preserved hydrogen-bonding environment around C299 and does not support protonation of the ADT ligand, *i.e.*, in H_{red}.[565] While the residues involved in proton transfer are mostly conserved within Group A, sensory-type [FeFe]-hydrogenases show drastic variations (**Table 4**).[441,444] It remains to be understood how protons are transferred in such enzymes; the influence of amino acids replacements on catalytic activity, bias and reversibility[29] certainly emphasize the influence of the outer coordination sphere.

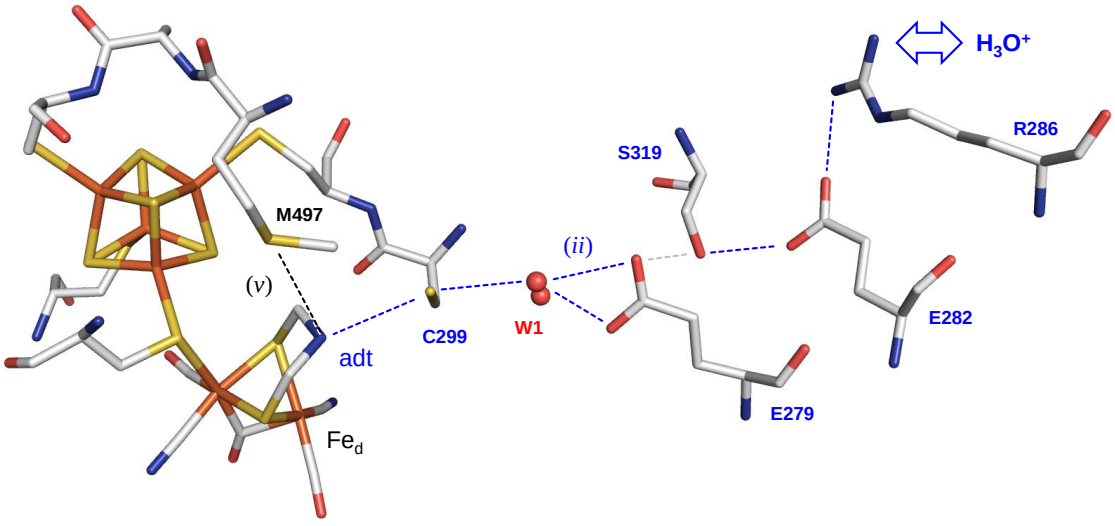

Figure 38 | The 'catalytic' proton transfer pathway in [FeFe]-hydrogenase *Cp*I. The sidechain of M497 may stabilizes the orientation of the ADT ligand by a hydrogen bond (*v*). Dashed blue lines represent the hydrogen-bonding network (*ii*) of the proton transfer pathway. Note that a bond between E279 and S319 is unlikely in the oxidized state (dashed grey line) but likely formed upon reduction and protonation of the cofactor. Drawn after PDB ID 4XDC. Atomic coloring: Fe, orange; S, yellow; C, gray; O, red; N, blue.

Next to the 'catalytic' proton transfer pathway, a comparison of several [FeFe]-hydrogenase crystal structures suggested the existence of a second, water-based proton transfer pathway.[489] Due to the lack of 'acidic' moieties in this trajectory (*e.g.*, glutamic acid residues), the difference in apparent pK_a compared the catalytic pathway allows controlling proton transfer to the diiron site and/or the [4Fe-4S] cluster.[513] **Figure 39** shows how a chain of water molecules permeates towards the intersection of the F- and H-domains, *i.e.*, C193, which coordinates the most proximal [4Fe-4S] cluster and C499, the later which in turn coordinates the H-cluster. Protonation of a cysteine ligand is rather uncommon in nature; however, quantum mechanical calculations of the IR spectra of $H_{ox}H$, $H_{red'}$, and H_{hyd} provided excellent agreement with the experimental CO/CN^- signature when C499 was protonated *in silico*.[566] As demonstrated in **Figure 32**, redox- and protonation changes in the second coordination sphere of the diiron site (*e.g.*, at the [4Fe-4S] cluster) result in small yet discernable IR band shifts. The spectroscopic characterization is in agreement with the pH-dependent population of $H_{ox}H$[489], the pH-dependent transition potential of the $H_{ox}/H_{red'}$ couple[502], and the observation that H_{hyd} is formed upon H_2 oxidation *via* $H_{ox}H$ directly.[447]

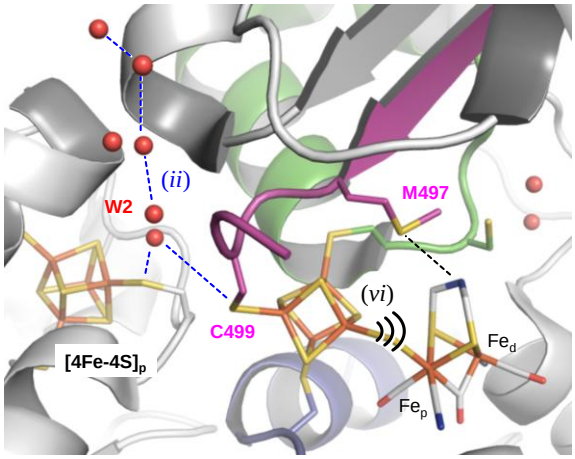

Figure 39 | The 'regulatory' proton transfer pathway in [FeFe]-hydrogenase *Cp*I. In most crystal structures of *Cp*I, a trajectory of water molecules (red spheres) can be found, putatively connected by hydrogen bonds (*ii*). This water channel 'W2' is located at the intersection of the accessory domain (white) and the catalytic domain (including the most proximal iron-sulfur cluster, $[4Fe\text{-}4S]_p$), leading up to cysteine C499 that coordinates the [4Fe-4S] cluster of the catalytic cofactor. Here, protonation and redox changes influence the diiron site (*vi*). Drawn after PDB ID 4XDC. Atomic coloring: Fe, orange; S, yellow; C, gray; O, red; N, blue.

Influencing the electron density distribution across the H-cluster, the second proton transfer path has been named 'regulatory'.[489] In general, electrons and protons tend to move in a concerted fashion, minimizing energetic barriers[22–24] and facilitating long-range coupling

between electron transfer and proton transfer, an extreme case of outer coordination sphere effects.[448,567,568] In the case of [FeFe]-hydrogenase, PCET shapes the electron density distribution across the H-cluster by locking reducing equivalents at the diiron site upon protonation of the ADT ligand[499] or formation of a bridging hydride (μH).[503] Similar ideas have been put forward to explain the pH-dependence of the [4Fe-4S] cluster[489,502], although this has been disputed.[569] The existence of two separate proton transfer pathways (**Figure 39**) complicates the analysis of the pH-dependence and led to conflicting results.[513] These differences have important implications for the understanding of [FeFe]-hydrogenase catalysis, as discussed elsewhere.[507]

3.2.5 Gas Channels in [FeFe]-hydrogenase

The mass transport of reactants like H_2, O_2, and CO within [FeFe]-hydrogenase *Cp*I has been studied using molecular dynamics.[466,570–572] Schulten and co-workers calculated how "the protein's natural equilibrium dynamic motion on the nanosecond timescale can define predetermined pathways for hydrophobic gas transport", arguing that permanent channels may not be needed.[570] **Figure 40A** depicts that this applies to small gases like H_2 in particular. But while CO and O_2 may not access the protein as easily as H_2, Mohammadi & Vashisth suggested defining a "network of pathways" that predicts gas diffusion more accurately[571] than the pathway A/B model (**Figure 40B**). This complexity must be met with a statistical approach to site-directed mutagenesis, therefore automated screening protocols[573,574] were employed understanding the influence of 'gas filters', *e.g.*, selectively precluding access of O_2 and CO to the active site (**Table 5**).[453,454] Currently, the role of hydrophobic gas channels in the outer coordination sphere is not well understood. With respect to CO inhibition, there is a remarkable variety that may help identifying certain trends. The rate of CO inhibition among different standard [FeFe]-hydrogenases was found to vary over three orders of magnitude[424,523] while sensory [FeFe]-hydrogenases[441,444] and [FeFe]-hydrogenase complexes show even lower CO affinities.[433] Apparently, non-conserved residues remote from the active site tune the reactivty; however, the identity of the responsible amino acids and the underlying mechanistic contributions are yet to be explored. In the second coordination sphere of the H-cluster, the replacement of the V296 and F290 in *Cr*HydA1 decreased the rate of CO inhibition ten-fold, but the effects on O_2 deactivation were not proportional.[466] The simultaneous variation of two residues located between the H-cluster and the proximal accessory cluster in *Cp*I moderately reduced the rate of inactivation.[453] As the diiron site has been shown to be the initial target of oxidation, this is an interesting observation that may hint at the role of the [4Fe-4S] cluster in the reaction with 'activated' O_2.[530,532,534]

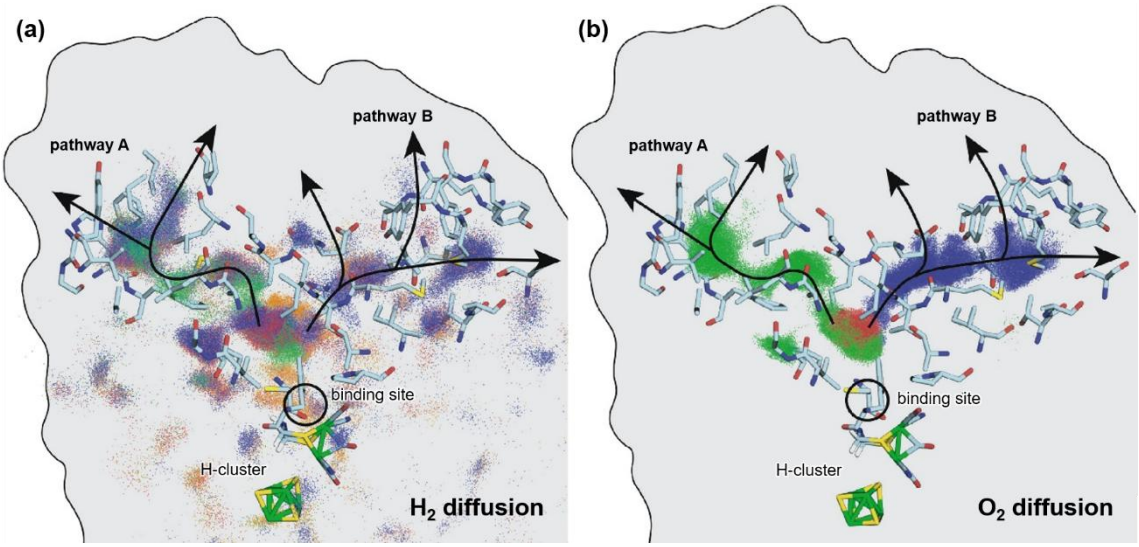

Figure 40 | Gas diffusion pathways in [FeFe]-hydrogenase. Representative simulations of 1000 copies of **(a)** H_2 diffusing out from the H-cluster and **(b)** of O_2 diffusing out from the H-cluster or from the middle of a previously identified H_2 channel. Possible exits, based on the proximity of the external solution, are highlighted with arrows. Contrary to H_2 diffusion, the O_2 molecules move collectively through the same pathway for a given simulation, though they may employ different pathways for different independent simulations. Reprinted (Adapted or Reprinted in part) with permission from ref. [570]. Copyright 2005 Cell Press.

4 Formate Dehydrogenase

Formate dehydrogenases (FDHs) are a diverse group of enzymes in bacteria, archaea, and eukaryotes that catalyze the reversible two electron and one proton abstraction of formate ($HCOO^-$) to produce CO_2 (**Eq. 3**).[575,576] In general, these enzymes are involved in diverse metabolic pathways but mostly in the production of CO_2 from formate.[577] Based on the low standard potential of formate oxidation ($E^{0'}$ = -430 mV vs SHE) prokaryotes derive energy by coupling it to the reduction to one of several terminal electron acceptors.[578] Some enzymes, however, were described to act as CO_2 reductases, with a preference for the reaction of reducing CO_2 to formate.[579]

Eq. 3 $$CO_2 + H^+ + 2e^- \rightleftharpoons HCOO^-$$

FDHs are divided into two major classes, into the metal-dependent and metal-independent FDH enzymes.[577] The metal-independent FDHs generally are NAD^+-dependent and distributed from bacteria to yeast, fungi, and plants.[580] These enzymes have no redox-active metal centers involved in catalysis, but instead NAD^+ is used as a cosubstrate and serves as a hydride acceptor for converting formate directly to CO_2.[581] In these proteins, formate is

positioned in proximity to the NAD^+ cosubstrate to facilitate the hydride transfer step. Since this review is focused on GPMs, only the metal-dependent FDHs will be described in detail.

The metal-dependent FDH enzymes are restricted to bacteria and archaea and contain either molybdenum (Mo) or tungsten (W) as metal ions in the active site.[576,582,583] They have a higher complexity by being composed of several subunits, which contain in addition to the active site bis-metal-binding pterin (MPT) guanine dinucleotide (bis-MGD) cofactor (**Figure 41A**) various additional cofactors, such as diverse Fe-S clusters, FMN, or hemes.[576]

4.1 The Metal-containing Cofactor of FDH

The metal-containing FDHs are members of the dimethylsulfoxide (DMSO) reductase family of mononuclear molybdenum (Moco) or tungsten cofactor (Wco)-containing enzymes.[584,585] In these enzymes, the active site in the oxidized state comprises a Mo or W ion present in the bis-MGD, which is coordinated by the two dithiolene groups from the two MGD moieties, a protein derived selenocysteine or cysteine ligand and a sixth ligand that is accepted to be a sulfido ligand (Figure 41B).

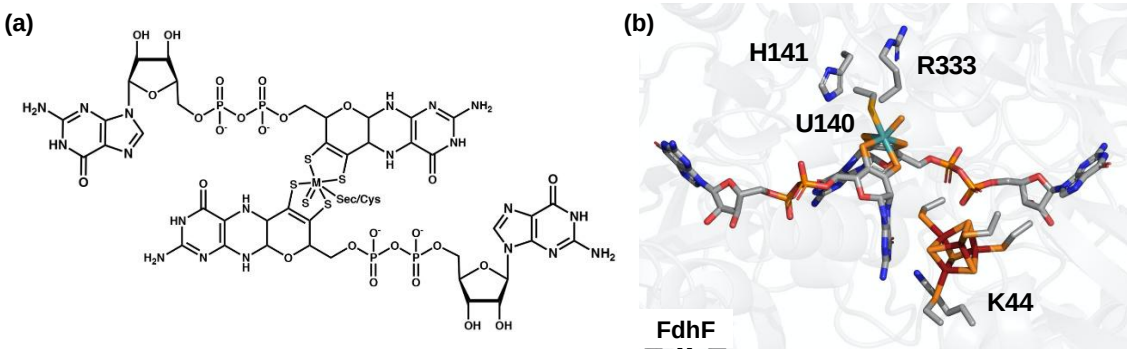

Figure 41 | The bis-metal binding pterin guanine dinucleotide cofactor (bis-MGD) present in formate dehydrogenases. (a) Members of the DMSO reductase family of molybdoenzymes bind the bis-MGD form of the cofactor in the active site. The bis-MGD in formate dehydrogenases coordinates the metal (depicted as M) by the dithiolene groups from two pterin ligands with the additional ligands being a sulfido group, and a sixth ligand which is either a selenocysteine (Sec) or a cysteine (Cys) from the amino acid backbone. (b) Representative depiction of the bis-MGD cofactor coordination environment in formate dehydrogenases, of *E. coli* FdhF in the oxidized state (PDB ID 1FDO).

Selenocysteine-containing enzymes have generally a higher turnover number than the cysteine-containing ones.[586] The analogous chemical properties of W and Mo, the similar active sites of W- and Mo-containing enzymes, and the fact that W can replace Mo in some enzymes have led to the conclusion that both Mo- and W-containing FDHs have the same

reaction mechanism.[582] The question of why in FDH enzymes both metal ions can be found while other enzymes of the DMSO reductase family exclusively function with only one type of metal ion is still not completely understood.[585,587,588] Generally, it was found that W-containing enzymes catalyze reactions with low redox potentials (−420 mV vs SHE), and it was shown that W^{IV} is a more reducing ion than Mo^{IV}.[588] Possibly for these reasons, the conversion of CO_2 to formate was demonstrated to occur preferentially for W-FDH enzymes.[589–591] However, the purified Mo-containing FDHs were also shown to perform CO_2 reduction in the presence of excess reducing equivalents.[579] In the cell, however, this reaction would thermodynamically not be favored.[578]

4.2 Structural Features of FDH

Overall, there is a great variety in the subunit architecture of metal-containing FDHs. The α-subunit, or the Moco/Wco containing domain, is highly conserved and minimally comprises the Moco/Wco binding site and a [4Fe-4S] cluster proximal to the Moco/Wco cofactor (**Figure 42**).[576,579] These α-subunits or domains are typically between 80–95 kDa and the overall folds are highly identical. In most cases, the Moco/Wco cofactor and the proximal [4Fe-4S] cluster interface with additional Fe-S clusters, either within the α-subunit or close by in a neighboring subunit.

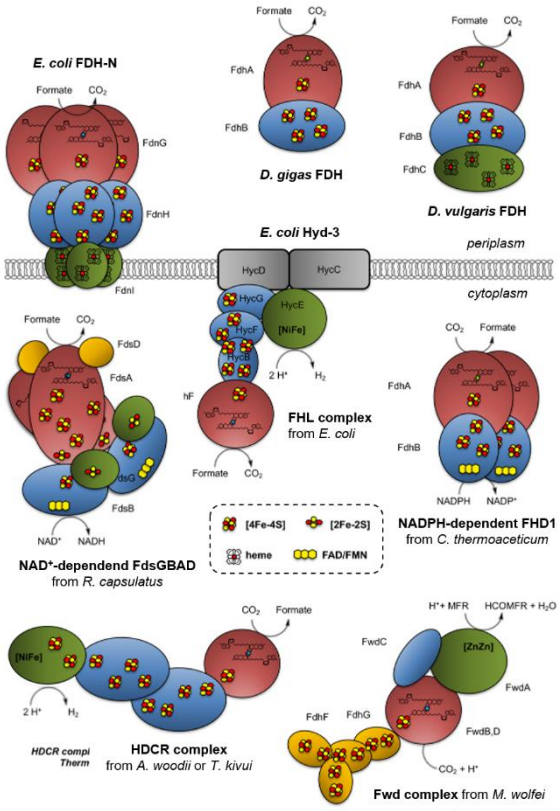

Figure 42 | Schematic overview of cytoplasmic and periplasmic FDHs. Localization of FDHs, their subunit organization and cofactor composition. Shown are the membrane bound respiratory FdnGHI from *E. coli*, the periplasmic FdhAB and FdhABC from the *D. gigas* and *D. vulgaris* Hildenborough, the formate hydrogen-lyase complex formed by (FdhF) and Hyd3 (HycBCDEFG) from *E. coli*, the cytoplasmic FDH from *R. capsulatus*, the cytoplasmic CO_2-reducing dimeric FDH (FdhAB) from the acetogen *Morella thermoaceticum*, the HDCR complex from *A. woodii* (Mo-containing) or from *T. kivui* (W-containing), and the formylmethanofuran dehydrogenase complex from *M. wolfei*.

Metal-dependent FDHs are found either in the cytosol, in the periplasm or are membrane-bound, facing the periplasm (**Figure 42**).[576,583] The enzymes are generally involved in diverse biochemical pathways and use different electron acceptors/mediators like hemes, ferredoxins, NAD^+, coenzyme F_{420}, or membrane quinols for the reaction of formate oxidation or CO_2 reduction.[592] The formate oxidation activity of FDH is typically followed *via* the reduction of methyl viologen (MV), benzyl viologen (BV), or NAD^+. Additionally, the analysis of 'catalytic' currents can be followed *via* protein film electrochemistry (**Table 7**).[593,594]

Table 7 | Oxidation kinetic parameters of structurally characterized FDH and formylmethanofuran dehydrogenase enzymes. Reported formate oxidation kinetic parameters for *E. coli*, *D. gigas*, and *D. vulgaris* Hildenborough FDH represent those following the enzymatic reduction of benzyl viologen; formylmethanofuran dehydrogenase follows the enzymatic reduction of methyl viologen, while for *R. capsulatus* FDH the enzymatic reduction of NAD^+ is reported.

Organism/ Type	***E. coli*** **FdhF**	***E. coli*** **FdnGHI**	***D. gigas*** **FdhAB**	***D. vulgaris*** **Hildenborough FdhAB**	***R. capsulatus*** **FdsGBAD**	***M. wolfeii*** **formylmethanofuran dehydrogenase**
Catalytic Subunit	FdhF	FdnG	FdhA	FdhA	FdsA	FwdB
Metal	Mo	Mo	W	W	Mo	W
PDB ID	1FDO, 2IV2	1KQF	1H0H	6SDR, 6SDV	6TGA, 6TG9	5T5I
Formate Oxidation Kinetic Parameters	k_{cat} = 2800 s^{-1} K_M = 26 mM K_d = 100 mM $K_{M\ BV}$ = 3 mM	N/A	k_{cat} = 138 s^{-1}	k_{cat} = 3684 s^{-1} K_M = 1 μM	k_{cat} = 36 s^{-1} K_M = 281 μM $K_{M\ NAD+}$ = 173 μM	k_{cat} = 18 s^{-1} K_M = 13 μM, $K_{M\ MV}$ = 400 μM
Ref.	[595]		[591]	[596]	[597]	[598]

Table 8 | Amino acid comparison and oxidation kinetic parameters of active site variants of structurally characterized FDH and formylmethanofuran dehydrogenase enzymes. Amino acid residues in the primary or secondary coordination sphere by which a role has been assigned or postulated are noted. Enzymatic activity of reported active site variants for respective organisms follow the same electron acceptor used as reported for the WT enzyme, as reported in **Table 7**.

Organism/ Type	***E. coli*** **FdhF**	***E. coli*** **FdnGHI**	***D. gigas*** **FdhAB**	***D. vulgaris*** **Hildenborough FdhAB**	***R. capsulatus*** **FdsGBAD**	***M. wolfeii*** **formylmethanofuran dehydrogenase**	**Function**	**Formate Oxidation Kinetic Parameters**	**Ref.**
Conserved amino acids	U140	U196	U158	U192	C386	C118	substrate binding, catalytic efficiency	*E. coli* (FdhF) U140C: k_{cat} = 9 s^{-1}, K_M = 9 mM, K_D = 5 mM, $K_{M\,BV}$ = 2 mM	586
	H141	H197	H159	H193	H387	H119	proton shuttling, channel gating	*R. capsulatus* H387M: k_{cat} = 34 s^{-1}, K_M = 3.6 mM *R. capsulatus* H387K: k_{cat} = 1 s^{-1}, K_M = 28 mM	599
	R333	R446	R407	R441	R587	R288	substrate binding, channel gating	*R. capsulatus* R587K: k_{cat} = 11 s^{-1}, K_M = 362 mM	599
	M157	M213	M175	M209	G403	I133	hydrophobic channel direction	N/A	
	V338	L450	V412	V446	V592	V293	hydrophobic interaction at bis-MGD	N/A	
	K44	K94	K56	K90	K295	I37	electron transfer to Fe-S relay	N/A	
	Q335	H448	E409	E443	Q589	H290	gating proton shuttling	N/A	
	V145	V201	V198	V197	G391	V123	hydrophobic interaction with active site Arg	N/A	
	Q339	Q452	Q413	Q447	Q593	N297	hydrophobic interaction with active site Arg	N/A	

In organisms that catalyze the oxidation of formate, this reaction is a key process for obtaining energy and reducing equivalents.[578] The CO_2 formed is usually incorporated predominantly into the Calvin-Benson cycle, as in autotrophic organisms.[577] Formate is a key metabolite for bacteria, arising as a metabolic product of bacterial fermentations and functioning as a growth substrate for many microorganisms (*e.g.*, methanogens and sulfate-reducing bacteria).[600–602]

Formate is also an intermediate in the energy metabolism of several prokaryotes, and formate is used as electron donor during anaerobic respiration in these organisms. Due to the low redox potential of the CO_2/formate couple, formate can be oxidized not only through the aerobic respiratory chain, but it also can serve as an electron donor for the anaerobic reduction of fumarate (E° fumarate/succinate = +30 mV vs SHE) and nitrate (E° nitrate/nitrite = +420 mV vs SHE) or nitrite (E° nitrite/NO = +375 mV vs SHE).[582]

Some FDHs are in complex with hydrogenases, like the formate-hydrogen-lyase (FHL) systems from *E. coli*, *Pectobacterium atrosepticum,* or *Clostridium carboxidovorans.*[603–606] Physiologically, the *E. coli* FHL is a membrane-bound system involved in formate oxidation and H_2 evolution under fermentative growth conditions.[607] This system contains the formate dehydrogenase subunit FdhF, and a membrane-bound, cytoplasm-faced [NiFe]-hydrogenase (**Section 3.1**).[608] Similar coupling of FDH and hydrogenase subunits are observed in some CO_2 reductases that catalyze the reduction of CO_2 to formate with the simultaneous and direct oxidation of H_2. For example, the enzyme from *Acetobacter woodii* is a tetramer, with one Moco/[4Fe-4S] cluster subunit, two subunits with four [4Fe-4S] clusters each, and one [FeFe]-hydrogenase subunit (**Section 3.2**).[432,609] A W-containing homologue has been identified in *Thermoanaerobacter kivui*.[266]

4.2.1 Carbon Dioxide Reduction and Coupled Catalysis

A distinct class of FDH-associated enzymes are those found in methanogenic archaea that are involved in hydrogenotrophic CO_2 fixation, *en route* toward the generation of methane (CH_4).[610,611] The first enzyme involved in reductive CO_2 fixation is the enzyme formylmethanofuran dehydrogenase, which is biased toward the reduction of CO_2 and the coupling of the intermediate product formate to the C_1-carrier methanofuran without the requirement of ATP.[612,613] Furthermore, some organisms that undergo methylotrophic or aceticlastic methanogenesis have an ability to produce CO_2 as a final step, also employing a formylmethanofuran dehydrogenase.[614,615] The basis for this biochemical transformation, until recently has been largely speculative. Similar to FDHs described above,

formylmethanofuran dehydrogenases are able to coordinate a bis-MGD cofactor with either Mo or W[598,610,616–621]; the enzyme also exhibits a distinct dinuclear Zn amidohydrolase motif that is involved in the condensation of formate and methanofuran.[622] The *Methanothermobacter* strains *M. marburgensis* and *M. wolfeii* harbor distinct operons of formylmethanofuran dehydrogenase that depend on the presence of tungstate (WO_4^{2-}) or molybdate (MoO_4^{2-}).[598,616–619,623] The former is constitutively expressed in both organisms, whereby a Mo-substituted isoenzyme has been also isolated.[621,624,625] Similarly, the genome of the hyperthermophilic methanogen *Methanopyrus kandleri* encodes for two W-containing formylmethanofuran dehydrogenases, with one that is also only expressed in the presence of Se.[626] Interestingly, distinct molybdopterin dinucleotides have been characterized for formylmethanofuran dehydrogenases from *M. marburgensis*, such as coordinating a molybdopterin adenine or hypoxanthine dinucleotide.[627]

4.2.2 Oxygen Sensitivity

Most FDH enzymes characterized so far are described to be inactivated on the presence of O_2 (referred to as oxygen-sensitive enzymes).[628–631] To prevent damage by O_2 and to stabilize the enzyme, inhibitors like azide (N_3^-) or nitrate (NO_3^-) are added during the purification of the enzyme, inhibitors that are known to significantly increase the stability of most FDH enzymes.[632] FDHs that exhibit activity in the presence of O_2 with inhibitor present (referred to as oxygen-tolerant enzymes) were described for the Mo-containing enzymes from *Rhodobacter capsulatus* and *Cupriavidus necator* and the W-containing enzyme from *Desulfovibrio vulgaris* Hildenborough.[596,597,633,634] What contributes to the higher stability of some enzymes (*e.g.*, from various *Desulfovibrio* specimen[591,635–638] and *Methylobacterium extorquens*[610,639]) in the presence of O_2 without inhibitor present, while other enzymes are extremely sensitive to the exposure of O_2 (*e.g.*, *E. coli* FdhF[628]) is not known so far. While hydrogenases act as oxygenases reducing O_2 to reactive oxygen species (**Section 3.2**) or water (**Section 3.1**), the O_2 sensitivity of FDH seems to follow other molecular principles. Recently, it was shown the enzyme from *R. capsulatus* is mainly sensitive to O_2 in the absence of N_3^-.[640,641] By extended X-ray absorption fine structure (EXAFS) spectroscopy, it was revealed that the exposure of the enzyme to O_2 results in a heterogenous ligandation at the Mo ion and to the exchange of the terminal sulfido ligand by an oxo ligand.[640,641] Azide stabilizes the sulfido ligand, suggesting that N_3^- binds in vicinity to the sulfido ligand and hinders thereby the access of O_2 to the active site sulfido group.

4.2.3 Cofactor Biosynthesis and Moco Sulfuration

The biosynthetic maturation process of FDHs, in conjunction with the number of redox cofactors, is critical to obtain a bis-MGD cofactor with the correct set of ligands at the active site.[642] FDHs, in conjunction with most Mo- and W-containing enzymes coordinate multiple redox centers in addition to the prosthetic Moco or Wco.[576] The maturation of bacterial bis-MGD-containing enzymes is a complex process leading to the insertion of the bulky bis-MGD cofactor into the apoenzyme. Most of these enzymes were shown to contain a specific chaperone for the insertion of the bis-MGD cofactor.[642] FDH together with its molecular chaperone seems to display an exception to this specificity rule, since the *E. coli* chaperone FdhD has been proven to be involved in the maturation of all three FDH enzymes present in the cell.[643–645] For the FDH FdsGBAD from *R. capsulatus* the two proteins FdsC and FdsD were identified to be essential for enzyme activity, but FdsC is not a subunit of the mature enzyme.[597] While FdsD is a subunit of the $(FdsGBAD)_2$ heterodimer,[592] it has only counterparts in some O_2-tolerant FDHs.[576] While an enzyme purified in the absence of FdsD was devoid of Moco, the role of this subunit is not clear so far.[597,646] On the other hand, FdsC shares high amino acid sequence identity to *E. coli* FdhD, the chaperone for the cytosolic *E. coli* formate dehydrogenase FdhF and the two membrane-bound FDHs FdnGHI and FdoGHI from *E. coli*.[646,647] FdhD was reported to be involved in the formation of the essential terminal sulfido ligand at the Mo ion facilitating the reaction between the L-cysteine desulfurase IscS[644] and FdhF-bound bis-MGD, a mechanism which is essential to yield active FdhF.[644] Initially, it was proposed that the two cysteine residues C121 and C124 in FdhD are involved in the sulfur transfer reaction from IscS further onto the bis-MGD in FdhF. For sulfuration of bis-MGD, FdhD specifically interacts with IscS in *E. coli*. It has been suggested that IscS transfers the sulfur from L-cysteine to FdhD in form of a persulfide. Located in a conserved CXXC motif of FdhD, cysteine C121 and C124 were proposed to be involved in the sulfur transfer process from IscS to bis-MGD by Magalon and co-workers[644] as well as Walburger, Arnoux, and co-workers.[645] FdhD was co-crystallized in complex with GDP suggesting direct binding of bis-MGD to FdhD; however, it was not possible to prove that the cofactor is bound in an active form.[648] A study using *R. capsulatus* FdsC provided evidence that the cofactor is indeed bound in the active form containing the terminal sulfido ligand, which was revealed by the insertion of MGD cofactor into TMAO reductase,[646] producing an active enzyme.[647] Further, a phylogenetic study revealed that the CXXC motif is not conserved among FdhD-like chaperones and by site-directed mutagenesis it was proven that the two cysteines in the CXXC motif are not essential, putting the mechanism of the persulfide-transfer involving

FdhD as a sulfurtransferase into question.[647] It therefore remains possible that IscS directly transfers the persulfide sulfur to the Mo ion in FdhD-bound bis-MGD, notably without the involvement of additional cysteine residues. The source of electrons for the reductive cleavage of the persulfide is also unknown. Directly comparing the chaperones FdhD from *E. coli* and FdsC from *R. capsulatus* in the same study revealed that their roles in the maturation of FDH enzymes from different subgroups can be exchanged.[647] In summary, the binding of sulfido-containing bis-MGD to the chaperone is a common characteristic of FdhD-like proteins and ensures insertion of a competent active site cofactor for catalysis.

4.3 Role of the Sulfido- and Amino Acid Ligands

The first coordination sphere at the active site cofactor of FDHs includes the sulfido ligand and the cysteine or selenocysteine ligand (**Figure 41A**).[629,649] The sulfido group was shown to act as a hydride acceptor from formate in the reaction of formate oxidation.[650] This reaction step was mainly established by electron paramagnetic resonance (EPR) spectroscopy, showing that the C_α hydrogen atom from formate is transferred to a ligand in the first coordination sphere, which resulted in the binding of a strongly coupled and solvent exchangeable proton, with a hyperfine constant of 20–30 MHz in the Mo^V state.[651–653] Similar hyperfine constant values were determined in the Mo-containing enzyme xanthine oxidase, where a hydrogen is transferred from the C_8 hydrogen atom of xanthine to the active site sulfido ligand at the Mo ion.[654] Similar to xanthine oxidase, previous studies showed that FDHs exhibited sensitivity to cyanide (CN^-).[655] In a recent X-ray absorption spectroscopy (XAS) study on *R. capsulatus* FDH it was shown that the sulfido ligand was lost forming thiocyanate (SCN^-), which represents another similarity with xanthine oxidase.[640] The resulting desulfo enzyme harbors an oxo group in place of the sulfido group, which is not able to act as hydride acceptor. However, examples of FDHs that exhibit apparent or partial CN^- insensitivity are known, including W-FDHs from *D. desulfuricans*[651,656] and *D. gigas*[638], as well as the W-containing isoenzyme of formylmethanofuran dehydrogenase from *M. marburgensis*.[618]

Formate dehydrogenases catalyze formate oxidation and CO_2 reduction at the bis-MGD with the involvement of amino acids in the first and second coordination sphere. Of these, the first amino acid of importance is the cysteine or selenocysteine residue that serves as a covalent linkage between the bis-MGD cofactor and the protein (**Figure 41**). Given the diversity of FDHs, the preference to encode for a selenocysteine residue has been discussed to reflect an evolutionary advantage. Selenium as being essential for bacteria was discovered by Pinsent

in 1954[657], whereby the activity of FDH was dependent on the presence of Se, and was later discovered to be in the form of a single SeCys residue encoded by the unique codon UGA.[658] Selenocysteine offers a lowered pK_a and improved performance as a nucleophile relative to cysteine that results in enzyme exhibiting an increased catalytic reactivity.[659] These considerations compelled Axley and co-workers in the early 1990s to investigate the essentiality of the residue in *E. coli* FdhF, by performing site-directed mutagenesis.[586] They showed that exchange of the active site selenocysteine to cysteine (U140C) in *E. coli* FdhF resulted in a reduction of k_{cat} by a factor of 300, and a decrease in $K_{M\ formate}$ relative to a constant K_M with BV as an electron acceptor (**Table 7**). While the reduction in k_{cat} is consistent with differences in chemical properties of Se vs. S, it also affected the relative affinity of the substrate formate at the active site.[586]

Despite the preliminary studies investigating the role of selenocysteine U140 in *E. coli* FdhF, the role of the amino acid ligand in catalysis is a matter of debate and not clear to date. As discussed in detail below, mainly two models exist, one in which the proteinaceous ligand remains bound to the Mo ion during catalysis and therefore has no direct role in the catalytic mechanism.[634] In the other model, the amino acid ligand is displaced from the Mo ion, thereby providing a coordination site for the substrate and it temporarily serving as a second coordination sphere ligand.[649] While in the Mo^V state of *E. coli* FdhF, it was shown that the Mo ion is hexacoordinated with the amino acid ligand[631], different data exist on the reduced Mo^{IV} state. In a reinterpretation of the crystallographic data of the formate-reduced *E. coli* FdhF enzyme it was suggested that the selenocysteine residue is dissociated from the Mo ion and shifted 12 Å away.[649] However, a recent crystal structure of the formate-reduced *D. vulgaris* Hildenborough W-FDH showed a hexacoordinated metal ion.[600] It needs to be considered that in these structures the oxidation state of the Mo/W ion is speculative (given the presence of multiple redox cofactors) and that none of the structures was solved in a high enough resolution to firmly establish the coordination of the substrate formate. On the contrary, different results have been obtained in XAS studies using different enzyme sources. In a recent study of the *R. capsulatus* enzyme it was suggested that in the Mo^V and the Mo^{VI} state the cysteine is a ligand to the Mo ion, while in the formate-reduced Mo^{IV} state (in the absence of N_3^-), the cysteine was displaced from the metal and instead a bond reflecting a Mo-O distance was present.[640] Contrary to this study, EXAFS data of the *E. coli* and *D. desulfuricans* enzymes in the oxidized and reduced states were interpreted with a hexacoordinated Mo ion.[660,661] Here, it needs to be pointed out that the data of the *E. coli* were derived in the presence of high concentrations of the inhibitor N_3^-, which influence the

binding of formate (discussed in more detail below). As for the *D. desulfuricans* enzyme the presence of the sulfido ligand is not clear, since it was not assigned by the EXAFS study.

To probe the displacement of the amino acid ligand, inhibition studies with iodoacetamide were performed, an alkylating agent that reacts with "free" thiols. For both the *E. coli* and the *R. capsulatus* enzymes an alkylation of the selenocysteine or cysteine ligand was identified, notably only in the formate-reduced and NO_3^-/N_3^- inhibited enzymes, but not in the oxidized enzyme.[586,599] However, no alkylation of the selenocysteine residue could be identified in the W-containing *D. vulgaris* enzyme.[600] The *E. coli* FdnGHI enzyme likewise is not alkylated when incubated with formate.[632] Heider and Böck speculated that this difference might be correlated to electron transfer from the reduced metal center to the [4Fe-4S] cluster and further to the final electron acceptor, since in some enzymes the Mo^V state is more stable than for other enzymes.[662] A fast reoxidation of the enzyme from the Mo^{IV} to the Mo^{VI} state might protect the enzyme from alkylation, while in enzymes with a long-lived reduced state, the amino acid ligand has a higher probability to be alkylated. In conclusion, while hexacoordination of the Mo ion in its Mo^V and Mo^{VI} states is established now, the coordination of the Mo^{IV} state needs to be clarified in future studies.

4.3.1 Amino Acids in the Second Coordination Sphere

In addition to the active site selenocysteine or cysteine residue, primary components of the second coordination sphere of all metal-containing FDHs include a highly conserved arginine and a histidine residue (**Figure 41B**) that have been proposed to ensure optimal substrate binding to and proton transfer away from the active site.[576] Site directed mutagenesis studies on *R. capsulatus* FDH revealed that in the H387M variant (equivalent to H141M in **Figure 41B**), the k_{cat} remained similar to that of wild-type enzyme, suggesting a similar orientation of H387 and M387 (**Table 7**).[599] However, in this variant, the pH optimum was lowered to 7.5 with a 19-fold increase in $K_M^{formate}$. The replacement of H387 with a lysine reduced the activity to 3% of that of the wild-type enzyme, accompanied by an increase in $K_M^{formate}$ and a shift of the pH optimum to 8.0. When R587 (equivalent to R333 in **Figure 41B**) was replaced by a lysine, retaining the positive charge of the side chain, ~30% of wild-type activity was obtained, however, accompanied by an increase in $K_M^{formate}$ and a shift in the pH optimum to 8.0 (**Table 7**). These results show that H387 influences the pH optimum of the reaction, while the drastic increase in $K_M^{formate}$ reveals a role for R587 in substrate binding at the active site.

4.3.2 Substrate Channels in the Outer Coordination Sphere

The first FDH structure characterized by X-ray diffraction (XRD) was the monomeric FdhF protein from *E. coli*, which was solved both in the oxidized (2.8 Å resolution) and formate-reduced (2.3 Å resolution) state (**Figure 43A** and **Figure 44A**).[629] The active site Mo ion was initially interpreted to carry a hydroxyl ligand; however, later the Mo-OH bond was reinterpreted as being a Mo-SH one.[649] Two other catalytically important amino acids in the active site were identified to be H141 and R333 (**Figure 41B**). These two residues are strictly conserved in all Mo- and W-containing FDHs, and their involvement in substrate binding and/or proton abstraction from the substrate has been proposed.[599] After substrate oxidation, electrons are transferred from Mo^{IV} to the nearby [4Fe-4S] cluster. Here, a conserved lysine K44 is located between one pterin ring of bis-MGD and the [4Fe-4S] cluster (**Figure 41B**), and an involvement of this residue in the electron transfer reaction has been suggested (**Figure 43A** and **Figure 44A**).[649]

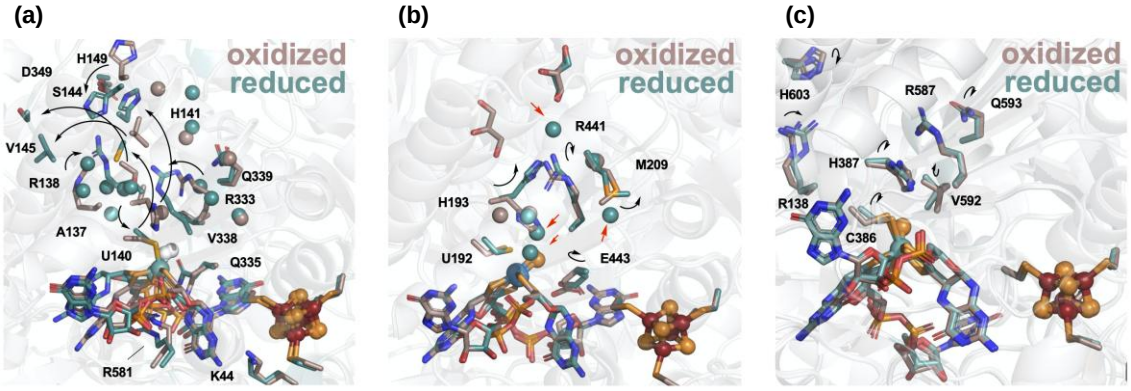

Figure 43 | Structural comparison of FDH undergoing redox change. Structures correspond to (a) *E. coli* FdhF oxidized (PDB ID: 1FDO) and formate-reduced (PDB ID: 2IV2), (b) *D. vulgaris* Hildenborough FDH oxidized (PDB ID: 6SDR) and formate-reduced (PDB ID: 6SDV), and (c) *R. capsulatus* FDH oxidized (PDB ID: 6TGA) and NADH-reduced (PDB ID: 6TG9). Participatory amino acids and bound H_2O and glycerol molecules (where appropriate) in the substrate-binding cleft of FDH are depicted in dark salmon in the oxidized state, and deep teal in the reduced state. The structural effect of specific amino acids accompanying redox changes are depicted with black arrows. The appearance of highlighted H_2O molecules in the reduced state are indicated with red arrows.

The second structure of an *E. coli* FDH enzyme is the one of FdnGHI (EcFDH-N) which was solved as a "mushroom shaped" $(\alpha\beta\gamma)_3$ heterotrimer of trimers, with subunits of 113, 32, and 21 kDa, respectively.[663] The crystal structure of FDH-N showed that the catalytic subunit of FdnG, composed of 982 amino acids, has an overall fold similar to the structure of FdhF. The substrate access funnel is opening down to the active site Mo ion, constructed of

predominantly positively charged residues thus facilitating substrate binding, and likewise appears similar to FdhF (**Figure 44B**). The Mo ion of oxidized FdnG binds the bis-MGD cofactor, while additionally coordinated by U196. A sixth ligand in the oxidized enzyme was initially modeled as a hydroxy species (at 2.2 Å), but in light of the reinterpretation of the FdhF structure, the sixth ligand is most likely a terminal sulfido species.[649] Overall the Mo coordination sphere closely resembles that seen in oxidized FdhF (**Figure 44A**), with an arginine and a histidine present in the active site, thus implying a conserved mechanism involving the same amino acids for formate oxidation.

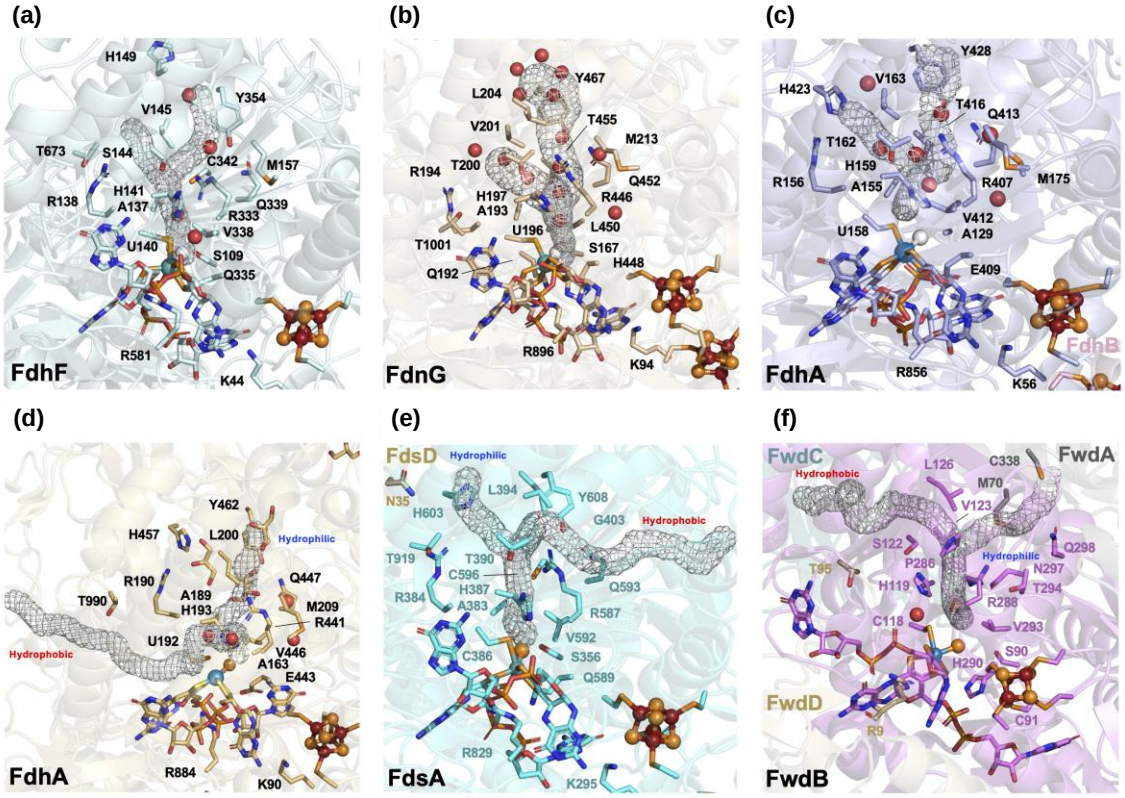

Figure 44 | Structural characterization of the active site of Mo/W–FDHs and formylmethanofuran dehydrogenases. Structures correspond to **(a)** *E. coli* FdhF (PDB ID 1FDO), **(b)** *E. coli* FdnG (PDB ID 1KQF), **(c)** *D. gigas* FdhA (PDB ID 1H0H), **(d)** *D. vulgaris* Hildenborough FdhA (PDB ID 6SDR), **(e)** *R. capsulatus* FdsA (PDB ID 6TGA), and **(f)** *M. wolfeii* formylmethanofuran dehydrogenase FwdABCD (PDB ID 5T5I). Key amino acid residues and bound H_2O molecules are depicted, where appropriate. Predicted substrate and gas channels, are noted for each enzyme; the hydrophobic channel predicted for *D. vulgaris Hildenborough* FDH was predicted from the reduced enzyme (PDB ID 6SDV). Subunits harboring the bis-MGD cofactor are labeled with black text. The hydrophilicity or hydrophobicity of the channel is noted. Channels were constructed via the CAVER plugin in PYMOL.

At the active site of *D. gigas* FDH, the W ion is bound to two MPT moieties, to a selenocysteine, and to an inorganic S or O ligand (**Figure 44C**).[636,637] The crystallographic data favor a S atom for the sixth ligand, although the resolution of the data did not permit unambiguous discrimination between O and S. As has been shown for other enzymes from the same family, the bis-MGD cofactor is buried in the protein, stabilized by an extensive network of hydrogen bonding interactions. The conserved lysine K56 bridges the pterin of the bis-MGD cofactor and the proximal [4Fe-4S] cluster. In vicinity of the buried W ion H159 and R407 are found (**Figure 44C**). Formate access to the active site could be facilitated by a channel of charged residues, including H159, R156, H423, H963, H376, K91, K444, K445, A587, and A407. CO_2 release from the active site might be facilitated by a hydrophobic channel, including V412, H159, W730, and Y428.

The crystal structure of the tungsten and SeCys containing FdhAB from *D. vulgaris* Hildenborough was solved in the oxidized and reduced form (**Figure 43B** and **Figure 44D**).[600] In the oxidized form, the W ion is hexacoordinated to four S atoms from the two dithiolenes, a Se atom from U192 and an indeterminate sulfur ligand (W-SH or W=S). The catalytic pocket and respective entrance channel are positively charged, and three glycerol molecules haven been modelled in this cleft. In the vicinity of the W ion there are two strictly conserved amino acids: H193, establishing a π-interaction with the Se atom of U192, and R441, which establishes a hydrogen bond with a cocrystallized glycerol molecule. A similar π-interaction is observed in the FDH from *D. gigas*, among respective residues H159, U158, and R407 (**Figure 44C**).[636] The glycerol closest to the W ion is hydrogen-bonded by S194 and H457, the second glycerol is oriented by R441, T450, and a water molecule oriented by Y462. A third glycerol is found at the channel entrance, oriented by a backbone contact including G207 and water molecules that connect with W492 and R206. These glycerol molecules probably occupy formate binding sites and may shed light on the formate shuttling mechanism.

In the formate-reduced form of FdhAB from *D. vulgaris* Hildenborough, a conformational rearrangement was observed, involving I191, U192, and H193 (**Figure 43B**).[600] The U192 C_α atom shifts up to 1.00 Å from the position occupied in the oxidized form while the Se atom remains coordinated to the W ion. Further, the catalytically relevant H193 moves away from the active site and a water molecule occupies the position of the imidazole ring, establishing a hydrogen bond with G442. Together, H193 and R441 are oriented in a *cis* conformation, relative to the *trans* orientation observed in the oxidized structure and other FDH structures.

This shift also resulted in assignment of a hydrophobic channel distinct from the hydrophilic one identified in the oxidized state (**Figure 44D**). The U192 loop shift is propagated to neighboring amino acids from different domains that promotes the tilt of the side chains of W533, F537, and F160. Overall, neither formate nor CO_2 were identified in the reduced structure, leaving the possibility that the reduced structure was solved after CO_2 release from the enzyme.

The cryogenic electron microscopy (cryo-EM) structure of *R. capsulatus* FDH revealed a 360 kDa dimer of FdsABGD heterotetramers in which the FdsD subunit is bound to the FdsA subunit (**Figure 43C** and **Figure 44E**).[592] In the oxidized structure, the active site structurally resembles that of *E. coli* FdhF with six ligands coordinated to the Mo ion represented by the two dithiolene groups of the bis-MGD molecule, the C386 ligand, and a sulfido ligand that is oriented towards V592 (**Figure 44E**). Additionally, the NADH-reduced cryo-EM structure was also solved; however, the protocol did not result in a full reduction to the Mo^{IV} state, instead the enzyme was only partially reduced to the Mo^{V} state.[592] In the Mo^{V} state, no structural changes at the bis-MGD pterin and dithiolenes were observed and C386 was present as a ligand to the Mo ion (**Figure 43C**). The inability of NADH to completely reduce the enzyme might either be dependent on unfavorable redox potentials of the cofactors for the back reaction or is based on the presence of 10 mM N_3^- that prevent complete reduction of the enzyme. Interestingly, in none of the structures clear evidence for stochiometric binding of N_3^- in any particular location of the EM map could be assigned.

Two reactant channel could be assigned in the cryo-EM structures, starting at the Mo ion and separating at the active site residue R587 into different exits (**Figure 44E**). The pore of the shorter channel is mainly formed by polar and charged residues suggesting channeling of hydrophilic substrate (*i.e.*, formate) from an entry site near FdsD to the active site. The channel-forming residues are similar to those in oxidized FdhF. The second channel bears predominantly hydrophobic residues suggesting the possibility of CO_2 transport to or away from the active site. FdhF contains a similar hydrophobic channel, which is however blocked by V145 and M157 in place of glycine residues in *R. capsulatus* FDH. Based on the positioning of R587 at the cross section of both channels, it has been suggested that this residue might control gate opening to each channel thereby facilitating efficient catalysis.[592,599] Intriguingly, the glycine residues are conserved in NAD^+-dependent FDHs while other FDHs display larger hydrophobic residues at this position.

The structural characterization of the W-containing formylmethanofuran dehydrogenase from *M. wolfeii* has provided considerable insight toward the importance of the second and outer coordination spheres in the FDH reaction (**Figure 44F**).[613] The enzyme, crystallized as a dimer and a tetramer of the FwdABCDFG heterohexamer, respectively, showed a modular composition of the catalytic subunits and 46 iron-sulfur clusters bound in the tetrameric supercomplex. Interestingly, an internal 43 Å-long hydrophilic water cavity separates the bis-MGD and the amidohydrolase active sites (**Figure 44F**). The interface of the subunits FwdB (housing the bis-MGD) and FwdA (housing the Zn_2-amidohydrolase site) that comprises the hydrophilic channel is distinct from the FdsD–FdsA interface characterized in the cryo-EM structure of *Rc*FDH.[592] However, several of the second coordination sphere residues that constitute this channel are similar, including H119, R288, N113, and N297 (*Mw*FwdA numbering). Interestingly, a H_2O molecule was found in proximity to the active site residue R288 at the interface of the hydrophobic and hydrophilic channels (**Figure 44F**). The lack of access by which exogenous formate might be expected to bind is consistent with the substantial differences in the substrate affinity of isoenzymes from *M. wolfeii* and the Mo-containing enzyme from *Methanosarcina barkeri.*[617,618]

Despite being an enzyme that is biased toward the reduction of CO_2, features of the hydrophobic channel associated with CO_2 binding are not so different relative to structurally characterized FDH counterparts (**Figure 44**). Similar to *Rc*FDH, *Dvh*FDH, and *Dg*FDH the hydrophobic channel principally begins at the interface of the active site H387 and R587 residues, (*Rc*FDH numbering) as an elaborate cavity characterized crystallographically without H_2O molecules bound.[613] While the cryo-EM map of the *Rc*FDH structure[592] does not allow for a direct comparison to assess the hydrophobicity of the channel, the predicted channel is nevertheless similar to that of the crystallographically characterized *Dv*H FDH enzyme.[600]

The hydrophilic channel was proposed to represent a conduit by which protons could be delivered to and from the bis-MGD cofactor in formylmethanofuran dehydrogenase.[622] This is insightful, with respect to clarifying the distinct, requisite pathways to deliver protons, electrons, and substrates. The proton transfer pathway starts at the active site H119 and C118 residue in vicinity of the distal pterin, whereby the protons are aided by numerous H_2O molecules toward H290 and C91 (*Mw*FwdA numbering, **Figure 44F**).[613] By comparison, other structurally characterized FDHs also exhibit residues at these positions that could in principle aid in proton shuttling to the active site. [592,600,629]

4.4 Inhibition of FDH in the First and Second Coordination Sphere

Inhibition of different FDH enzymes has been studied intensively using various inhibitors, and among them the most prominent one is N_3^-, which is an isoelectronic molecule to CO_2. Azide has been thought to be a transition analogue for the FDH reaction, and is most often used during the purification of FDHs to protect the enzyme from oxidative damage and loss of the sulfido ligand.[640] Inhibition of FDH using pseudohalides of varying electron donor strengths (e.g., N_3^-, OCN^-, NO_2^-, and NO_3^-) have been precursorily characterized in solution-based, *in vitro* assays[595,628,655,664–667]. While all inhibitors were more potent to inhibit formate oxidation, N_3^- and OCN^- are generally reported to be mixed-type inhibitors, revealing two binding sites with one being competitive and the other binding site being non-competitive. By comparison, NO_2^- and NO_3^- have been shown to be competitive inhibitors using formate as a substrate.[664] In the crystal structure of *E. coli* FdhF, NO_2^- was proposed to be coordinated to the Mo ion.[629]

Recently, in a chronoamperometry study of *E. coli* FdhF these pseudohalide inhibitors were used to study their binding to the reduced and oxidized enzyme.[668] The inhibition studies revealed that inhibitor binding is oxidation state-dependent, since potential- and formate-dependent results could be ascribed to differences in population of the oxidation state Hirst, Reisner, and co-workers concluded that N_3^-, OCN^-, and NO_3^- bind directly to a vacant coordination site of the Mo ion and that these inhibitors bind more tightly to Mo^{VI} than to Mo^{IV}.[668] In addition, it further was suggested that the selenocysteine residue in *E. coli* FdhF has to dissociate from the Mo ion to generate the vacant position to which the inhibitors can bind.

4.5 The Catalytic Mechanism of Formate Oxidation

While metal-dependent FDH enzymes have been studied for several decades and the *E. coli* FdhF enzyme was among the first molybdoenzymes to be crystalized[629], details of the reaction mechanism, involving the first and second coordination sphere remain poorly understood, and the catalytic mechanism of formate oxidation is still unclear. As will be described below, the numerous mechanisms proposed for FDH reflect a lack in clarity of the coordination environment and oxidation state of the bis-MGD cofactor. Overall, the formate oxidation mechanism is believed to be similar between Mo-containing and W-containing FDHs.

To form CO_2 from formate, FDH enzymes have to catalyze the transfer of one proton and two electrons. Currently, it is assumed that this reaction is not an O atom transfer reaction, as

characteristic of many Mo/W-bis-MGD family enzymes.[584] It has been proposed that the reaction product is CO_2 rather than bicarbonate (HCO_3^-), the product expected in an O atom transfer mechanism. This assumption was first proposed by Thauer and co-workers in 1975 in the characterization of the FDH from *Clostridium pasteurianum*[669] and has been supported in 1998 by Khangulov and co-workers on *Ec*FDH–H by determining the product formation using of ^{13}C-labeled formate in ^{18}O-enriched water.[650]

A recent study by Fourmond and co-workers applied an electrochemical approach on the *Dvh*FDH enzyme to confirm that the substrate of FDHs for the backreaction of CO_2 reduction is CO_2 rather than HCO_3^-.[593] The method consisted in monitoring the changes in activity that occur during the slow relaxation of the equilibrium between CO_2 and bicarbonate.[593] However, as already pointed out in 1968 by Benedict, Cooper, and co-workers[670], it still remains possible that these observations are rather a reflection of the binding of the preferred molecule to the active site, rather than what is happening directly at the active site (*i.e.*, catalysis). It therefore might be possible that a charged HCO_3^- molecule is hindered from entering the active site *via* the hydrophobic channel, while CO_2 could enter easily. At the active site cofactor, CO_2 then could react with H_2O to form HCO_3^-, which would provide the substrate for the reaction of CO_2 reduction. This option has so far been neglected in most studies and should be considered, since in some structures a water molecule has been identified in the active site bound in vicinity to the conserved arginine residue, as discussed above (**Figure 44**). It also needs to be considered that $H_2{}^{18}O$ exchange in the active site of the enzyme might be slow and therefore the reason why Khangulov and co-workers did not find ^{18}O-labeled CO_2 in their approach.[650] In this respect, approaches that factor second and outer coordination sphere effects regarding CO_2 production or formate diffusion would provide significant insight toward clarifying the formate oxidation/CO_2 reduction mechanism.

Overall, on the basis of different experimental data and theoretical calculations, different catalytic mechanisms for FDHs have been proposed, which we want to describe in more detail (**Figure 45**). As explained above, a central question is whether the amino acid ligand (selenocysteine or cysteine) remains coordinated to the Mo- or W metal during catalysis or whether it dissociates to provide a vacant site for substrate binding. Further questions relate to the involvement of the second coordination sphere residues that also serve a critical role in the reaction mechanism.

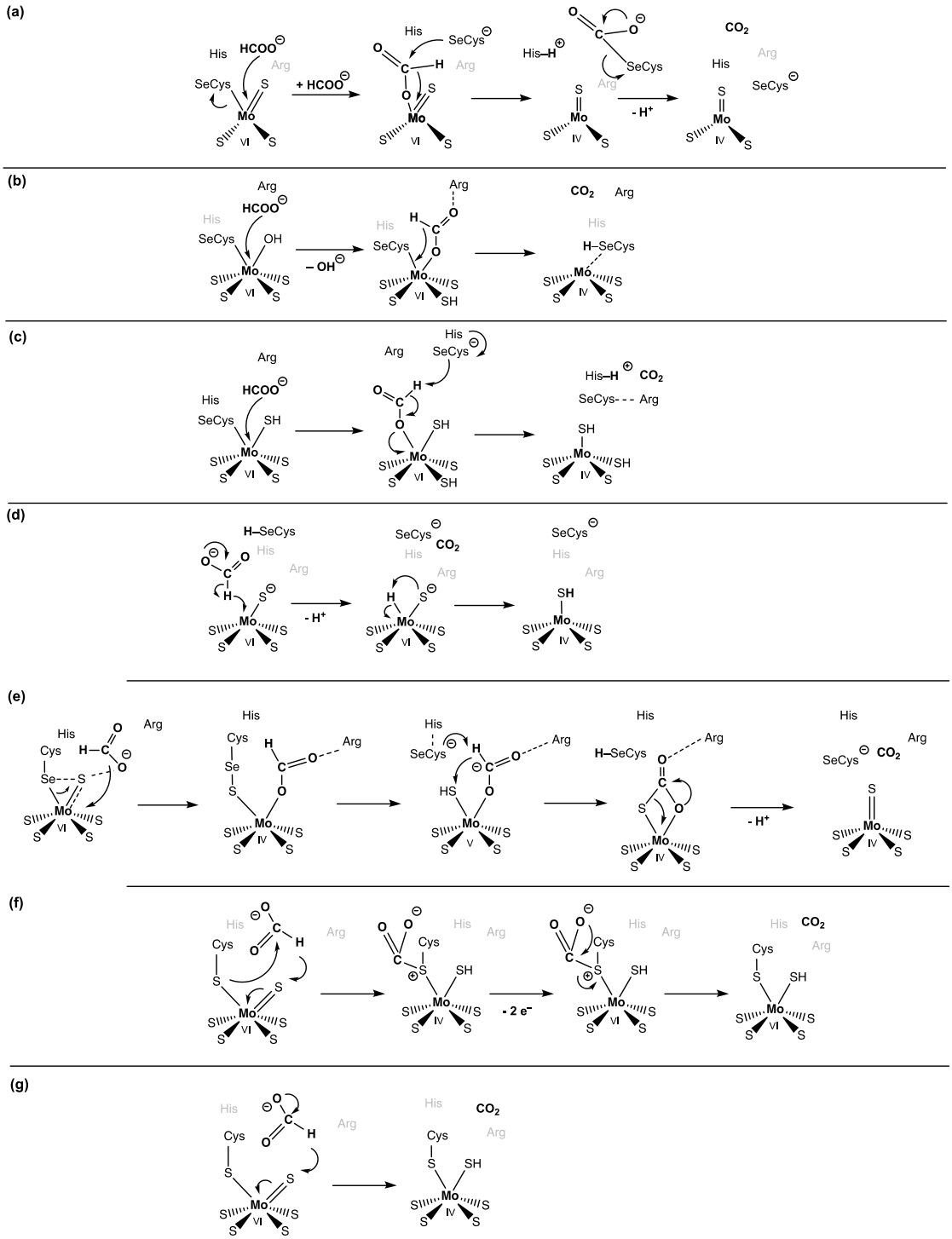

Figure 45 | Proposed reaction mechanisms for formate oxidation by FDH enzymes. (a) Mechanism proposed by Heider and Böck in 1993; **(b)** Mechanism proposed by Sun and co-workers in 1997; **(c)** Mechanism proposed by Raaijmakers and Romao in 2006; **(d)** Mechanism proposed by Cerqueira, Gonzales, Moura, and co-workers in 2011; **(e)** Mechanism proposed by Zampella and co-workers in 2012; **(f)** Mechanism proposed by Dong and Ryde in 2018. **(g)** Mechanism proposed by Hille and co-workers in 2016; Details are given in the text. Active site residues without a defined role in an individual mechanism are depicted in gray.

The first mechanism was proposed by Heider and Böck in 1993, before the crystal structure of *E. coli* FdhF was described (**Figure 45A**).[662] In this mechanism, the binding of only one pterin ligand is proposed (the existence of two dithiolene MPT groups as ligands to the metal ion were first observed in the crystal structure of the *Pyrococcus furiosus* W-containing aldehyde-ferredoxin-oxidoreductase in 1995),[671] one oxo ligand, and the fifth ligand being the selenocysteine residue. The authors suggested that binding of formate to the active site displaces the selenocysteine ligand from the Mo ion and the selenide then initiates formate oxidation by a nucleophilic attack to the Mo-bound formyl group. Carboxyl transfer to the selenocysteine residue would releases CO_2 in the next step. Following the first crystal structure of *E. coli* FdhF solved by Sun and co-workers in 1997[629] and concurrent XAS studies,[660] it was suggested that the Mo ion is coordinated by a hydroxyl group instead of a terminal sulfur atom (**Figure 45B**). The subsequent identification of a terminal sulfido group in the first coordination sphere of Mo and the observation that the loop containing U140 was shifted away (12 Å) from the Mo ion in the formate-reduced *E. coli* FdhF led to a reformulation of that mechanism (**Figure 45C**).[649] Romao and Raaijmakers suggested that upon formate binding to the active site, U140 is displaced from the Mo ion. After formate binding to the Mo ion through an O atom, The U140 selenol anion (Se^-, with R333 as counter ion) would deprotonate formate at the C_α atom and two electrons are transferred to the metal center simultaneously to form Mo^{IV}. Subsequently, the proton is transferred to H141, which changes its conformation in the reduced enzyme. After CO_2 release and rebinding of the selenocysteine ligand, the Mo ion is in a hexacoordinated form, with the sulfido group as the axial ligand.[660] The catalytic cycle would be completed with the oxidation of Mo^{IV} to Mo^{VI}, *via* intramolecular electron transfer to the [4Fe-4S] center. Theoretical calculations of the activation energy for C–H bond cleavage showed that the proton abstraction is much more favored with an unbound selenocysteine (19 kcal/mol compared to 36 kcal/mol for bound selenocysteine). In this mechanistic proposal, the conserved arginine R133 facilitates formate binding and histidine H141 acts as the final proton acceptor.[649] The terminal sulfido ligand of the Mo ion, on the contrary, would have no active role in formate oxidation.

Another mechanism was proposed based on theoretical calculations involving selenocysteine dissociation from the Mo ion through a ‘sulfur shift’ (**Figure 45D**).[656] In this mechanism, Cerqueira, Gonzales, Moura, and co-workers proposed that the oxidized enzyme is hexacoordinated by the two MGD molecules plus the selenocysteine and the terminal sulfido

group. When formate enters the active site, oriented by the positively charged arginine (*e.g.*, R333 in *E. coli* FdhF the repulsive environment generated would trigger a ligand shift to yield a Mo-S-SeCys moiety. This would create a vacant position to which the formate could bind. Subsequently, the S-SeCys bond is cleaved and the selenol anion abstracts the formate C_α proton (analog to the model in **Figure 45C**). Carbon dioxide is subsequently released. The catalytic cycle would be completed with the oxidation of Mo^{IV} to Mo^{VI} via intramolecular electron transfer to the [4Fe-4S] center and deprotonation of the selenocysteine residue. In the absence of formate, the selenocysteine-containing loop (*e.g.*, V139, U140, and H141 in *E. coli* FdhF, see **Figure 43A**) is reoriented, and the Mo-S-SeCys bond reformed. This proposal[656] is in agreement with the increased acidity of the selenocysteine side chain ($pK_a \approx 5.2$), which allows the existence of a selenol anion at physiological pH values. The alkaline pK_a value of a cysteine side chain ($pK_a \approx 8.2$) would prevent a cysteine residue having such a function. The pK_a values of both amino acids have been evoked to explain why the U140C variant of *E. coli* FdhF shows a 300-fold activity decrease.[586] In addition, the high activation energy calculated for the proton transfer from formate to selenol (SeH) is in agreement with the isotopic effect studies[650] that showed that the formate C–H bond cleavage is the rate-limiting step of the catalytic cycle. The role of the sulfido ligand, however, is also unclear in this mechanism.

An additional mechanism was proposed by Zampella and co-workers in a computational study (**Figure 45E**).[672] In this mechanism formate first binds to the Mo ion by displacing the selenocysteine group, then Mo abstracts a hydride ion from formate, giving a Mo-H species and releasing CO_2. Upon recovery of the pentacoordinated Mo ion, the sulfido group is protonated at the expense of the hydride species. In this mechanism, also the role of the sulfido group is unclear and a Mo-H bond is very unusual. Following theoretical assumptions, Dong and Ryde recently proposed an additional mechanism (**Figure 45F**).[673] They proposed that the sulfido ligand abstracts a hydride ion from the substrate, yielding Mo^{IV}-SH; however, distinct from any other mechanism, carboxylate was considered binding to the cysteine ligand, forming a thiocarbonate/cysteine zwitterion. Upon charge compensation, CO_2 leaves the enzyme and the Mo ion is oxidized back to the Mo^{VI} state. Finally, Hille and Niks proposed a mechanism that is based on experimental data[583,634] and considers binding of formate to the second coordination sphere without contacting the Mo ion (**Figure 45G**).[674] In their proposal, the sulfido ligand abstracts a hydride ion from formate, resulting in a two electron-reduced intermediate Mo^{IV}-SH, and CO_2 is released. In this mechanism, however, the (seleno-) cysteine would not be involved and the role of the metal ion is only to provide a hydride acceptor by coordinating the sulfido ligand.

4.5.1 Conversion of FDH to a Nitrate Reductase

The sulfur shift-based mechanism to oxidize formate, described above and depicted in **Figure 45A**, has also been evoked to explain the nitrate reduction catalyzed by periplasmatic nitrate reductases (NR).[656] The FDH and nitrate reductase active sites are surprisingly superimposable[599], with the later harboring a Mo ion coordinated by the two characteristic MGD molecules, one terminal sulfido group, and a cysteine sulfur atom.[675] In addition, the nitrate reductase active site also comprises conserved threonine and methionine residues (arginine and histidine, in FDH). In the oxidized active site of both enzymes, the Mo/W ion is hexacoordinated and a sulfur shift is needed to displace the selenocysteine or cysteine residue to create a vacant position for substrate binding (i.e., formate or nitrate).[590,656]

The similarities between FDH and nitrate reductases were highlighted by converting *Rc*FDH to an enzyme with nitrate reductase activity.[599] This was achieved by exchanging the histidine H387 to a methionine residue and the arginine R587 to a threonine residue, both that are conserved in nitrate reductases. In addition, an additional arginine residue was inserted to the active site of *Rc*FDH and this enzyme variant showed bis-MGD dependent nitrate reductase activity. However, the involvement of the sulfido ligand of this enzyme variant for nitrate reductase activity is not clear, since also an enzyme form containing an oxo ligand instead of the sulfido ligand was able to reduce nitrate.[599] Nitrate reductases catalyzes the typical O atom transfer mechanism characteristic for all other molybdoenzymes.[675]

4.5.2 Second and Outer Coordination Sphere Effects on Electron Transfer

In addition to the active site Mo/W ion, the sulfido ligand, and active site residues involved in CO_2 reduction and formate oxidation of FDH and formylmethanofuran dehydrogenases, additional components are critical toward the catalytic activity. For example, a feature common to all FDHs and formylmethanofuran dehydrogenases is the coordination of a [4Fe-4S] cluster that is within electron channeling distance to the bis-MGD cofactor (**Figure 41**). For all FDH enzymes identified to date, a [4Fe-4S] cluster is within 12 Å of the Mo/W ion, and within 6 Å of the proximal pterin of the bis-MGD (**Figure 44**).[592,600,622,663,676,677] This iron-sulfur cluster is proposed to be the entry point of the electron transfer pathway by which electrons that are generated from formate oxidation or are needed for CO_2 reduction are passed along, respectively. Reduction of this $[4Fe\text{-}4S]^{2+/+}$ cluster has been observed by EPR spectroscopy, using either formate or dithionite as a reductant. These are typically conditions by which the bis-MGD cofactor can also become reduced to a Mo^{V}/W^{V} oxidation state, which complicated the spectral analysis. Early characterization work of FDH from

Methanobacterium formicicum to differentiate the [4Fe-4S] cluster from the Mo^{V}/W^{V} signal showed that this cluster had *g*-values of 2.047, 1.948, and 1.911[652,653]; however, it should be noted that this FDH also can bind a [2Fe-2S] cluster whose g-values would overlap.[576] By comparison, reduction of the proximal [4Fe-4S] cluster in *Ec*FDH–H (an FDH that coordinates only one [4Fe-4S] cluster) gave a similar assignment (*g*-values of 2.045, 1.957, and 1.840). Similar assignments have been made for the corresponding iron-sulfur clusters for several FDHs by which EPR spectral data is available.[650]

As a participatory component in the redox events catalyzed by the bis-MGD cofactor, perhaps it is not surprising that communication with the proximal [4Fe-4S] cluster is essential for the catalytic reaction. However, there are few examples of FDHs by which concomitant catalytic activity and loss of the proximal [4Fe-4S] cluster has been shown. For example, a EPR spectral characterization of the FDH from *C. necator* FDH has shown that under conditions by which the [4Fe-4S] cluster is reduced and the bis-MGD is poised in the paramagnetic Mo^{V} state, electron-electron spin coupling between the two paramagnetic centers occurs, primarily reflected in the loss of sharpness of the Mo(V)-based ^{1}H hyperfine splitting.[634] As EPR spectroscopy cannot characterize the diamagnetic oxidation states of the bis-MGD cofactor and iron-sulfur cluster, a parallel, multifaceted spectroscopic approach is required to identify all oxidation states.

In addition to participation of the proximal [4Fe-4S] cluster in the catalytic activity of the bis-MGD cofactor, an additional, undercharacterized aspect of FDH catalysis relates to the two molybdopterin guanine dinucleotide ligands that coordinate the Mo/W ion. These relatively large, pterin-based ligands are non-innocent and redox active, meaning that they partake in the electron transfer reactions between the Mo/W ion and the proximal [4Fe-4S] cluster immediately preceding or following catalysis. By comparison, the longer [4Fe-4S] cluster–Mo/W distance (13–16 Å) observed relative to the shorter proximal [4Fe-4S]–(proximal) MGD distance (6–10 Å) supports the presumption that the proximal MGD ligand links the FDH redox events at the Mo/W ion with the iron-sulfur cluster electron conduit.[592,600,622,663,676,677] So far, all bacterial FDHs coordinate two MGD ligands at the active site; however, distinct nucleotides were identified to be bound in place of the guanine in FDH-like enzymes from archaea (e.g. formylmethanofuran dehydrogenase from *M. marburgensis*). The reason for this remains unclear so far.

5 CO Dehydrogenase

5.1 Physiological Function and Structure of CODH

CO dehydrogenases (CODHs) are gas-processing metalloenzymes that catalyze the reversible oxidation of CO to CO_2 (**Eq. 4**). There are two unrelated classes: One is a Mo-based enzyme exclusively found in aerobic carboxydotrophs.[678,679] These CODHs catalyze the reaction in the direction of CO oxidation (CO_2 release) and will not be discussed here any further. The other is a class of metalloenzymes found mainly in anaerobic bacteria and archaea hosting a Ni- and Fe-containing cofactor, which catalyze both CO oxidation and CO_2 reduction.[680]

Eq. 4 $$CO + H_2O \rightleftharpoons CO_2 + 2\,H^+ + 2\,e^-$$

Organisms such as *Rhodospirillum rubrum* (*Rr*) and *Carboxydothermus hydrogenoformans* (*Ch*) use the enzyme CODH to oxidize CO to CO_2.[681] The reaction occurs at the so-called 'C-cluster', a unique [Ni-3Fe-4S] cluster with an additional Fe ion. The enzyme is a homodimer that houses two identical C-clusters and three electron transferring metal centers: two 'B-clusters' of the [4Fe-4S] type and one 'D-cluster' located at the interface of the two monomers (**Figure 46A**). The latter is either a [4Fe-4S] cluster (*e.g.*, in *Rr*CODH) or a [2Fe-2S] cluster (*e.g.*, in CODH from *Desulvovibrio desulfuricans, Dv*).[682] In **Figure 46B**, the proposed proton transfer pathway towards the C-cluster is shown (see **Section 5.3**).

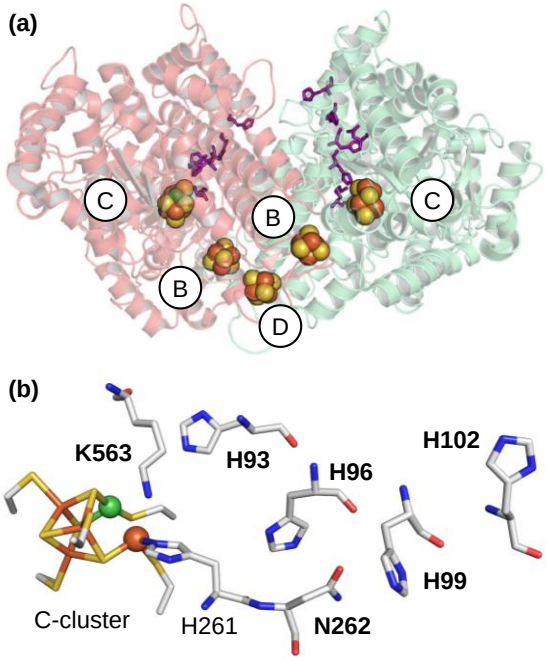

Figure 46 | Structure of CODH. Overall structure of *Ch*CODH II (PDB ID 1SU8). Each monomer of the *Ch*CODH II homodimer is represented with a different color. The spheres represent the inorganic cofactors, labelled cluster B–D. The C-cluster is the catalytic active site cofactor. The purple amino acids correspond to the putative proton transfer pathway. **(b)**

Close up view of the C-cluster and residues putatively involved in proton transfer (PDB ID 3B52).

In acetogenic bacteria such as *Moorella thermoacetica* (*Mt*) and methanogenic archaea such as *Methanosarcina barkeri* (*Mb*), a homodimeric CODH is present as part of bifunctional enzyme complexes. This may be in association with the enzyme acetyl-CoA synthase (ACS) in the ACS/CODH complex, which allows acetyl-CoA formation using a CO molecule produced by the reduction of CO_2 as part of the Wood−Ljungdahl carbon fixation pathway[683], or in an acetyl-CoA decarbonylase/synthase (ACDS) complex that degrades acetyl-CoA to form methane and CO_2.[684] The ACS/CODH complex is a large $\alpha_2\beta_2$ tetramer that associates two β CODH subunits and two α ACS subunits. The CO produced from CO_2 at the C-cluster is combined with a methyl group and coenzyme A (CoA) to form acetyl-CoA at the A-cluster of the ACS (α) subunit; *in vitro*, acetyl-CoA synthesis can also occur using CO as a substrate.[685]

Carboxydothermus hydrogenoformans (*Ch*) illustrates the diversity of possible functions of CODHs, since its genome encodes four different isoenzymes[681]: *Ch*CODH I, which is likely involved on respiration on CO; *Ch*CODH II, proposed to provide electrons to form NADPH; *Ch*CODH III, which is incorporated in a bifunctional ACS/CODH complex; and *Ch*CODH IV, proposed to be involved in resistance against O_2.[686] Eisen and co-workers originally proposed that the genome encodes a fifth CODH in *C. hydrogenoformans* [681], but the latter is more likely to be a hybrid cluster protein.

5.2 Structure and Placidity of the C-cluster

The structure of the C-cluster has been heavily debated, but the current consensus is that it comprises a [Ni-3Fe-4S] cluster coordinated to a unique fourth iron ion (Fe_u); the latter was also referred to as the 'dangling Fe' or 'ferrous component II' (**Figure 47A**).[687] The [Ni-3Fe-4S] cluster is coordinated by four cysteines as in classical [4Fe-4S] clusters including C333, C446, C476, and C526 (*Dv*CODH II numbering). The dangling Fe ion is coordinated by cysteine C295 and histidine H261. The catalytic active site is completed by histidine H93 and lysine K563 that are within hydrogen-bonding distances from the O atoms of the bound reactant, CO_2.[687] Neighboring C295, cysteine C294 and is highly conserved among CODHs. It is found in all clades except D, C1.3, and A4 of the classification proposed by Sako and co-workers[688]; however, no CODH with verified activity lacks this cysteine residue. Mutating C294 into a serine prevented the assembly of the C cluster in the case of *Mt* ACS/CODH[689],

and yielded a C-cluster devoid of Ni in the case of *Dv*CODH.[690] Exposure to air of *Dv*CODH crystals yielded an alternative form of the C-cluster in which the Ni ion occupies the position of the dangling iron, which moved a little further (**Figure 47B**). In this configuration, cysteine C295 becomes a bridging ligand between the Fe and Ni ions and C294 coordinates the dangler ion. This state is formed reversibly, as reducing the crystals gives back the 'classical' coordination of the C-cluster, and may be involved in the high resistance of *Dv*CODH to O_2 damage.[691,692] Additionally, C294 may be involved in the insertion of the active site, which would explain the lack of C-cluster when it is mutated into a serine. This hypothesis is also consistent with the fact that mutation of H261 and C295 yield an enzyme devoid of Ni.[693] Histidine H261 and C295 are ligands to the dangling Fe ion in the usual form of the C-cluster (**Figure 47B**), but bind the Ni ion in the oxidized C-cluster.

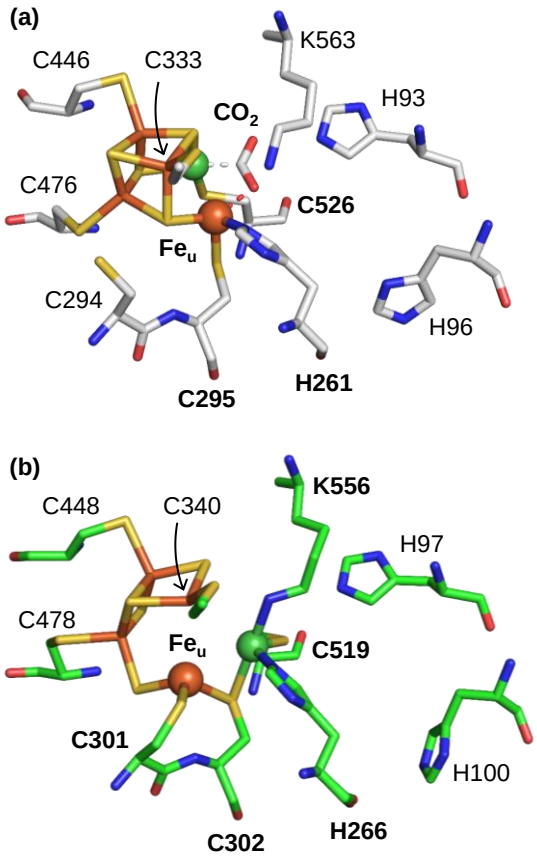

Figure 47 | Structure of the catalytic C-cluster of CODH. (a) Close up view of the CO_2-bound active site (*Ch*CODH II, PDB ID 3B52), with a representation of most of the amino acids discussed here. Fe_u refers to the 'dangling' iron ion. **(b)** View of the active site of *Dv*CODH (PDB ID 6B6W) in the oxidized, protected state (C_{ox}). The orientation is the same as in the left panel. Metal-coordinating residues are bold. Atomic coloring: Ni, green; Fe, orange; S, yellow; C, gray; O, red; N, blue.

The role of the cysteine ligands to the C-cluster was investigated by site-directed mutagenesis on *Rr*CODH. Cysteines C338, C451, C481, and C531 (corresponding to C333, C446, C476, and C526 in *Ch*CODH II) were mutated into serine or alanine residues.[694] None of the mutations affected the incorporation of Ni; however, most of the mutants lost their activity, except the C451S and C531A variant, which retained ~1.4% and 0.1% of CO oxidation activity, respectively. The exact reason for the decreased activity is not known yet, but redox effects may be involved. While the EPR signature of C_{red2} (see below) was observed in the reduced C451S variant, no C_{red1} could be detected under the redox conditions in which the wild-type *Rr*CODH usually gives C_{red1}.[694]

The C-cluster of CODHs may exist in at least three redox states: the fully oxidized, inactive, and EPR-silent 'C_{ox}' state, which is reduced at potentials of –100 mV to the paramagnetic 'C_{red1}' state (g = 2.01, 1.81, and 1.65). Below approximately –500 mV, the 'C_{red2}' state is formed (g = 1.97, 1.87, and 1.75), which is two electrons more reduced than C_{red1}. An EPR-silent, singly reduced state 'C_{int}' has been postulated to exist as a transition between C_{red1} and C_{red2}, but it was never isolated.[695] The consensus is that C_{red1}, C_{int}, and C_{red2} are catalytic intermediates.[680,696] The proposed mechanisms all assume that the structure of the CO_2-bound enzyme (**Figure 47A**) corresponds to a catalytic intermediate and that the binding of CO_2 is followed by the breaking of the bond between the C and the O coordinated to the dangling Fe ion, yielding a CO-bound Ni ion and a hydroxo ligand on the dangling Fe (**Figure 48**). The main dispute for the time being is the nature of the C_{red2} state. According to the model by Jeoung and Dobbek[687], C_{red2} corresponds to a Ni^0 state with a hydroxo ligand on the dangling Fe and no extraneous ligand on the nickel (this state is indicated by C_{red2}^* in **Figure 48**).[687] Based on DFT computations, Fontecilla-Camps, Amara, and co-workers have proposed instead that the C_{red2} state is a Ni^{2+} hydride (this state is indicated by $C_{red2}^\dagger$ in **Figure 48**), and that the CO_2-bound structure is the result of the unusual insertion of CO_2 into the Ni-H bond[697], even though insertion of CO_2 into a M-H bond usually results in the production of formate.[698] De Gioia, Greco, and co-workers have recently used density functional theory (DFT) calculations to investigate the binding of CO_2 to different redox states of the active site C-cluster; their results appear to be incompatible with the presence of a Ni-H species in C_{red2}, thus favoring C_{red2}^* over $C_{red2}^\dagger$.[699] They calculated that the binding is governed by the protonation states of histidine H93 and lysine K563 (equivalent H93 and K563 in *Ch*CODH II, **Figure 47**), and opened the possibility that CO_2 may also bind to the C_{int} redox state.

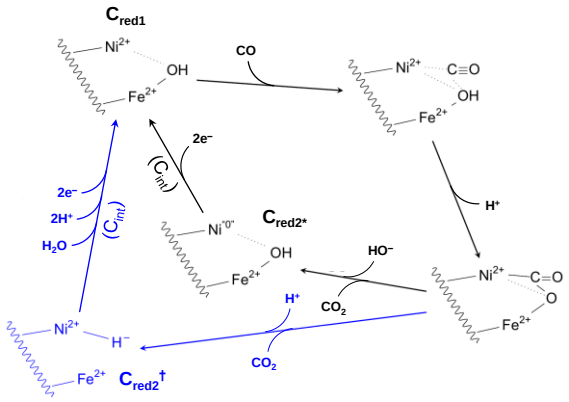

Figure 48 | Proposed mechanisms for the oxidation of CO to CO_2 by CODH. The black scheme is the original proposal by Jeoung and Dobbek.[687,696] The blue part is the modification to that scheme proposed by Fontecilla-Camps, Amara, and co-workers.[697] For the sake of clarity, we have only indicated the arrows in the direction of CO oxidation, but CO_2 reduction is supposed to follow the exact same steps in reverse order.

5.3 Substrate Access and Product Egress

The diffusion of CO and CO_2 has been investigated both in monofunctional CODH and in the bifunctional ACS/CODH complex. In ACS/CODH, the site of CO production and the site of CO utilization are over 70 Å apart. As CO does not leak to the solvent when the ACS/CODH complex produces acetyl-CoA using CO_2 as a substrate, a gastight channel was proposed that would guide the CO molecule from the C-cluster towards the A-cluster, where CO is condensed with a methyl group and coenzyme A.[700,701]

The search for cavities in the X-ray structure of ACS/CODH and the identification of Xe binding sites[685,702,703] defines the long hydrophobic channel that connects the four active sites in the tetrameric ACS/CODH complex (**Figure 49**). This channel is blocked but the A-cluster is accessible to the solvent for methyl transfer in the so-called open conformation of ACS/CODH.[703,704] Support for these channels transporting CO from the C-cluster to the A-cluster comes from the observation that mutations of the conserved alanine residues that line the putative channel in the ACS subunit of *Mt* ACS/CODH (A110C, A222L, and A265M) only have an effect of the rate of acetyl-CoA production when CO_2 is used as a substrate.[705,706] The mutations have a no significant effect on the CO oxidation activity, and only a moderate effect on the rate of acetyl-CoA production from CO. The acetyl-coA synthesis from CO is strongly inhibited by CO in wild-type ACS/CODH, but not in the three channel variants; this is explained by the possibility that part of the activity in wild-type ACS/CODH is due to CO molecules entering at the C-cluster and crossing the channel

towards the A-cluster, combined with CO crowding in the channel regulating the flow of CO from the C-cluster.[705]

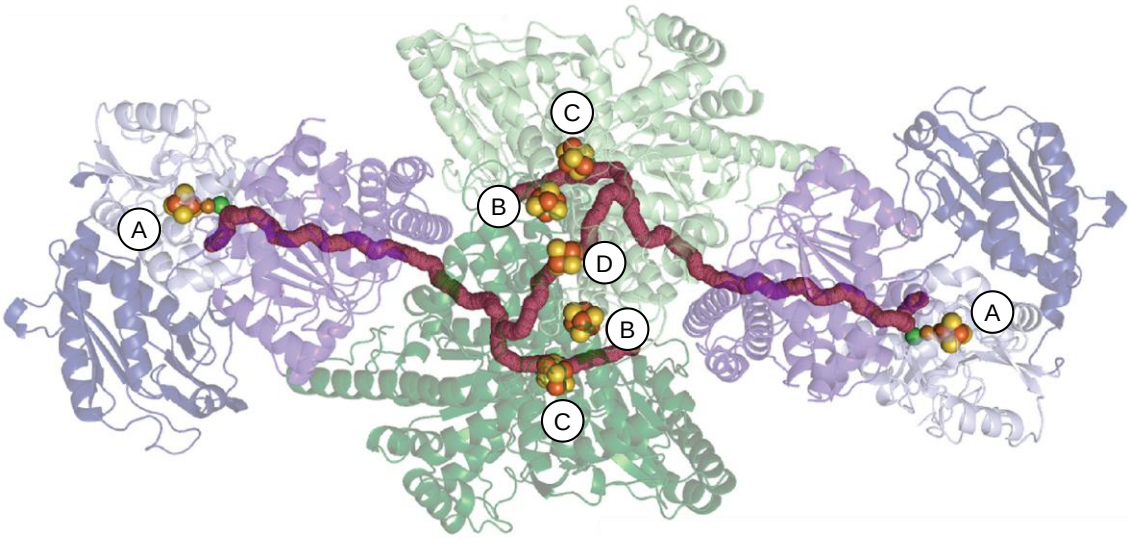

Figure 49 | Hydrophobic gas channels in CODH. Structure of the ACS/CODH from *Moorella thermoacetica* (PDB ID 2Z8Y), indicating the position of the clusters A–D, and marking the long hydrophobic channel that connects them. Reprinted (Adapted or Reprinted in part) with permission from ref. [707]. Copyright 2022 Elsevier.

The question of how CO_2 reaches the C-cluster of ACS/CODH is less clear. It has been suggested that CO_2 may enter the enzyme at the level of the A-cluster (which would involve transport against the opposite flux of CO)[704], or via the water channel along the ββ subunit interface[708], or along dynamically formed pathways that are not detected as clear cavities in the crystal structure.[709] The latter hypothesis has been investigated in molecular dynamics (MD) calculations, according to which CO_2 transport is controlled by two strictly conserved histidine residues, H113 and H116 (H93 and H96 in *Ch*CODH II, **Figure 47**). Upon reduction of CO_2, a hydrogen-bond network in the active site pocket becomes rigid enough to prevent CO from exiting the protein via the CO_2 access pathway, and directs CO from the C-cluster to the A-cluster.[709]

In the CODH subunit of Mt ACS/CODH, histidines H113 and H116, along with H119 and H122, asparagine N284 and lysine K587 were proposed to be involved in proton transfer between the solvent and the C-cluster (H93, H96, H99, H102, N262, and K563 in *Ch*CODH II, see **Figure 46B**). Variants H116A and H122A did not show catalytic turnover but activity could be restored by introducing a histidine as a neighboring amino acid.[689] Based on a series of single and multiple site-directed mutagenesis replacements, Kim and co-workers proposed

that protons first go to histidine H113 or lysine K587, then necessarily H116, then either H119, asparagine N284 or a water molecule, and finally to the solvent-exposed histidine H122.

Additional hydrophobic cavities have been identified through calculations in the monofunctional CODH from *C. hydrogenoformans* and *R. rubrum*.[710,711] Structure comparison suggests that bulky residues that are present in ACS/CODH block some of the pathways that are functional in reactant diffusion in *Ch*CODH and *Rr*CODH, and whose presence in the ACS/CODH complex would prevent effective channeling of CO from the C-cluster to the A-cluster.[703]

5.4 Diversity of CO Dehydrogenase

Figure 50 represents a sequence alignment of the main CODHs that have been studied so far, with the exception of the ACS/CODH from *Methanosarcina barkeri* (*Mb*). All amino acid residues that have been modified by mutagenesis so far are indicated using red backgrounds, and the amino acids within 8 Å of the Ni ion of the active site are framed in red. **Figure 50** shows that the environment of the active site is highly conserved, with only a few positions with non-conserved amino acids, and a few more with small variations, notably at position 293 (with isoleucine, leucine, or methionine), 311 (with asparagine, histidine, or serine), 312 (with tyrosine, serine, histidine or phenylalanine), 331 (with valine or tyrosine), 444 (with valine, alanine, or cysteine), 478 (with alanine, serine, or threonine), 529 (with asparagine or cysteine), 560 (with methionine, glutamine, or tyrosine), 561 (with histidine, serine, or threonine), and 561 with serine, histidine, or threonine). Positions 477, 479, and 559 are not conserved.

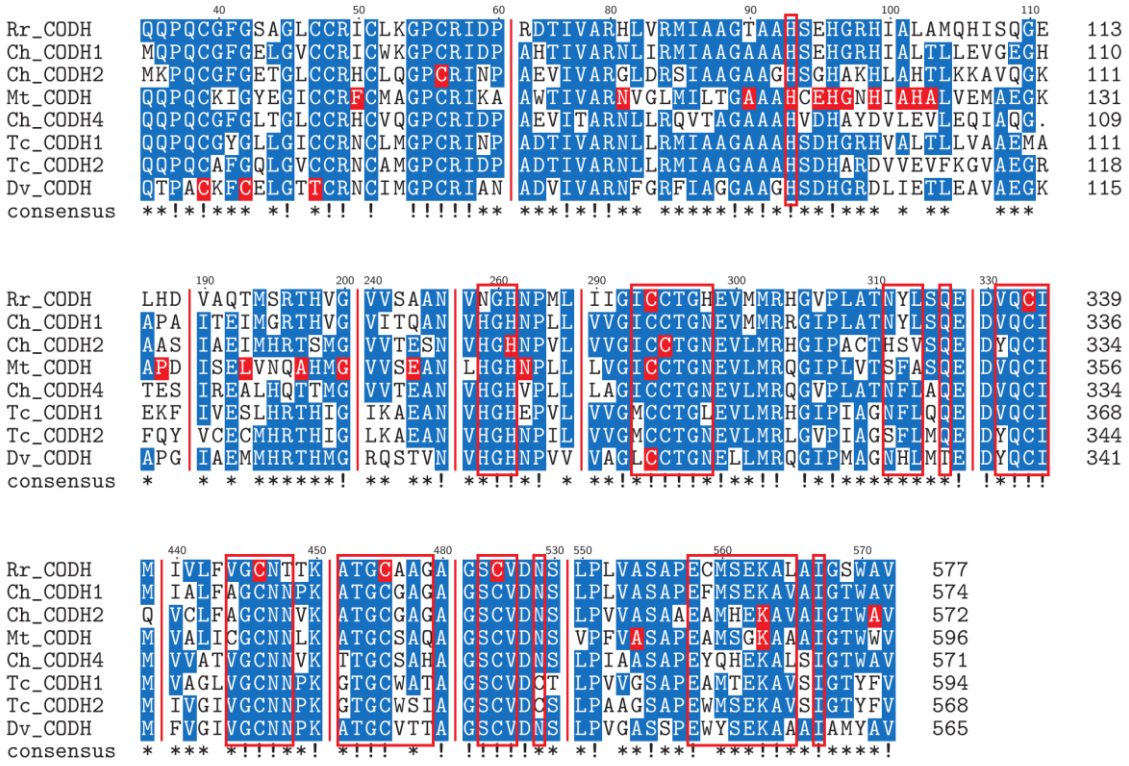

Figure 50 | Sequence alignment of the main CODHs studied so far. Conservation is indicated by a blue background. The amino acids with a red background have been modified by site-directed mutagenesis in the literature. The red frames correspond to the amino acids within 8 A of any atom from inorganic C-cluster. The numbering is that of *Ch*CODH II.

In spite of this high sequence identity, the properties of the CODH appear to change greatly from one CODH to another. Regarding the K_m for CO, the values range from 20 nM for *Ch*CODH IV to 30 μM for *Rr* CODH, with other values between 0.5–3μM for *Dv*CODH, *Ch*CODH I, and *Tc*CODH I+II from *Thermococcus sp. AM4*.[686,712–715] To date, no clear pattern has been noticed relating the sequence and the values of K_m, and no mutation has been published that affects the K_m for CO. K_m values for CO_2 reduction are much higher than those for CO oxidation, and in some cases they could not be determined because it was not possible to saturate the enzyme with CO_2. They range from 0.2 mM for *Rr*, 0.47 mM for *Tc*CODH I, to values undetermined but larger than 2 mM (*Ch*CODH I) or 7 mM (*Tc*CODH II).[714–716] Similarly to CO, no mutation yet is known to affect the K_m for CO_2.

CODHs have been said to be highly O_2-sensitive[680], but in fact the reactivity of CODHs with O_2 varies greatly, from *Rr*CODH being entirely destroyed by a 10 s exposure to O_2[717] to *Dv*CODH, losing only 70% of its activity upon aerobic purification[692], and reactivating almost fully upon reduction after exposure to O_2[691], a property that is reminiscent of the well-known reductive activation of [NiFe]-hydrogenases (**Section 3.1**) and certain [FeFe]-hydrogenases

(**Section 3.2**). *Ch*CODH IV requires much higher concentrations of O_2 than the other CODHs to lose 50% of its activity, but unlike *Dv*CODH it does not reactivate upon reduction.[686] This has been attributed to the presence of a bulky phenylalanine residue on the backside of the C-cluster (F307), in the position corresponding to S312 in *Ch*CODH II (**Figure 50**). However, *Tc*CODH I+II, which also feature a phenylalanine in the same position (F346 and F322, respectively), do not share the exceptionally high resistance of *Ch*CODH IV against O_2.[714]

Perhaps the best understood reactivity with O_2 is that of *Dv*CODH, which harbors a [2Fe-2S] cluster as the D-cluster, unlike the other CODHs characterized so far, which hold a [4Fe4S] cluster. The [2Fe-2S] type D-cluster of *Dv*CODH is at least partially responsible for the high O_2 resistance of *Dv*CODH, since upon mutation to a 'classical' [4Fe-4S] cluster, the enzyme loses the ability to be purified aerobically.[692] Deletion of the D-cluster also prevents C-cluster assembly[690], which shows that the maturation of the active site is also sensitive to either long-distance effects, or long-range electron transfer.

6 Concluding Remarks

Throughout **Sections 2–5**, we have seen how the activity of gas-processing metalloenzymes (GPMs) is defined by second and outer coordination sphere effects. As noted in **Section 1**, the optimized catalysis of GPMs has been afforded through tailored evolution of the active site cofactors from abiotic minerals and peptide 'nests' coordinating these inorganic microcompartments.[15–20] Several factors that drive second and outer coordination sphere effects in nitrogenase, hydrogenase, FDH and CODH have been described herein. It will be difficult to understand GPMs without knowledge about the structure and electronic properties of the metallic cofactors; however, we emphasize that bioinorganic chemistry must explore beyond the first coordination sphere. Concluding this article, we will highlight a number of common motifs including mass transport (**Section 6.1**), redox leveling (**Section 6.2**), and the stabilization of reactive geometries (**Section 6.3**). The developed concepts may inspire the design of biomimetic catalysts for the transformation of N_2, H_2, CO_2, and CO as critical feedstock in 'green' energy conversion.

6.1 Mass Transport

Under ambient conditions, N_2, H_2, CO_2, and CO are small volatile molecules with mostly hydrophobic properties. Such reactants approach the active site cofactor by molecular diffusion. Wolfenden and co-workers discussed how enzymatic catalysis is occasionally limited by mass transport, demonstrating the efficiency of GPMs like superoxide dismutase

and carbonic anhydrase.[718] At the example of hydrogenase, FDH, and CODH we saw that proteinaceous 'gas filters' influence the catalytic rates and substrate selectivity (**Sections 3–5**). While hydrophobic channels and pockets are routinely identified in xenon- or krypton-pressurized protein crystals[719], the collective motion of the protein fold and packing defects[720] complicate the identification of individual 'gate keepers', *i.e.*, amino acid residues of key importance. From the viewpoint of synthetic chemistry, we note that it may not be necessary to install molecular gas filters. In recent years, redox hydrogels have been demonstrated to facilitate enzymatic turnover in the presence of gaseous inhibitors, *e.g.*, by reducing O_2 before it reaches the enzyme.[721–723]

Proton transfer is another mass transport phenomenon critical to the performance of GPMs. In **Section 1**, we compared the basic reactions catalyzed by nitrogenase, hydrogenase, FDH and CODH (**Eq. 1–4**). Each reaction includes at least one proton. Protons are transferred *via* water molecules and the hydrophilic groups of a protein when hydrogen-bonded or in hydrogen-bonding distance (2.7–3.3 Å).[724] These criteria make proton transfer pathways extremely reliant on protein structural dynamics. In *Av*NifDK of the Mo-nitrogenase, second coordination sphere residues R96, Q191, and H195 (analogous to K83, Q176, and H180 in *Av*VnfDGK of the V-nitrogenase) are potentially involved in proton transfer and hydrogen bonding to catalytic intermediates that replace the bridging sulfide ligand S2B (**Figure 14**). Additionally, the homocitrate ligand may be involved[232], but any outer coordination sphere effects on proton transfer have yet to be unraveled. The cysteine residue that coordinates the active site cofactor of nitrogenase (C275 in *Av*NifDK, C257 in *Av*VnfDGK) is not involved in proton transfer, which is a marked difference from hydrogenase where cysteines of the first and second coordination sphere play key roles in proton transfer.[298] In [NiFe]-hydrogenase *Dv*MF, nickel-coordinating C546 accepts a proton after heterolytic H_2 splitting. Glutamic acid residue E34 represents a proton relay before the proton is released into bulk water (**Figure 22**). In [FeFe]-hydrogenase *Cp*1, cysteine C299 close to the distal iron ion (Fe_d) of the H-cluster functions as a relay site between cofactor and a ~20 Å proton transfer pathway including two glutamic acid residues (E279, E282), a serine residue (S319), and a small water cluster (**Figure 39**). In the primary sequence, C299 is followed by C300, which binds to the [4Fe-4S] part of the H-cluster. A similar motif can be found in *Ec*FDH where Mo-binding selenocysteine U140 is followed by histidine H141 (**Figure 42**), the later which has been suggested to play a key role in proton transfer. In the outer coordination sphere, R333 may be involved in proton transfer, but the molecular details of this event are yet to be understood.[576] Similar to FDH and nitrogenase, histidines are the most likely proton relay sites in CODH.

Based on biochemical experiments with various SDM variants of *Ch*CODH II, a trajectory between the catalytic C-cluster and bulk solvent including H93, H96, H99, H102, N262, and K563 has been proposed (**Figure 48**). Hydrogenases, on the contrary, rely on cysteine and glutamic acid residues primarily[298], resulting in an overall pK_a decrease of 2–3 compared to histidine-based proton transfer pathways. This may reflect the necessity for a tightly controlled proton transfer in systems that exclusively catalyze H_2 oxidation and proton reduction.

6.2 Redox Leveling

While proton transfer demands short distances, the probability for electrons to tunnel across distances as far as 18 Å is high enough to enable electron transfer within biologically relevant time scales.[725] Conductive wires are formed by iron-sulfur clusters in nitrogenase, hydrogenase, FDH, and CODH, guiding electrons back and forth between the active site cofactor and redox proteins like ferredoxin, flavodoxin, or cytochrome. The 'accessory' clusters of GPMs are determined by first and second coordination sphere effects to ensure directional electron transfer. For example, the replacement of a cysteine by a histidine ligand at the distal [4Fe-4S] cluster in [FeFe]-hydrogenase has a strong effect on activity.[419] In special cases, the electronic properties are flexible and controlled by the enzyme. Examples include the P-cluster in nitrogenase that changes its geometry upon reduction (**Figure 3**) or the proximal iron-sulfur cluster in O_2-tolerant [NiFe]-hydrogenases (**Figure 24**). In [FeFe]-hydrogenase, a protonation event at the backend of the H-cluster has been shown to affect the redox potential (**Figure 39**). These special cases demonstrate how enzymes modulate electron transfer in a flexible way.

Compared to the branching chains of metal clusters found in electron bifurcating/confurcating enzymes[265,266,726], the GPMs discussed in this review are wired in a straightforward fashion. The sophistication, however, lies in the spatio-temporal coupling of redox and protonation events at the active site cofactor, which allows for an accumulation of charges at mild potentials ('redox leveling'). This is clearly illustrated in the Lowe-Thorneley model for N_2 reduction (**Figure 6**) and holds true for H_2 turnover as well (**Figure 21** and **Figure 34**). The mechanistic details in FDH and CODH are less well understood, but similar proposals have been considered (**Figure 45** and **Figure 48**). How do GPMs facilitate proton-coupled electron transfer? While the electron transfer chains are hard-wired, the distance constraints of proton transfer allow for flexible fine tuning, *e.g.*, by small changes in protein structure as demonstrated in [NiFe]- and [FeFe]-hydrogenase.[298] The data discussed in this review now

suggest that metalloenzymes initiate PCET by guiding protons to the cofactor. Here, the catalytic redox reaction is induced only upon arrival of the proton (and other reactants like N_2, CO_2, or CO). As tunneling is a quantum mechanical phenomenon, the formal requirements of PCET are fulfilled.[22–24] From the viewpoint of synthetic chemistry, we note that molecular wiring may not be necessary. For example, when biomimetic Ni-complexes were deposited in a conductive hydrogel, redox events could be triggered by external electric fields.[727] At variance, the design of proton transfer pathways seems to be imperative for efficient electron transfer and catalysis.[557]

6.3 Stabilization of Reactive Geometries

Second coordination sphere effects are not limited to mass transport and redox leveling. In nitrogenase, hydrogen-bonding between H195 and R96 with bridging ligands in position S2B or between Q191 and terminal ligands (**Figure 14**) stabilizes the reactive geometry of the active site cofactor. Ligands include N_2, CO, or H. Position S3A might be catalytically relevant as well; in *Av*NifDK of the Mo-nitrogenase, a putative N_2 ligand has been identified as being hydrogen-bonded to backbone amines of G356 and G357 (**Figure 12**). In hydrogenases, potential hydrogen-bonding contacts inspired the assignment of CO and CN^- ligands. This includes S502, P478 and R479 in [NiFe]-hydrogenase *Dv*MF (**Figure 19**). Arginine 479 may also form a frustrated Lewis pair (FLP) with the Ni-Fe cofactor and has been suggested to be part of the 'outer-shell canopy', an alternative proton transfer pathway.[728] The mechanism shown in **Figure 22** favors C546 as FLP but the role of R479 in polarizing the bridging ligand cannot be excluded.[362] Arginine 96 and H195 at the nitrogenase cofactor may have a similar function (**Figure 14**). In [FeFe]-hydrogenase, the ADT ligand serves as 'internal' FLP; however, hydrogen-bonding with the adjacent C299 and M497 residues (**Figure 38**) was found to be of key importance for efficient proton transfer and catalysis. Another methionine, M353, may destabilize the μCO ligand and contribute to the flexible geometry of the diiron site (**Figure 37**). Around the proximal CN^- ligand, strong hydrogen bonding with P231 and S232 was confirmed whereas any contacts around the distal CN^- ligand remain speculation (**Figure 36**). The catalytic mechanism of FDH is controversial and various proposals co-exist (**Figure 45**). The involvement of R333 and H141 seems to be accepted, which represents a similar mechanistic element to those employed by [NiFe]-hydrogenase and nitrogenase. Histidines play important roles in CODH, across all coordination spheres. In the reduced, CO_2-bound state of *Ch*CODH II, H93 and K563 are in hydrogen-bonding distance to the substrate, stabilizing the reactive geometry (**Figure 47**). Lysine K563 is turned into a nickel ligand in the oxidized state, switching between the first

and second coordination sphere.[682] This behavior is reminiscent of C367 in [FeFe]-hydrogenase *Cb*A5H (C299 in *Cp*I) binding to Fe_d in the O_2-inhibited state (**Figure 35**). From the viewpoint of synthetic chemistry, hydrophilic groups in the second coordination sphere should have dual functions. Our data emphasize that histidines, arginines, and cysteines serve as hydrogen-bonding partners to substrates like N_2, H, CO_2, and CO, stabilizing reactive geometries. However, without contact to residues involved in proton transfer in the outer coordination sphere (**Section 6.1**), efficient catalysis cannot be achieved.

Author Information

Corresponding Author

Sven Timo Stripp – Experimental Molecular Biophysics, Department of Physics, Freie Universität Berlin, 14195 Berlin, Germany;

https://orcid.org/0000-0002-8412-0258; E-mail: sven.stripp@gmail.com

Complete contact information is available at:
https://pubs.acs.org/10.1021/acs.chemrev.xxxxxxx

Notes

The author declare no conflict of interest.

Biographies

Sven T. Stripp graduated in Biology and Biotechnology and received his Ph.D. degree from Ruhr-Universität Bochum, Germany. Afterwards, he moved to Freie Universität Berlin for postdoctoral studies on surface-enhanced vibrational spectroscopy. Since 2015 he has been a group leader in the Department of Physics where he develops *in situ* FTIR, Raman, and UV/vis spectroscopic approaches to investigate metalloenzymes under biologically relevant conditions. He habilitated in Physical Chemistry in 2021.

ORCID 0000-0002-8412-0258

Benjamin R. Duffus received his B.A. in chemistry (*cum laude*) from Concordia College (Moorhead, MN) in 2005. Following postgraduate study in synthetic inorganic chemistry at Texas A&M University, he completed his Ph.D. at Montana State University in 2014, focusing on the biosynthesis of complex iron-sulfur clusters. Since 2014, he is a postdoctoral research associate in Molecular Enzymology at the University of Potsdam, Germany. His interests blend biochemical and spectroscopic approaches toward mechanistic and biosynthetic studies of metalloenzymes, with a focus toward complex, iron-sulfur cluster molybdoenzymes.

ORCID 0000-0002-0343-4328

Vincent Fourmond received his PhD at the Université Paris Descartes in 2007. After two post-docs in the groups of Christophe Léger and Vincent Artero, he became permanent CNRS

research associate in 2011. His interests lie in using kinetics to understand the mechanism of redox metalloenzymes, and in the development of the general purpose data analysis software QSoas.

ORCID 0000-0001-9837-6214

Christophe Léger received his Ph.D. from the University of Bordeaux and was a postdoc in the group of Fraser Armstrong from 1999 to 2002. He is "Directeur de Recherche" at CNRS. His interests lie in kinetic and mechanistic studies of complex metalloenzymes.

ORCID 0000-0002-8871-6059

Silke Leimkühler received her Ph.D. in 1998 from Ruhr-Universität Bochum, Germany. After post-doctoral studies at the Duke University, USA, she returned to Germany as a research group leader to the Technical-University of Braunschweig. In 2004 she accepted a Junior-Professor position at the University of Potsdam, Germany, and since 2009 she is a full professor in Molecular Enzymology at the same institute. Her research interests focus on molybdenum cofactor biosynthesis, molybdoenzyme enzymology, and iron-sulfur cluster assembly.

ORCID 0000-0003-3238-2122

Shun Hirota received his Ph.D. from the Graduate University for Advanced Studies in Japan. After postdoctoral studies in Japan and the US, he joined Nagoya University as an assistant professor in 1996 and became an associate professor at Kyoto Pharmaceutical University in 2002. He was invited to Nara Institute of Science and Technology as a full professor in 2007. His research interests include structures, functions, and reaction mechanisms of metalloproteins.

ORCID 0000-0002-6104-1119

Yilin Hu received her Ph.D. in Biochemistry from Loma Linda University, USA. She was a postdoctoral fellow at the University of California, Irvine, and is currently Professor at the same institute. She focuses on studies related to nitrogenase mechanism and assembly, with an emphasis on the genetic manipulation of nitrogenase systems.

ORCID 0000-0002-9088-2865

Andrew J. Jasniewski received his B.S. degree from the University of Wisconsin—Madison working with Thomas Brunold on functional models of the Mn-dependent superoxide dismutase. He then moved to the University of Minnesota to study the structures and spectroscopy of nonheme diiron enzymes and related model complexes with Lawrence Que Jr., receiving his Ph.D. degree in 2017. He currently works at the University of California, Irvine with Markus Ribbe and Yilin Hu on the biochemistry and spectroscopy of nitrogenase.

ORCID 0000-0001-7614-0796

Hideaki Ogata received his Ph.D. from Kyoto University, Japan in 2003. After a short period of the postdoctoral research at Himeji Institute of Technology, he joined the Max Planck Institute for Chemical Energy Conversion, Mülheim an der Ruhr, Germany where he worked

as a group leader until 2017. He is a specially appointed associate professor at Hokkaido University, Japan. His research interests are structural and spectroscopic studies of metalloenzymes.

ORCID 0000-0002-2894-2417

Markus W. Ribbe received his Ph.D. in Microbiology from the University of Bayreuth, Germany. He was a postdoctoral fellow at the University of California, Irvine, and is now Chancellor's Professor at the same institute. He focuses on the mechanistic investigation of nitrogenase catalysis and assembly by combined biochemical, spectroscopic, and structural approaches.

ORCID 0000-0002-7366-1526

Acknowledgements

Sven T. Stripp was supported by the Deutsche Forschungsgemeinschaft (DFG) *via* the SPP 1927 priority program "Iron-Sulfur for Life" Grant No. STR1554/5-1. Jifu Duan is acknowledged for helpful comments on Table 5. Guodong Rao is acknowledged for the simulation of EPR spectra in Figure 32. The work of Christophe Leger and Vincent Fourmond was supported by Centre National de la Recherche Scientifique (CNRS), Aix Marseille Université, Agence Nationale de la Recherche (ANR-11-BSV5-0005, ANR-12-BS08-0014, ANR-14-CE05-0010, ANR-15-CE05-0020, ANR-16-CE29-0010, ANR-17-CE11-0027, ANR-18-CE05-0029), and the Excellence Initiative of Aix-Marseille University – A*MIDEX, a French "Investissements d'Avenir" programme (ANR-11-IDEX-0001-02).

The work of Silke Leimkühler was supported by the Deutsche Forschungsgemeinschaft (DFG) *via* the SPP 1927 priority program "Iron-Sulfur for Life" Grant No. E1171-15-2 and by the EXC 2008/1 (UniSysCat), funded by Germany´s Excellence Strategy – EXC 2008 – 390540038 – UniSysCat.

The work of Shun Hirota and Hideaki Ogata was supported by the Grant-in-Aid from the Japan Society for the Promotion of Science (JSPS Category B, No. JP21H02060 to SH and No. JP20H03215 to HO).

Markus W. Ribbe and Yilin Hu were supported by NIH-NIGMS grants GM67626 (to MWR and YH) and GM141046 (to YH and MWR.), which funded research related to nitrogenase assembly and catalysis, respectively. The authors were also supported by the Department of Energy grants DOE (BES) DE-SC0016510 (to YH and MWR) and DE-SC0014470 (to MWR. and YH), which funded work related to the mechanistic investigation of ammonia formation by nitrogenase engineering and hydrocarbon formation by nitrogenase hybrid systems, respectively. In addition, the authors were supported by NSF grants CHE-1904131 (to MWR and YH.) and CHE-1651398 (to YH) that supported work related to CO activation by nitrogenase and CO_2 reduction by nitrogenase Fe proteins, respectively.

References

(1) Holm, R. H.; Solomon, E. I. Preface: Bioinorganic Enzymology. *Chem. Rev.* **1996**, *96*, 2237–2238.

(2) Holm, R. H.; Solomon, E. I. Preface: Biomimetic Inorganic Chemistry. *Chem. Rev.* **2004**, *104*, 347–348.

(3) Holm, R. H.; Solomon, E. I. Introduction: Bioinorganic Enzymology II. *Chem. Rev.* **2014**, *114*, 4039–4040.

(4) McEvoy, J. P.; Brudvig, G. W. Water-Splitting Chemistry of Photosystem II. *Chem. Rev.* **2006**, *106*, 4455–4483.

(5) Vinyard, D. J.; Ananyev, G. M.; Charles Dismukes, G. Photosystem II: The Reaction Center of Oxygenic Photosynthesis. *Annu. Rev. Biochem.* **2013**, *82*, 577–606.

(6) Vinyard, D. J.; Brudvig, G. W. Progress Toward a Molecular Mechanism of Water Oxidation in Photosystem II. *Annu. Rev. Phys. Chem.* **2017**, *68*, 101–116.

(7) Babcock, G. T.; Wikström, M. Oxygen Activation and the Conversation of Energy in Cell Respiration. *Nature* **1992**, *356*, 301–308.

(8) Yoshikawa, S.; Muramoto, K.; Shinzawa-Itoh, K. Proton-Pumping Mechanism of Cytochrome c Oxidase. *Annu. Rev. Biophys.* **2011**, *40*, 205–223.

(9) Wikström, M.; Krab, K.; Sharma, V. Oxygen Activation and Energy Conservation by Cytochrome c Oxidase. *Chem. Rev.* **2018**, *118*, 2469–2490.

(10) Fontecilla-Camps, J. C.; Amara, P.; Cavazza, C.; Nicolet, Y.; Volbeda, A. Structure-Function Relationships of Anaerobic Gas-Processing Metalloenzymes. *Nature* **2009**, *460*, 814–822.

(11) Brandes, J. A.; Boctor, N. Z.; Cody, G. D.; Cooper, B. A.; Hazen, R. M.; Yoder, H. S. Abiotic Nitrogen Reduction on the Early Earth. *Nature* **1998**, *395*, 365–367.

(12) Russell, M. J. The Alkaline Solution to the Emergence of Life: Energy, Entropy and Early Evolution. *Acta Biotheor.* **2007**, *55*, 133–179.

(13) Konkena, B.; junge Puring, K.; Sinev, I.; Piontek, S.; Khavryuchenko, O.; Dürholt, J. P.; Schmid, R.; Tüysüz, H.; Muhler, M.; Schuhmann, W.; et al. Pentlandite Rocks as Sustainable and Stable Efficient Electrocatalysts for Hydrogen Generation. *Nat. Commun.* **2016**, *7*, 12269.

(14) McGlynn, S. E.; Mulder, D. W.; Shepard, E. M.; Broderick, J. B.; Peters, J. W. Hydrogenase Cluster Biosynthesis: Organometallic Chemistry Nature's Way. *Dalt. Trans.* **2009**, No. 22, 4274–4285.

(15) Nitschke, W.; McGlynn, S. E.; Milner-White, E. J.; Russell, M. J. On the Antiquity of Metalloenzymes and Their Substrates in Bioenergetics. *Biochim. Biophys. Acta - Bioenerg.* **2013**, *1827*, 871–881.

(16) Russell, M. J.; Nitschke, W.; Branscomb, E. The Inevitable Journey to Being. *Philos. Trans. R. Soc. B Biol. Sci.* **2013**, *368*, 20120254.

(17) Sousa, F. L.; Thiergart, T.; Landan, G.; Nelson-Sathi, S.; Pereira, I. A. C.; Allen, J. F.; Lane, N.; Martin, W. F. Early Bioenergetic Evolution. *Philos. Trans. R. Soc. B Biol. Sci.* **2013**, *368*.

(18) Milner-White, E. J.; Russell, M. J. Sites for Phosphates and Iron-Sulfur Thiolates in the First Membranes: 3 to 6 Residue Anion-Binding Motifs (Nests). *Orig. Life Evol. Biosph.* **2005**, *35*, 19–27.

(19) Milner-White, E. J.; Russell, M. J. Predicting the Conformations of Peptides and Proteins in Early Evolution. *Biol. Direct* **2008**, *3*, 3.

(20) Hanscam, R.; Shepard, E. M.; Broderick, J. B.; Copié, V.; Szilagyi, R. K. Secondary Structure Analysis of Peptides with Relevance to Iron–Sulfur Cluster Nesting. *J. Comput. Chem.* **2019**, *40*, 515–526.

(21) Beinert, H.; Holm, R. H.; Münck, E. Iron-Sulfur Clusters: Nature's Modular,

Multipurpose Structures. *Science* . **1997**, *277*, 653–659.
(22) Dempsey, J. L.; Winkler, J. R.; Gray, H. B. Proton-Coupled Electron Flow in Protein Redox Machines. *Chem. Rev.* **2010**, *110*, 7024–7039.
(23) Warren, J. J.; Tronic, T. A.; Mayer, J. M. Thermochemistry of Proton-Coupled Electron Transfer Reagents and Its Implications. *Chem. Rev.* **2010**, *110*, 6961–7001.
(24) Hammes-Schiffer, S. Proton-Coupled Electron Transfer: Moving Together and Charging Forward. *J. Am. Chem. Soc.* **2015**, *137*, 8860–8871.
(25) Banerjee, R.; Lipscomb, J. D. Small-Molecule Tunnels in Metalloenzymes Viewed as Extensions of the Active Site. *Acc. Chem. Res.* **2021**, *54*, 2185–2195.
(26) Winkler, M.; Esselborn, J.; Happe, T. Molecular Basis of [FeFe]-Hydrogenase Function: An Insight into the Complex Interplay between Protein and Catalytic Cofactor. *Biochim. Biophys. Acta* **2013**, *1827*, 974–985.
(27) Gray, H. B.; Winkler, J. R. Electron Transfer in Proteins. *Annu. Rev. Biochem.* **1996**, *65*, 537–561.
(28) Mulder, D. W.; Peters, J. W.; Raugei, S. Catalytic Bias in Oxidation–Reduction Catalysis. *Chem. Commun.* **2021**, *57*, 713–720.
(29) Fourmond, V.; Plumeré, N.; Léger, C. Reversible Catalysis. *Nat. Rev. Chem.* **2021**, *5*, 348–360.
(30) Zhang, X.; Ward, B. B.; Sigman, D. M. Global Nitrogen Cycle: Critical Enzymes, Organisms, and Processes for Nitrogen Budgets and Dynamics. *Chem. Rev.* **2020**, *120*, 5308–5351.
(31) Logan, J. A. Nitrogen Oxides in the Troposphere: Global and Regional Budgets. *J. Geophys. Res. Ocean.* **1983**, *88*, 10785–10807.
(32) Liaw, Y. P.; Sisterson, D. L.; Miller, N. L. Comparison of Field, Laboratory, and Theoretical Estimates of Global Nitrogen Fixation by Lightning. *J. Geophys. Res. Atmos.* **1990**, *95*, 22489–22494.
(33) Cleveland, C. C.; Townsend, A. R.; Schimel, D. S.; Fisher, H.; Howarth, R. W.; Hedin, L. O.; Perakis, S. S.; Latty, E. F.; Von Fischer, J. C.; Elseroad, A.; et al. Global Patterns of Terrestrial Biological Nitrogen (N2) Fixation in Natural Ecosystems. *Global Biogeochem. Cycles* **1999**, *13*, 623–645.
(34) Noxon, J. F. Atmospheric Nitrogen Fixation by Lightning. *Geophys. Res. Lett.* **1976**, *3*, 463–465.
(35) Noxon, J. F. Tropospheric NO2. *J. Geophys. Res. Ocean.* **1978**, *83*, 3051–3057.
(36) Darwent, B. deB. *Bond Dissociation Energies in Simple Molecules*; U.S. National Bureau of Standards: [Washington], 1970.
(37) Raymond, J.; Siefert, J. L.; Staples, C. R.; Blankenship, R. E. The Natural History of Nitrogen Fixation. *Mol. Biol. Evol.* **2004**, *21*, 541–554.
(38) Boyd, E. S.; Hamilton, T. L.; Peters, J. W. An Alternative Path for the Evolution of Biological Nitrogen Fixation. *Front. Microbiol.* **2011**, *2*, 205.
(39) Mus, F.; Colman, D. R.; Peters, J. W.; Boyd, E. S. Geobiological Feedbacks, Oxygen, and the Evolution of Nitrogenase. *Free Radic. Biol. Med.* **2019**, *140*, 250–259.
(40) Zehr, J. P.; Capone, D. G. Changing Perspectives in Marine Nitrogen Fixation. *Science* . **2020**, *368*, eaay9514.
(41) Fan, K.; Weisenhorn, P.; Gilbert, J. A.; Shi, Y.; Bai, Y.; Chu, H. Soil PH Correlates with the Co-Occurrence and Assemblage Process of Diazotrophic Communities in Rhizosphere and Bulk Soils of Wheat Fields. *Soil Biol. Biochem.* **2018**, *121*, 185–192.
(42) Wang, C.; Zheng, M.; Song, W.; Wen, S.; Wang, B.; Zhu, C.; Shen, R. Impact of 25 Years of Inorganic Fertilization on Diazotrophic Abundance and Community Structure in an Acidic Soil in Southern China. *Soil Biol. Biochem.* **2017**, *113*, 240–249.
(43) Gaby, J. C.; Buckley, D. H. Assessment of Nitrogenase Diversity in the Environment. In *Biological Nitrogen Fixation*; 2015; pp 209–216.

(44) Noar, J. D.; Bruno-Bárcena, J. M. Azotobacter Vinelandii: The Source of 100 Years of Discoveries and Many More to Come. *Microbiology* **2018**, *164*, 421–436.
(45) Huber, H.; Thomm, M.; König, H.; Thies, G.; Stetter, K. O. Methanococcus Thermolithotrophicus, a Novel Thermophilic Lithotrophic Methanogen. *Arch. Microbiol.* **1982**, *132*, 47–50.
(46) Belay, N.; Sparling, R.; Daniels, L. Dinitrogen Fixation by a Thermophilic Methanogenic Bacterium. *Nature* **1984**, *312*, 286–288.
(47) Weidner, S.; Pühler, A.; Küster, H. Genomics Insights into Symbiotic Nitrogen Fixation. *Curr. Opin. Biotechnol.* **2003**, *14*, 200–205.
(48) Stougaard, J. Genetics and Genomics of Root Symbiosis. *Curr. Opin. Plant Biol.* **2001**, *4*, 328–335.
(49) Ribbe, M. W.; Hu, Y.; Hodgson, K. O.; Hedman, B. Biosynthesis of Nitrogenase Metalloclusters. *Chem. Rev.* **2014**, *114*, 4063–4080.
(50) Buren, S.; Jimenez-Vicente, E.; Echavarri-Erasun, C.; Rubio, L. M. Biosynthesis of Nitrogenase Cofactors. *Chem. Rev.* **2020**, *120*, 4921–4968.
(51) Jasniewski, A. J.; Lee, C. C.; Ribbe, M. W.; Hu, Y. Reactivity, Mechanism, and Assembly of the Alternative Nitrogenases. *Chem. Rev.* **2020**, *120*, 5107–5157.
(52) Seefeldt, L. C.; Yang, Z.-Y.; Lukoyanov, D. A.; Harris, D. F.; Dean, D. R.; Raugei, S.; Hoffman, B. M. Reduction of Substrates by Nitrogenases. *Chem. Rev.* **2020**, *120*, 5082–5106.
(53) Seefeldt, L. C.; Yang, Z.-Y.; Duval, S.; Dean, D. R. Nitrogenase Reduction of Carbon-Containing Compounds. *Biochim. Biophys. Acta, Bioenerg.* **2013**, *1827*, 1102–1111.
(54) Schlögl, R. Catalytic Synthesis of Ammonia—A "Never-Ending Story"? *Angew. Chemie Int. Ed.* **2003**, *42*, 2004–2008.
(55) Burgess, B. K. Substrate Reactions of Nitrogenase. In *Molybdenum Enzymes*; 1985; pp 161–219.
(56) Thorneley, R. N. F.; Lowe, D. J. Kinetics and Mechanism of the Nitrogenase Enzyme System. In *Molybdenum Enzymes*; Spiro, T. G., Ed.; Metal Ions In Biology; Wiley: New York, 1985; pp 221–284.
(57) Burgess, B. K.; Wherland, S.; Newton, W. E.; Stiefel, E. I. Nitrogenase Reactivity: Insight into the Nitrogen-Fixing Process through Hydrogen-Inhibition and HD-Forming Reactions. *Biochemistry* **1981**, *20*, 5140–5146.
(58) Jensen, B. B.; Burris, R. H. Effect of High PN2 and High PD2 on Ammonia Production, Hydrogen Evolution, and Hydrogen Deuteride Formation by Nitrogenases. *Biochemistry* **1985**, *24*, 1141–1147.
(59) Burgess, B. K.; Corbin, J. L.; Rubinson, J. F.; Li, J. g; Dilworth, M. J.; Newton, W. E. Nitrogenase Reactivity. In *Advances in Nitrogen Fixation Research: Proceedings of the 5th International Symposium on Nitrogen Fixation, Noordwijkerhout, The Netherlands, August 28 – September 3, 1983*; Veeger, C., Newton, W. E., Eds.; Springer Netherlands: Dordrecht, 1984; p 146.
(60) Hoffman, B. M.; Lukoyanov, D.; Yang, Z.-Y.; Dean, D. R.; Seefeldt, L. C. Mechanism of Nitrogen Fixation by Nitrogenase: The Next Stage. *Chem. Rev.* **2014**, *114*, 4041–4062.
(61) Einsle, O.; Rees, D. C. Structural Enzymology of Nitrogenase Enzymes. *Chem. Rev.* **2020**, *120*, 4969–5004.
(62) Van Stappen, C.; Decamps, L.; Cutsail, G. E.; Bjornsson, R.; Henthorn, J. T.; Birrell, J. A.; Debeer, S. The Spectroscopy of Nitrogenases. *Chem. Rev.* **2020**, *120*, 5005–5081.
(63) Rutledge, H. L.; Tezcan, F. A. Electron Transfer in Nitrogenase. *Chem. Rev.* **2020**, *120*, 5158–5193.
(64) Dingler, C.; Kuhla, J.; Wassink, H.; Oelze, J. Levels and Activities of Nitrogenase Proteins in Azotobacter Vinelandii Grown at Different Dissolved Oxygen

Concentrations. *J. Bacteriol.* **1988**, *170*, 2148–2152.
(65) Kim, J.; Rees, D. C. Crystallographic Structure and Functional Implications of the Nitrogenase Molybdenum–Iron Protein from Azotobacter Vinelandii. *Nature* **1992**, *360*, 553–560.
(66) Spatzal, T.; Aksoyoglu, M.; Zhang, L.; Andrade, S. L. A.; Schleicher, E.; Weber, S.; Rees, D. C.; Einsle, O. Evidence for Interstitial Carbon in Nitrogenase FeMo Cofactor. *Science* . **2011**, *334*, 940.
(67) Georgiadis, M. M.; Komiya, H.; Chakrabarti, P.; Woo, D.; Kornuc, J. J.; Rees, D. C. Crystallographic Structure of the Nitrogenase Iron Protein from Azotobacter Vinelandii. *Science* . **1992**, *257*, 1653–1659.
(68) Jasniewski, A.; Sickerman, N.; Hu, Y.; Ribbe, M. The Fe Protein: An Unsung Hero of Nitrogenase. *Inorganics* **2018**, *6*, 25.
(69) Schindelin, H.; Kisker, C.; Schlessman, J. L.; Howard, J. B.; Rees, D. C. Structure of ADP·AlF4 – Stabilized Nitrogenase Complex and Its Implications for Signal Transduction. *Nature* **1997**, *387*, 370–376.
(70) Tezcan, F. A.; Kaiser, J. T.; Mustafi, D.; Walton, M. Y.; Howard, J. B.; Rees, D. C. Nitrogenase Complexes: Multiple Docking Sites for a Nucleotide Switch Protein. *Science* . **2005**, *309*, 1377–1380.
(71) Peters, J. W.; Fisher, K.; Newton, W. E.; Dean, D. R. Involvement of the P Cluster in Intramolecular Electron Transfer within the Nitrogenase MoFe Protein. *J. Biol. Chem.* **1995**, *270*, 27007–27013.
(72) Chan, M. K.; Kim, J.; Rees, D. C. The Nitrogenase FeMo-Cofactor and P-Cluster Pair: 2.2 Å Resolution Structures. *Science* . **1993**, *260*, 792–794.
(73) Pierik, A. J.; Wassink, H.; Haaker, H.; Hagen, W. R. Redox Properties and EPR Spectroscopy of the P Clusters of Azotobacter Vinelandii MoFe Protein. *Eur. J. Biochem.* **1993**, *212*, 51–61.
(74) Smith, B. E.; Lang, G. Mössbauer Spectroscopy of the Nitrogenase Proteins from Klebsiella Pneumoniae. Structural Assignments and Mechanistic Conclusions. *Biochem. J.* **1974**, *137*, 169–180.
(75) Huynh, B. H.; Henzl, M. T.; Christner, J. A.; Zimmermann, R.; Orme-Johnson, W. H.; Münck, E. Nitrogenase XII. Mössbauer Studies of the MoFe Protein from Clostridium Pasteurianum W5. *Biochim. Biophys. Acta, Protein Struct.* **1980**, *623*, 124–138.
(76) Zimmermann, R.; Münck, E.; Brill, W. J.; Shah, V. K.; Henzl, M. T.; Rawlings, J.; Orme-Johnson, W. H. Nitrogenase X: Mössbauer and EPR Studies on Reversibly Oxidized MoFe Protein from Azotobacter Vinelandii OP Nature of the Iron Centers. *Biochim. Biophys. Acta - Protein Struct.* **1978**, *537*, 185–207.
(77) McLean, P. A.; Papaefthymiou, V.; Orme-Johnson, W. H.; Münck, E. Isotopic Hybrids of Nitrogenase. Mössbauer Study of MoFe Protein with Selective 57Fe Enrichment of the P-Cluster. *J. Biol. Chem.* **1987**, *262*, 12900–12903.
(78) Peters, J. W.; Stowell, M. H. B.; Soltis, S. M.; Finnegan, M. G.; Johnson, M. K.; Rees, D. C. Redox-Dependent Structural Changes in the Nitrogenase P-Cluster. *Biochemistry* **1997**, *36*, 1181–1187.
(79) Keable, S. M.; Vertemara, J.; Zadvornyy, O. A.; Eilers, B. J.; Danyal, K.; Rasmussen, A. J.; De Gioia, L.; Zampella, G.; Seefeldt, L. C.; Peters, J. W. Structural Characterization of the Nitrogenase Molybdenum-Iron Protein with the Substrate Acetylene Trapped near the Active Site. *J. Inorg. Biochem.* **2018**, *180*, 129–134.
(80) Mayer, S. M.; Lawson, D. M.; Gormal, C. A.; Roe, S. M.; Smith, B. E. New Insights into Structure-Function Relationships in Nitrogenase: A 1.6 Å Resolution X-Ray Crystallographic Study of Klebsiella Pneumoniae MoFe-Protein. *J. Mol. Biol.* **1999**, *292*, 871–891.
(81) Danyal, K.; Dean, D. R.; Hoffman, B. M.; Seefeldt, L. C. Electron Transfer within

Nitrogenase: Evidence for a Deficit-Spending Mechanism. *Biochemistry* **2011**, *50*, 9255–9263.
(82) Danyal, K.; Mayweather, D.; Dean, D. R.; Seefeldt, L. C.; Hoffman, B. M. Conformational Gating of Electron Transfer from the Nitrogenase Fe Protein to MoFe Protein. *J. Am. Chem. Soc.* **2010**, *132*, 6894–6895.
(83) Seefeldt, L. C.; Hoffman, B. M.; Peters, J. W.; Raugei, S.; Beratan, D. N.; Antony, E.; Dean, D. R. Energy Transduction in Nitrogenase. *Acc. Chem. Res.* **2018**, *51*, 2179–2186.
(84) Rupnik, K.; Lee, C. C.; Wiig, J. A.; Hu, Y.; Ribbe, M. W.; Hales, B. J. Nonenzymatic Synthesis of the P-Cluster in the Nitrogenase MoFe Protein: Evidence of the Involvement of All-Ferrous [Fe4S4]0 Intermediates. *Biochemistry* **2014**, *53*, 1108–1116.
(85) Kim, J.; Rees, D. C. Structural Models for the Metal Centers in the Nitrogenase Molybdenum-Iron Protein. *Science* . **1992**, *257*, 1677–1682.
(86) Lancaster, K. M.; Roemelt, M.; Ettenhuber, P.; Hu, Y.; Ribbe, M. W.; Neese, F.; Bergmann, U.; DeBeer, S. X-Ray Emission Spectroscopy Evidences a Central Carbon in the Nitrogenase Iron-Molybdenum Cofactor. *Science* . **2011**, *334*, 974–977.
(87) Wiig, J. A.; Hu, Y.; Lee, C. C.; Ribbe, M. W. Radical SAM-Dependent Carbon Insertion into the Nitrogenase M-Cluster. *Science* . **2012**, *337*, 1672–1675.
(88) Wiig, J. A.; Hu, Y.; Ribbe, M. W. Refining the Pathway of Carbide Insertion into the Nitrogenase M-Cluster. *Nat. Commun.* **2015**, *6*, 8034.
(89) Spatzal, T.; Perez, K. A.; Einsle, O.; Howard, J. B.; Rees, D. C. Ligand Binding to the FeMo-Cofactor: Structures of CO-Bound and Reactivated Nitrogenase. *Science* . **2014**, *345*, 1620–1623.
(90) Spatzal, T.; Perez, K. A.; Howard, J. B.; Rees, D. C. Catalysis-Dependent Selenium Incorporation and Migration in the Nitrogenase Active Site Iron-Molybdenum Cofactor. *Elife* **2015**, *4*, e11620.
(91) Kang, W.; Lee, C. C.; Jasniewski, A. J.; Ribbe, M. W.; Hu, Y. Structural Evidence for a Dynamic Metallocofactor during N 2 Reduction by Mo-Nitrogenase. *Science* . **2020**, *368*, 1381–1385.
(92) Sippel, D.; Einsle, O. The Structure of Vanadium Nitrogenase Reveals an Unusual Bridging Ligand. *Nat. Chem. Biol.* **2017**, *13*, 956–960.
(93) Sippel, D.; Rohde, M.; Netzer, J.; Trncik, C.; Gies, J.; Grunau, K.; Djurdjevic, I.; Decamps, L.; Andrade, S. L. A.; Einsle, O. A Bound Reaction Intermediate Sheds Light on the Mechanism of Nitrogenase. *Science* . **2018**, *359*, 1484–1489.
(94) Rohde, M.; Grunau, K.; Einsle, O. CO Binding to the FeV Cofactor of CO- Reducing Vanadium Nitrogenase at Atomic Resolution. *Angew. Chemie Int. Ed.* **2020**, *59*, 23626–23630.
(95) Rohde, M.; Laun, K.; Zebger, I.; Stripp, S. T.; Einsle, O. Two Ligand-Binding Sites in CO-Reducing V Nitrogenase Reveal a General Mechanistic Principle. *Sci. Adv.* **2021**, *7*, eabg4474.
(96) Orme-Johnson, W. H.; Hamilton, W. D.; Jones, T. L.; Tso, M. Y. W.; Burris, R. H.; Shah, V. K.; Brill, W. J. Electron Paramagnetic Resonance of Nitrogenase and Nitrogenase Components from Clostridium Pasteurianum W5 and Azotobacter Vinelandii OP. *Proc. Natl. Acad. Sci.* **1972**, *69*, 3142–3145.
(97) Yoo, S. J.; Angove, H. C.; Papaefthymiou, V.; Burgess, B. K.; Münck, E. Mössbauer Study of the MoFe Protein of Nitrogenase from Azotobacter Vinelandii Using Selective 57Fe Enrichment of the M-Centers. *J. Am. Chem. Soc.* **2000**, *122*, 4926–4936.
(98) Bjornsson, R.; Lima, F. A.; Spatzal, T.; Weyhermuller, T.; Glatzel, P.; Bill, E.; Einsle, O.; Neese, F.; DeBeer, S. Identification of a Spin-Coupled Mo(III) in the Nitrogenase

Iron-Molybdenum Cofactor. *Chem. Sci.* **2014**, *5*, 3096–3103.
(99) Morgan, T. V; Mortenson, L. E.; McDonald, J. W.; Watt, G. D. Comparison of Redox and EPR Properties of the Molybdenum Iron Proteins of Clostridium Pasteurianum and Azotobacter Vinelandii Nitrogenases. *J. Inorg. Biochem.* **1988**, *33*, 111–120.
(100) Burgess, B. K.; Lowe, D. J. Mechanism of Molybdenum Nitrogenase. *Chem. Rev.* **1996**, *96*, 2983–3012.
(101) Bjornsson, R.; Neese, F.; DeBeer, S. Revisiting the Mössbauer Isomer Shifts of the FeMoco Cluster of Nitrogenase and the Cofactor Charge. *Inorg. Chem.* **2017**, *56*, 1470–1477.
(102) Benediktsson, B.; Bjornsson, R. QM/MM Study of the Nitrogenase MoFe Protein Resting State: Broken-Symmetry States, Protonation States, and QM Region Convergence in the FeMoco Active Site. *Inorg. Chem.* **2017**, *56*, 13417–13429.
(103) Spatzal, T.; Schlesier, J.; Burger, E.-M.; Sippel, D.; Zhang, L.; Andrade, S. L. A.; Rees, D. C.; Einsle, O. Nitrogenase FeMoco Investigated by Spatially Resolved Anomalous Dispersion Refinement. *Nat. Commun.* **2016**, *7*, 10902.
(104) O'Donnell, M. J.; Smith, B. E. Electron-Paramagnetic-Resonance Studies on the Redox Properties of the Molybdenum-Iron Protein of Nitrogenase between +50 and −450 MV. *Biochem. J.* **1978**, *173*, 831–838.
(105) Watt, G. D.; Burns, A.; Lough, S.; Tennent, D. L. Redox and Spectroscopic Properties of Oxidized MoFe Protein from Azotobacter Vinelandii. *Biochemistry* **1980**, *19*, 4926–4932.
(106) Walker, J. E.; Saraste, M.; Runswick, M. J.; Gay, N. J. Distantly Related Sequences in the Alpha- and Beta-Subunits of ATP Synthase, Myosin, Kinases and Other ATP-Requiring Enzymes and a Common Nucleotide Binding Fold. *EMBO J.* **1982**, *1*, 945–951.
(107) Howard, J. B.; Rees, D. C. Structural Basis of Biological Nitrogen Fixation. *Chem. Rev.* **1996**, *96*, 2965–2982.
(108) Jang, S. B.; Seefeldt, L. C.; Peters, J. W. Insights into Nucleotide Signal Transduction in Nitrogenase: Structure of an Iron Protein with MgADP Bound. *Biochemistry* **2000**, *39*, 14745–14752.
(109) Chen, L.; Gavini, N.; Tsuruta, H.; Eliezer, D.; Burgess, B. K.; Doniach, S.; Hodgson, K. O. MgATP-Induced Conformational Changes in the Iron Protein from Azotobacter Vinelandii, as Studied by Small-Angle X-Ray Scattering. *J. Biol. Chem.* **1994**, *269*, 3290–3294.
(110) Ryle, M. J.; Seefeldt, L. C. Elucidation of a MgATP Signal Transduction Pathway in the Nitrogenase Iron Protein: Formation of a Conformation Resembling the MgATP-Bound State by Protein Engineering. *Biochemistry* **1996**, *35*, 4766–4775.
(111) Ryle, M. J.; Lanzilotta, W. N.; Seefeldt, L. C.; Scarrow, R. C.; Jensen, G. M. Circular Dichroism and X-Ray Spectroscopies of Azotobacter Vinelandii Nitrogenase Iron Protein: MgATP AND MgADP INDUCED PROTEIN CONFORMATIONAL CHANGES AFFECTING THE [4Fe-4S] CLUSTER AND CHARACTERIZATION OF A [2Fe-2S] FORM. *J. Biol. Chem.* **1996**, *271*, 1551–1557.
(112) Stephens, P. J.; McKenna, C. E.; Smith, B. E.; Nguyen, H. T.; McKenna, M.-C.; Thomson, A. J.; Devlin, F.; Jones, J. B. Circular Dichroism and Magnetic Circular Dichroism of Nitrogenase Proteins. *Proc. Natl. Acad. Sci.* **1979**, *76*, 2585–2589.
(113) Liu, J.; Chakraborty, S.; Hosseinzadeh, P.; Yu, Y.; Tian, S.; Petrik, I.; Bhagi, A.; Lu, Y. Metalloproteins Containing Cytochrome, Iron-Sulfur, or Copper Redox Centers. *Chem. Rev.* **2014**, *114*, 4366–4369.
(114) Lindahl, P. A.; Day, E. P.; Kent, T. A.; Orme-Johnson, W. H.; Münck, E. Mössbauer, EPR, and Magnetization Studies of the Azotobacter Vinelandii Fe Protein. Evidence for a [4Fe-4S]1+ Cluster with Spin S = 3/2. *J. Biol. Chem.* **1985**, *260*, 11160–11173.

(115) Yates, M. G. Electron Transport to Nitrogenase in Azotobacter Chroococcum: Azotobacter Flavodoxin Hydroquinone as an Electron Donor. *FEBS Lett.* **1972**, *27*, 63–67.
(116) Thorneley, R. N.; Deistung, J. Electron-Transfer Studies Involving Flavodoxin and a Natural Redox Partner, the Iron Protein of Nitrogenase. Conformational Constraints on Protein-Protein Interactions and the Kinetics of Electron Transfer within the Protein Complex. *Biochem. J.* **1988**, *253*, 587–595.
(117) Bennett, L. T.; Jacobson, M. R.; Dean, D. R. Isolation, Sequencing, and Mutagenesis of the NifF Gene Encoding Flavodoxin from Azotobacter Vinelandii. *J. Biol. Chem.* **1988**, *263*, 1364–1369.
(118) Duyvis, M. G.; Wassink, H.; Haaker, H. Nitrogenase of Azotobacter Vinelandii: Kinetic Analysis of the Fe Protein Redox Cycle. *Biochemistry* **1998**, *37*, 17345–17354.
(119) Setubal, J. C.; Santos, P. dos; Goldman, B. S.; Ertesvåg, H.; Espin, G.; Rubio, L. M.; Valla, S.; Almeida, N. F.; Balasubramanian, D.; Cromes, L.; et al. Genome Sequence of *Azotobacter Vinelandii*, an Obligate Aerobe Specialized To Support Diverse Anaerobic Metabolic Processes. *J. Bacteriol.* **2009**, *191*, 4534–4545.
(120) Sickerman, N. S.; Rettberg, L. A.; Lee, C. C.; Hu, Y.; Ribbe, M. W. Cluster Assembly in Nitrogenase. *Essays Biochem.* **2017**, *61*, 271–279.
(121) Hu, Y.; Corbett, M. C.; Fay, A. W.; Webber, J. A.; Hedman, B.; Hodgson, K. O.; Ribbe, M. W. Nitrogenase Reactivity with P-Cluster Variants. *Proc. Natl. Acad. Sci.* **2005**, *102*, 13825–13830.
(122) Hu, Y.; Fay, A. W.; Lee, C. C.; Ribbe, M. W. P-Cluster Maturation on Nitrogenase MoFe Protein. *Proc. Natl. Acad. Sci.* **2007**, *104*, 10424–10429.
(123) Lee, C. C.; Blank, M. A.; Fay, A. W.; Yoshizawa, J. M.; Hu, Y.; Hodgson, K. O.; Hedman, B.; Ribbe, M. W. Stepwise Formation of P-Cluster in Nitrogenase MoFe Protein. *Proc. Natl. Acad. Sci.* **2009**, *106*, 18474–18478.
(124) Rupnik, K.; Hu, Y.; Lee, C. C.; Wiig, J. A.; Ribbe, M. W.; Hales, B. J. P+ State of Nitrogenase P-Cluster Exhibits Electronic Structure of a [Fe4S4]+ Cluster. *J. Am. Chem. Soc.* **2012**, *134*, 13749–13754.
(125) Kennedy, C.; Dean, D. The NifU, NifS and NifV Gene Products Are Required for Activity of All Three Nitrogenases of Azotobacter Vinelandii. *Mol. Gen. Genet.* **1992**, *231*, 494–498.
(126) Zheng, L.; Dean, D. R. Catalytic Formation of a Nitrogenase Iron-Sulfur Cluster. *J. Biol. Chem.* **1994**, *269*, 18723–18726.
(127) Shah, V. K.; Allen, J. R.; Spangler, N. J.; Ludden, P. W. In Vitro Synthesis of the Iron-Molybdenum Cofactor of Nitrogenase. Purification and Characterization of NifB Cofactor, the Product of NIFB Protein. *J. Biol. Chem.* **1994**, *269*, 1154–1158.
(128) Sickerman, N. S.; Ribbe, M. W.; Hu, Y. Nitrogenase Cofactor Assembly: An Elemental Inventory. *Acc. Chem. Res.* **2017**, *50*, 2834–2841.
(129) Wiig, J. A.; Hu, Y.; Ribbe, M. W. NifEN-B Complex of Azotobacter Vinelandii Is Fully Functional in Nitrogenase FeMo Cofactor Assembly. *Proc. Natl. Acad. Sci.* **2011**, *108*, 8623–8627.
(130) Kang, W.; Rettberg, L. A.; Stiebritz, M. T.; Jasniewski, A. J.; Tanifuji, K.; Lee, C. C.; Ribbe, M. W.; Hu, Y. X-Ray Crystallographic Analysis of NifB with a Full Complement of Clusters: Structural Insights into the Radical SAM-Dependent Carbide Insertion During Nitrogenase Cofactor Assembly. *Angew. Chemie Int. Ed.* **2021**, *60*, 2364–2370.
(131) Rettberg, L. A.; Wilcoxen, J.; Lee, C. C.; Stiebritz, M. T.; Tanifuji, K.; Britt, R. D.; Hu, Y. Probing the Coordination and Function of Fe4S4 Modules in Nitrogenase Assembly Protein NifB. *Nat. Commun.* **2018**, *9*, 2824.
(132) Jasniewski, A. J.; Wilcoxen, J.; Tanifuji, K.; Hedman, B.; Hodgson, K. O.; Britt, R. D.;

Hu, Y.; Ribbe, M. W. Spectroscopic Characterization of an Eight-Iron Nitrogenase Cofactor Precursor That Lacks the "9th Sulfur." *Angew. Chemie Int. Ed.* **2019**, *58*, 14703–14707.
(133) Tanifuji, K.; Lee, C. C.; Sickerman, N. S.; Tatsumi, K.; Ohki, Y.; Hu, Y.; Ribbe, M. W. Tracing the 'Ninth Sulfur' of the Nitrogenase Cofactor via a Semi-Synthetic Approach. *Nat. Chem.* **2018**, *10*, 568–572.
(134) Hu, Y.; Corbett, M. C.; Fay, A. W.; Webber, J. A.; Hodgson, K. O.; Hedman, B.; Ribbe, M. W. FeMo Cofactor Maturation on NifEN. *Proc. Natl. Acad. Sci.* **2006**, *103*, 17119–17124.
(135) Yoshizawa, J. M.; Blank, M. A.; Fay, A. W.; Lee, C. C.; Wiig, J. A.; Hu, Y.; Hodgson, K. O.; Hedman, B.; Ribbe, M. W. Optimization of FeMoco Maturation on NifEN. *J. Am. Chem. Soc.* **2009**, *131*, 9321–9325.
(136) Hu, Y.; Corbett, M. C.; Fay, A. W.; Webber, J. A.; Hodgson, K. O.; Hedman, B.; Ribbe, M. W. Nitrogenase Fe Protein: A Molybdate/Homocitrate Insertase. *Proc. Natl. Acad. Sci.* **2006**, *103*, 17125–17130.
(137) Fay, A. W.; Blank, M. A.; Rebelein, J. G.; Lee, C. C.; Ribbe, M. W.; Hedman, B.; Hodgson, K. O.; Hu, Y. Assembly Scaffold NifEN: A Structural and Functional Homolog of the Nitrogenase Catalytic Component. *Proc. Natl. Acad. Sci.* **2016**, *113*, 9504–9508.
(138) Tezcan, F. A.; Kaiser, J. T.; Howard, J. B.; Rees, D. C. Structural Evidence for Asymmetrical Nucleotide Interactions in Nitrogenase. *J. Am. Chem. Soc.* **2015**, *137*, 146–149.
(139) Fisher, K.; Dilworth, M. J.; Newton, W. E. Differential Effects on N2 Binding and Reduction, HD Formation, and Azide Reduction with α-195His- and α-191Gln-Substituted MoFe Proteins of Azotobacter Vinelandii Nitrogenase. *Biochemistry* **2000**, *39*, 15570–15577.
(140) Yang, Z.-Y.; Khadka, N.; Lukoyanov, D.; Hoffman, B. M.; Dean, D. R.; Seefeldt, L. C. On Reversible H2 Loss upon N2 Binding to FeMo-Cofactor of Nitrogenase. *Proc. Natl. Acad. Sci.* **2013**, *110*, 16327–16332.
(141) Chatt, J.; Pearman, A. J.; Richards, R. L. The Reduction of Mono-Coordinated Molecular Nitrogen to Ammonia in a Protic Environment. *Nature* **1975**, *253*, 39–40.
(142) Chatt, J.; Pearman, A. J.; Richards, R. L. Relevance of Oxygen Ligands to Reduction of Ligating Dinitrogen. *Nature* **1976**, *259*, 204.
(143) Chatt, J.; Pearman, A. J.; Richards, R. L. Conversion of Dinitrogen in Its Molybdenum and Tungsten Complexes into Ammonia and Possible Relevance to the Nitrogenase Reaction. *J. Chem. Soc. Dalt. Trans.* **1977**, No. 19, 1852–1860.
(144) Chatt, J.; Pearman, A. J.; Richards, R. L. Diazenido (Iminonitrosyl) (N2H), Hydrazido(2-) (N2H2, and Hydrazido(1-) (N2H3) Ligands as Intermediates in the Reduction of Ligating Dinitrogen to Ammonia. *J. Organomet. Chem.* **1975**, *101*, C45–C47.
(145) Yandulov, D. V; Schrock, R. R. Reduction of Dinitrogen to Ammonia at a Well-Protected Reaction Site in a Molybdenum Triamidoamine Complex. *J. Am. Chem. Soc.* **2002**, *124*, 6252–6253.
(146) Yandulov, D. V; Schrock, R. R. Catalytic Reduction of Dinitrogen to Ammonia at a Single Molybdenum Center. *Science* . **2003**, *301*, 76–78.
(147) Hinnemann, B.; Nørskov, J. K. Catalysis by Enzymes: The Biological Ammonia Synthesis. *Top. Catal.* **2006**, *37*, 55–70.
(148) Tanabe, Y.; Nishibayashi, Y. Developing More Sustainable Processes for Ammonia Synthesis. *Coord. Chem. Rev.* **2013**, *257*, 2551–2564.
(149) Harris, D. F.; Lukoyanov, D. A.; Kallas, H.; Trncik, C.; Yang, Z.-Y.; Compton, P.; Kelleher, N.; Einsle, O.; Dean, D. R.; Hoffman, B. M.; et al. Mo-, V-, and Fe-

Nitrogenases Use a Universal Eight-Electron Reductive-Elimination Mechanism To Achieve N2 Reduction. *Biochemistry* **2019**, *58*, 3293–3301.
(150) Harris, D. F.; Yang, Z.-Y.; Dean, D. R.; Seefeldt, L. C.; Hoffman, B. M. Kinetic Understanding of N2 Reduction versus H2 Evolution at the E4(4H) Janus State in the Three Nitrogenases. *Biochemistry* **2018**, *57*, 5706–5714.
(151) Einsle, O.; Tezcan, F. A.; Andrade, S. L. A.; Schmid, B.; Yoshida, M.; Howard, J. B.; Rees, D. C. Nitrogenase MoFe-Protein at 1.16 Å Resolution: A Central Ligand in the FeMo-Cofactor. *Science* . **2002**, *297*, 1696–1700.
(152) Thomann, H.; Bernardo, M.; Newton, W. E.; Dean, D. R. N Coordination of FeMo Cofactor Requires His-195 of the MoFe Protein Alpha Subunit and Is Essential for Biological Nitrogen Fixation. *Proc. Natl. Acad. Sci.* **1991**, *88*, 6620–6623.
(153) DeRose, V. J.; Kim, C.-H.; Newton, W. E.; Dean, D. R.; Hoffman, B. M. Electron Spin Echo Envelope Modulation Spectroscopic Analysis of Altered Nitrogenase MoFe Proteins from Azotobacter Vinelandii. *Biochemistry* **1995**, *34*, 2809–2814.
(154) Lee, H.-I.; Thrasher, K. S.; Dean, D. R.; Newton, W. E.; Hoffman, B. M. 14N Electron Spin−Echo Envelope Modulation of the S = 3/2 Spin System of the Azotobacter Vinelandii Nitrogenase Iron−Molybdenum Cofactor. *Biochemistry* **1998**, *37*, 13370–13378.
(155) Schmid, B.; Ribbe, M. W.; Einsle, O.; Yoshida, M.; Thomas, L. M.; Dean, D. R.; Rees, D. C.; Burgess, B. K. Structure of a Cofactor-Deficient Nitrogenase MoFe Protein. *Science* . **2002**, *296*, 352–356.
(156) Fay, A. W.; Hu, Y.; Schmid, B.; Ribbe, M. W. Molecular Insights into Nitrogenase FeMoco Insertion – The Role of His 274 and His 451 of MoFe Protein α Subunit. *J. Inorg. Biochem.* **2007**, *101*, 1630–1641.
(157) Hu, Y.; Fay, A. W.; Ribbe, M. W. Molecular Insights into Nitrogenase FeMo Cofactor Insertion: The Role of His 362 of the MoFe Protein α Subunit in FeMo Cofactor Incorporation. *JBIC J. Biol. Inorg. Chem.* **2007**, *12*, 449–460.
(158) Hu, Y.; Fay, A. W.; Schmid, B.; Makar, B.; Ribbe, M. W. Molecular Insights into Nitrogenase FeMoco Insertion: TRP-444 OF MoFe PROTEIN α-SUBUNIT LOCKS FeMoco IN ITS BINDING SITE*. *J. Biol. Chem.* **2006**, *281*, 30534–30541.
(159) Kim, J.; Woo, D.; Rees, D. C. X-Ray Crystal Structure of the Nitrogenase Molybdenum-Iron Protein from Clostridium Pasteurianum at 3.0-Å Resolution. *Biochemistry* **1993**, *32*, 7104–7115.
(160) Shah, V. K.; Brill, W. J. Isolation of an Iron-Molybdenum Cofactor from Nitrogenase. *Proc. Natl. Acad. Sci.* **1977**, *74*, 3249–3253.
(161) Burgess, B. K. The Iron-Molybdenum Cofactor of Nitrogenase. *Chem. Rev.* **1990**, *90*, 1377–1406.
(162) Tanifuji, K.; Ohki, Y. Metal–Sulfur Compounds in N2 Reduction and Nitrogenase-Related Chemistry. *Chem. Rev.* **2020**, *120*, 5194–5251.
(163) Lundell, D. J.; Howard, J. B. Isolation and Partial Characterization of Two Different Subunits from the Molybdenum-Iron Protein of Azotobacter Vinelandii Nitrogenase. *J. Biol. Chem.* **1978**, *253*, 3422–3426.
(164) Hausinger, R. P.; Howard, J. B. The Amino Acid Sequence of the Nitrogenase Iron Protein from Azotobacter Vinelandii. *J. Biol. Chem.* **1982**, *257*, 2483–2490.
(165) Brigle, K. E.; Newton, W. E.; Dean, D. R. Complete Nucleotide Sequence of the Azotobacter Vinelandii Nitrogenase Structural Gene Cluster. *Gene* **1985**, *37*, 37–44.
(166) Wang, S. Z.; Chen, J. S.; Johnson, J. L. Distinct Structural Features of the .Alpha. and .Beta. Subunits of Nitrogenase Molybdenum-Iron Protein of Clostridium Pasteurianum: An Analysis of Amino Acid Sequences. *Biochemistry* **1988**, *27*, 2800–2810.
(167) Holland, D.; Zilberstein, A.; Zamir, A.; Sussman, J. L. A Quantitative Approach to Sequence Comparisons of Nitrogenase MoFe Protein α- and β-Subunits Including the

Newly Sequenced NifK Gene from Klebsiella Pneumoniae. *Biochem. J.* **1987**, *247*, 277–285.
(168) Ioannidis, I.; Buck, M. Nucleotide Sequence of the Klebsiella Pneumoniae NifD Gene and Predicted Amino Acid Sequence of the α-Subunit of Nitrogenase MoFe Protein. *Biochem. J.* **1987**, *247*, 287–291.
(169) Brigle, K. E.; Setterquist, R. A.; Dean, D. R.; Cantwell, J. S.; Weiss, M. C.; Newton, W. E. Site-Directed Mutagenesis of the Nitrogenase MoFe Protein of Azotobacter Vinelandii. *Proc. Natl. Acad. Sci.* **1987**, *84*, 7066–7069.
(170) Dean, D. R.; Brigle, K. E.; May, H. D.; Newton, W. E. Site-Directed Mutagenesis of the Nitrogenase MoFe Protein. In *Nitrogen fixation: hundred years after*; Bothe, H., de Bruijn, F. J., Newton, W. E., Eds.; Gustav Fischer: Stuttgart; New York, 1988; pp 107–113.
(171) Kent, H. M.; Baines, M.; Gormal, C.; Smith, B. E.; Buck, M. Analysis of Site-Directed Mutations in the α-and β-Subunits of Klebsiella Pneumoniae Nitrogenase. *Mol. Microbiol.* **1990**, *4*, 1497–1504.
(172) Kent, H. M.; Ioannidis, I.; Gormal, C.; Smith, B. E.; Buck, M. Site-Directed Mutagenesis of the Klebsiella Pneumoniae Nitrogenase. Effects of Modifying Conserved Cysteine Residues in the α- and β-Subunits. *Biochem. J.* **1989**, *264*, 257–264.
(173) Meyer, J. Iron–Sulfur Protein Folds, Iron–Sulfur Chemistry, and Evolution. *JBIC J. Biol. Inorg. Chem.* **2008**, *13*, 157–170.
(174) Christiansen, J.; Cash, V. L.; Seefeldt, L. C.; Dean, D. R. Isolation and Characterization of an Acetylene-Resistant Nitrogenase. *J. Biol. Chem.* **2000**, *275*, 11459–11464.
(175) Christiansen, J.; Seefeldt, L. C.; Dean, D. R. Competitive Substrate and Inhibitor Interactions at the Physiologically Relevant Active Site of Nitrogenase*. *J. Biol. Chem.* **2000**, *275*, 36104–36107.
(176) Mayer, S. M.; Niehaus, W. G.; Dean, D. R. Reduction of Short Chain Alkynes by a Nitrogenase α-70Ala-Substituted MoFe Protein. *J. Chem. Soc. Dalt. Trans.* **2002**, No. 5, 802–807.
(177) Barney, B. M.; Igarashi, R. Y.; Dos Santos, P. C.; Dean, D. R.; Seefeldt, L. C. Substrate Interaction at an Iron-Sulfur Face of the FeMo-Cofactor during Nitrogenase Catalysis. *J. Biol. Chem.* **2004**, *279*, 53621–53624.
(178) Dos Santos, P. C.; Mayer, S. M.; Barney, B. M.; Seefeldt, L. C.; Dean, D. R. Alkyne Substrate Interaction within the Nitrogenase MoFe Protein. *J. Inorg. Biochem.* **2007**, *101*, 1642–1648.
(179) Yang, Z.-Y.; Dean, D. R.; Seefeldt, L. C. Molybdenum Nitrogenase Catalyzes the Reduction and Coupling of CO to Form Hydrocarbons. *J. Biol. Chem.* **2011**, *286*, 19417–19421.
(180) Benton, P. M. C.; Mayer, S. M.; Shao, J.; Hoffman, B. M.; Dean, D. R.; Seefeldt, L. C. Interaction of Acetylene and Cyanide with the Resting State of Nitrogenase α-96-Substituted MoFe Proteins. *Biochemistry* **2001**, *40*, 13816–13825.
(181) Maskos, Z.; Fisher, K.; Sørlie, M.; Newton, W. E.; Hales, B. J. Variant MoFe Proteins of Azotobacter Vinelandii: Effects of Carbon Monoxide on Electron Paramagnetic Resonance Spectra Generated during Enzyme Turnover. *JBIC J. Biol. Inorg. Chem.* **2005**, *10*, 394–406.
(182) Scott, D. J.; May, H. D.; Newton, W. E.; Brigle, K. E.; Dean, D. R. Role for the Nitrogenase MoFe Protein α-Subunit in FeMo-Cofactor Binding and Catalysis. *Nature* **1990**, *343*, 188–190.
(183) Fisher, K.; Dilworth, M. J.; Kim, C.-H.; Newton, W. E. Azotobacter Vinelandii Nitrogenases Containing Altered MoFe Proteins with Substitutions in the FeMo-

Cofactor Environment: Effects on the Catalyzed Reduction of Acetylene and Ethylene. *Biochemistry* **2000**, *39*, 2970–2979.
(184) Sørlie, M.; Christiansen, J.; Lemon, B. J.; Peters, J. W.; Dean, D. R.; Hales, B. J. Mechanistic Features and Structure of the Nitrogenase α-Gln195 MoFe Protein. *Biochemistry* **2001**, *40*, 1540–1549.
(185) Scott, D. J.; Dean, D. R.; Newton, W. E. Nitrogenase-Catalyzed Ethane Production and CO-Sensitive Hydrogen Evolution from MoFe Proteins Having Amino Acid Substitutions in an Alpha-Subunit FeMo Cofactor-Binding Domain. *J. Biol. Chem.* **1992**, *267*, 20002–20010.
(186) Fisher, K.; Hare, N. D.; Newton, W. E. Another Role for CO with Nitrogenase? CO Stimulates Hydrogen Evolution Catalyzed by Variant Azotobacter Vinelandii Mo-Nitrogenases. *Biochemistry* **2014**, *53*, 6151–6160.
(187) Kim, C.-H.; Newton, W. E.; Dean, D. R. Role of the MoFe Protein α-Subunit Histidine-195 Residue in FeMo-Cofactor Binding and Nitrogenase Catalysis. *Biochemistry* **1995**, *34*, 2798–2808.
(188) Dilworth, M. J.; Fisher, K.; Kim, C.-H.; Newton, W. E. Effects on Substrate Reduction of Substitution of Histidine-195 by Glutamine in the α-Subunit of the MoFe Protein of Azotobacter Vinelandii Nitrogenase. *Biochemistry* **1998**, *37*, 17495–17505.
(189) Lee, H.-I.; Sørlie, M.; Christiansen, J.; Yang, T.-C.; Shao, J.; Dean, D. R.; Hales, B. J.; Hoffman, B. M. Electron Inventory, Kinetic Assignment (En), Structure, and Bonding of Nitrogenase Turnover Intermediates with C2H2 and CO. *J. Am. Chem. Soc.* **2005**, *127*, 15880–15890.
(190) Shen, J.; Dean, D. R.; Newton, W. E. Evidence for Multiple Substrate-Reduction Sites and Distinct Inhibitor-Binding Sites from an Altered Azotobacter Vinelandii Nitrogenase MoFe Protein. *Biochemistry* **1997**, *36*, 4884–4894.
(191) Fisher, K.; Dilworth, M. J.; Kim, C.-H.; Newton, W. E. Azotobacter Vinelandii Nitrogenases with Substitutions in the FeMo-Cofactor Environment of the MoFe Protein: Effects of Acetylene or Ethylene on Interactions with H+, HCN, and CN-. *Biochemistry* **2000**, *39*, 10855–10865.
(192) Simpson, F. B.; Burris, R. H. A Nitrogen Pressure of 50 Atmospheres Does Not Prevent Evolution of Hydrogen by Nitrogenase. *Science* . **1984**, *224*, 1095–1097.
(193) Dilworth, M. J. Acetylene Reduction by Nitrogen-Fixing Preparations from Clostridium Pasteurianum. *Biochim. Biophys. Acta, Gen. Subj.* **1966**, *127*, 285–294.
(194) Seefeldt, L. C.; Hoffman, B. M.; Dean, D. R. Mechanism of Mo-Dependent Nitrogenase. *Annu. Rev. Biochem.* **2009**, *78*, 701–722.
(195) Lowe, D. J.; Fisher, K.; Thorneley, R. N. Klebsiella Pneumoniae Nitrogenase. Mechanism of Acetylene Reduction and Its Inhibition by Carbon Monoxide. *Biochem. J.* **1990**, *272*, 621–625.
(196) McLean, P. A.; Dixon, R. A. Requirement of NifV Gene for Production of Wild-Type Nitrogenase Enzyme in Klebsiella Pneumoniae. *Nature* **1981**, *292*, 655–656.
(197) Liang, J.; Madden, M.; Shah, V. K.; Burris, R. H. Citrate Substitutes for Homocitrate in Nitrogenase of a NifV Mutant of Klebsiella Pneumoniae. *Biochemistry* **1990**, *29*, 8577–8581.
(198) Dilworth, M. J.; Eady, R. R. Hydrazine Is a Product of Dinitrogen Reduction by the Vanadium-Nitrogenase from Azotobacter Chroococcum. *Biochem. J.* **1991**, *277*, 465–468.
(199) Thorneley, R. N. F.; Eady, R. R.; Lowe, D. J. Biological Nitrogen Fixation by Way of an Enzyme-Bound Dinitrogen-Hydride Intermediate. *Nature* **1978**, *272*, 557–558.
(200) Rivera-Ortiz, J. M.; Burris, R. H. Interactions among Substrates and Inhibitors of Nitrogenase. *J. Bacteriol.* **1975**, *123*, 537–545.
(201) Hwang, J. C.; Chen, C. H.; Burris, R. H. Inhibition of Nitrogenase-Catalyzed

Reductions. *Biochim. Biophys. Acta - Bioenerg.* **1973**, *292*, 256–270.
(202) Davis, L. C.; Henzl, M. T.; Burris, R. H.; Orme-Johnson, W. H. Iron-Sulfur Clusters in the Molybdenum-Iron Protein Component of Nitrogenase. Electron Paramagnetic Resonance of the Carbon Monoxide Inhibited State. *Biochemistry* **1979**, *18*, 4860–4869.
(203) Lowe, D. J.; Eady, R. R.; Thorneley, R. N. F. Electron-Paramagnetic-Resonance Studies on Nitrogenase of Klebsiella Pneumoniae. Evidence for Acetylene- and Ethylene-Nitrogenase Transient Complexes. *Biochem. J.* **1978**, *173*, 277–290.
(204) Davis, L. C.; Shah, V. K.; Brill, W. J. Nitrogenase: VII. Effect of Component Ratio, ATP and H2, on the Distribution of Electrons to Alternative Substrates. *Biochim. Biophys. Acta - Enzymol.* **1975**, *403*, 67–78.
(205) Benton, P. M. C.; Christiansen, J.; Dean, D. R.; Seefeldt, L. C. Stereospecificity of Acetylene Reduction Catalyzed by Nitrogenase. *J. Am. Chem. Soc.* **2001**, *123*, 1822–1827.
(206) Hoffman, B. M.; Lukoyanov, D.; Dean, D. R.; Seefeldt, L. C. Nitrogenase: A Draft Mechanism. *Acc. Chem. Res.* **2013**, *46*, 587–595.
(207) Bergmann, J.; Oksanen, E.; Ryde, U. Critical Evaluation of a Crystal Structure of Nitrogenase with Bound N2 Ligands. *JBIC J. Biol. Inorg. Chem.* **2021**, *26*, 341–353.
(208) Kang, W.; Lee, C. C.; Jasniewski, A. J.; Ribbe, M. W.; Hu, Y. Response to Comment on "Structural Evidence for a Dynamic Metallocofactor during N2 Reduction by Mo-Nitrogenase." *Science* . **2021**, *371*, eabe5856.
(209) Peters, J. W.; Einsle, O.; Dean, D. R.; DeBeer, S.; Hoffman, B. M.; Holland, P. L.; Seefeldt, L. C. Comment on "Structural Evidence for a Dynamic Metallocofactor during N2 Reduction by Mo-Nitrogenase." *Science* . **2021**, *371*, eabe5481.
(210) Lockshin, A.; Burris, R. H. Inhibitors of Nitrogen Fixation in Extracts from Clostridium Pasteurianum. *Biochim. Biophys. Acta - Gen. Subj.* **1965**, *111*, 1–10.
(211) Cameron, L. M.; Hales, B. J. Investigation of CO Binding and Release from Mo-Nitrogenase during Catalytic Turnover. *Biochemistry* **1998**, *37*, 9449–9456.
(212) Yates, M. G. Nitrogenase of Azotobacter Chroococcum: A New Electronparamagnetic-Resonance Signal Associated with a Transient Species of the MoFe Protein during Catalysis. *FEBS Lett.* **1976**, *72*, 127–130.
(213) Christie, P. D.; Lee, H.-I.; Cameron, L. M.; Hales, B. J.; Orme-Johnson, W. H.; Hoffman, B. M. Identification of the CO-Binding Cluster in Nitrogenase MoFe Protein by ENDOR of 57Fe Isotopomers. *J. Am. Chem. Soc.* **1996**, *118*, 8707–8709.
(214) Lee, C. C.; Fay, A. W.; Weng, T.-C.; Krest, C. M.; Hedman, B.; Hodgson, K. O.; Hu, Y.; Ribbe, M. W. Uncoupling Binding of Substrate CO from Turnover by Vanadium Nitrogenase. *Proc. Natl. Acad. Sci.* **2015**, *112*, 13845–13849.
(215) Lee, C. C.; Wilcoxen, J.; Hiller, C. J.; Britt, R. D.; Hu, Y. Evaluation of the Catalytic Relevance of the CO-Bound States of V-Nitrogenase. *Angew. Chemie Int. Ed.* **2018**, *57*, 3411–3414.
(216) Hiller, C. J.; Lee, C. C.; Stiebritz, M. T.; Rettberg, L. A.; Hu, Y. Strategies Towards Capturing Nitrogenase Substrates and Intermediates via Controlled Alteration of Electron Fluxes. *Chem. A Eur. J.* **2019**, *25*, 2389–2395.
(217) Lee, H. I.; Cameron, L. M.; Hales, B. J.; Hoffman, B. M. CO Binding to the FeMo Cofactor of CO-Inhibited Nitrogenase: 13CO and 1H Q-Band ENDOR Investigation. *J. Am. Chem. Soc.* **1997**, *119*, 10121–10126.
(218) George, S. J.; Ashby, G. A.; Wharton, C. W.; Thorneley, R. N. F. Time-Resolved Binding of Carbon Monoxide to Nitrogenase Monitored by Stopped-Flow Infrared Spectroscopy. *J. Am. Chem. Soc.* **1997**, *119*, 6450–6451.
(219) Pollock, R. C.; Lee, H.-I.; Cameron, L. M.; DeRose, V. J.; Hales, B. J.; Orme-Johnson, W. H.; Hoffman, B. M. Investigation of CO Bound to Inhibited Forms of Nitrogenase

MoFe Protein by 13C ENDOR. *J. Am. Chem. Soc.* **1995**, *117*, 8686–8687.
(220) Maskos, Z.; Hales, B. J. Photo-Lability of CO Bound to Mo-Nitrogenase from Azotobacter Vinelandii. *J. Inorg. Biochem.* **2003**, *93*, 11–17.
(221) Yan, L.; Dapper, C. H.; George, S. J.; Wang, H.; Mitra, D.; Dong, W.; Newton, W. E.; Cramer, S. P. Photolysis of Hi-CO Nitrogenase – Observation of a Plethora of Distinct CO Species Using Infrared Spectroscopy. *Eur. J. Inorg. Chem.* **2011**, *2011*, 2064–2074.
(222) Moore, V. G.; Tittsworth, R. C.; Hales, B. J. Construction and Characterization of Hybrid Component 1 from V-Nitrogenase Containing FeMo Cofactor. *J. Am. Chem. Soc.* **1994**, *116*, 12101–12102.
(223) Hu, Y.; Lee, C. C.; Ribbe, M. W. Extending the Carbon Chain: Hydrocarbon Formation Catalyzed by Vanadium/Molybdenum Nitrogenases. *Science* . **2011**, *333*, 753–755.
(224) Lee, C. C.; Hu, Y.; Ribbe, M. W. Vanadium Nitrogenase Reduces CO. *Science* . **2010**, *329*, 642.
(225) Lee, C. C.; Hu, Y.; Ribbe, M. W. Unique Features of the Nitrogenase VFe Protein from Azotobacter Vinelandii. *Proc. Natl. Acad. Sci.* **2009**, *106*, 9209–9214.
(226) Buscagan, T. M.; Perez, K. A.; Maggiolo, A. O.; Rees, D. C.; Spatzal, T. Structural Characterization of Two CO Molecules Bound to the Nitrogenase Active Site. *Angew. Chemie Int. Ed.* **2021**, *60*, 5704–5707.
(227) Dance, I. How Does Vanadium Nitrogenase Reduce CO to Hydrocarbons? *Dalt. Trans.* **2011**, *40*, 5516–5527.
(228) Dance, I. The Pathway for Serial Proton Supply to the Active Site of Nitrogenase: Enhanced Density Functional Modeling of the Grotthuss Mechanism. *Dalt. Trans.* **2015**, *44*, 18167–18186.
(229) Dance, I. Computational Investigations of the Chemical Mechanism of the Enzyme Nitrogenase. *ChemBioChem* **2020**, *21*, 1671–1709.
(230) Cao, L.; Caldararu, O.; Ryde, U. Protonation States of Homocitrate and Nearby Residues in Nitrogenase Studied by Computational Methods and Quantum Refinement. *J. Phys. Chem. B* **2017**, *121*, 8242–8262.
(231) Imperial, J.; Hoover, T. R.; Madden, M. S.; Ludden, P. W.; Shah, V. K. Substrate Reduction Properties of Dinitrogenase Activated in Vitro Are Dependent upon the Presence of Homocitrate or Its Analogs during Iron-Molybdenum Cofactor Synthesis. *Biochemistry* **1989**, *28*, 7796–7799.
(232) Siegbahn, P. E. M. A Major Structural Change of the Homocitrate Ligand of Probable Importance for the Nitrogenase Mechanism. *Inorg. Chem.* **2018**, *57*, 1090–1095.
(233) McLean, P. A.; Smith, B. E.; Dixon, R. A. Nitrogenase of Klebsiella Pneumoniae NifV Mutants. Investigation of the Novel Carbon Monoxide-Sensitivity of Hydrogen Evolution by the Mutant Enzyme. *Biochem. J.* **1983**, *211*, 589–597.
(234) Newton, W. E.; Vichitphan, K.; Fisher, K. Substrate Reduction and CO Susceptibility of the ΔnifV and α-Q191K MoFe Proteins of Azotobacter Vinelandii Nitrogenase. In *13th International Congress on Nitrogen Fixation*; Finan, T. M., O'Brian, M. R., Layzell, D. B., Vassey, J. K., Newton, W. E., Eds.; CABI Publishing: Hamilton, Ontario, Canada, 2001; p 370.
(235) Liedtke, J.; Lee, C. C.; Tanifuji, K.; Jasniewski, A. J.; Ribbe, M. W.; Hu, Y. Characterization of a Mo-Nitrogenase Variant Containing a Citrate-Substituted Cofactor. *ChemBioChem* **2021**, *22*, 151–155.
(236) Newcomb, M. P.; Lee, C. C.; Tanifuji, K.; Jasniewski, A. J.; Liedtke, J.; Ribbe, M. W.; Hu, Y. A V-Nitrogenase Variant Containing a Citrate-Substituted Cofactor. *ChemBioChem* **2020**, *21*, 1742–1748.
(237) Mayer, S. M.; Gormal, C. A.; Smith, B. E.; Lawson, D. M. Crystallographic Analysis

of the MoFe Protein of Nitrogenase from a NifV Mutant of Klebsiella Pneumoniae Identifies Citrate as a Ligand to the Molybdenum of Iron Molybdenum Cofactor (FeMoco)*. *J. Biol. Chem.* **2002**, *277*, 35263–35266.
(238) Seefeldt, L. C.; Rasche, M. E.; Ensign, S. A. Carbonyl Sulfide and Carbon Dioxide as New Substrates, and Carbon Disulfide as a New Inhibitor, of Nitrogenase. *Biochemistry* **1995**, *34*, 5382–5389.
(239) Rebelein, J. G.; Hu, Y.; Ribbe, M. W. Differential Reduction of CO2 by Molybdenum and Vanadium Nitrogenases. *Angew. Chemie Int. Ed.* **2014**, *53*, 11543–11546.
(240) Yang, Z.-Y.; Moure, V. R.; Dean, D. R.; Seefeldt, L. C. Carbon Dioxide Reduction to Methane and Coupling with Acetylene to Form Propylene Catalyzed by Remodeled Nitrogenase. *Proc. Natl. Acad. Sci.* **2012**, *109*, 19644–19648.
(241) Zheng, Y.; Harris, D. F.; Yu, Z.; Fu, Y.; Poudel, S.; Ledbetter, R. N.; Fixen, K. R.; Yang, Z.-Y.; Boyd, E. S.; Lidstrom, M. E.; et al. A Pathway for Biological Methane Production Using Bacterial Iron-Only Nitrogenase. *Nat. Microbiol.* **2018**, *3*, 281–286.
(242) Gaffron, H. Reduction of Carbon Dioxide with Molecular Hydrogen in Green Algae. *Nature* **1939**, *3614*, 204–205.
(243) Kluyver, A. J.; Manten, A. Some Observations on the Metabolism of Bacteria Oxidizing Molecular Hydrogen. *Antonie Van Leeuwenhoek* **1942**, *8*, 71–85.
(244) Gest, H. Oxidation and Evolution of Molecular Hydrogen by Microorganisms. *Bacteriol. Rev.* **1954**, *18*, 43–73.
(245) Schwartz, E.; Friedrich, B. The H2-Metabolizing Prokaryotes. In *The Prokaryotes*; Dworkin, M., Falkow, S., Rosenberg, E., Schleifer, K.-H., Stackebrandt, E., Eds.; Springer: New York, 2006; pp 496–563.
(246) Greening, C.; Biswas, A.; Carere, C. R.; Jackson, C. J.; Taylor, M. C.; Stott, M. B.; Cook, G. M.; Morales, S. E. Genomic and Metagenomic Surveys of Hydrogenase Distribution Indicate H2 Is a Widely Utilised Energy Source for Microbial Growth and Survival. *ISME J.* **2016**, *10*, 761–777.
(247) Benoit, S. L.; Maier, R. J.; Sawers, R. G.; Greening, C. Molecular Hydrogen Metabolism: A Widespread Trait of Pathogenic Bacteria and Protists. *Microbiol. Mol. Biol. Rev.* **2020**, *84*, e00092-19.
(248) Das, D.; Veziroğlu, T. N. Hydrogen Production by Biological Processes: A Survey of Literature. *Int. J. Hydrogen Energy* **2001**, *26*, 13–28.
(249) Tamagnini, P.; Axelsson, R.; Lindberg, P.; Oxelfelt, F.; Wünschiers, R.; Lindblad, P. Hydrogenases and Hydrogen Metabolism of Cyanobacteria. *Microbiol. Mol. Biol. Rev.* **2002**, *66*, 1–20.
(250) Melis, A.; Happe, T. Trails of Green Alga Hydrogen Research - from Hans Gaffron to New Frontiers. *Photosynth. Res.* **2004**, *80*, 401–409.
(251) Lubitz, W.; Ogata, H.; Rüdiger, O.; Reijerse, E. Hydrogenases. *Chem. Rev.* **2014**, *114*, 4081–4148.
(252) Vignais, P. M.; Billoud, B. Occurrence, Classification, and Biological Function of Hydrogenases: An Overview. *Chem. Rev.* **2007**, *107*, 4206–4272.
(253) Shima, S.; Pilak, O.; Vogt, S.; Schick, M.; Stagni, M. S.; Meyer-Klaucke, W.; Warkentin, E.; Thauer, R. K.; Ermler, U. The Crystal Structure of [Fe]-Hydrogenase Reveals the Geometry of the Active Site. *Science* . **2008**, *321*, 572–575.
(254) Thauer, R. K.; Kaster, A.-K.; Goenrich, M.; Schick, M.; Hiromoto, T.; Shima, S. Hydrogenases from Methanogenic Archaea, Nickel, a Novel Cofactor, and H2 Storage. *Annu. Rev. Biochem.* **2010**, *79*, 507–536.
(255) Huang, G.; Wagner, T.; Ermler, U.; Shima, S. Methanogenesis Involves Direct Hydride Transfer from H2 to an Organic Substrate. *Nat. Rev. Chem.* **2020**, *4*, 213–221.
(256) Bothe, H.; Schmitz, O.; Yates, M. G.; Newton, W. E. Nitrogen Fixation and Hydrogen Metabolism in Cyanobacteria. *Microbiol. Mol. Biol. Rev.* **2010**, *74*, 529–551.

(257) Fritsch, J.; Lenz, O.; Friedrich, B. Structure, Function and Biosynthesis of O2-Tolerant Hydrogenases. *Nat. Rev.* **2013**, *11*, 106–114.
(258) Parkin, A.; Sargent, F. The Hows and Whys of Aerobic H2 Metabolism. *Curr. Opin. Chem. Biol.* **2012**, *16*, 26–34.
(259) Shafaat, H. S.; Rüdiger, O.; Ogata, H.; Lubitz, W. [NiFe] Hydrogenases: A Common Active Site for Hydrogen Metabolism under Diverse Conditions. *Biochim. Biophys. Acta* **2013**, *1827*, 986–1002.
(260) Armstrong, F. A.; Fontecilla-Camps, J. C. A Natural Choice for Activating Hydrogen. *Science* . **2008**, *321*, 498–499.
(261) Horner, D. S.; Foster, P. G.; Embley, T. M. Iron Hydrogenases and the Evolution of Anaerobic Eukaryotes. *Mol. Biol. Evol.* **2000**, *17*, 1695–1709.
(262) Meyer, J. [FeFe] Hydrogenases and Their Evolution: A Genomic Perspective. *Cell. Mol. Life Sci.* **2007**, *64*, 1063–1084.
(263) Hemschemeier, A.; Happe, T. Alternative Photosynthetic Electron Transport Pathways during Anaerobiosis in the Green Alga Chlamydomonas Reinhardtii. *Biochim. Biophys. Acta - Bioenerg.* **2011**, *1807*, 919–926.
(264) Melis, A.; Zhang, L.; Forestier, M.; Ghirardi, M. L.; Seibert, M. Sustained Photobiological Hydrogen Gas Production upon Reversible Inactivation of Oxygen Evolution in the Green Alga Chlamydomonas Reinhardtii. *Plant Physiol.* **2000**, *122*, 127–136.
(265) Buckel, W.; Thauer, R. K. Flavin-Based Electron Bifurcation, A New Mechanism of Biological Energy Coupling. *Chem. Rev.* **2018**, *118*, 3862–3886.
(266) Schuchmann, K.; Chowdhury, N. P.; Müller, V. Complex Multimeric [FeFe] Hydrogenases: Biochemistry, Physiology and New Opportunities for the Hydrogen Economy. *Front. Microbiol.* **2018**, *9*, 2911.
(267) Land, H.; Senger, M.; Berggren, G.; Stripp, S. T. Current State of [FeFe]-Hydrogenase Research - Biodiversity and Spectroscopic Investigations. *ACS Catal.* **2020**, *10*, 7069–7086.
(268) Fasano, A.; Land, H.; Fourmond, V.; Berggren, G.; Léger, C. Reversible or Irreversible Catalysis of H+/H2Conversion by FeFe Hydrogenases. *J. Am. Chem. Soc.* **2021**, *143*, 20320–20325.
(269) Søndergaard, D.; Pedersen, C. N. S.; Greening, C. HydDB: A Web Tool for Hydrogenase Classification and Analysis. *Sci. Rep.* **2016**, *6*, 34212.
(270) Nishikawa, K.; Ogata, H.; Higuchi, Y. Structural Basis of the Function of [NiFe]-Hydrogenases. *Chem. Lett.* **2020**, *49*, 164–173.
(271) Volbeda, A.; Charon, M.; Piras, C.; Hatchikian, E. C.; Frey, M.; Fontecilla-Camps, J. C. Crystal Structure of the Nickel–Iron Hydrogenase from Desulfovibrio Gigas. *Nature* **1995**, *373*, 580–587.
(272) Higuchi, Y.; Yagi, T.; Yasuoka, N. Unusual Ligand Structure in Ni-Fe Active Center and an Additional Mg Site in Hydrogenase Revealed by High Resolution X-Ray Structure Analysis. *Structure* **1997**, *5*, 1671–1680.
(273) Ogata, H.; Nishikawa, K.; Lubitz, W. Hydrogens Detected by Subatomic Resolution Protein Crystallography in a [NiFe] Hydrogenase. *Nature* **2015**, *520*, 571–574.
(274) Ogata, H.; Mizoguchi, Y.; Mizuno, N.; Miki, K.; Adachi, S. ichi; Yasuoka, N.; Yagi, T.; Yamauchi, O.; Hirota, S.; Higuchi, Y. Structural Studies of the Carbon Monoxide Complex of [NiFe] Hydrogenase from Desulfovibrio Vulgaris Miyazaki F: Suggestion for the Initial Activation Site for Dihydrogen. *J. Am. Chem. Soc.* **2002**, *124*, 11628–11635.
(275) Ogata, H.; Hirota, S.; Nakahara, A.; Komori, H.; Shibata, N.; Kato, T.; Kano, K.; Higuchi, Y. Activation Process of [NiFe] Hydrogenase Elucidated by High-Resolution X-Ray Analyses: Conversion of the Ready to the Unready State. *Structure* **2005**, *13*,

1635–1642.
(276) Higuchi, Y.; Ogata, H.; Miki, K.; Yasuoka, N.; Yagi, T. Removal of the Bridging Ligand Atom at the Ni-Fe Active Site of [NiFe] Hydrogenase upon Reduction with H2, as Revealed by X-Ray Structure Analysis at 1.4 Å Resolution. *Structure* **1999**, *7*, 549–556.
(277) Volbeda, A.; Martin, L.; Cavazza, C.; Matho, M.; Faber, B. W.; Roseboom, W.; Albracht, S. P. J.; Garcin, E.; Rousset, M.; Fontecilla-Camps, J. C. Structural Differences between the Ready and Unready Oxidized States of [NiFe] Hydrogenases. *J. Biol. Inorg. Chem.* **2005**, *10*, 239–249.
(278) Ogata, H.; Kellers, P.; Lubitz, W. The Crystal Structure of the [NiFe] Hydrogenase from the Photosynthetic Bacterium Allochromatium Vinosum: Characterization of the Oxidized Enzyme (Ni-A State). *J. Mol. Biol.* **2010**, *402*, 428–444.
(279) Mills, D. J.; Vitt, S.; Strauss, M.; Shima, S.; Vonck, J. De Novo Modeling of the F420-Reducing [NiFe]-Hydrogenase from a Methanogenic Archaeon by Cryo-Electron Microscopy. *Elife* **2013**, *2*, e00218.
(280) Vitt, S.; Ma, K.; Warkentin, E.; Moll, J.; Pierik, A. J.; Shima, S.; Ermler, U. The F-420-Reducing [NiFe]-Hydrogenase Complex from Methanothermobacter Marburgensis, the First X-Ray Structure of a Group 3 Family Member. *J. Mol. Biol.* **2014**, *426*, 2813–2826.
(281) Schafer, C.; Bommer, M.; Hennig, S. E.; Jeoung, J. H.; Dobbek, H.; Lenz, O. Structure of an Actinobacterial-Type [NiFe]-Hydrogenase Reveals Insight into O-2-Tolerant H-2 Oxidation. *Structure* **2016**, *24*, 285–292.
(282) Matias, P. M.; Soares, C. M.; Saraiva, L. M.; Coelho, R.; Morais, J.; Le Gall, J.; Carrondo, M. A. [NiFe] Hydrogenase from Desulfovibrio Desulfuricans ATCC 27774: Gene Sequencing, Three-Dimensional Structure Determination and Refinement at 1.8 Å and Modelling Studies of Its Interaction with the Tetrahaem Cytochrome c 3. *J. Biol. Inorg. Chem.* **2001**, *6*, 63–81.
(283) Bowman, L.; Flanagan, L.; Fyfe, P. K.; Parkin, A.; Hunter, W. N.; Sargent, F. How the Structure of the Large Subunit Controls Function in an Oxygen-Tolerant [NiFe]-Hydrogenase. *Biochem. J.* **2014**, *458*, 449–458.
(284) Shomura, Y.; Taketa, M.; Nakashima, H.; Tai, H.; Nakagawa, H.; Ikeda, Y.; Ishii, M.; Igarashi, Y.; Nishihara, H.; Yoon, K. S.; et al. Structural Basis of the Redox Switches in the NAD+-Reducing Soluble [NiFe]-Hydrogenase. *Science* . **2017**, *357*, 928–932.
(285) Noor, N. D. M.; Matsuura, H.; Nishikawa, K.; Tai, H. L.; Hirota, S.; Kim, J.; Kang, J. Y.; Tateno, M.; Yoon, K. S.; Ogo, S.; et al. Redox-Dependent Conformational Changes of a Proximal [4Fe-4S] Cluster in Hyb-Type [NiFe]-Hydrogenase to Protect the Active Site from O2. *Chem. Commun.* **2018**, *54*, 12385–12388.
(286) Volbeda, A.; Amara, P.; Darnault, C.; Mouesca, J.-M.; Parkin, A.; Roessler, M. M.; Armstrong, F. A.; Fontecilla-Camps, J. C. X-Ray Crystallographic and Computational Studies of the O2-Tolerant [NiFe]-Hydrogenase 1 from Escherichia Coli. *Proc. Natl. Acad. Sci. U. S. A.* **2012**, *109*, 5305–5310.
(287) Beaton, S. E.; Evans, R. M.; Finney, A. J.; Lamont, C. M.; Armstrong, F. A.; Sargent, F.; Carr, S. B. The Structure of Hydrogenase-2 from Escherichia Coli : Implications for H2-Driven Proton Pumping. *Biochem. J.* **2018**, *475*, 1353–1370.
(288) Fritsch, J.; Scheerer, P.; Frielingsdorf, S.; Kroschinsky, S.; Friedrich, B.; Lenz, O.; Spahn, C. M. T. The Crystal Structure of an Oxygen-Tolerant Hydrogenase Uncovers a Novel Iron-Sulphur Centre. *Nature* **2011**, *479*, 249–252.
(289) Shomura, Y.; Yoon, K. S.; Nishihara, H.; Higuchi, Y. Structural Basis for a [4Fe-3S] Cluster in the Oxygen-Tolerant Membrane-Bound [NiFe]-Hydrogenase. *Nature* **2011**, *479*, 253–256.
(290) Frielingsdorf, S.; Fritsch, J.; Schmidt, A.; Hammer, M.; Löwenstein, J.; Siebert, E.;

Pelmenschikov, V.; Jaenicke, T.; Kalms, J.; Rippers, Y.; et al. Reversible [4Fe-3S] Cluster Morphing in an O2-Tolerant [NiFe] Hydrogenase. *Nat. Chem. Biol.* **2014**, *10*, 378–385.
(291) Happe, R. P.; Roseboom, W.; Pierik, A. J.; Albracht, S. P. J.; Bagley, K. A. Biological Activition of Hydrogen. *Nature* **1997**, *385*, 126.
(292) Pierik, A. J.; Roseboom, W.; Happe, R. P.; Bagley, K. A.; Albracht, P. J. Carbon Monoxide and Cyanide as Intrinsic Ligands to Iron in the Active Site of [NiFe]-Hydrogenases. *J. Biol. Chem.* **1999**, *274*, 3331–3337.
(293) Lubitz, W.; Ogata, H.; Rudiger, O.; Reijerse, E. Hydrogenases. *Chem. Rev.* **2014**, *114*, 4081–4148.
(294) Armstrong, F. A.; Evans, R. M.; Hexter, S. V; Murphy, B. J.; Roessler, M. M.; Wul, P. Guiding Principles of Hydrogenase Catalysis Instigated and Clarified by Protein Film Electrochemistry. *Acc. Chem. Res.* **2016**, *49*, 884–892.
(295) Ash, P. A.; Hidalgo, R.; Vincent, K. A. Proton Transfer in the Catalytic Cycle of [NiFe] Hydrogenases: Insight from Vibrational Spectroscopy. *ACS Catal.* **2017**, *7*, 2471–2485.
(296) Greene, B. L.; Vansuch, G. E.; Chica, B. C.; Adams, M. W. W.; Dyer, R. B. Applications of Photogating and Time Resolved Spectroscopy to Mechanistic Studies of Hydrogenases. *Acc. Chem. Res.* **2017**, *50*, 2718–2726.
(297) Tai, H.; Higuchi, Y.; Hirota, S. Comprehensive Reaction Mechanisms at and near the Ni-Fe Active Sites of [NiFe] Hydrogenases. *Dalt. Trans.* **2018**, *47*, 4408–4423.
(298) Tai, H.; Hirota, S.; Stripp, S. T. Proton Transfer Mechanisms in Bimetallic Hydrogenases. *Acc. Chem. Res.* **2021**, No. 54, 232–241.
(299) Ogata, H.; Lubitz, W.; Higuchi, Y. Structure and Function of [NiFe] Hydrogenases. *J. Biochem.* **2016**, *160*, 251–258.
(300) Baltazar, C. S. A.; Marques, M. C.; Soares, C. M.; DeLacey, A. M.; Pereira, I. A. C.; Matias, P. M. Nickel-Iron-Selenium Hydrogenases - An Overview. *Eur. J. Inorg. Chem.* **2011**, No. 7, 948–962.
(301) Garcin, E.; Vernede, X.; Hatchikian, E. C.; Volbeda, A.; Frey, M.; Fontecilla-Camps, J. C. The Crystal Structure of a Reduced [NiFeSe] Hydrogenase Provides an Image of the Activated Catalytic Center. *Structure* **1999**, *7*, 557–566.
(302) Marques, M. C.; Tapia, C.; Gutiérrez-sanz, O.; Ramos, A. R.; Keller, K. L.; Wall, J. D.; Lacey, A. L. De; Matias, P. M.; Pereira, I. A. C. The Direct Role of Selenocysteine in [NiFeSe] Hydrogenase Maturation and Catalysis. *Nat. Chem. Biol.* **2017**, *13*, 544–550.
(303) Ceccaldi, P.; Marques, M. C.; Fourmond, V.; Pereira, I. C.; Léger, C. Oxidative Inactivation of NiFeSe Hydrogenase. *Chem. Commun.* **2015**, *51*, 14223–14226.
(304) Volbeda, A.; Amara, P.; Iannello, M.; De Lacey, A. L.; Cavazza, C.; Carlos Fontecilla-Campsa, J. Structural Foundations for the O2 Resistance of Desulfomicrobium Baculatum [NiFeSe]-Hydrogenase. *Chem. Commun.* **2013**, *49*, 7061–7063.
(305) Yagi, T.; Kimura, K.; Daidoji, H.; Sakai, F.; Tamura, S. Properties of Purified Hydrogenase from the Particulate Fraction of Desulfovibrio Vulgaris, Miyazaki. *J. Biochem.* **1976**, *79*, 661–671.
(306) Yahata, N.; Saitoh, T.; Takayama, Y.; Ozawa, K.; Ogata, H.; Higuchi, Y.; Akutsu, H. Redox Interaction of Cytochrome C3 with [NiFe] Hydrogenase from Desulfovibrio Vulgaris Miyazaki F. *Biochemistry* **2006**, *45*, 1653–1662.
(307) Yagi, T.; Higuchi, Y. Studies on Hydrogenase. *Proc. Japan Acad. Ser. B-Physical Biol. Sci.* **2013**, *89*, 16–33.
(308) Volbeda, A.; Darnault, C.; Parkin, A.; Sargent, F.; Armstrong, F. A.; Fontecilla-Camps, J. C. Crystal Structure of the O(2)-Tolerant Membrane-Bound Hydrogenase 1 from Escherichia Coli in Complex with Its Cognate Cytochrome B. *Structure* **2013**, *21*, 184–190.

(309) Tai, H.; Hirota, S. Mechanism and Application of the Catalytic Reaction of [NiFe] Hydrogenase: Recent Developments. *Chembiochem* **2020**, *21*, 1573–1581.
(310) Leroux, F.; Dementin, S.; Burlat, B.; Cournac, L.; Volbeda, A.; Champ, S.; Martin, L.; Guigliarelli, B.; Bertrand, P.; Fontecilla-Camps, J.; et al. Experimental Approaches to Kinetics of Gas Diffusion in Hydrogenase. *Proc. Natl. Acad. Sci. U. S. A.* **2008**, *105*, 11188–11193.
(311) Liebgott, P.-P.; de Lacey, A. L.; Burlat, B.; Cournac, L.; Richaud, P.; Brugna, M.; Fernandez, V. M.; Guigliarelli, B.; Rousset, M.; Léger, C.; et al. Original Design of an Oxygen-Tolerant [NiFe] Hydrogenase: Major Effect of a Valine-to-Cysteine Mutation near the Active Site. *J. Am. Chem. Soc.* **2011**, *133*, 986–997.
(312) Abou Hamdan, A.; Dementin, S.; Liebgott, P. P.; Gutierrez-Sanz, O.; Richaud, P.; De Lacey, A. L.; Roussett, M.; Bertrand, P.; Cournac, L.; Léger, C. Understanding and Tuning the Catalytic Bias of Hydrogenase. *J. Am. Chem. Soc.* **2012**, *134*, 8368–8371.
(313) van Gastel, M.; Stein, M.; Brecht, M.; Schroder, O.; Lendzian, F.; Bittl, R.; Ogata, H.; Higuchi, Y.; Lubitz, W. A Single-Crystal ENDOR and Density Functional Theory Study of the Oxidized States of the [NiFe] Hydrogenase from Desulfovibrio Vulgaris Miyazaki F. *J. Biol. Inorg. Chem.* **2006**, *11*, 41–51.
(314) Pandelia, M.-E.; Ogata, H.; Lubitz, W. Intermediates in the Catalytic Cycle of [NiFe] Hydrogenase: Functional Spectroscopy of the Active Site. *ChemPhysChem* **2010**, *11*, 1127–1140.
(315) Fernandez, V. M.; Hatchikian, E. C.; Patil, D. S.; Cammack, R. ESR-Detectable Nickel and Iron-Sulphur Centres in Relation to the Reversible Activation of Desulfovibrio Gigas Hydrogenase. *Biochim. Biophys. Acta - Gen. Subj.* **1986**, *883*, 145–154.
(316) Barilone, J. L.; Ogata, H.; Lubitz, W.; Van Gastel, M. Structural Differences between the Active Sites of the Ni-A and Ni-B States of the [NiFe] Hydrogenase: An Approach by Quantum Chemistry and Single Crystal ENDOR Spectroscopy. *Phys. Chem. Chem. Phys.* **2015**, *17*, 16204–16212.
(317) Maroney, M. J. Nailing down Hydrogenase. *Nat. Chem. Biol.* **2013**, *9*, 11–12.
(318) Pandelia, M. E.; Ogata, H.; Currell, L. J.; Flores, M.; Lubitz, W. Probing Intermediates in the Activation Cycle of [NiFe] Hydrogenase by Infrared Spectroscopy: The Ni-SIr State and Its Light Sensitivity. *J. Biol. Inorg. Chem.* **2009**, *14*, 1227–1241.
(319) Fichtner, C.; Laurich, C.; Bothe, E.; Lubitz, W. Spectroelectrochemical Characterization of the [NiFe] Hydrogenase of Desulfovibrio Vulgaris Miyazaki F. *Biochemistry* **2006**, *45*, 9706–9716.
(320) Bleijlevens, B.; van Broekhuizen, F. a; De Lacey, A. L.; Roseboom, W.; Fernandez, V. M.; Albracht, S. P. J. The Activation of the [NiFe]-Hydrogenase from Allochromatium Vinosum. An Infrared Spectro-Electrochemical Study. *J. Biol. Inorg. Chem.* **2004**, *9*, 743–752.
(321) De Lacey, A. L.; Hatchikian, E. C.; Volbeda, A.; Frey, M.; Fontecilla-Camps, J. C.; Fernandez, V. M. Infrared-Spectroelectrochemical Characterization of the [NiFe] Hydrogenase of Desulfovibrio Gigas. *J. Am. Chem. Soc.* **1997**, *119*, 7181–7189.
(322) Millo, D.; Pandelia, M.-E.; Utesch, T.; Wisitruangsakul, N.; Mroginski, M. a; Lubitz, W.; Hildebrandt, P.; Zebger, I. Spectroelectrochemical Study of the [NiFe] Hydrogenase from Desulfovibrio Vulgaris Miyazaki F in Solution and Immobilized on Biocompatible Gold Surfaces. *J. Phys. Chem.* **2009**, *113*, 15344–15351.
(323) Breglia, R.; Greco, C.; Fantucci, P.; De Gioia, L.; Bruschi, M. Reactivation of the Ready and Unready Oxidized States of [NiFe]-Hydrogenases: Mechanistic Insights from DFT Calculations. *Inorg. Chem.* **2019**, *58*, 279–293.
(324) De Lacey, A. L.; Pardo, A.; Fernández, V. M.; Dementin, S.; Adryanczyk-Perrier, G.; Hatchikian, C. E.; Rousset, M. FTIR Spectroelectrochemical Study of the Activation and Inactivation Processes of [NiFe] Hydrogenases: Effects of Solvent Isotope

Replacement and Site-Directed Mutagenesis. *J. Biol. Inorg. Chem.* **2004**, *9*, 636–642.
(325) DeLacey, A. L.; Fernandez, V. M.; Rousset, M.; Cavazza, C.; Hatchikian, E. C. Spectroscopic and Kinetic Characterization of Active Site Mutants of Desulfovibrio Fructosovorans Ni-Fe Hydrogenase. *J. Biol. Inorg. Chem.* **2003**, *8*, 129–134.
(326) Evans, R. M.; Ash, P. A.; Beaton, S. E.; Brooke, E. J.; Vincent, K. A.; Carr, S. B.; Armstrong, F. A. Mechanistic Exploitation of a Self-Repairing, Blocked Proton Transfer Pathway in an O2-Tolerant [NiFe]-Hydrogenase. *J. Am. Chem. Soc.* **2018**, *140*, 10208–10220.
(327) Ogata, H.; Kramer, T.; Wang, H.; Schilter, D.; Pelmenschikov, V.; van Gastel, M.; Neese, F.; Rauchfuss, T. B.; Gee, L. B.; Scott, A. D.; et al. Hydride Bridge in [NiFe]-Hydrogenase Observed by Nuclear Resonance Vibrational Spectroscopy. *Nat. Commun.* **2015**, *6*, 7890.
(328) Wang, H. X.; Yoda, Y.; Ogata, H.; Tanaka, Y.; Lubitz, W. A Strenuous Experimental Journey Searching for Spectroscopic Evidence of a Bridging Nickel-Iron-Hydride in [NiFe] Hydrogenase. *J. Synchrotron Radiat.* **2015**, *22*, 1334–1344.
(329) Kamali, S.; Wang, H. X.; Mitra, D.; Ogata, H.; Lubitz, W.; Manor, B. C.; Rauchfuss, T. B.; Byrne, D.; Bonnefoy, V.; Jenney, F. E.; et al. Observation of the Fe-CN and Fe-CO Vibrations in the Active Site of [NiFe] Hydrogenase by Nuclear Resonance Vibrational Spectroscopy. *Angew. Chemie-International Ed.* **2013**, *52*, 724–728.
(330) Ogo, S.; Ichikawa, K.; Kishima, T.; Matsumoto, T.; Nakai, H.; Kusaka, K.; Ohhara, T. A Functional [NiFe]Hydrogenase Mimic That Catalyzes Electron and Hydride Transfer from H2. *Science* . **2013**, *339*, 682–684.
(331) Manor, B. C.; Rauchfuss, T. B. Hydrogen Activation by Biomimetic [NiFe]-Hydrogenase Model Containing Protected Cyanide Cofactors. *J. Am. Chem. Soc.* **2013**, *135*, 11895–11900.
(332) Chambers, G. M.; Huynh, M. T.; Li, Y.; Hammes-Schiffer, S.; Rauchfuss, T. B.; Reijerse, E.; Lubitz, W. Models of the Ni-L and Ni-SIa States of the [NiFe]-Hydrogenase Active Site. *Inorg. Chem.* **2016**, *55*, 419–431.
(333) Ulloa, O. A.; Huynh, M. T.; Richers, C. P.; Bertke, J. A.; Nilges, M. J.; Hammes-Schiffer, S.; Rauchfuss, T. B. Mechanism of H2 Production by Models for the [NiFe]-Hydrogenases: Role of Reduced Hydrides. *J. Am. Chem. Soc.* **2016**, *138*, 9234–9245.
(334) Dong, G.; Phung, Q. M.; Hallaert, S. D.; Pierloot, K.; Ryde, U. H2 Binding to the Active Site of [NiFe] Hydrogenase Studied by Multiconfigurational and Coupled-Cluster Methods. *Phys. Chem. Chem. Phys.* **2017**, *19*, 10590–10601.
(335) Dong, G.; Ryde, U.; Aa Jensen, H. J.; Hedegard, E. D. Exploration of H2 Binding to the [NiFe]-Hydrogenase Active Site with Multiconfigurational Density Functional Theory. *Phys. Chem. Chem. Phys.* **2018**, *20*, 794–801.
(336) Bruschi, M.; Tiberti, M.; Guerra, A.; De Gioia, L. Disclosure of Key Stereoelectronic Factors for Efficient H2 Binding and Cleavage in the Active Site of [NiFe]-Hydrogenases. *J. Am. Chem. Soc.* **2014**, *136*, 1803–1814.
(337) Brazzolotto, D.; Gennari, M.; Queyriaux, N.; Simmons, T. R.; Pécaut, J.; Demeshko, S.; Meyer, F.; Orio, M.; Artero, V.; Duboc, C. Nickel-Centred Proton Reduction Catalysis in a Model of [NiFe] Hydrogenase. *Nat. Chem.* **2016**, *8*, 1054–1060.
(338) Dong, G.; Phung, Q. M.; Pierloot, K.; Ryde, U. Reaction Mechanism of [NiFe] Hydrogenase Studied by Computational Methods. *Inorg. Chem.* **2018**, *57*, 15289–15298.
(339) Pandelia, M. E.; Ogata, H.; Currell, L. J.; Flores, M.; Lubitz, W. Inhibition of the [NiFe] Hydrogenase from Desulfovibrio Vulgaris Miyazaki F by Carbon Monoxide: An FTIR and EPR Spectroscopic Study. *Biochim. Biophys. Acta - Bioenerg.* **2010**, *1797*, 304–313.
(340) Ilina, Y.; Lorent, C.; Katz, S.; Jeoung, J.; Shima, S.; Horch, M.; Zebger, I.; Dobbek, H.

X- ray Crystallography and Vibrational Spectroscopy Reveal the Key Determinants of Biocatalytic Dihydrogen Cycling by [NiFe] Hydrogenases. *Angew. Chemie Int. Ed.* **2019**, *58*, 18710–18714.

(341) Horch, M.; Schoknecht, J.; Mroginski, M. A.; Lenz, O.; Hildebrandt, P.; Zebger, I. Resonance Raman Spectroscopy on [NiFe] Hydrogenase Provides Structural Insights into Catalytic Intermediates and Reactions. *J. Am. Chem. Soc.* **2014**, *136*, 9870–9873.

(342) Stein, M.; van Lenthe, E.; Baerends, E. J.; Lubitz, W. Relativistic DFT Calculations of the Paramagnetic Intermediates of [NiFe] Hydrogenase. Implications for the Enzymatic Mechanism. *J. Am. Chem. Soc.* **2001**, *123*, 5839–5840.

(343) Brecht, M.; Van Gastel, M.; Buhrke, T.; Friedrich, B.; Lubitz, W. Direct Detection of a Hydrogen Ligand in the [NiFe] Center of the Regulatory H2-Sensing Hydrogenase from Ralstonia Eutropha in Its Reduced State by HYSCORE and ENDOR Spectroscopy. *J. Am. Chem. Soc.* **2003**, *125*, 13075–13083.

(344) Foerster, S.; Stein, M.; Brecht, M.; Ogata, H.; Higuchi, Y.; Lubitz, W. Single Crystal EPR Studies of the Reduced Active Site of [NiFe] Hydrogenase from Desulfovibrio Vulgaris Miyazaki F. *J. Am. Chem. Soc.* **2003**, *125*, 83–93.

(345) Hidalgo, R.; Ash, P. A.; Healy, A. J.; Vincent, K. A. Infrared Spectroscopy during Electrocatalytic Turnover Reveals the Ni-L Active Site State during H2 Oxidation by a NiFe Hydrogenase. *Angew. Chemie - Int. Ed.* **2015**, *54*, 7110–7113.

(346) Murphy, B. J.; Hidalgo, R.; Roessler, M. M.; Evans, R. M.; Ash, P. A.; Myers, W. K.; Vincent, K. A.; Armstrong, F. A. Discovery of Dark PH-Dependent H+ Migration in a [NiFe]-Hydrogenase and Its Mechanistic Relevance: Mobilizing the Hydrido Ligand of the Ni-C Intermediate. *J. Am. Chem. Soc.* **2015**, *137*, 8484–8489.

(347) Tai, H.; Nishikawa, K.; Higuchi, Y.; Mao, Z.-W.; Hirota, S. Cysteine SH and Glutamate COOH Contributions to [NiFe] Hydrogenase Proton Transfer Revealed by Highly Sensitive FTIR Spectroscopy. *Angew. Chemie Int. Ed.* **2019**, *58*, 13285–13290.

(348) Tai, H.; Nishikawa, K.; Suzuki, M.; Higuchi, Y.; Hirota, S. Control of the Transition between Ni-C and Ni-SIastates by the Redox State of the Proximal Fe-S Cluster in the Catalytic Cycle of [NiFe] Hydrogenase. *Angew. Chemie - Int. Ed.* **2014**, *53*, 13817–13820.

(349) Tai, H.; Nishikawa, K.; Inoue, S.; Higuchi, Y.; Hirota, S. FT-IR Characterization of the Light-Induced Ni-L2 and Ni-L3 States of [NiFe] Hydrogenase from Desulfovibrio Vulgaris Miyazaki F. *J. Phys. Chem. B* **2015**, *119*, 13688–13674.

(350) Greene, B. L.; Wu, C. H.; McTernan, P. M.; Adams, M. W. W.; Dyer, R. B. Proton-Coupled Electron Transfer Dynamics in the Catalytic Mechanism of a [NiFe]-Hydrogenase. *J. Am. Chem. Soc.* **2015**, *137*, 4558–4566.

(351) Greene, B. L.; Wu, C.; Vansuch, G. E.; Adams, M. W. W.; Dyer, R. B. Proton Inventory and Dynamics in the Ni a -S to Ni a -C Transition of a [NiFe] Hydrogenase. *Biochemistry* **2016**, *55*, 1813–1825.

(352) Greene, B. L.; Vansuch, G. E.; Wu, C. H.; Adams, M. W. W.; Dyer, R. B. Glutamate Gated Proton-Coupled Electron Transfer Activity of a [NiFe]-Hydrogenase. *J. Am. Chem. Soc.* **2016**, *138*, 13013–13021.

(353) Kampa, M.; Pandelia, M. E.; Lubitz, W.; Van Gastel, M.; Neese, F. A Metal-Metal Bond in the Light-Induced State of [Nife] Hydrogenases with Relevance to Hydrogen Evolution. *J. Am. Chem. Soc.* **2013**, *135*, 3915–3925.

(354) Siebert, E.; Horch, M.; Rippers, Y.; Fritsch, J.; Frielingsdorf, S.; Lenz, O.; Velazquez Escobar, F.; Siebert, F.; Paasche, L.; Kuhlmann, U.; et al. Resonance Raman Spectroscopy as a Tool to Monitor the Active Site of Hydrogenases. *Angew. Chemie Int. Ed.* **2013**, *52*, 5162–5165.

(355) Ogata, H.; Lubitz, W.; Higuchi, Y. [NiFe] Hydrogenases: Structural and Spectroscopic Studies of the Reaction Mechanism. *Dalt. Trans.* **2009**, *9226*, 7577–7587.

(356) Teixeira, V. H.; Soares, C. M.; Baptista, A. M. Proton Pathways in a [NiFe]-Hydrogenase: A Theoretical Study. *Proteins* **2008**, *70*, 1010–1022.
(357) Galván, I. F.; Volbeda, A.; Fontecilla-Camps, J. C.; Field, M. J. A QM/MM Study of Proton Transport Pathways in a [NiFe] Hydrogenase. *Proteins Struct. Funct. Genet.* **2008**, *73*, 195–203.
(358) Dementin, S.; Burlat, B.; De Lacey, A. L.; Pardo, A.; Adryanczyk-Perrier, G.; Guigliarelli, B.; Fernandez, V. M.; Rousset, M. A Glutamate Is the Essential Proton Transfer Gate during the Catalytic Cycle of the [NiFe] Hydrogenase. *J. Biol. Chem.* **2004**, *279*, 10508–10513.
(359) Oteri, F.; Baaden, M.; Lojou, E.; Sacquin-Mora, S. Multiscale Simulations Give Insight into the Hydrogen in and out Pathways of [NiFe]-Hydrogenases from Aquifex Aeolicus and Desulfovibrio Fructosovorans. *J. Phys. Chem. B* **2014**, *118*, 13800–13811.
(360) Dong, G.; Ryde, U. Protonation States of Intermediates in the Reaction Mechanism of [NiFe] Hydrogenase Studied by Computational Methods. *J. Biol. Inorg. Chem.* **2016**, *21*, 383–394.
(361) Evans, R. M.; Brooke, E. J.; Wehlin, S. A. M.; Nomerotskaia, E.; Sargent, F.; Carr, S. B.; Phillips, S. E. V.; Armstrong, F. A. Mechanism of Hydrogen Activation by [NiFe] Hydrogenases. *Nat. Chem. Biol.* **2016**, *12*, 46–50.
(362) Brooke, E. J.; Evans, R. M.; Islam, S. T. A.; Roberts, G. M.; Wehlin, S. A. M.; Carr, S. B.; Phillips, S. E. V; Armstrong, F. A. Importance of the Active Site "Canopy" Residues in an O2-Tolerant [NiFe]-Hydrogenase. *Biochemistry* **2017**, *56*, 132–142.
(363) Vansuch, G. E.; Wu, C.-H.; Haja, D. K.; Blair, S. A.; Chica, B.; Johnson, M. K.; Adams, M. W. W.; Dyer, R. B. Metal–Ligand Cooperativity in the Soluble Hydrogenase-1 from Pyrococcus Furiosus. *Chem. Sci.* **2020**, *11*, 8572–8581.
(364) Fichtner, C.; van Gastel, M.; Lubitz, W. Wavelength Dependence of the Photo-Induced Conversion of the Ni-C to the Ni-L Redox State in the [NiFe] Hydrogenase of Desulfovibrio Vulgaris Miyazaki F. *Phys. Chem. Chem. Phys.* **2003**, *5*, 5507–5513.
(365) van der Zwaan, J. W.; Albracht, S. P. J.; Fontijn, R. D.; Slater, E. C. Monovalent Nickel in Hydrogenase from Chromatium Vinosum. Light Sensitivity and Evidence for Direct Interaction with Hydrogen. *FEBS Lett.* **1985**, *179*, 271–277.
(366) Medina, M.; Williams, R.; Cammack, R.; Hatchikian, E. C. Studies of Light-Induced Nickel EPR Signals in Desulfovibrio Gigas Hydrogenase. *J. Chem. Soc. Faraday Trans.* **1994**, *90*, 2921–2924.
(367) Medina, M.; Hatchikian, E. C.; Cammack, R. Studies of Light-Induced Nickel EPR Signals in Hydrogenase: Comparison of Enzymes with and without Selenium. *Biochim. Biophys. Acta - Bioenerg.* **1996**, *1275*, 227–236.
(368) Bondar, A. N.; Elstner, M.; Suhai, S.; Smith, J. C.; Fischer, S. Mechanism of Primary Proton Transfer in Bacteriorhodopsin. *Structure* **2004**, *12*, 1281–1288.
(369) Abou-Hamdan, A.; Ceccaldi, P.; Lebrette, H.; Gutierrez-Sanz, O.; Richaud, P.; Cournac, L.; Guigliarelli, B.; de Lacey, A. L.; Léger, C.; Volbeda, A.; et al. A Threonine Stabilizes the NiC and NiR Catalytic Intermediates of [NiFe]-Hydrogenase. *J. Biol. Chem.* **2015**, *290*, 8550–8558.
(370) Roberts, L. M.; Lindahl, P. A. Analysis of Oxidative Titrations of Desulfovibrio Gigas Hydrogenase; Implications for the Catalytic Mechanism. *Biochemistry* **1994**, *33*, 14339–14350.
(371) Radu, V.; Frielingsdorf, S.; Lenz, O.; Jeuken, L. J. C. Reactivation from the Ni-B State in [NiFe] Hydrogenase of Ralstonia Eutropha Is Controlled by Reduction of the Superoxidised Proximal Cluster. *Chem. Commun.* **2016**, *52*, 2632–2635.
(372) Evans, R. M.; Parkin, A.; Roessler, M. M.; Murphy, B. J.; Adamson, H.; Lukey, M. J.; Sargent, F.; Volbeda, A.; Fontecilla-Camps, J. C.; Armstrong, F. a. Principles of Sustained Enzymatic Hydrogen Oxidation in the Presence of Oxygen – The Crucial

Influence of High Potential Fe–S Clusters in the Electron Relay of [NiFe]-Hydrogenases. *J. Am. Chem. Soc.* **2013**, *135*, 2694–2707.
(373) Pandelia, M. E.; Fourmond, V.; Tron-Infossi, P.; Lojou, E.; Bertrand, P.; Léger, C.; Giudici-Orticoni, M. T.; Lubitz, W. Membrane-Bound Hydrogenase I from the Hyperthermophilic Bacterium Aquifex Aeolicus: Enzyme Activation, Redox Intermediates and Oxygen Tolerance. *J. Am. Chem. Soc.* **2010**, *132*, 6991–7004.
(374) Lubitz, W.; Reijerse, E.; van Gastel, M. [NiFe] and [FeFe] Hydrogenases Studied by Advanced Magnetic Resonance Techniques. *Chem. Rev.* **2007**, *107*, 4331–4365.
(375) Pandelia, M. E.; Nitschke, W.; Infossi, P.; Giudici-Orticoni, M. T.; Bill, E.; Lubitz, W. Characterization of a Unique [FeS] Cluster in the Electron Transfer Chain of the Oxygen Tolerant [NiFe] Hydrogenase from Aquifex Aeolicus. *Proc. Natl. Acad. Sci. U. S. A.* **2011**, *108*, 6097–6102.
(376) Pandelia, M. E.; Bykov, D.; Izsak, R.; Infossi, P.; Giudici-Orticoni, M. T.; Bill, E.; Neese, F.; Lubitz, W. Electronic Structure of the Unique [4Fe-3S] Cluster in O 2-Tolerant Hydrogenases Characterized by 57Fe Mössbauer and EPR Spectroscopy. *Proc. Natl. Acad. Sci. U. S. A.* **2013**, *110*, 483–488.
(377) Mouesca, J.-M.; Amara, P.; Fontecilla-Camps, J. C. Electronic States of the O2-Tolerant [NiFe] Hydrogenase Proximal Cluster. *Proc. Natl. Acad. Sci.* **2013**, *110*, E2538.
(378) Pandelia, M.-E.; Bykov, D.; Izsak, R.; Infossi, P.; Giudici-Orticoni, M.-T.; Bill, E.; Neese, F.; Lubitz, W. Reply to Mouesca et Al.: Electronic Structure of the Proximal [4Fe-3S] Cluster of O2-Tolerant [NiFe] Hydrogenases. *Proc. Natl. Acad. Sci.* **2013**, *110*, E2539.
(379) Mouesca, J. M.; Fontecilla-Camps, J. C.; Amara, P. The Structural Plasticity of the Proximal [4Fe3S] Cluster Is Responsible for the O2 Tolerance of Membrane-Bound [NiFe] Hydrogenases. *Angew. Chemie - Int. Ed.* **2013**, *52*, 2002–2006.
(380) Goris, T.; Wait, A. F.; Saggu, M.; Fritsch, J.; Heidary, N.; Stein, M.; Zebger, I.; Lendzian, F.; Armstrong, F. A.; Friedrich, B.; et al. A Unique Iron-Sulfur Cluster Is Crucial for Oxygen Tolerance of a [NiFe]-Hydrogenase. *Nat. Chem. Biol.* **2011**, *7*, 310–318.
(381) Lukey, M. J.; Roessler, M. M.; Parkin, A.; Evans, R. M.; Davies, R. A.; Lenz, O.; Friedrich, B.; Sargent, F.; Armstrong, F. A. Oxygen-Tolerant [NiFe]-Hydrogenases: The Individual and Collective Importance of Supernumerary Cysteines at the Proximal Fe-S Cluster. *J. Am. Chem. Soc.* **2011**, *133*, 16881–16892.
(382) Lauterbach, L.; Lenz, O. Catalytic Production of Hydrogen Peroxide and Water by Oxygen-Tolerant [NiFe]-Hydrogenase during H-2 Cycling in the Presence of O-2. *J. Am. Chem. Soc.* **2013**, *135*, 17897–17905.
(383) Karstens, K.; Wahlefeld, S.; Horch, M.; Grunzel, M.; Lauterbach, L.; Lendzian, F.; Zebger, I.; Lenz, O. Impact of the Iron-Sulfur Cluster Proximal to the Active Site on the Catalytic Function of an O-2-Tolerant NAD(+)-Reducing [NiFe]-Hydrogenase. *Biochemistry* **2015**, *54*, 389–403.
(384) Dance, I. What Is the Trigger Mechanism for the Reversal of Electron Flow in Oxygen-Tolerant [NiFe] Hydrogenases? *Chem. Sci.* **2015**, *6*, 1433–1443.
(385) Roessler, M. M.; Evans, R. M.; Davies, R. A.; Harmer, J.; Armstrong, F. A. EPR Spectroscopic Studies of the Fe-S Clusters in the O-2-Tolerant [NiFe]-Hydrogenase Hyd-1 from Escherichia Coli and Characterization of the Unique [4Fe-3S] Cluster by HYSCORE. *J. Am. Chem. Soc.* **2012**, *134*, 15581–15594.
(386) Tai, H.; Xu, L.; Inoue, S.; Nishikawa, K.; Higuchi, Y.; Hirota, S. Photoactivation of the Ni-SIr State to the Ni-SIa State in [NiFe] Hydrogenase: FT-IR Study on the Light Reactivity of the Ready Ni-SIr State and as-Isolated Enzyme Revisited. *Phys. Chem. Chem. Phys.* **2016**, *18*, 22025–22030.

(387) Tai, H.; Xu, L.; Nishikawa, K.; Higuchi, Y.; Hirota, S. Equilibrium between Inactive Ready Ni-SIr and Active Ni-SIa States of [NiFe] Hydrogenase Studied by Utilizing Ni-SIr-to-Ni-SIa Photoactivation. *Chem. Commun.* **2017**, *53*, 10444–10447.
(388) Rousset, M.; Montet, Y.; Guigliarelli, B.; Forget, N.; Asso, M.; Bertrand, P.; Fontecilla-Camps, J. C.; Hatchikian, E. C. [3Fe-4S] to [4Fe-4S] Cluster Conversion in Desulfovibrio Fructosovorans [NiFe] Hydrogenase by Site-Directed Mutagenesis. *Proc. Natl. Acad. Sci. U. S. A.* **1998**, *95*, 11625–11630.
(389) Dementin, S.; Belle, V.; Bertrand, P.; Guigliarelli, B.; Adryanczyk-Perrier, G.; De Lacey, A. L.; Fernandez, V. M.; Rousset, M.; Léger, C. Changing the Ligation of the Distal [4Fe4S] Cluster in NiFe Hydrogenase Impairs Inter- and Intramolecular Electron Transfers. *J. Am. Chem. Soc.* **2006**, *128*, 5209–5218.
(390) Dementin, S.; Burlat, B.; Fourmond, V.; Leroux, F.; Liebgott, P.-P.; Abou Hamdan, A.; Léger, C.; Rousset, M.; Guigliarelli, B.; Bertrand, P. Rates of Intra- and Intermolecular Electron Transfers in Hydrogenase Deduced from Steady-State Activity Measurements. *J. Am. Chem. Soc.* **2011**, *133*, 10211–10221.
(391) Petrenko, A.; Stein, M. Distal [FeS]-Cluster Coordination in [NiFe]-Hydrogenase Facilitates Intermolecular Electron Transfer. *Int. J. Mol. Sci.* **2017**, *18*, 100.
(392) Yonemoto, I. T.; Smith, H. O.; Weyman, P. D. Designed Surface Residue Substitutions in [NiFe] Hydrogenase That Improve Electron Transfer Characteristics. *Int. J. Mol. Sci.* **2015**, *16*, 2020–2033.
(393) Yonemoto, I. T.; Clarkson, B. R.; Smith, H. O.; Weyman, P. D. A Broad Survey Reveals Substitution Tolerance of Residues Ligating FeS Clusters in [NiFe] Hydrogenase. *BMC Biochem.* **2014**, *15*, 10.
(394) Yonemoto, I. T.; Matteri, C. W.; Nguyen, T. A.; Smith, H. O.; Weyman, P. D. Dual Organism Design Cycle Reveals Small Subunit Substitutions That Improve [NiFe] Hydrogenase Hydrogen Evolution. *J. Biol. Eng.* **2013**, *7*, 17.
(395) Adamson, H.; Robinson, M.; Wright, J. J.; Flanagan, L. A.; Walton, J.; Elton, D.; Gavaghan, D. J.; Bond, A. M.; Roessler, M. M.; Parkin, A. Retuning the Catalytic Bias and Overpotential of a [NiFe]-Hydrogenase via a Single Amino Acid Exchange at the Electron Entry/Exit Site. *J. Am. Chem. Soc.* **2017**, *139*, 10677–10686.
(396) Vidal-Limon, A. M.; Tafoya, P.; Santini, B. L.; Contreras, O. E.; Aguila, S. A. Electron Transfer Pathways Analysis of Oxygen Tolerant [NiFe]-Hydrogenases for Hydrogen Production: A Quantum Mechanics/Molecular Mechanics - Statistical Coupled Analysis. *Int. J. Hydrog. Energy* **2017**, *42*, 20494–20502.
(397) Montet, Y.; Amara, P.; Volbeda, A. Gas Access to the Active Site of Ni-Fe Hydrogenases Probed by X-Ray Crystallography and Molecular Dynamics. *Nat. Struct. Biol.* **1997**, *4*, 523–526.
(398) Volbeda, A. High-Resolution Crystallographic Analysis of Desulfovibrio Fructosovorans [NiFe] Hydrogenase. *Int. J. Hydrogen Energy* **2002**, *27*, 1449–1461.
(399) Topin, J.; Rousset, M.; Antonczak, S.; Golebiowski, J. Kinetics and Thermodynamics of Gas Diffusion in a NiFe Hydrogenase. *Proteins-Structure Funct. Bioinforma.* **2012**, *80*, 677–682.
(400) Kalms, J.; Schmidt, A.; Frielingsdorf, S.; van der Linden, P.; von Stetten, D.; Lenz, O.; Carpentier, P.; Scheerer, P. Krypton Derivatization of an O2 -Tolerant Membrane-Bound [NiFe] Hydrogenase Reveals a Hydrophobic Tunnel Network for Gas Transport. *Angew. Chem. Int. Ed.* **2016**, *55*, 5586–5590.
(401) Kalms, J.; Schmidt, A.; Frielingsdorf, S.; Utesch, T.; Gotthard, G.; von Stetten, D.; van der Linden, P.; Royant, A.; Mroginski, M. A.; Carpentier, P.; et al. Tracking the Route of Molecular Oxygen in O2-Tolerant Membrane-Bound [NiFe] Hydrogenase. *Proc. Natl. Acad. Sci. USA* **2018**, *115*, E2229–E2237.
(402) Wang, P. H.; Best, R. B.; Blumberger, J. Multiscale Simulation Reveals Multiple

Pathways for H2 and O2 Transport in a [NiFe]-Hydrogenase. *J. Am. Chem. Soc.* **2011**, *133*, 3548–3556.
(403) Buhrke, T.; Lenz, O.; Krauss, N.; Friedrich, B. Oxygen Tolerance of the H2-Sensing [NiFe] Hydrogenase from Ralstonia Eutropha H16 Is Based on Limited Access of Oxygen to the Active Site. *J. Biol. Chem.* **2005**, *280*, 23791–23796.
(404) Duché, O.; Elsen, S.; Cournac, L.; Colbeau, A. Enlarging the Gas Access Channel to the Active Site Renders the Regulatory Hydrogenase HupUV of Rhodobacter Capsulatus O2 Sensitive without Affecting Its Transductory Activity. *FEBS J.* **2005**, *272*, 3899–3908.
(405) Hamdan, A. A.; Liebgott, P. P.; Fourmond, V.; Gutiérrez-Sanz, O.; De Lacey, A. L.; Infossi, P.; Rousset, M.; Dementin, S.; Léger, C. Relation between Anaerobic Inactivation and Oxygen Tolerance in a Large Series of NiFe Hydrogenase Mutants. *Proc. Natl. Acad. Sci. U. S. A.* **2012**, *109*, 19916–19921.
(406) Liebgott, P.; Leroux, F.; Burlat, B.; Dementin, S. Relating Diffusion along the Substrate Tunnel and Oxygen Sensitivity in Hydrogenase. *Nat. Chem. Biol.* **2009**, *6*, 63–70.
(407) Dementin, S.; Leroux, F.; Cournac, L.; de Lacey, A. L.; Volbeda, A.; Leger, C.; Burlat, B.; Martinez, N.; Champ, S.; Martin, L.; et al. Introduction of Methionines in the Gas Channel Makes [NiFe] Hydrogenase Aero-Tolerant. *J. Am. Chem. Soc.* **2009**, *131*, 10156–10164.
(408) Wang, P. H.; Blumberger, J. Mechanistic Insight into the Blocking of CO Diffusion in [NiFe]-Hydrogenase Mutants through Multiscale Simulation. *Proc. Natl. Acad. Sci. U. S. A.* **2012**, *109*, 6399–6404.
(409) Liebgott, P. P.; Leroux, F.; Burlat, B.; Dementin, S.; Baffert, C.; Lautier, T.; Fourmond, V.; Ceccaldi, P.; Cavazza, C.; Meynial-Salles, I.; et al. Relating Diffusion along the Substrate Tunnel and Oxygen Sensitivity in Hydrogenase. *Nat. Chem. Biol.* **2010**, *6*, 63–70.
(410) Fourmond, V.; Infossi, P.; Giudici-Orticoni, M.-T.; Bertrand, P.; Léger, C. "Two-Step" Chronoamperometric Method for Studying the Anaerobic Inactivation of an Oxygen Tolerant NiFe Hydrogenase. *J. Am. Chem. Soc.* **2010**, *132*, 4848–4857.
(411) del Barrio, M.; Guendon, C.; Kpebe, A.; Baffert, C.; Fourmond, V.; Brugna, M.; Léger, C. Valine-to-Cysteine Mutation Further Increases the Oxygen Tolerance of Escherichia Coli NiFe Hydrogenase Hyd-1. *ACS Catal.* **2019**, *9*, 4084–4088.
(412) Marques, M. C.; Coelho, R.; Pereira, I. A. C.; Matias, P. M. Redox State-Dependent Changes in the Crystal Structure of [NiFeSe] Hydrogenase from Desulfovibrio Vulgaris Hildenborough. *Int. J. Hydrog. Energy* **2013**, *38*, 8664–8682.
(413) Zacarias, S.; Temporão, A.; Barrio, M. del; Fourmond, V.; Léger, C.; Matias, P. M.; Pereira, I. A. C. A Hydrophilic Channel Is Involved in Oxidative Inactivation of a [NiFeSe] Hydrogenase. *ACS Catal.* **2019**, *9*, 8509–8519.
(414) Peters, J. W.; Lanzilotta, W. N.; Lemon, B. J.; Seefeldt, L. C. X-Ray Crystal Structure of the Fe-Only Hydrogenase (CpI) from Clostridium Pasteurianum to 1.8 Angstrom Resolution. *Science* **1998**, *282*, 1853–1858.
(415) Lemon, B. J.; Peters, J. W. Binding of Exogenously Added Carbon Monoxide at the Active Site of the Iron-Only Hydrogenase (CpI) from Clostridium Pasteurianum. *Biochemistry* **1999**, *38*, 12969–12973.
(416) Lemon, B. J.; Peters, J. W. Photochemistry at the Active Site of the Carbon Monoxide Inhibited Form of the Iron-Only Hydrogenase (CpI). *J. Am. Chem. Soc.* **2000**, *122*, 3793–3794.
(417) Gorwa, M. F.; Croux, C.; Soucaille, P. Molecular Characterization and Transcriptional Analysis of the Putative Hydrogenase Gene of Clostridium Acetobutylicum ATCC 824. *J. Bacteriol.* **1996**, *178*, 2668–2675.

(418) Gauquelin, C.; Baffert, C.; Richaud, P.; Kamionka, E.; Etienne, E.; Guieysse, D.; Girbal, L.; Fourmond, V.; André, I.; Guigliarelli, B.; et al. Roles of the F-Domain in [FeFe] Hydrogenase. *Biochim. Biophys. Acta - Bioenerg.* **2018**, *1859*, 69–77.
(419) Artz, J. H.; Mulder, D. W.; Ratzloff, M. W.; Lubner, C. E.; Zadvornyy, O. A.; LeVan, A. X.; Williams, S. G.; Adams, M. W. W.; Jones, A. K.; King, P. W.; et al. Reduction Potentials of [FeFe]-Hydrogenase Accessory Iron–Sulfur Clusters Provide Insights into the Energetics of Proton Reduction Catalysis. *J. Am. Chem. Soc.* **2017**, *139*, 9544–9550.
(420) Pierik, A. J.; Hagen, W. R.; Redeker, J. S.; Wolbert, R. B. G.; Boersma, M.; Verhagen, M. F. J. M.; Grande, H. J.; Veeger, C.; Mutsaers, P. H. a; Sands, R. H.; et al. Redox Properties of the Iron-Sulfur Clusters in Activated Fe-Hydrogenase from Desulfovibrio Vulgaris (Hildenborough). *Eur. J. Biochem.* **1992**, *209*, 63–72.
(421) Nicolet, Y.; Piras, C.; Legrand, P.; Hatchikian, C. E.; Fontecilla-Camps, J. C. Desulfovibrio Desulfuricans Iron Hydrogenase: The Structure Shows Unusual Coordination to an Active Site Fe Binuclear Center. *Structure* **1999**, *7*, 13–23.
(422) Nicolet, Y.; de Lacey, A. L.; Vernède, X.; Fernandez, V. M.; Hatchikian, E. C.; Fontecilla-Camps, J. C. Crystallographic and FTIR Spectroscopic Evidence of Changes in Fe Coordination Upon Reduction of the Active Site of the Fe-Only Hydrogenase from Desulfovibrio d Esulfuricans. *J. Am. Chem. Soc.* **2001**, *123*, 1596–1601.
(423) Caserta, G.; Adamska-Venkatesh, A.; Pecqueur, L.; Atta, M.; Artero, V.; Roy, S.; Reijerse, E.; Lubitz, W.; Fontecave, M. Chemical Assembly of Multiple Metal Cofactors: The Heterologously Expressed Multidomain [FeFe]-Hydrogenase from Megasphaera Elsdenii. *Biochim. Biophys. Acta - Bioenerg.* **2016**, *1857*, 1734–1740.
(424) Caserta, G.; Papini, C.; Adamska-Venkatesh, A.; Pecqueur, L.; Sommer, C.; Reijerse, E.; Lubitz, W.; Gauquelin, C.; Meynial-Salles, I.; Pramanik, D.; et al. Engineering an [FeFe]-Hydrogenase: Do Accessory Clusters Influence O2 Resistance and Catalytic Bias? *J. Am. Chem. Soc.* **2018**, *140*, 5516–5526.
(425) Winkler, M.; Duan, J.; Rutz, A.; Felbek, C.; Scholtysek, L.; Lampret, O.; Jaenecke, J.; Apfel, U.-P.; Gilardi, G.; Valetti, F.; et al. A Safety Cap Protects Hydrogenase from Oxygen Attack. *Nat. Commun.* **2021**, *12*, 756.
(426) Happe, T.; Naber, J. D. Isolation, Characterization and N- terminal Amino Acid Sequence of Hydrogenase from the Green Alga Chlamydomonas Reinhardtii. *Eur. J. Biochem.* **1993**, *214*, 475–481.
(427) Winkler, M.; Hemschemeier, A.; Gotor, C.; Melis, A.; Happe, T. [FeFe]-Hydrogenases in Green Algae: Photo-Fermentation and Hydrogen Evolution under Sulfur Deprivation. *Int. J. Hydrogen Energy* **2002**, *27*, 1431–1439.
(428) Kamp, C.; Silakov, A.; Winkler, M.; Reijerse, E. J.; Lubitz, W.; Happe, T. Isolation and First EPR Characterization of the [FeFe]-Hydrogenases from Green Algae. *Biochim. Biophys. Acta* **2008**, *1777*, 410–416.
(429) Sybirna, K.; Antoine, T.; Lindberg, P.; Fourmond, V.; Rousset, M.; Méjean, V.; Bottin, H. Shewanella Oneidensis: A New and Efficient System for Expression and Maturation of Heterologous [Fe-Fe] Hydrogenase from Chlamydomonas Reinhardtii. *BMC Biotechnol.* **2008**, *8*, 73.
(430) Stripp, S. T.; Sanganas, O.; Happe, T.; Haumann, M. The Structure of the Active Site H-Cluster of [FeFe] Hydrogenase from the Green Alga Chlamydomonas Reinhardtii Studied by X-Ray Absorption Spectroscopy. *Biochemistry* **2009**, *48*, 5042–5049.
(431) Mulder, D. W.; Boyd, E. S.; Sarma, R.; Lange, R. K.; Endrizzi, J. A.; Broderick, J. B.; Peters, J. W. Stepwise [FeFe]-Hydrogenase H-Cluster Assembly Revealed in the Structure of HydA(DeltaEFG). *Nature* **2010**, *465*, 248–251.
(432) Schuchmann, K.; Müller, V. Direct and Reversible Hydrogenation of CO2 to Formate by a Bacterial Carbon Dioxide Reductase. *Science* . **2013**, *342*, 1382–1386.

(433) Ceccaldi, P.; Schuchmann, K.; Müller, V.; Elliott, S. J. The Hydrogen Dependent CO2 Reductase: The First Completely Co Tolerant FeFe-Hydrogenase. *Energy Environ. Sci.* **2017**, *10*, 503–508.
(434) Lipscomb, G. L.; Schut, G. J.; Thorgersen, M. P.; Nixon, W. J.; Kelly, R. M.; Adams, M. W. W. Engineering Hydrogen Gas Production from Formate in a Hyperthermophile by Heterologous Production of an 18-Subunit Membrane-Bound Complex. *J. Biol. Chem.* **2014**, *289*, 2873–2879.
(435) Pierik, A. J.; Hulstein, M.; Hagen, W. R.; Albracht, S. P. J. A Low-Spin Iron with CN and CO as Intrinsic Ligands Forms the Core of the Active Site in [Fe]-Hydrogenases. *Eur. J. Biochem.* **1998**, *258*, 572–578.
(436) Pandey, A. S.; Harris, T. V; Giles, L. J.; Peters, J. W.; Szilagyi, R. K. Dithiomethylether as a Ligand in the Hydrogenase H-Cluster. *J. Am. Chem. Soc.* **2008**, *130*, 4533–4540.
(437) Silakov, A.; Wenk, B.; Reijerse, E.; Lubitz, W. 14N HYSCORE Investigation of the H-Cluster of [FeFe] Hydrogenase: Evidence for a Nitrogen in the Dithiol Bridge. *Phys. Chem. Chem. Phys.* **2009**, *11*, 6592–6599.
(438) Vignais, P. M.; Billoud, B.; Meyer, J. Classification and Phylogeny of Hydrogenases. *FEMS Microbiol. Rev.* **2001**, *25*, 455–501.
(439) Horner, D. S.; Heil, B.; Happe, T.; Embley, T. M. Iron Hydrogenases - Ancient Enzymes in Modern Eukaryotes. *Trends Biochem. Sci.* **2002**, *27*, 148–153.
(440) Calusinska, M.; Happe, T.; Joris, B.; Wilmotte, A. The Surprising Diversity of Clostridial Hydrogenases: A Comparative Genomic Perspective. *Microbiology* **2010**, *156*, 1575–1588.
(441) Chongdar, N.; Birrell, J. A.; Pawlak, K.; Sommer, C.; Reijerse, E. J.; Rüdiger, O.; Lubitz, W.; Ogata, H. Unique Spectroscopic Properties of the H-Cluster in a Putative Sensory [FeFe] Hydrogenase. *J. Am. Chem. Soc.* **2018**, *140*, 1057−1068.
(442) Chongdar, N.; Pawlak, K.; Rüdiger, O.; Reijerse, E. J.; Rodríguez-Maciá, P.; Lubitz, W.; Birrell, J. A.; Ogata, H. Spectroscopic and Biochemical Insight into an Electron-Bifurcating [FeFe] Hydrogenase. *J. Biol. Inorg. Chem.* **2020**, *25*, 135–149.
(443) Land, H.; Ceccaldi, P.; Mészáros, L. S.; Lorenzi, M.; Redman, H. J.; Senger, M.; Stripp, S. T.; Berggren, G. Discovery of Novel [FeFe]-Hydrogenases for Biocatalytic H2-Production. *Chem. Sci.* **2019**, *10*, 9941–9948.
(444) Land, H.; Sekretaryova, A. N.; Huang, P.; Redman, H. J.; Németh, B.; Polidori, N.; Mészáros, L.; Senger, M.; Stripp, S. T.; Berggren, G. Characterization of a Putative Sensory [FeFe]-Hydrogenase Provides New Insight into the Role of the Active Site Architecture. *Chem. Sci.* **2020**, *11*, 12789–12801.
(445) Furlan, C.; Chongdar, N.; Gupta, P.; Lubitz, W.; Ogata, H.; James, N.; Birrell, J. A. Structural Insight on the Mechanism of an Electron-Bifurcating [FeFe] Hydrogenase. *ChemRxiv* **2021**, 1–13.
(446) Lampret, O.; Esselborn, J.; Haas, R.; Rutz, A.; Booth, R. L.; Kertess, L.; Wittkamp, F.; Megarity, C. F.; Armstrong, F. A.; Winkler, M.; et al. The Final Steps of [FeFe]-Hydrogenase Maturation. *Proc. Natl. Acad. Sci. U. S. A.* **2019**, *116*, 15802–15810.
(447) Winkler, M.; Senger, M.; Duan, J.; Esselborn, J.; Wittkamp, F.; Hofmann, E.; Apfel, U.-P.; Stripp, S. T.; Happe, T. Accumulating the Hydride State in the Catalytic Cycle of [FeFe]-Hydrogenases. *Nat. Commun.* **2017**, *8*, 16115.
(448) Lampret, O.; Duan, J.; Hofmann, E.; Winkler, M.; Armstrong, F. A.; Happe, T. The Roles of Long-Range Proton-Coupled Electron Transfer in the Directionality and Efficiency of [FeFe]-Hydrogenases. *Proc. Natl. Acad. Sci. U. S. A.* **2020**, *117*, 20520–20529.
(449) Duan, J.; Senger, M.; Esselborn, J.; Engelbrecht, V.; Wittkamp, F.; Apfel, U.-P.; Hofmann, E.; Stripp, S. T.; Happe, T.; Winkler, M. Crystallographic and Spectroscopic

Assignment of the Proton Transfer Pathway in [FeFe]-Hydrogenases. *Nat. Commun.* **2018**, *9*, 4726.
(450) Cornish, A. J.; Ginovska, B.; Thelen, A.; Da Silva, J. C. S.; Soares, T. A.; Raugei, S.; Dupuis, M.; Shaw, W. J.; Hegg, E. L. Single-Amino Acid Modifications Reveal Additional Controls on the Proton Pathway of [FeFe]-Hydrogenase. *Biochemistry* **2016**, *55*, 3165–3173.
(451) Knörzer, P.; Silakov, A.; Foster, C. E.; Armstrong, F. A.; Lubitz, W.; Happe, T. Importance of the Protein Framework for Catalytic Activity of [FeFe]-Hydrogenases. *J. Biol. Chem.* **2012**, *287*, 1489–1499.
(452) Bingham, A. S.; Smith, P. R.; Swartz, J. R. Evolution of an [FeFe] Hydrogenase with Decreased Oxygen Sensitivity. *Int. J. Hydrogen Energy* **2012**, *37*, 2965–2976.
(453) Koo, J.; Swartz, J. R. System Analysis and Improved [FeFe] Hydrogenase O2 Tolerance Suggest Feasibility for Photosynthetic H2 Production. *Metab. Eng.* **2018**, *49*, 21–27.
(454) Koo, J. Enhanced Aerobic H2 Production by Engineering an [FeFe] Hydrogenase from Clostridium Pasteurianum. *Int. J. Hydrogen Energy* **2020**, *45*, 10673–10679.
(455) Morra, S.; Giraudo, A.; Di Nardo, G.; King, P. W.; Gilardi, G.; Valetti, F. Site Saturation Mutagenesis Demonstrates a Central Role for Cysteine 298 as Proton Donor to the Catalytic Site in CaHydA [FeFe]-Hydrogenase. *PLoS One* **2012**, *7*, e48400.
(456) Morra, S.; Maurelli, S.; Chiesa, M.; Mulder, D. W.; Ratzloff, M. W.; Giamello, E.; King, P. W.; Gilardi, G.; Valetti, F. The Effect of a C298D Mutation in CaHydA [FeFe]-Hydrogenase: Insights into the Protein-Metal Cluster Interaction by EPR and FTIR Spectroscopic Investigation. *Biochim. Biophys. Acta - Bioenerg.* **2016**, *1857*, 98–106.
(457) Mulder, D. W.; Guo, Y.; Ratzloff, M. W.; King, P. W. Identification of a Catalytic Iron-Hydride at the H-Cluster of [FeFe]-Hydrogenase. *J. Am. Chem. Soc.* **2017**, *139*, 83–86.
(458) Mulder, D. W.; Ratzloff, M. W.; Bruschi, M.; Greco, C.; Koonce, E.; Peters, J. W.; King, P. W. Investigations on the Role of Proton-Coupled Electron Transfer in Hydrogen Activation by [FeFe]-Hydrogenase. *J. Am. Chem. Soc.* **2014**, *136*, 15394–15402.
(459) Pham, C. C.; Mulder, D. W.; Pelmenschikov, V.; King, P. W.; Ratzloff, M. W.; Wang, H.; Mishra, N.; Alp, E. E.; Zhao, J.; Hu, M. Y.; et al. Terminal Hydride Species in [FeFe]- Hydrogenases Are Vibrationally Coupled to the Active Site Environment. *Angew. Chemie Int. Ed.* **2018**, *57*, 10605–10609.
(460) Rumpel, S.; Sommer, C.; Reijerse, E.; Farès, C.; Lubitz, W. Direct Detection of the Terminal Hydride Intermediate in [FeFe] Hydrogenase by NMR Spectroscopy. *J. Am. Chem. Soc.* **2018**, *140*, 3863–3866.
(461) Rodríguez-Maciá, P.; Kertess, L.; Burnik, J.; Birrell, J. A.; Hofmann, E.; Lubitz, W.; Happe, T.; Rüdiger, O. His-Ligation to the [4Fe-4S] Subcluster Tunes the Catalytic Bias of [FeFe] Hydrogenase. *J. Am. Chem. Soc.* **2019**, *141*, 472–481.
(462) Kertess, L.; Adamska-Venkatesh, A.; Rodríguez-Maciá, P.; Rüdiger, O.; Lubitz, W.; Happe, T. Influence of the [4Fe-4S] Cluster Coordinating Cysteines on Active Site Maturation and Catalytic Properties of C. Reinhardtii [FeFe]-Hydrogenase. *Chem. Sci.* **2017**, *8*, 8127–8137.
(463) Orain, C.; Saujet, L.; Gauquelin, C.; Soucaille, P.; Meynial-Salles, I.; Baffert, C.; Fourmond, V.; Bottin, H.; Léger, C. Electrochemical Measurements of the Kinetics of Inhibition of Two FeFe Hydrogenases by O 2 Demonstrate That the Reaction Is Partly Reversible. *J. Am. Chem. Soc.* **2015**, *137*, 12580–12587.
(464) Sybirna, K.; Ezanno, P.; Baffert, C.; Léger, C.; Bottin, H. Arginine171 of Chlamydomonas Reinhardtii [Fe-Fe] Hydrogenase HydA1 Plays a Crucial Role in

Electron Transfer to Its Catalytic Center. *Int. J. Hydrogen Energy* **2013**, *38*, 2998–3002.
(465) Lampret, O.; Adamska-Venkatesh, A.; Konegger, H.; Wittkamp, F.; Apfel, U.-P.; Reijerse, E. J.; Lubitz, W.; Rüdiger, O.; Happe, T.; Winkler, M. Interplay between CN – Ligands and the Secondary Coordination Sphere of the H-Cluster in [FeFe]-Hydrogenases. *J. Am. Chem. Soc.* **2017**, *139*, 18222–18230.
(466) Kubas, A.; Orain, C.; Sancho, D. De; Saujet, L.; Sensi, M.; Gauquelin, C.; Meynial-salles, I.; Soucaille, P.; Bottin, H.; Baffert, C.; et al. Mechanism of O2 Diffusion and Reduction in FeFe Hydrogenases. *Nat. Chem.* **2016**, *9*, 88–95.
(467) Winkler, M.; Kuhlgert, S.; Hippler, M.; Happe, T. Characterization of the Key Step for Light-Driven Hydrogen Evolution in Green Algae. *J. Biol. Chem.* **2009**, *284*, 36620–36627.
(468) Engelbrecht, V.; Liedtke, K.; Rutz, A.; Yadav, S.; Günzel, A.; Happe, T. One Isoform for One Task? The Second Hydrogenase of Chlamydomonas Reinhardtii Prefers Hydrogen Uptake. *Int. J. Hydrogen Energy* **2021**, *46*, 7165–7175.
(469) Berggren, G.; Adamska, A.; Lambertz, C.; Simmons, T. R.; Esselborn, J.; Atta, M.; Gambarelli, S.; Mouesca, J.-M.; Reijerse, E.; Lubitz, W.; et al. Biomimetic Assembly and Activation of [FeFe]-Hydrogenases. *Nature* **2013**, *499*, 66–69.
(470) Esselborn, J.; Lambertz, C.; Adamska-Venkatesh, A.; Simmons, T.; Berggren, G.; Noth, J.; Siebel, J.; Hemschemeier, A.; Artero, V.; Reijerse, E.; et al. Spontaneous Activation of [FeFe]-Hydrogenases by an Inorganic [2Fe] Active Site Mimic. *Nat. Chem. Biol.* **2013**, *9*, 607–609.
(471) Adamska-Venkatesh, A.; Krawietz, D.; Siebel, J. F.; Weber, K.; Happe, T.; Reijerse, E.; Lubitz, W. New Redox States Observed in [FeFe] Hydrogenases Reveal Redox Coupling within the H-Cluster. *J. Am. Chem. Soc.* **2014**, *136*, 11339–11346.
(472) Siebel, J. F.; Adamska-Venkatesh, A.; Weber, K.; Rumpel, S.; Reijerse, E.; Lubitz, W. Hybrid [FeFe]-Hydrogenases with Modified Active Sites Show Remarkable Residual Enzymatic Activity. *Biochemistry* **2015**, *54*, 1474–1483.
(473) Adamska-Venkatesh, A.; Simmons, T. R.; Siebel, J. F.; Artero, V.; Fontecave, M.; Reijerse, E.; Lubitz, W. Artificially Maturated [FeFe] Hydrogenase from Chlamydomonas Reinhardtii: A HYSCORE and ENDOR Study of a Non-Natural H-Cluster. *Phys. Chem. Chem. Phys.* **2015**, *17*, 5421–5430.
(474) Adamska-Venkatesh, A.; Roy, S.; Siebel, J. F.; Simmons, T. R.; Fontecave, M.; Artero, V.; Reijerse, E.; Lubitz, W. Spectroscopic Characterization of the Bridging Amine in the Active Site of [FeFe] Hydrogenase Using Isotopologues of the H-Cluster. *J. Am. Chem. Soc.* **2015**, *137*, 12744–12747.
(475) Reijerse, E. J.; Pham, C. C.; Pelmenschikov, V.; Gilbert-Wilson, R.; Adamska-Venkatesh, A.; Siebel, J. F.; Gee, L. B.; Yoda, Y.; Tamasaku, K.; Lubitz, W.; et al. Direct Observation of an Iron-Bound Terminal Hydride in [FeFe]-Hydrogenase by Nuclear Resonance Vibrational Spectroscopy. *J. Am. Chem. Soc.* **2017**, *139*, 4306–4309.
(476) Noth, J.; Esselborn, J.; Güldenhaupt, J.; Brünje, A.; Sawyer, A.; Apfel, U.-P.; Gerwert, K.; Hofmann, E.; Winkler, M.; Happe, T. [FeFe]-Hydrogenase with Chalcogenide Substitutions at the H-Cluster Maintains Full H2 Evolution Activity. *Angew. Chemie Int. Ed.* **2016**, *55*, 8396–8400.
(477) Kertess, L.; Wittkamp, F.; Sommer, C.; Esselborn, J.; Rüdiger, O.; Reijerse, E. J.; Hofmann, E.; Lubitz, W.; Winkler, M.; Happe, T.; et al. Chalcogenide Substitution in the [2Fe] Cluster of [FeFe]-Hydrogenases Conserves High Enzymatic Activity. *Dalt. Trans.* **2017**, *46*, 16947–16958.
(478) Sommer, C.; Rumpel, S.; Roy, S.; Farès, C.; Artero, V.; Fontecave, M.; Reijerse, E.; Lubitz, W. Spectroscopic Investigations of a Semi-Synthetic [FeFe] Hydrogenase with

Propane Di-Selenol as Bridging Ligand in the Binuclear Subsite: Comparison to the Wild Type and Propane Di-Thiol Variants. *JBIC J. Biol. Inorg. Chem.* **2018**, *23*, 481–491.

(479) Sommer, C.; Richers, C. P.; Lubitz, W.; Rauchfuss, T. B.; Reijerse, E. J. A [RuRu] Analogue of an [FeFe]-Hydrogenase Traps the Key Hydride Intermediate of the Catalytic Cycle. *Angew. Chemie Int. Ed.* **2018**, *57*, 5429–5432.

(480) Duan, J.; Mebs, S.; Laun, K.; Wittkamp, F.; Heberle, J.; Hofmann, E.; Apfel, U.-P.; Winkler, M.; Senger, M.; Haumann, M.; et al. Geometry of the Catalytic Active Site in [FeFe]-Hydrogenase Is Determined by Hydrogen Bonding and Proton Transfer. *ACS Catal.* **2019**, *9*, 9140–9149.

(481) Esselborn, J.; Muraki, N.; Klein, K.; Engelbrecht, V.; Metzler-Nolte, N.; Apfel, U.-P.; Hofmann, E.; Kurisu, G.; Happe, T. A Structural View of Synthetic Cofactor Integration into [FeFe]-Hydrogenases. *Chem. Sci.* **2016**, *7*, 959–968.

(482) Popescu, C.; Münck, E. Electronic Structure of the H Cluster in [FeFe]-Hydrogenases. *J. Am. Chem. Soc.* **1999**, No. 5, 15054–15061.

(483) Pereira, A. S. S.; Tavares, P.; Moura, I.; Moura, J. J. G. J.; Huynh, B. H. H. Mössbauer Characterization of the Iron-Sulfur Clusters in Desulfovibrio v Ulgaris Hydrogenase. *J. Am. Chem. Soc.* **2001**, *123*, 2771–2782.

(484) Silakov, A.; Reijerse, E. J.; Albracht, S. P. J.; Hatchikian, E. C.; Lubitz, W. The Electronic Structure of the H-Cluster in the [FeFe]-Hydrogenase from Desulfovibrio Desulfuricans: A Q-Band 57Fe-ENDOR and HYSCORE Study. *J. Am. Chem. Soc.* **2007**, *129*, 11447–11458.

(485) Sidabras, J. W.; Duan, J.; Winkler, M.; Happe, T.; Hussein, R.; Zouni, A.; Suter, D.; Schnegg, A.; Lubitz, W.; Reijerse, E. J. Extending Electron Paramagnetic Resonance to Nanoliter Volume Protein Single Crystals Using a Self-Resonant Microhelix. *Sci. Adv.* **2019**, *5*, eaay1394.

(486) De Lacey, A. L.; Stadler, C.; Cavazza, C.; Hatchikian, E. C.; Fernandez, V. M. FTIR Characterization of the Active Site of the Fe-Hydrogenase from Desulfovibrio Desulfuricans. *J. Am. Chem. Soc.* **2000**, *122*, 11232–11233.

(487) Chen, Z.; Lemon, B. J.; Huang, S.; Swartz, D. J.; Peters, J. W.; Bagley, K. A. Infrared Studies of the CO-Inhibited Form of the Fe-Only Hydrogenase from Clostridium Pasteurianum I: Examination of Its Light Sensitivity at Cryogenic Temperatures. *Biochemistry* **2002**, *41*, 2036–2043.

(488) Roseboom, W.; De Lacey, A. L.; Fernandez, V. M.; Hatchikian, E. C.; Albracht, S. P. J. The Active Site of the [FeFe]-Hydrogenase from Desulfovibrio Desulfuricans. II. Redox Properties, Light Sensitivity and CO-Ligand Exchange as Observed by Infrared Spectroscopy. *J. Biol. Inorg. Chem.* **2006**, *11*, 102–118.

(489) Senger, M.; Mebs, S.; Duan, J.; Shulenina, O.; Laun, K.; Kertess, L.; Wittkamp, F.; Apfel, U.-P.; Happe, T.; Winkler, M.; et al. Protonation/Reduction Dynamics at the [4Fe–4S] Cluster of the Hydrogen-Forming Cofactor in [FeFe]-Hydrogenases. *Phys. Chem. Chem. Phys.* **2018**, *20*, 3128–3140.

(490) Goldet, G.; Brandmayr, C.; Stripp, S. T.; Happe, T.; Cavazza, C.; Fontecilla-Camps, J. C.; Armstrong, F. A. Electrochemical Kinetic Investigations of the Reactions of [FeFe]-Hydrogenases with Carbon Monoxide and Oxygen: Comparing the Importance of Gas Tunnels and Active-Site Electronic/Redox Effects. *J. Am. Chem. Soc.* **2009**, *131*, 14979–14989.

(491) Telser, J.; Benecky, M. J.; Adams, M. W. W.; Mortenson, L. E.; Hoffman, B. M. An EPR and Electron Nuclear Double Resonance Investigation of Carbon Monoxide Binding to Hydrogenase I (Bidirectional) from Clostridium Pasteurianum W5. *J. Biol. Chem.* **1986**, *261*, 13536–13541.

(492) Telser, J.; Benecky, M. J.; Adams, M. W. W.; Mortenson, L. E.; Hoffman, B. M. EPR

and Electron Nuclear Double Resonance Investigation of Oxidized Hydrogenase II (Uptake) from Clostridium Pasteurianum W5. Effects of Carbon Monoxide Binding. *J. Biol. Chem.* **1987**, *262*, 6589–6594.
(493) Reijerse, E.; Birrell, J. A.; Lubitz, W. Spin Polarization Reveals the Coordination Geometry of the [FeFe] Hydrogenase Active Site in Its CO-Inhibited State. *J. Phys. Chem. Lett.* **2020**, *11*, 4597–4602.
(494) Senger, M.; Mebs, S.; Duan, J.; Wittkamp, F.; Apfel, U.-P.; Heberle, J.; Haumann, M.; Stripp, S. T. Stepwise Isotope Editing of [FeFe]-Hydrogenases Exposes Cofactor Dynamics. *Proc. Natl. Acad. Sci. U. S. A.* **2016**, *113*, 8454–8459.
(495) Laun, K.; Mebs, S.; Duan, J.; Wittkamp, F.; Apfel, U.-P.; Happe, T.; Winkler, M.; Haumann, M.; Stripp, S. T. Spectroscopical Investigations on the Redox Chemistry of [FeFe]-Hydrogenases in the Presence of Carbon Monoxide. *MOLECULES* **2018**, *23*, 1669.
(496) Zilberman, S.; Stiefel, E. I.; Cohen, M. H.; Car, R. Resolving the CO / CN Ligand Arrangement in CO-Inactivated [FeFe] Hydrogenase by First Principles Density Functional Theory Calculations. *Inorg. Chem.* **2006**, *45*, 5715–5717.
(497) Greco, C.; Bruschi, M.; Heimdal, J.; Fantucci, P.; De Gioia, L.; Ryde, U. Structural Insights into the Active-Ready Form of [FeFe]-Hydrogenase and Mechanistic Details of Its Inhibition by Carbon Monoxide. *Inorg. Chem.* **2007**, *46*, 7256–7258.
(498) Yu, L.; Greco, C.; Bruschi, M.; Ryde, U.; De Gioia, L.; Reiher, M. Targeting Intermediates of [FeFe]-Hydrogenase by CO and CN Vibrational Signatures. *Inorg. Chem.* **2011**, *50*, 3888–3900.
(499) Sommer, C.; Adamska-Venkatesh, A.; Pawlak, K.; Birrell, J. A.; Rüdiger, O.; Reijerse, E. J.; Lubitz, W. Proton Coupled Electronic Rearrangement within the H-Cluster as an Essential Step in the Catalytic Cycle of [FeFe] Hydrogenases. *J. Am. Chem. Soc.* **2017**, *139*, 1440–1443.
(500) Katz, S.; Noth, J.; Horch, M.; Shafaat, H. S.; Happe, T.; Hildebrandt, P.; Zebger, I. Vibrational Spectroscopy Reveals the Initial Steps of Biological Hydrogen Evolution. *Chem. Sci.* **2016**, *7*, 6746–6752.
(501) Singleton, M. L.; Bhuvanesh, N.; Reibenspies, J. H.; Darensbourg, M. Y. Synthetic Support of De Novo Design: Sterically Bulky [FeFe]-Hydrogenase Models. *Angew. Chemie Int. Ed.* **2008**, *47*, 9492–9495.
(502) Senger, M.; Laun, K.; Wittkamp, F.; Duan, J.; Haumann, M.; Happe, T.; Winkler, M.; Apfel, U.-P.; Stripp, S. T. Proton-Coupled Reduction of the Catalytic [4Fe-4S] Cluster in [FeFe]-Hydrogenases. *Angew. Chemie Int. Ed.* **2017**, *56*, 16503–16506.
(503) Mebs, S.; Senger, M.; Duan, J.; Wittkamp, F.; Apfel, U.-P.; Happe, T.; Winkler, M.; Stripp, S. T.; Haumann, M. Bridging Hydride at Reduced H-Cluster Species in [FeFe]-Hydrogenases Revealed by Infrared Spectroscopy, Isotope Editing, and Quantum Chemistry. *J. Am. Chem. Soc.* **2017**, *139*, 12157–12160.
(504) Birrell, J. A.; Pelmenschikov, V.; Mishra, N.; Wang, H.; Yoda, Y.; Rauchfuss, T. B.; Cramer, S. P.; Lubitz, W.; Debeer, S. Spectroscopic and Computational Evidence That [FeFe] Hydrogenases Operate Exclusively with CO-Bridged Intermediates. *J. Am. Chem. Soc.* **2020**, *142*, 222–232.
(505) Lorent, C.; Katz, S.; Duan, J.; Kulka, C. J.; Caserta, G.; Teutloff, C.; Yadav, S.; Apfel, U.-P.; Winkler, M.; Happe, T.; et al. Shedding Light on Proton and Electron Dynamics in [FeFe] Hydrogenases. *J. Am. Chem. Soc.* **2020**, *142*, 5493–5497.
(506) Stripp, S. T.; Mebs, S.; Haumann, M. Temperature Dependence of Structural Dynamics at the Catalytic Cofactor of [FeFe]-Hydrogenase. *Inorg. Chem.* **2020**, *59*, 16474–16488.
(507) Haumann, M.; Stripp, S. T. The Molecular Proceedings of Biological Hydrogen Turnover. *Acc. Chem. Res.* **2018**, *51*, 1755–1763.

(508) Siegbahn, P. E. M.; Liao, R. Z. Energetics for Proton Reduction in FeFe Hydrogenase. *J. Phys. Chem. A* **2020**, *124*, 10540–10549.
(509) Kleinhaus, J. T.; Wittkamp, F.; Yadav, S.; Siegmund, D.; Apfel, U.-P. [FeFe]-Hydrogenases: Maturation and Reactivity of Enzymatic Systems and Overview of Biomimetic Models. *Chem. Soc. Rev.* **2021**, No. 50, 1668–1784.
(510) Birrell, J. A.; Rodríguez-Maciá, P.; Reijerse, E. J.; Martini, M. A.; Lubitz, W. The Catalytic Cycle of [FeFe] Hydrogenase: A Tale of Two Sites. *Coord. Chem. Rev.* **2021**, *449*, 214191.
(511) Albracht, S. P. J.; Roseboom, W.; Hatchikian, E. C. The Active Site of the [FeFe]-Hydrogenase from Desulfovibrio Desulfuricans. I. Light Sensitivity and Magnetic Hyperfine Interactions as Observed by Electron Paramagnetic Resonance. *J. Biol. Inorg. Chem.* **2006**, *11*, 88–101.
(512) Adamska-Venkatesh, A.; Silakov, A.; Lambertz, C.; Rüdiger, O.; Happe, T.; Reijerse, E.; Lubitz, W. Identification and Characterization of the "Super-Reduced" State of the H-Cluster in [FeFe] Hydrogenase: A New Building Block for the Catalytic Cycle? *Angew. Chemie Int. Ed.* **2012**, *51*, 11458–11462.
(513) Laun, K.; Baranova, I.; Duan, J.; Kertess, L.; Wittkamp, F.; Apfel, U.-P.; Happe, T.; Senger, M.; Stripp, S. T. Site-Selective Protonation of the One-Electron Reduced Cofactor in [FeFe]-Hydrogenase. *Dalt. Trans.* **2021**, *50*, 3641–3650.
(514) Krasna, A. I.; Rittenberg, D. The Mechanism of Action of the Enzyme Hydrogenase1. *J. Am. Chem. Soc.* **1954**, *76*, 3015–3020.
(515) Pelmenschikov, V.; Birrell, J. A.; Pham, C. C.; Mishra, N.; Wang, H.; Sommer, C.; Reijerse, E.; Richers, C. P.; Tamasaku, K.; Yoda, Y.; et al. Reaction Coordinate Leading to H2 Production in [FeFe]-Hydrogenase Identified by Nuclear Resonance Vibrational Spectroscopy and Density Functional Theory. *J. Am. Chem. Soc.* **2017**, *139*, 16894–16902.
(516) Hajj, V.; Baffert, C.; Sybirna, K.; Meynial-Salles, I.; Soucaille, P.; Bottin, H.; Fourmond, V.; Léger, C. FeFe Hydrogenase Reductive Inactivation and Implication for Catalysis. *Energy Environ. Sci.* **2014**, *7*, 715–719.
(517) Patil, D. S.; Moura, J. J.; He, S. H.; Teixeira, M.; Prickril, B. C.; DerVartanian, D. V; Peck, H. D.; LeGall, J.; Huynh, B. H. EPR-Detectable Redox Centers of the Periplasmic Hydrogenase from Desulfovibrio Vulgaris. *J. Biol. Chem.* **1988**, *263*, 18732–18738.
(518) van der Spek, T. M.; Arendsen, A. F.; Happe, R. P.; Yun, S.; Bagley, K. A.; Stufkens, D. J.; Hagen, W. R.; Albracht, S. P. J.; Spek, T. M.; Arendsen, A. F.; et al. Similarities in the Architecture of the Active Sites of Ni-Hydrogenases and Fe-Hydrogenases Detected by Means of Infrared Spectroscopy. *Eur. J. Biochem.* **1996**, *237*, 629–634.
(519) Westen, H. M. van der; Mayhew, S. G.; Veeger, C. Separation of Hydrogenase from Intact Cells of Desulfovibrio Vulgaris Purification and Properties. *FEBS Lett.* **1978**, *86*, 122–126.
(520) Rodríguez-Maciá, P.; Reijerse, E. J.; Van Gastel, M.; Debeer, S.; Lubitz, W.; Rüdiger, O.; Birrell, J. A. Sulfide Protects [FeFe] Hydrogenases from O2. *J. Am. Chem. Soc.* **2018**, *140*, 9346–9350.
(521) Rodríguez-Maciá, P.; Galle, L. M.; Bjornsson, R.; Lorent, C.; Zebger, I.; Yoda, Y.; Cramer, S. P.; DeBeer, S.; Span, I.; Birrell, J. A. Caught in the Hinact: Crystal Structure and Spectroscopy Reveal a Sulfur Bound to the Active Site of an O2-Stable State of [FeFe] Hydrogenase. *Angew. Chemie - Int. Ed.* **2020**, *59*, 16786–16794.
(522) Felbek, C.; Arrigoni, F.; de Sancho, D.; Jacq-Bailly, A.; Best, R. B.; Fourmond, V.; Bertini, L.; Léger, C. Mechanism of Hydrogen Sulfide-Dependent Inhibition of FeFe Hydrogenase. *ACS Catal.* **2021**, *11*, 15162–15176.
(523) Parkin, A.; Cavazza, C.; Fontecilla-Camps, J. C.; Armstrong, F. a. Electrochemical

Investigations of the Interconversions between Catalytic and Inhibited States of the [FeFe]-Hydrogenase from Desulfovibrio Desulfuricans. *J. Am. Chem. Soc.* **2006**, *128*, 16808–16815.
(524) del Barrio, M.; Sensi, M.; Fradale, L.; Bruschi, M.; Greco, C.; de Gioia, L.; Bertini, L.; Fourmond, V.; Léger, C. Interaction of the H-Cluster of FeFe Hydrogenase with Halides. *J. Am. Chem. Soc.* **2018**, *140*, 5485–5492.
(525) Morra, S.; Arizzi, M.; Valetti, F.; Gilardi, G. Oxygen Stability in the New [FeFe]-Hydrogenase from Clostridium Beijerinckii SM10 (CbA5H). *Biochemistry* **2016**, *55*, 5897–5900.
(526) Bruska, M. K.; Stiebritz, M. T.; Reiher, M. Regioselectivity of H-Cluster Oxidation. *J. Am. Chem. Soc.* **2011**, *133*, 20588–20603.
(527) Stiebritz, M. T.; Reiher, M. Hydrogenases and Oxygen. *Chem. Sci.* **2012**, *3*, 1739–1751.
(528) Finkelmann, A. R.; Stiebritz, M. T.; Reiher, M. Activation Barriers of Oxygen Transformation at the Active Site of [FeFe] Hydrogenases. *Inorg. Chem.* **2014**, *53*, 11890–11902.
(529) Kubas, A.; De Sancho, D.; Best, R. B.; Blumberger, J. Aerobic Damage to [FeFe]-Hydrogenases: Activation Barriers for the Chemical Attachment of O2. *Angew. Chemie - Int. Ed.* **2014**, *53*, 4081–4084.
(530) Stripp, S. T.; Goldet, G.; Brandmayr, C.; Sanganas, O.; Vincent, K. A.; Haumann, M.; Armstrong, F. A.; Happe, T. How Oxygen Attacks [FeFe] Hydrogenases from Photosynthetic Organisms. *Proc. Natl. Acad. Sci. U. S. A.* **2009**, *106*, 17331–17336.
(531) Lambertz, C.; Leidel, N.; Havelius, K. G. V; Noth, J.; Chernev, P.; Winkler, M.; Happe, T.; Haumann, M. O2 Reactions at the Six-Iron Active Site (H-Cluster) in [FeFe]-Hydrogenase. *J. Biol. Chem.* **2011**, *286*, 40614–40623.
(532) Swanson, K. D.; Ratzloff, M. W.; Mulder, D. W.; Artz, J. H.; Ghose, S.; Hoffman, A.; White, S.; Zadvornyy, O. A.; Broderick, J. B.; Bothner, B.; et al. [FeFe]-Hydrogenase Oxygen Inactivation Is Initiated at the H Cluster 2Fe Subcluster. *J. Am. Chem. Soc.* **2015**, *137*, 1809–1816.
(533) Mebs, S.; Kositzki, R.; Duan, J.; Kertess, L.; Senger, M.; Wittkamp, F.; Apfel, U.-P.; Happe, T.; Stripp, S. T.; Winkler, M.; et al. Hydrogen and Oxygen Trapping at the H-Cluster of [FeFe]-Hydrogenase Revealed by Site-Selective Spectroscopy and QM/MM Calculations. *BBA - Bioenerg.* **2017**, *1859*, 28–41.
(534) Esselborn, J.; Kertess, L.; Apfel, U.-P.; Hofmann, E.; Happe, T. Loss of Specific Active-Site Iron Atoms in Oxygen-Exposed [FeFe]-Hydrogenase Determined by Detailed X-Ray Structure Analyses. *J. Am. Chem. Soc.* **2019**, *141*, 17721–17728.
(535) Kuchenreuther, J. M.; Britt, R. D.; Swartz, J. R. New Insights into [FeFe] Hydrogenase Activation and Maturase Function. *PLoS One* **2012**, *7*, e45850.
(536) Mulder, D. W.; Ortillo, D. O.; Gardenghi, D. J.; Naumov, A. V.; Ruebush, S. S.; Szilagyi, R. K.; Huynh, B.; Broderick, J. B.; Peters, J. W. Activation of HydA(DeltaEFG) Requires a Preformed [4Fe-4S] Cluster. *Biochemistry* **2009**, *48*, 6240–6248.
(537) Böck, A.; King, P. W.; Blokesch, M.; Posewitz, M. C. Maturation of Hydrogenases. In *Advances In Microbial Physiology*; 2006; Vol. 51, pp 1–71.
(538) McGlynn, S. E.; Shepard, E. M.; Winslow, M. a; Naumov, A. V; Duschene, K. S.; Posewitz, M. C.; Broderick, W. E.; Broderick, J. B.; Peters, J. W. HydF as a Scaffold Protein in [FeFe] Hydrogenase H-Cluster Biosynthesis. *FEBS Lett.* **2008**, *582*, 2183–2187.
(539) Caserta, G.; Pecqueur, L.; Adamska-Venkatesh, A.; Papini, C.; Roy, S.; Artero, V.; Atta, M.; Reijerse, E.; Lubitz, W.; Fontecave, M. Structural and Functional Characterization of the Hydrogenase-Maturation HydF Protein. *Nat. Chem. Biol.* **2017**,

13, 779–784.
(540) Scott, A. G.; Szilagyi, R. K.; Mulder, D. W.; Ratzloff, M. W.; Byer, A. S.; King, P. W.; Broderick, W. E.; Shepard, E. M.; Broderick, J. B. Compositional and Structural Insights into the Nature of the H-Cluster Precursor on HydF. *Dalt. Trans.* **2018**, *47*, 9521–9535.
(541) Shepard, E. M.; Duffus, B. R.; George, S. J.; McGlynn, S. E.; Challand, M. R.; Swanson, K. D.; Roach, P. L.; Cramer, S. P.; Peters, J. W.; Broderick, J. B. [FeFe]-Hydrogenase Maturation: HydG-Catalyzed Synthesis of Carbon Monoxide. *J. Am. Chem. Soc.* **2010**, *132*, 9247–9249.
(542) Driesener, R. C.; Challand, M. R.; McGlynn, S. E.; Shepard, E. M.; Boyd, E. S.; Broderick, J. B.; Peters, J. W.; Roach, P. L. [FeFe]-Hydrogenase Cyanide Ligands Derived from S-Adenosylmethionine-Dependent Cleavage of Tyrosine. *Angew. Chemie Int. Ed.* **2010**, *49*, 1687–1690.
(543) Kuchenreuther, J. M.; Myers, W. K.; Suess, D. L. M.; Stich, T. a; Pelmenschikov, V.; Shiigi, S. a; Cramer, S. P.; Swartz, J. R.; Britt, R. D.; George, S. J. The HydG Enzyme Generates an Fe(CO)2(CN) Synthon in Assembly of the FeFe Hydrogenase H-Cluster. *Science* . **2014**, *343*, 424–427.
(544) Nicolet, Y.; Pagnier, A.; Zeppieri, L.; Martin, L.; Amara, P.; Fontecilla-Camps, J. C. Crystal Structure of HydG from Carboxydothermus Hydrogenoformans: A Trifunctional [FeFe]-Hydrogenase Maturase. *ChemBioChem* **2015**, *16*, 397–402.
(545) Rao, G.; Tao, L.; Suess, D. L. M.; Britt, R. D. A [4Fe-4S]-Fe(CO)(CN)-l-Cysteine Intermediate Is the First Organometallic Precursor in [FeFe] Hydrogenase H-Cluster Bioassembly. *Nat. Chem.* **2018**, *10*, 555–560.
(546) Betz, J. N.; Boswell, N. W.; Fugate, C. J.; Holliday, G. L.; Akiva, E.; Scott, A. G.; Babbitt, P. C.; Peters, J. W.; Shepard, E. M.; Broderick, J. B. Hydrogenase Maturation: Insights into the Role Hyde Plays in Dithiomethylamine Biosynthesis. *Biochemistry* **2015**, *54*, 1807–1818.
(547) Rohac, R.; Amara, P.; Benjdia, A.; Martin, L.; Ruffié, P.; Favier, A.; Berteau, O.; Mouesca, J. M.; Fontecilla-Camps, J. C.; Nicolet, Y. Carbon-Sulfur Bond-Forming Reaction Catalysed by the Radical SAM Enzyme HydE. *Nat. Chem.* **2016**, *8*, 491–500.
(548) Rao, G.; Tao, L.; Britt, R. D. Serine Is the Molecular Source of the NH(CH2)2 Bridgehead Moiety of the in Vitro Assembled [FeFe] Hydrogenase H-Cluster Guodong. *Chem. Sci.* **2020**, *11*, 1241–1247.
(549) Simmons, T. R.; Berggren, G.; Bacchi, M.; Fontecave, M.; Artero, V. Mimicking Hydrogenases: From Biomimetics to Artificial Enzymes. *Coord. Chem. Rev.* **2014**, *270–271*, 127–150.
(550) Artero, V.; Berggren, G.; Atta, M.; Caserta, G.; Roy, S.; Pecqueur, L.; Fontecave, M. From Enzyme Maturation to Synthetic Chemistry: The Case of Hydrogenases. *Acc. Chem. Res.* **2015**, *48*, 2380–2387.
(551) Peters, J. W. Structure and Mechanism of Iron-Only Hydrogenases. *Curr. Opin. Struct. Biol.* **1999**, *9*, 670–676.
(552) Adamska-Venkatesh, A.; Simmons, T. R.; Siebel, J. F.; Artero, V.; Fontecave, M.; Reijerse, E.; Lubitz, W. Artificially Maturated [FeFe] Hydrogenase from Chlamydomonas Reinhardtii: A HYSCORE and ENDOR Study of a Non-Natural H-Cluster. *Phys. Chem. Chem. Phys.* **2015**, *17*, 5421–5430.
(553) Bruschi, M.; Greco, C.; Kaukonen, M.; Fantucci, P.; Ryde, U.; De Gioia, L. Influence of the [2Fe]H Subcluster Environment on the Properties of Key Intermediates in the Catalytic Cycle of [FeFe] Hydrogenases: Hints for the Rational Design of Synthetic Catalysts. *Angew. Chemie Int. Ed.* **2009**, *48*, 3503–3506.
(554) Braga, D.; Grepioni, F. Hydrogen-Bonding Interactions with the CO Ligand in the Solid State. *Acc. Chem. Res.* **1997**, *30*, 81–87.

(555) Artz, J. H.; Zadvornyy, O. A.; Mulder, D. W.; Keable, S. M.; Cohen, A. E.; Ratzloff, M. W.; Williams, S. G.; Ginovska, B.; Kumar, N.; Song, J.; et al. Tuning Catalytic Bias of Hydrogen Gas Producing Hydrogenases. *J. Am. Chem. Soc.* **2020**, *142*, 1227–1235.
(556) Ratzloff, M. W.; Artz, J. H.; Mulder, D. W.; Collins, R. T.; Furtak, T. E.; King, P. W. CO-Bridged H-Cluster Intermediates in the Catalytic Mechanism of [FeFe]-Hydrogenase CaI. *J. Am. Chem. Soc.* **2018**, *140*, 7623–7628.
(557) Ginovska-Pangovska, B.; Dutta, A.; Reback, M. L.; Linehan, J. C.; Shaw, W. J. Beyond the Active Site: The Impact of the Outer Coordination Sphere on Electrocatalysts for Hydrogen Production and Oxidation. *Acc. Chem. Res.* **2014**, *47*, 2621–2630.
(558) Esmieu, C.; Raleiras, P.; Berggren, G. From Protein Engineering to Artificial Enzymes-Biological and Biomimetic Approaches towards Sustainable Hydrogen Production. *Sustain. Energy Fuels* **2018**, *2*, 724–750.
(559) Amanullah, S.; Saha, P.; Nayek, A.; Ahmed, M. E.; Dey, A. Biochemical and Artificial Pathways for the Reduction of Carbon Dioxide, Nitrite and the Competing Proton Reduction: Effect of 2ndsphere Interactions in Catalysis. *Chem. Soc. Rev.* **2021**, *50*, 3755–3823.
(560) Hong, G.; Cornish, A. J.; Hegg, E. L.; Pachter, R. On Understanding Proton Transfer to the Biocatalytic [Fe-Fe](H) Sub-Cluster in [Fe-Fe]H(2)Ases: QM/MM MD Simulations. *Biochim. Biophys. Acta* **2011**, *1807*, 510–517.
(561) Sode, O.; Voth, G. A. Electron Transfer Activation of a Second Water Channel for Proton Transport in [FeFe]-Hydrogenase. *J. Chem. Phys.* **2014**, *141*, 22D527.
(562) Ginovska-Pangovska, B.; Ho, M.-H.; Linehan, J. C.; Cheng, Y.; Dupuis, M.; Raugei, S.; Shaw, W. J. Molecular Dynamics Study of the Proposed Proton Transport Pathways in [FeFe]-Hydrogenase. *Biochim. Biophys. Acta* **2014**, *1837*, 131–138.
(563) Long, H.; King, P. W.; Chang, C. H. Proton Transport in Clostridium Pasteurianum [FeFe] Hydrogenase I: A Computational Study. *J. Phys. Chem. B* **2014**, *118*, 890–900.
(564) Cornish, A. J.; Gärtner, K.; Yang, H.; Peters, J. W.; Hegg, E. L. Mechanism of Proton Transfer in [FeFe]-Hydrogenase from Clostridium Pasteurianum. *J. Biol. Chem.* **2011**, *19*, 38341–38347.
(565) Senger, M.; Eichmann, V.; Laun, K.; Duan, J.; Wittkamp, F.; Knör, G.; Apfel, U.-P.; Happe, T.; Winkler, M.; Heberle, J.; et al. How [FeFe]-Hydrogenase Facilitates Bidirectional Proton Transfer. *J. Am. Chem. Soc.* **2019**, *141*, 17394–17403.
(566) Mebs, S.; Duan, J.; Wittkamp, F.; Stripp, S. T.; Happe, T.; Apfel, U.-P.; Winkler, M.; Haumann, M. Differential Protonation at the Catalytic Six-Iron Cofactor of [FeFe]-Hydrogenases Revealed by 57 Fe Nuclear Resonance X-Ray Scattering and Quantum Mechanics/Molecular Mechanics Analyses. *Inorg. Chem.* **2019**, *58*, 4000–4013.
(567) Gray, H. B.; Winkler, J. R. Long-Range Electron Transfer. *Proc. Natl. Acad. Sci. U. S. A.* **2005**, *102*, 3534–3539.
(568) Kaila, V. R. I. Long-Range Proton-Coupled Electron Transfer in Biological Energy Conversion: Towards Mechanistic Understanding of Respiratory Complex I. *J. R. Soc. Interface* **2018**, *15*, 20170916.
(569) Rodríguez-Maciá, P.; Breuer, N.; DeBeer, S.; Birrell, J. A. Insight into the Redox Behavior of the [4Fe-4S] Subcluster in [FeFe] Hydrogenases. *ACS Catal.* **2020**, *10*, 13084–13095.
(570) Cohen, J.; Kim, K.; King, P.; Seibert, M.; Schulten, K. Finding Gas Diffusion Pathways in Proteins: Application to O2 and H2 Transport in CpI [FeFe]-Hydrogenase and the Role of Packing Defects. *Structure* **2005**, *13*, 1321–1329.
(571) Mohammadi, M.; Vashisth, H. Pathways and Thermodynamics of Oxygen Diffusion in [FeFe]-Hydrogenase. *J. Phys. Chem. B* **2017**, *121*, 10007.
(572) Liu, Y.; Mohammadi, M.; Vashisth, H. Diffusion Network of CO in FeFe-

Hydrogenase. *J. Chem. Phys.* **2018**, *149*, 204108.
(573) Stapleton, J. A.; Swartz, J. R. A Cell-Free Microtiter Plate Screen for Improved [FeFe] Hydrogenases. *PLoS One* **2010**, *5*, e10554.
(574) Stapleton, J. A.; Swartz, J. R. Development of an in Vitro Compartmentalization Screen for High-Throughput Directed Evolution of [FeFe] Hydrogenases. *PLoS One* **2010**, *5*, e15275.
(575) Appel, A. M.; Bercaw, J. E.; Bocarsly, A. B.; Dobbek, H.; Dubois, D. L.; Dupuis, M.; Ferry, J. G.; Fujita, E.; Hille, R.; Kenis, P. J. A.; et al. Frontiers, Opportunities, and Challenges in Biochemical and Chemical Catalysis of CO2 Fixation. *Chem. Rev.* **2013**, *113*, 6621–6658.
(576) Hartmann, T.; Schwanhold, N.; Leimkühler, S. Assembly and Catalysis of Molybdenum or Tungsten-Containing Formate Dehydrogenases from Bacteria. *BBA - Proteins Proteomics* **2015**, *1854*, 1090–1100.
(577) Maia, L. B.; Moura, I.; Moura, J. J. G. Carbon Dioxide Utilisation—The Formate Route. In *Enzymes for Solving Humankind's Problems*; Moura, J. J. G., Moura, I., Maia, L. B., Eds.; Springer Nature Switzerland: Cham, Switzerland, 2021; pp 29–81.
(578) Thauer, R. K.; Jungermann, K.; Decker, K. Energy Conservation in Chemotrophic Anaerobic Bacteria. *Bacteriol. Rev.* **1977**, *41*, 100–180.
(579) Nielsen, C. F.; Lange, L.; Meyer, A. S. Classification and Enzyme Kinetics of Formate Dehydrogenases for Biomanufacturing via CO2 Utilization. *Biotechnol. Adv.* **2019**, *37*, 107408.
(580) Popov, V. O.; Lamzin, V. S. NAD+-Dependent Formate Dehydrogenase. *Biochem. J.* **1994**, *301*, 625–643.
(581) Schirwitz, K.; Schmidt, A.; Lamzin, V. S. High-Resolution Structures of Formate Dehydrogenase from Candida Boidinii. *Protein Sci.* **2007**, *16*, 1146–1156.
(582) Maia, L. B.; Moura, J. J.; Moura, I. Molybdenum and Tungsten-Dependent Formate Dehydrogenases. *J. Biol. Inorg. Chem.* **2015**, *20*, 287–309.
(583) Niks, D.; Hille, R. Molybdenum- and Tungsten-Containing Formate Dehydrogenases and Formylmethanofuran Dehydrogenases: Structure, Mechanism, and Cofactor Insertion. *Protein Sci.* **2019**, *28*, 111–122.
(584) Hille, R. The Mononuclear Molybdenum Enzymes. *Chem. Rev.* **1996**, *96*, 2757–2816.
(585) Hille, R.; Hall, J.; Basu, P. The Mononuclear Molybdenum Enzymes. *Chem. Rev.* **2014**, *114*, 3963–4038.
(586) Axley, M. J.; Böck, A.; Stadtman, T. C. Catalytic Properties of an Escherichia Coli Formate Dehydrogenase Mutant in Which Sulfur Replaces Selenium. *Proc. Natl. Acad. Sci. U. S. A.* **1991**, *88*, 8450–8454.
(587) Kletzin, A.; Adams, M. W. Tungsten in Biological Systems. *FEMS Microbiol. Rev.* **1996**, *18*, 5–63.
(588) Johnson, M. K.; Rees, D. C.; Adams, M. W. Tungstoenzymes. *Chem. Rev.* **1996**, *96*, 2817–2840.
(589) Brondino, C. D.; Passeggi, M. C.; Caldeira, J.; Almendra, M. J.; Feio, M. J.; Moura, J. J.; Moura, I. Incorporation of Either Molybdenum or Tungsten into Formate Dehydrogenase from Desulfovibrio Alaskensis NCIMB 13491; EPR Assignment of the Proximal Iron-Sulfur Cluster to the Pterin Cofactor in Formate Dehydrogenases from Sulfate-Reducing Bacteria. *J. Biol. Inorg. Chem.* **2004**, *9*, 145–151.
(590) Moura, J. J.; Brondino, C. D.; Trincao, J.; Romao, M. J. Mo and W Bis-MGD Enzymes: Nitrate Reductases and Formate Dehydrogenases. *J. Biol. Inorg. Chem.* **2004**, *9*, 791–799.
(591) Almendra, M. J.; Brondino, C. D.; Gavel, O.; Pereira, A. S.; Tavares, P.; Bursakov, S.; Duarte, R.; Caldeira, J.; Moura, J. J. G.; Moura, I. Purification and Characterization of a Tungsten-Containing Formate Dehydrogenase from Desulfovibrio Gigas.

Biochemistry **1999**, *38*, 16366–16372.
(592) Radon, C.; Mittelstädt, G.; Duffus, B. R.; Bürger, J.; Hartmann, T.; Mielke, T.; Teutloff, C.; Leimkühler, S.; Wendler, P. Cryo-EM Structures Reveal Intricate Fe-S Cluster Arrangement and Charging in Rhodobacter Capsulatus Formate Dehydrogenase. *Nat. Commun.* **2020**, *11*, 1912.
(593) Meneghello, M.; Oliveira, A. R.; Jacq-Bailly, A.; Pereira, I. A. C.; Leger, C.; Fourmond, V. Formate Dehydrogenases Reduce CO2 Rather than HCO3-: An Electrochemical Demonstration. *Angew. Chemie Int. Ed.* **2021**, *60*, 9964–9967.
(594) Meneghello, M.; Léger, C.; Fourmond, V. Electrochemical Studies of CO 2 - Reducing Metalloenzymes. *Chem. – A Eur. J.* **2021**, *27*, 17542–17553.
(595) Axley, M. J.; Grahame, D. A. Kinetics for Formate Dehydrogenase of Escherichia Coli Formate-Hydrogenlyase. *J. Biol. Chem.* **1991**, *266*, 13731–13736.
(596) da Silva, S. M.; Pimentel, C.; Valente, F. M. A.; Rodrigues-Pousada, C.; Pereira, I. A. C. Tungsten and Molybdenum Regulation of Formate Dehydrogenase Expression in Desulfovibrio Vulgaris Hildenborough. *J. Bacteriol.* **2011**, *193*, 2909–2916.
(597) Hartmann, T.; Leimkühler, S. The Oxygen-Tolerant and NAD+-Dependent Formate Dehydrogenase from Rhodobacter Capsulatus Is Able to Catalyze the Reduction of CO2 to Formate. *FEBS J.* **2013**, *280*, 6083–6096.
(598) Schmitz, R. A.; Richter, M.; Linder, D.; Thauer, R. K. A Tungsten-Containing Active Formylmethanofuran Dehydrogenase in the Thermophilic Archaeon Methanobacterium Wolfei. *Eur. J. Biochem.* **1992**, *207*, 559–565.
(599) Hartmann, T.; Schrapers, P.; Utesch, T.; Nimtz, M.; Rippers, Y.; Dau, H.; Mroginski, M. A.; Haumann, M.; Leimkühler, S. The Molybdenum Active Site of Formate Dehydrogenase Is Capable of Catalyzing C-H Bond Cleavage and Oxygen Atom Transfer Reactions. *Biochemistry* **2016**, *55*, 2381–2389.
(600) Oliveira, A. R.; Mota, C.; Mourato, C.; Domingos, R. M.; Santos, M. F. A.; Gesto, D.; Guigliarelli, B.; Santos-Silva, T.; Romao, M. J.; Pereira, I. A. C. Toward the Mechanistic Understanding of Enzymatic CO2 Reduction. *ACS Catal.* **2020**, *10*, 3844–3856.
(601) Plugge, C. M.; Zhang, W.; Scholten, J. C.; Stams, A. J. Metabolic Flexibility of Sulfate-Reducing Bacteria. *Front. Microbiol.* **2011**, *2*, 81.
(602) Stams, A. J.; Plugge, C. M. Electron Transfer in Syntrophic Communities of Anaerobic Bacteria and Archaea. *Nat. Rev. Microbiol.* **2009**, *7*, 568–577.
(603) Rossmann, R.; Sawers, G.; Böck, A. Mechanism of Regulation of the Formate-Hydrogenlyase Pathway by Oxygen, Nitrate, and PH: Definition of the Formate Regulon. *Mol. Microbiol.* **1991**, *5*, 2807–2814.
(604) Lamont, C. M.; Kelly, C. L.; Pinske, C.; Buchanan, G.; Palmer, T.; Sargent, F. Expanding the Substrates for a Bacterial Hydrogenlyase Reaction. *Microbiology* **2017**, *163*, 649–653.
(605) Finney, A. J.; Lowden, R.; Fleszar, M.; Albareda, M.; Coulthurst, S. J.; Sargent, F. The Plant Pathogen Pectobacterium Atrosepticum Contains a Functional Formate Hydrogenlyase-2 Complex. *Mol. Microbiol.* **2019**, *112*, 1440–1452.
(606) Ramio-Pujol, S.; Ganigue, R.; Baneras, L.; Colprim, J. Impact of Formate on the Growth and Productivity of Clostridium Ljungdahlii PETC and Clostridium Carboxidivorans P7 Grown on Syngas. *Int. Microbiol.* **2014**, *17*, 195–204.
(607) Sawers, G.; Suppmann, B. Anaerobic Induction of Pyruvate Formate-Lyase Gene Expression Is Mediated by the ArcA and FNR Proteins. *J. Bacteriol.* **1992**, *174*, 3474–3478.
(608) Sawers, G. The Hydrogenases and Formate Dehydrogenases of Escherichia Coli. *Antonie Van Leeuwenhoek* **1994**, *66*, 57–88.
(609) Schwarz, F. M.; Schuchmann, K.; Müller, V. Hydrogenation of CO2 at Ambient

Pressure Catalyzed by a Highly Active Thermostable Biocatalyst. *Biotechnol. Biofuels* **2018**, *11*, 237.
(610) Vorholt, J. A.; Thauer, R. K. Molybdenum and Tungsten Enzymes in C1 Metabolism. In *Metals Ions in Biological System: Volume 39: Molybdenum and Tungsten: Their Roles in Biological Processes.*; Sigel, A., Sigel, H., Eds.; CRC Press: Boc Raton, FL, USA, 2002; Vol. 39, pp 571–619.
(611) Thauer, R. K. Biochemistry of Methanogenesis: A Tribute to Marjory Stephenson:1998 Marjory Stephenson Prize Lecture. *Microbiology* **1998**, *144*, 2377–2406.
(612) Börner, G.; Karrasch, M.; Thauer, R. K. Formylmethanofuran Dehydrogenase-Activity in Cell-Extracts of Methanobacterium-Thermoautotrophicum and of Methanosarcina-Barkeri. *Febs Lett.* **1989**, *244*, 21–25.
(613) Wagner, T.; Ermler, U.; Shima, S. The Methanogenic CO2 Reducing-and-Fixing Enzyme Is Bifunctional and Contains 46 [4Fe-4S] Clusters. *Science* . **2016**, *354*, 114–117.
(614) Welte, C.; Kröninger, L.; Deppenmeier, U. Experimental Evidence of an Acetate Transporter Protein and Characterization of Acetate Activation in Aceticlastic Methanogenesis of Methanosarcina Mazei. *FEMS Microbiol. Lett.* **2014**, *359*, 147–153.
(615) Kurth, J. M.; Op den Camp, H. J. M.; Welte, C. U. Several Ways One Goal—Methanogenesis from Unconventional Substrates. *Appl. Microbiol. Biotechnol.* **2020**, *104*, 6839–6854.
(616) Schmitz, R. A.; Albracht, S. P.; Thauer, R. K. A Molybdenum and a Tungsten Isoenzyme of Formylmethanofuran Dehydrogenase in the Thermophilic Archaeon Methanobacterium Wolfei. *Eur. J. Biochem.* **1992**, *209*, 1013–1018.
(617) Schmitz, R. A.; Albracht, S. P. J.; Thauer, R. K. Properties of the Tungsten-Substituted Molybdenum Formylmethanofuran Dehydrogenase from Methanobacterium Wolfei. *Febs Lett.* **1992**, *309*, 78–81.
(618) Bertram, P. A.; Karrasch, M.; Schmitz, R. A.; Bocher, R.; Albracht, S. P. J.; Thauer, R. K. Formylmethanofuran Dehydrogenases from Methanogenic Archaea: Substrate Specificity, EPR Properties and Reversible Inactivation by Cyanide of the Molybdenum or Tungsten Iron-Sulfur Proteins. *Eur. J. Biochem.* **1994**, *220*, 477–484.
(619) Bertram, P. A.; Schmitz, R. A.; Linder, D.; Thauer, R. K. Tungstate Can Substitute for Molybdate in Sustaining Growth of Methanobacterium Thermoautotrophicum. Identification and Characterization of a Tungsten Isoenzyme of Formylmethanofuran Dehydrogenase. *Arch. Microbiol.* **1994**, *161*, 220–228.
(620) Schmitz, R. A.; Bertram, P. A.; Thauer, R. K. Tungstate Does Not Support Synthesis of Active Formylmethanofuran Dehydrogenase in Methanosarcina Barkeri. *Arch. Microbiol.* **1994**, *161*, 528–530.
(621) Hochheimer, I.; Schmitz, R. A.; Thauer, R. K.; Hedderich, R. The Tungsten Formylmethanofuran Dehydrogenase from Methanobacterium Thermoautotrophicum Contains Sequence Motifs Characteristic for Enzymes Containing Molybdopterin Dinucleotide. *Eur. J. Biochem.* **1995**, *234*, 910–920.
(622) Wagner, T.; Ermler, U.; Shima, S. The Methanogenic CO2 Reducing-and-Fixing Enzyme Is Bifunctional and Contains 46 [4Fe-4S] Clusters. *Science* . **2016**, *354*, 114–117.
(623) Bertram, P. A.; Thauer, R. K. Thermodynamics of the Formylmethanofuran Dehydrogenase Reaction in Methanobacterium Thermoautotrophicum. *Eur. J. Biochem.* **1994**, *226*, 811–818.
(624) Hochheimer, A.; Hedderich, R.; Thauer, R. K. The Formylmethanofuran Dehydrogenase Isoenzymes in Methanobacterium Wolfei and Methanobacterium Thermoautotrophicum: Induction of the Molybdenum Isoenzyme by Molybdate and Constitutive Synthesis of the Tungsten Isoenzyme. *Arch. Microbiol.* **1998**, *170*, 389–

393.
(625) Hochheimer, A.; Linder, D.; Thauer, R. K.; Hedderich, R. The Molybdenum Formylmethanofuran Dehydrogenase Operon and the Tungsten Formylmethanofuran Dehydrogenase Operon from Methanobacterium Thermoautotrophicum - Structures and Transcriptional Regulation. *Eur. J. Biochem.* **1996**, *242*, 156–162.
(626) Vorholt, J. A.; Vaupel, M.; Thauer, R. K. A Selenium-Dependent and a Selenium-Independent Formylmethanofuran Dehydrogenase and Their Transcriptional Regulation in the Hyperthermophilic Methanopyrus Kandleri. *Mol. Microbiol.* **1997**, *23*, 1033–1042.
(627) Börner, G.; Karrasch, M.; Thauer, R. K. Molybdopterin Adenine Dinucleotide and Molybdopterin Hypoxanthine Dinucleotide in Formylmethanofuran Dehydrogenase from Methanobacterium Thermoautotrophicum (Marburg). *FEBS Lett.* **1991**, *290*, 31–34.
(628) Axley, M. J.; Grahame, D. A.; Stadtman, T. C. Escherichia Coli Formate-Hydrogen Lyase. Purification and Properties of the Selenium-Dependent Formate Dehydrogenase Component. *J. Biol. Chem.* **1990**, *265*, 18213–18218.
(629) Boyington, J. C.; Gladyshev, V. N.; Khangulov, S. V.; Stadtman, T. C.; Sun, P. D. Crystal Structure of Formate Dehydrogenase H: Catalysis Involving Mo, Molybdopterin, Selenocysteine, and an Fe4S4 Cluster. *Science* . **1997**, *275*, 1305–1308.
(630) Gladyshev, V. N.; Boyington, J. C.; Khangulov, S. V; Grahame, D. A.; Stadtman, T. C.; Sun, P. D. Characterization of Crystalline Formate Dehydrogenase H from Escherichia Coli. Stabilization, EPR Spectroscopy, and Preliminary Crystallographic Analysis. *J. Biol. Chem.* **1996**, *271*, 8095–8100.
(631) Gladyshev, V. N.; Khangulov, S. V; Axley, M. J.; Stadtman, T. C. Coordination of Selenium to Molybdenum in Formate Dehydrogenase H from Escherichia Coli. *Proc. Natl. Acad. Sci. U. S. A.* **1994**, *91*, 7708–7711.
(632) Enoch, H. G.; Lester, R. L. The Purification and Properties of Formate Dehydrogenase and Nitrate Reductase from Escherichia Coli. *J. Biol. Chem.* **1975**, *250*, 6693–6705.
(633) Oh, J. I.; Bowien, B. Structural Analysis of the Fds Operon Encoding the NAD+-Linked Formate Dehydrogenase of Ralstonia Eutropha. *J. Biol. Chem.* **1998**, *273*, 26349–26360.
(634) Niks, D.; Duvvuru, J.; Escalona, M.; Hille, R. Spectroscopic and Kinetic Properties of the Molybdenum-Containing, NAD+-Dependent Formate Dehydrogenase from Ralstonia Eutropha. *J. Biol. Chem.* **2016**, *291*, 1162–1174.
(635) Riederer-Henderson, M. A.; Peck, H. D. In Vitro Requirements for Formate Dehydrogenase Activity from Desulfovibrio. *Can. J. Microbiol.* **1986**, *32*, 425–429.
(636) Raaijmakers, H.; Macieira, S.; Dias, J. M.; Teixeira, S.; Bursakov, S.; Huber, R.; Moura, J. J. G.; Moura, I.; Romao, M. J. Gene Sequence and the 1.8 A Crystal Structure of the Tungsten-Containing Formate Dehydrogenase from Desulfovibrio Gigas. *Structure* **2002**, *10*, 1261–1272.
(637) Raaijmakers, H.; Teixeira, S.; Dias, J. M.; Almendra, M. J.; Brondino, C. D.; Moura, I.; Moura, J. J.; Romao, M. J. Tungsten-Containing Formate Dehydrogenase from Desulfovibrio Gigas: Metal Identification and Preliminary Structural Data by Multi-Wavelength Crystallography. *J. Biol. Chem.* **2001**, *6*, 398–404.
(638) Riederer-Henderson, M. A.; Peck, H. D. Properties of Formate Dehydrogenase from Desulfovibrio Gigas. *Can. J. Microbiol.* **1986**, *32*, 430–435.
(639) Laukel, M.; Chistoserdova, L.; Lidstrom, M. E.; Vorholt, J. A. The Tungsten-Containing Formate Dehydrogenase from Methylobacterium Extorquens AM1: Purification and Properties. *Eur. J. Biochem.* **2003**, *270*, 325–333.
(640) Duffus, B. R.; Schrapers, P.; Schuth, N.; Mebs, S.; Dau, H.; Leimkühler, S.; Haumann, M. Anion Binding and Oxidative Modification at the Molybdenum Cofactor of

Formate Dehydrogenase from Rhodobacter Capsulatus Studied by X-Ray Absorption Spectroscopy. *Inorg. Chem.* **2020**, *59*, 214–225.
(641) Schrapers, P.; Hartmann, T.; Kositzki, R.; Dau, H.; Reschke, S.; Schulzke, C.; Leimkühler, S.; Haumann, M. Sulfido and Cysteine Ligation Changes at the Molybdenum Cofactor during Substrate Conversion by Formate Dehydrogenase (FDH) from Rhodobacter Capsulatus. *Inorg. Chem.* **2015**, *54*, 3260–3271.
(642) Iobbi-Nivol, C.; Leimkühler, S. Molybdenum Enzymes, Their Maturation and Molybdenum Cofactor Biosynthesis in Escherichia Coli. *Biochim. Biophys. Acta* **2013**, *1827*, 1086–1101.
(643) Abaibou, H.; Pommier, J.; Benoit, S.; Giordano, G.; Mandrand-Berthelot, M. A. Expression and Characterization of the Escherichia Coli Fdo Locus and a Possible Physiological Role for Aerobic Formate Dehydrogenase. *J. Bacteriol.* **1995**, *177*, 7141–7149.
(644) Thome, R.; Gust, A.; Toci, R.; Mendel, R.; Bittner, F.; Magalon, A.; Walburger, A. A Sulfurtransferase Is Essential for Activity of Formate Dehydrogenases in Escherichia Coli. *J. Biol. Chem.* **2012**, *287*, 4671–4678.
(645) Arnoux, P.; Ruppelt, C.; Oudouhou, F.; Lavergne, J.; Siponen, M. I.; Toci, R.; Mendel, R. R.; Bittner, F.; Pignol, D.; Magalon, A.; et al. Sulphur Shuttling across a Chaperone during Molybdenum Cofactor Maturation. *Nat. Commun.* **2015**, *6*, 6148.
(646) Böhmer, N.; Hartmann, T.; Leimkühler, S. The Chaperone FdsC for Rhodobacter Capsulatus Formate Dehydrogenase Binds the Bis-Molybdopterin Guanine Dinucleotide Cofactor. *FEBS Lett.* **2014**, *588*, 531–537.
(647) Schwanhold, N.; Iobbi-Nivol, C.; Lehmann, A.; Leimkühler, S. Same but Different: Comparison of Two System-Specific Molecular Chaperones for the Maturation of Formate Dehydrogenases. *PLoS One* **2018**, *13*, e0201935.
(648) Arias-Cartin, R.; Grimaldi, S.; Arnoux, P.; Guigliarelli, B.; Magalon, A. Cardiolipin Binding in Bacterial Respiratory Complexes: Structural and Functional Implications. *Biochim. Biophys. Acta* **2012**, *1817*, 1937–1949.
(649) Raaijmakers, H. C.; Romao, M. J. Formate-Reduced E. Coli Formate Dehydrogenase H: The Reinterpretation of the Crystal Structure Suggests a New Reaction Mechanism. *J. Biol. Inorg. Chem.* **2006**, *11*, 849–854.
(650) Khangulov, S. V; Gladyshev, V. N.; Dismukes, G. C.; Stadtman, T. C. Selenium-Containing Formate Dehydrogenase H from Escherichia Coli: A Molybdopterin Enzyme That Catalyzes Formate Oxidation without Oxygen Transfer. *Biochemistry* **1998**, *37*, 3518–3528.
(651) Rivas, M. G.; Gonzalez, P. J.; Brondino, C. D.; Moura, J. J.; Moura, I. EPR Characterization of the Molybdenum(V) Forms of Formate Dehydrogenase from Desulfovibrio Desulfuricans ATCC 27774 upon Formate Reduction. *J. Inorg. Biochem.* **2007**, *101*, 1617–1622.
(652) Barber, M. J.; Siegel, L. M.; Schauer, N. L.; May, H. D.; Ferry, J. G. Formate Dehydrogenase from Methanobacterium Formicicum: Electron Paramagnetic Resonance Spectroscopy of the Molybdenum and Iron-Sulfur Centers. *J. Biol. Chem.* **1983**, *258*, 839–845.
(653) Barber, M. J.; May, H. D.; Ferry, J. G. Inactivation of Formate Dehydrogenase from Methanobacterium Formicicum by Cyanide. *Biochemistry* **1986**, *25*, 8150–8155.
(654) Malthouse, J. P.; Gutteridge, S.; Bray, R. C. Rapid Type 2 Molybdenum(V) Electron-Paramagnetic Resonance Signals from Xanthine Oxidase and the Structure of the Active Centre of the Enzyme. *Biochem. J.* **1980**, *185*, 767–770.
(655) Thauer, R. K.; Fuchs, G.; Käufer, B. Reduced Ferredoxin: CO2 Oxidoreductase from Clostridium Pasteurianum. Effect of Ligands to Transition Metals on the Activity and the Stability of the Enzyme. *Hoppe Seylers Zeitschrift für Physiol. Chemie* **1975**, *356*,

653–662.
(656) Mota, C. S.; Rivas, M. G.; Brondino, C. D.; Moura, I.; Moura, J. J.; Gonzalez, P. J.; Cerqueira, N. M. The Mechanism of Formate Oxidation by Metal-Dependent Formate Dehydrogenases. *J. Biol. Inorg. Chem.* **2011**, *16*, 1255–1268.
(657) Pinsent, J. The Need for Selenite and Molybdate in the Formation of Formic Dehydrogenase by Members of the Coli-Aerogenes Group of Bacteria. *Biochem. J.* **1954**, *57*, 10–16.
(658) Zinoni, F.; Birkmann, A.; Leinfelder, W.; Böck, A. Cotranslational Insertion of Selenocysteine into Formate Dehydrogenase from Escherichia-Coli Directed by a Uga Codon. *Proc. Natl. Acad. Sci. U. S. A.* **1987**, *84*, 3156–3160.
(659) Reich, H. J.; Hondal, R. J. Why Nature Chose Selenium. *ACS Chem. Biol.* **2016**, *11*, 821–841.
(660) George, G. N.; Colangelo, C. M.; Dong, J.; Scott, R. A.; Khangulov, S. V; Gladyshev, V. N.; Stadtman, T. C. X-Ray Absorption Spectroscopy of the Molybdenum Site of Escherichia Coli Formate Dehydrogenase. *J. Am. Chem. Soc.* **1998**, *120*, 1267–1273.
(661) George, G. N.; Costa, C.; Moura, J. G.; Moura, I. Observation of Ligand-Based Redox Chemistry at the Active Site of a Molybdenum Enzyme. *J. Am. Chem. Soc.* **1999**, *121*, 2625–2626.
(662) Heider, J.; Bock, A. Selenium Metabolism in Micro-Organisms. *Adv. Microb. Physiol.* **1993**, *35*, 71–109.
(663) Jormakka, M.; Törnroth, S.; Byrne, B.; Iwata, S. Molecular Basis of Proton Motive Force Generation: Structure of Formate Dehydrogenase-N. *Science* . **2002**, *295*, 1863–1868.
(664) Jollie, D. R.; Lipscomb, J. D. Formate Dehydrogenase from Methylosinus Trichosporium Ob3b: Purification and Spectroscopic Characterization of the Cofactors. *J. Biol. Chem.* **1991**, *266*, 21853–21863.
(665) Friedebold, J.; Bowien, B. Physiological and Biochemical Characterization of the Soluble Formate Dehydrogenase, a Molybdoenzyme from Alcaligenes Eutrophus. *J. Bacteriol.* **1993**, *175*, 4719–4728.
(666) Yamamoto, I.; Saiki, T.; Liu, S.-M.; Ljungdahl, L. G. Purification and Properties of NADP-Dependent Formate Dehydrogenase from Clostridium Thermoaceticum, a Tungsten-Selenium-Iron Protein. *J. Biol. Chem.* **1983**, *258*, 1826–1832.
(667) Schauer, N. L.; Ferry, J. G. Properties of Formate Dehydrogenase in Methanobacterium Formicicum. *J. Bacteriol.* **1982**, *150*, 1–7.
(668) Robinson, W. E.; Bassegoda, A.; Reisner, E.; Hirst, J. Oxidation-State-Dependent Binding Properties of the Active Site in a Mo-Containing Formate Dehydrogenase. *J. Am. Chem. Soc.* **2017**, *139*, 9927–9936.
(669) THAUER, R. K.; KAUFER, B.; FUCHS, G. The Active Species of "CO2" Utilized by Reduced Ferredoxin: CO2 Oxidoreductase from Clostridium Pasteurianum. *Eur. J. Biochem.* **1975**, *55*, 111–117.
(670) Cooper, T. G.; Tchen, T. T.; Wood, H. G.; Benedict, C. R. The Carboxylation of Phosphoenolpyruvate and Pyruvate. I. The Active Species of "CO2" Utilized by Phosphoenolpyruvate Carboxykinase, Carboxytransphosphorylase, and Pyruvate Carboxylase. *J. Biol. Chem.* **1968**, *243*, 3857–3863.
(671) Chan, M. K.; Mukund, S.; Kletzin, A.; Adams, M. W. W.; Rees, D. C. Structure of a Hyperthermophilic Tungstopterin Enzyme, Aldehyde Ferredoxin Oxidoreductase. *Science* . **1995**, *267*, 1463–1469.
(672) Tiberti, M.; Papaleo, E.; Russo, N.; Gioia, L. De; Zampella, G. Evidence for the Formation of a Mo − H Intermediate in the Catalytic Cycle of Formate Dehydrogenase. *Inorg. Chem.* **2012**, *51*, 8331−8339.
(673) Dong, G.; Ryde, U. Reaction Mechanism of Formate Dehydrogenase Studied by

Computational Methods. *J. Biol. Inorg. Chem.* **2018**, *23*, 1243–1254.
(674) Niks, D.; Hille, R. Reductive Activation of CO2 by Formate Dehydrogenases. *Methods Enzymol.* **2018**, *613*, 277–295.
(675) Najmudin, S.; Gonzalez, P. J.; Trincao, J.; Coelho, C.; Mukhopadhyay, A.; Cerqueira, N. M.; Romao, C. C.; Moura, I.; Moura, J. J.; Brondino, C. D.; et al. Periplasmic Nitrate Reductase Revisited: A Sulfur Atom Completes the Sixth Coordination of the Catalytic Molybdenum. *J. Biol. Inorg. Chem.* **2008**, *13*, 737–753.
(676) Boyington, J. C.; Gladyshev, V. N.; Khangulov, S. V; Stadtman, T. C.; Sun, P. D. Crystal Structure of Formate Dehydrogenase H: Catalysis Involving Mo, Molybdopterin, Selenocysteine, and an Fe4S4 Cluster. *Science* . **1997**, *275*, 1305–1308.
(677) Raaijmakers, H.; Macieira, S.; Dias, J. M.; Teixeira, S.; Bursakov, S.; Huber, R.; Moura, J. J.; Moura, I.; Romao, M. J. Gene Sequence and the 1.8 A Crystal Structure of the Tungsten-Containing Formate Dehydrogenase from Desulfovibrio Gigas. *Structure* **2002**, *10*, 1261–1272.
(678) Hille, R.; Dingwall, S.; Wilcoxen, J. The Aerobic CO Dehydrogenase from Oligotropha Carboxidovorans. *J. Biol. Inorg. Chem.* **2015**, *20*, 243–251.
(679) Kaufmann, P.; Duffus, B. R.; Teutloff, C.; Leimkühler, S. Functional Studies on Oligotropha Carboxidovorans Molybdenum-Copper CO Dehydrogenase Produced in Escherichia Coli. *Biochemistry* **2018**, *57*, 2889–2901.
(680) Can, M.; Armstrong, F. A.; Ragsdale, S. W. Structure, Function, and Mechanism of the Nickel Metalloenzymes, CO Dehydrogenase, and Acetyl-CoA Synthase. *Chem. Rev.* **2014**, *114*, 4149–4174.
(681) Wu, M.; Ren, Q.; Durkin, A. S.; Daugherty, S. C.; Brinkac, L. M.; Dodson, R. J.; Madupu, R.; Sullivan, S. A.; Kolonay, J. F.; Nelson, W. C.; et al. Life in Hot Carbon Monoxide: The Complete Genome Sequence of Carboxydothermus Hydrogenoformans Z-2901. *PLoS Genet.* **2005**, *1*, e65.
(682) Wittenborn, E. C.; Merrouch, M.; Ueda, C.; Fradale, L.; Léger, C.; Fourmond, V.; Pandelia, M.-E.; Dementin, S.; Drennan, C. L. Redox-Dependent Rearrangements of the NiFeS Cluster of Carbon Monoxide Dehydrogenase. *Elife* **2018**, *7*, e39451.
(683) Ragsdale, S. W.; Pierce, E. Acetogenesis and the Wood-Ljungdahl Pathway of CO2 Fixation. *Biochim. Biophys. Acta - Proteins Proteomics* **2008**, *1784*, 1873–1898.
(684) Gong, W.; Hao, B.; Wei, Z.; Ferguson, D. J.; Tallant, T.; Krzycki, J. A.; Chan, M. K. Structure of the A2ε2 Ni-Dependent CO Dehydrogenase Component of the Methanosarcina Barkeri Acetyl-CoA Decarbonylase/Synthase Complex. *Proc. Natl. Acad. Sci. U. S. A.* **2008**, *105*, 9558–9563.
(685) Doukov, T. I.; Iverson, T. M.; Seravalli, J.; Ragsdale, S. W.; Drennan, C. L. A Ni-Fe-Cu Center in a Bifunctional Carbon Monoxide Dehydrogenase/Acetyl-CoA Synthase. *Science* . **2002**, *298*, 567–572.
(686) Domnik, L.; Merrouch, M.; Goetzl, S.; Jeoung, J. H.; Léger, C.; Dementin, S.; Fourmond, V.; Dobbek, H. CODH-IV: A High-Efficiency CO-Scavenging CO Dehydrogenase with Resistance to O2. *Angew. Chemie - Int. Ed.* **2017**, *56*, 15466–15469.
(687) Jeoung, J.-H.; Dobbek, H. Carbon Dioxide Activation at the Ni,Fe-Cluster of Anaerobic Carbon Monoxide Dehydrogenase. *Science* **2007**, *318*, 1461–1464.
(688) Inoue, M.; Nakamoto, I.; Omae, K.; Oguro, T.; Ogata, H.; Yoshida, T.; Sako, Y. Structural and Phylogenetic Diversity of Anaerobic Carbon-Monoxide Dehydrogenases. *Front. Microbiol.* **2019**, *9*, 3353.
(689) Kim, E. J.; Feng, J.; Bramlett, M. R.; Lindahl, P. A. Evidence for a Proton Transfer Network and a Required Persulfide-Bond-Forming Cysteine Residue in Ni-Containing Carbon Monoxide Dehydrogenases. *Biochemistry* **2004**, *43*, 5728–5734.
(690) Wittenborn, E. C.; Cohen, S. E.; Merrouch, M.; Léger, C.; Fourmond, V.; Dementin,

S.; Drennan, C. L. Structural Insight into Metallocofactor Maturation in Carbon Monoxide Dehydrogenase. *J. Biol. Chem.* **2019**, *294*, 13017–13026.
(691) Merrouch, M.; Hadj-Saïd, J.; Domnik, L.; Dobbek, H.; Léger, C.; Dementin, S.; Fourmond, V. O2 Inhibition of Ni-Containing CO Dehydrogenase Is Partly Reversible. *Chem. - A Eur. J.* **2015**, *21*, 18934–18938.
(692) Wittenborn, E. C.; Guendon, C.; Merrouch, M.; Benvenuti, M.; Fourmond, V.; Léger, C.; Drennan, C. L.; Dementin, S. The Solvent-Exposed Fe-S D-Cluster Contributes to Oxygen-Resistance in Desulfovibrio Vulgaris Ni-Fe Carbon Monoxide Dehydrogenase. *ACS Catal.* **2020**, *10*, 7328–7335.
(693) Inoue, T.; Takao, K.; Yoshida, T.; Wada, K.; Daifuku, T.; Yoneda, Y.; Fukuyama, K.; Sako, Y. Cysteine 295 Indirectly Affects Ni Coordination of Carbon Monoxide Dehydrogenase-II C-Cluster. *Biochem. Biophys. Res. Commun.* **2013**, *441*, 13–17.
(694) Jeon, W. B.; Singer, S. W.; Ludden, P. W.; Rubio, L. M. New Insights into the Mechanism of Nickel Insertion into Carbon Monoxide Dehydrogenase: Analysis of Rhodospirillum Rubrum Carbon Monoxide Dehydrogenase Variants with Substituted Ligands to the [Fe3S4] Portion of the Active-Site C-Cluster. *J. Biol. Inorg. Chem.* **2005**, *10*, 903–912.
(695) Fraser, D. M.; Lindahl, P. A. Evidence for a Proposed Intermediate Redox State in the CO/CO2 Active Site of Acetyl-CoA Synthase (Carbon Monoxide Dehydrogenase) from Clostridium Thermoaceticum. *Biochemistry* **1999**, *38*, 15706–15711.
(696) Lindahl, P. A. Implications of a Carboxylate-Bound C-Cluster Structure of Carbon Monoxide Dehydrogenase. *Angew. Chemie - Int. Ed.* **2008**, *47*, 4054–4056.
(697) Amara, P.; Mouesca, J.-M.; Volbeda, A.; Fontecilla-Camps, J. C. Carbon Monoxide Dehydrogenase Reaction Mechanism: A Likely Case of Abnormal CO 2 Insertion to a Ni−H − Bond. *Inorg. Chem.* **2011**, *50*, 1868–1878.
(698) Yang, J. Y.; Kerr, T. A.; Wang, X. S.; Barlow, J. M. Reducing CO2 to HCO2- at Mild Potentials: Lessons from Formate Dehydrogenase. *J. Am. Chem. Soc.* **2020**, *142*, 19438–19445.
(699) Breglia, R.; Arrigoni, F.; Sensi, M.; Greco, C.; Fantucci, P.; De Gioia, L.; Bruschi, M. First-Principles Calculations on Ni,Fe-Containing Carbon Monoxide Dehydrogenases Reveal Key Stereoelectronic Features for Binding and Release of CO2to/ from the C-Cluster. *Inorg. Chem.* **2021**, *60*, 387–402.
(700) Maynard, E. L.; Lindahl, P. A. Evidence of a Molecular Tunnel Connecting the Active Sites for CO2 Reduction and Acetyl-CoA Synthesis in Acetyl-CoA Synthase from Clostridium Thermoaceticum. *J. Am. Chem. Soc.* **1999**, *121*, 9221–9222.
(701) Seravalli, J.; Ragsdale, S. W. Channeling of Carbon Monoxide during Anaerobic Carbon Dioxide Fixation. *Biochemistry* **2000**, *39*, 1274–1277.
(702) Darnault, C.; Volbeda, A.; Kim, E. J.; Legrand, P.; Vernède, X.; Lindahl, P. A.; Fontecilla-Camps, J. C. Ni-Zn-[Fe4-S4] and Ni-Ni-[Fe4-S4] Clusters in Closed and Open α Subunits of Acetyl-CoA Synthase/Carbon Monoxide Dehydrogenase. *Nat. Struct. Biol.* **2003**, *10*, 271–279.
(703) Doukov, T. I.; Blasiak, L. C.; Seravalli, J.; Ragsdale, S. W.; Drennan, C. L. Xenon in and at the End of the Tunnel of Bifunctional Carbon Monoxide Dehydrogenase/Acetyl-CoA Synthase. *Biochemistry* **2008**, *47*, 3474–3483.
(704) Volbeda, A.; Fontecilla-Camps, J. C. Crystallographic Evidence for a CO/CO2 Tunnel Gating Mechanism in the Bifunctional Carbon Monoxide Dehydrogenase/Acetyl Coenzyme A Synthase from Moorella Thermoacetica. *J. Biol. Inorg. Chem.* **2004**, *9*, 525–532.
(705) Tan, X.; Loke, H. K.; Fitch, S.; Lindahl, P. A. The Tunnel of Acetyl-Coenzyme A Synthase/Carbon Monoxide Dehydrogenase Regulates Delivery of CO to the Active Site. *J. Am. Chem. Soc.* **2005**, *127*, 5833–5839.

(706) Tan, X.; Lindahl, P. A. Tunnel Mutagenesis and Ni-Dependent Reduction and Methylation of the α Subunit of Acetyl Coenzyme A Synthase/Carbon Monoxide Dehydrogenase. *J. Biol. Inorg. Chem.* **2008**, *13*, 771–778.
(707) Biester, A.; Dementin, S.; Drennan, C. L. Visualizing the Gas Channel of a Monofunctional Carbon Monoxide Dehydrogenase. *J. Inorg. Biochem.* **2022**, *230*, 111774.
(708) Tan, X.; Volbeda, A.; Fontecilla-Camps, J. C.; Lindahl, P. A. Function of the Tunnel in Acetylcoenzyme A Synthase/Carbon Monoxide Dehydrogenase. *J. Biol. Inorg. Chem.* **2006**, *11*, 371–378.
(709) Wang, P. H.; Bruschi, M.; De Gioia, L.; Blumberger, J. Uncovering a Dynamically Formed Substrate Access Tunnel in Carbon Monoxide Dehydrogenase/Acetyl-CoA Synthase. *J. Am. Chem. Soc.* **2013**, *135*, 9493–9502.
(710) Dobbek, H.; Svetlitchnyi, V.; Gremer, L.; Huber, R.; Meyer, O. Crystal Structure of a Carbon Monoxide Dehydrogenase Reveals a [Ni-4Fe-5S] Cluster. *Science* **2001**, *293*, 1281–1285.
(711) Drennan, C. L.; Heo, J.; Sintchak, M. D.; Schreiter, E.; Ludden, P. W. Life on Carbon Monoxide: X-Ray Structure of Rhodospirillum Rubrum Ni-Fe-S Carbon Monoxide Dehydrogenase. *Proc. Natl. Acad. Sci. U. S. A.* **2001**, *98*, 11973–11978.
(712) Ensign, S. A.; Hyman, M. R.; Ludden, P. W. Nickel-Specific, Slow-Binding Inhibition of Carbon Monoxide Dehydrogenase from Rhodospirillum Rubrum by Cyanide. *Biochemistry* **1989**, *28*, 4973–4979.
(713) Hadj-Saïd, J.; Pandelia, M. E.; Léger, C.; Fourmond, V.; Dementin, S. The Carbon Monoxide Dehydrogenase from Desulfovibrio Vulgaris. *Biochim. Biophys. Acta - Bioenerg.* **2015**, *1847*, 1574–1583.
(714) Benvenuti, M.; Meneghello, M.; Guendon, C.; Jacq-Bailly, A.; Jeoung, J.-H.; Dobbek, H.; Léger, C.; Fourmond, V.; Dementin, S. The Two CO-Dehydrogenases of Thermococcus Sp. AM4. *Biochim. Biophys. Acta - Bioenerg.* **2020**, *1861*, 148188.
(715) Parkin, A.; Seravalli, J.; Vincent, K. A.; Ragsdale, S. W.; Armstrong, F. A. Rapid and Efficient Electrocatalytic CO2/CO Interconversions by Carboxydothermus Hydrogenoformans CO Dehydrogenase I on an Electrode. *J. Am. Chem. Soc.* **2007**, *129*, 10328–10329.
(716) Ensign, S. A. Reactivity of Carbon Monoxide Dehydrogenase from Rhodospirillum Rubrum with Carbon Dioxide, Carbonyl Sulfide, and Carbon Disulfide. *Biochemistry* **1995**, *34*, 5372–5381.
(717) Bonham, D.; Murrell, S. A.; Ludden, P. W. Carbon Monoxide Dehydrogenase from Rhodospirillum Rubrum. *J. Bacteriol.* **1984**, *159*, 693–699.
(718) Snider, M. G.; Temple, B. S.; Wolfenden, R. The Path to the Transition State in Enzyme Reactions: A Survey of Catalytic Efficiencies. *J. Phys. Org. Chem.* **2004**, *17*, 586–591.
(719) Prangé, T.; Schiltz, M.; Pernot, L.; Colloc'h, N.; Longhi, S.; Bourguet, W.; Fourme, R. Exploring Hydrophobic Sites in Proteins With Xenon or Krypton. *Proteins Struct. Funct. Genet.* **1998**, *30*, 61–73.
(720) Richards, F. M. Areas, Volumes, Packing and Protein Structure. *Annual review of biophysics and bioengineering*. June 1977, pp 151–176.
(721) Plumeré, N.; Rüdiger, O.; Oughli, A. A.; Williams, R.; Vivekananthan, J.; Pöller, S.; Schuhmann, W.; Lubitz, W. A Redox Hydrogel Protects Hydrogenase from High-Potential Deactivation and Oxygen Damage. *Nat. Chem.* **2014**, *6*, 822–827.
(722) Li, H.; Buesen, D.; Dementin, S.; Léger, C.; Fourmond, V.; Plumeré, N. Complete Protection of O2-Sensitive Catalysts in Thin Films. *J. Am. Chem. Soc.* **2019**, *141*, 16734–16742.
(723) Hardt, S.; Stapf, S.; Filmon, D. T.; Birrell, J. A.; Rüdiger, O.; Fourmond, V.; Léger, C.;

Plumeré, N. Reversible H2 Oxidation and Evolution by Hydrogenase Embedded in a Redox Polymer Film. *Nat. Catal.* **2021**, *4*, 251–258.
(724) Wraight, C. A. Chance and Design-Proton Transfer in Water, Channels and Bioenergetic Proteins. *Biochim. Biophys. Acta - Bioenerg.* **2006**, *1757*, 886–912.
(725) Gray, H. B.; Winkler, J. R. Electron Tunneling through Proteins. *Q. Rev. Biophys.* **2003**, *36*, 341–372.
(726) Feng, X.; Schut, G. J.; Haja, D. K.; Adams, M. W. W.; Li, H. Structure and Electron Transfer Pathways of an Electron-Bifurcating NiFe-Hydrogenase. *Sci. Adv.* **2022**, *8*, 1–14.
(727) Oughli, A. A.; Ruff, A.; Boralugodage, N. P.; Rodríguez-Maciá, P.; Plumeré, N.; Lubitz, W.; Shaw, W. J.; Schuhmann, W.; Rüdiger, O. Dual Properties of a Hydrogen Oxidation Ni-Catalyst Entrapped within a Polymer Promote Self-Defense against Oxygen. *Nat. Commun.* **2018**, *9*, 864.
(728) Evans, R. M.; Brooke, E. J.; Wehlin, S. A.; Nomerotskaia, E.; Sargent, F.; Carr, S. B.; Phillips, S. E.; Armstrong, F. A. Mechanism of Hydrogen Activation by [NiFe] Hydrogenases. *Nat. Chem. Biol.* **2016**, *12*, 46–50.

Table of Contents